Investigation of Nanostructure-Induced Localized Light Phenomena Using Ultrafast Laser Spectroscopy

Dissertation zur Erlangung
des naturwissenschaftlichen Doktorgrades
der Julius-Maximilians-Universität Würzburg

vorgelegt von

Christian Kramer

aus Würzburg

Würzburg 2017

Eingereicht bei der Fakultät für Chemie und Pharmazie am ____________________

Gutachter der schriftlichen Arbeit
1. Gutachter: Prof. Dr. T. Brixner
2. Gutachter: ____________________

Prüfer des öffentlichen Promotionskolloquiums
1. Prüfer: Prof. Dr. T. Brixner
2. Prüfer: ____________________
3. Prüfer: ____________________

Datum des Promotionskolloquiums: ____________________

Doktorurkunde ausgehändigt am ____________________

List of Publications

[1] M. Aeschlimann, T. Brixner, A. Fischer, C. Kramer, P. Melchior, W. Pfeiffer, C. Schneider, C. Strüber, P. Tuchscherer, and D.V. Voronine.
Coherent Two-Dimensional Nanoscopy.
Science **333**, 1723–1726 (2011).
http://science.sciencemag.org/content/333/6050/1723

[2] M. Aeschlimann, T. Brixner, D. Differt, U. Heinzmann, M. Hensen, C. Kramer, F. Lükermann, P. Melchior, W. Pfeiffer, M. Piecuch, C. Schneider, H. Stiebig, C. Strüber, and P. Thielen.
Perfect Absorption in Nanotextured Thin Films via Anderson-Localized Photon Modes.
Nature Photonics **9**, 663–668 (2015).
http://www.nature.com/nphoton/journal/v9/n10/full/nphoton.2015.159.html

[3] M. Aeschlimann, T. Brixner, A. Fischer, M. Hensen, B. Huber, D. Kilbane, C. Kramer, W. Pfeiffer, M. Piecuch, and P. Thielen.
Determination of Local Optical Response Functions of Nanostructures with Increasing Complexity by Using Single and Coupled Lorentzian Oscillator Models.
Applied Physics B, 122:199 (2016).
http://link.springer.com/article/10.1007/s00340-016-6471-3

[4] C. Kramer, M. Schäferling, T. Weiss, H. Giessen, and T. Brixner.
Analytic Optimization of Near-Field Optical Chirality Enhancement.
ACS Photonics **4**, 396–406 (2017).
http://pubs.acs.org/doi/abs/10.1021/acsphotonics.6b00887

[5] M. Aeschlimann, T. Brixner, M. Cinchetti, B. Frisch, B. Hecht, M. Hensen, B. Huber, C. Kramer, E. Krauss, T. Löber, W. Pfeiffer, M. Piecuch, and P. Thielen.
Cavity-Assisted Ultrafast Long-Range Periodic Energy Transfer between Plasmonic Nanoantennas.
Submitted for publication (2017).

[6] M. Aeschlimann, T. Brixner, M. Cinchetti, N. Haag, M. Hensen, B. Huber, C. Kramer, J. Kollamana, W. Pfeiffer, M. Piecuch, C. Schneider, B. Stadtmüller, and P. Thielen.
Long-Lived Coherence at a Ferromagnet-Organic Interface.
In preparation (2017).

Parts of this PhD thesis have been published in some of the peer-reviewed journal articles listed on pp. III–IV. The following table itemizes to what extent the text and the figures of the publications have been reused at which position in this work. The sources of adapted figures are additionally indicated at the end of the corresponding figure captions.

Publication	Usage	Dissertation
Ref. [1][1]		
pp. 1–2; SI pp. 2–4,	text reproduced, modified, and extended; figures adapted	pp. 8–15
Ref. [2]		
pp. 1–5; SI pp. 2–5, 10–11, 16–28	text reproduced, modified, and extended; figures adapted	pp. 27–50
Ref. [4][2]		
pp. 1–9; SI pp. 1–2, 4–5, 10–19	text reproduced, minor modifications; figures adapted	pp. 77–104
SI pp. 2–4, 6–10	text reproduced, minor modifications; figure adapted	pp. 117–123
Ref. [5] (submitted)		
	text reproduced, modified, and extended; figures adapted	pp. 51–64
	figure in part adapted	p. 65
	text reproduced, modified, and extended; figures adapted	pp. 70–76

---

[1] Reproduced in part and adapted with permission from Science, 2011, **333**, 1723–1726. © (2011) American Association for the Advancement of Science.

[2] Reproduced and adapted with permission from ACS Photonics, 2017, **4**, 396–406. This article is available under the ACS AuthorChoice license. Further permission requests should be directed to the ACS. © (2017) American Chemical Society.

Contents

1 Introduction

The nature of light has always been fascinating from the researchers' point of view. After gaining knowledge about how light can be generated, artificial light sources such as incandescent light bulbs [7], gas-discharge lamps [8], and light emitting diodes (LEDs) [9, 10] were developed and facilitate our daily life. But light is not only important to us in order to perceive our environment. The interaction of light with matter leads to a manifold of interesting phenomena. For instance, the absorption of sunlight, i.e., the energy transfer from sunlight to matter, is the fundamental basis for photosynthesis and thus for life on our planet. The understanding of the mechanism behind this phenomenon gave rise to the invention of many useful applications, e.g., in solar cell technology where the direct conversion of sunlight into electricity is studied. Moreover, reflection on surfaces provides the opportunity of routing light into desired directions. In 1960, the development of the laser [11, 12] — a device that emits coherent light on the basis of stimulated emission of electromagnetic radiation — enabled guiding light over larger distances as well as focusing it onto tighter spots. This opened up new possibilities to steer light and was the starting point for a variety of new research fields. In laser spectroscopy, the interaction of matter with incident laser light is exploited to obtain information about the optical response of investigated samples. In order to resolve light-induced dynamics, pulsed lasers with finite spectral bandwidth are employed. Very fast processes such as transition states of chemical reactions [13, 14] can be explored with a temporal resolution in the femtosecond regime by using ultrashort laser pulses. Furthermore, it is even possible to coherently control the outcome of light-matter interactions, e.g., the products of photodissociation reactions, via femtosecond pulse shaping techniques [15, 16].

One scientific goal of the last decades was to study and/or control light-induced dynamics not only with ever-improving temporal resolution but also on ever-smaller volumes. However, in the far field, light cannot be spatially confined below the optical diffraction limit which is given by its wavelength, i.e., several hundreds of nanometers [17]. Artificially fabricated nanomaterials such as photonic nanocrystals [18] or plasmonic nanostructures [19] can be utilized to manipulate and tailor electromagnetic fields at the nanoscale and therefore well below this limit. For instance, the resonant excitation of a metallic nanoparticle leads to the formation of a localized surface plasmon resonance, i.e., a coherent mode of electromagnetic fields and the collective electronic motion at the surface of the particle. As a consequence of this resonance, the resulting near field in the vicinity of the particle is locally enhanced. Since the interaction of light with such nanomaterials strongly depends on the local position, it is important to get insights into both the temporal and spatial evolution of the local fields.

In this thesis, three localized light phenomena arising from the interaction with nanostructured materials are investigated by using ultrafast laser spectroscopy with high temporal and high spatial resolution. The outline of this thesis is as follows. After the introduction, the theoretical basics and the experimental implementation of coherent two-dimensional (2D) nanoscopy are described in Chapter 2. This novel spectroscopic technique was introduced in 2011 within a collaboration of our research group with the research groups of Martin Aeschlimann and Walter Pfeiffer, and ensures femtosecond time resolution as well as spatial resolution at the nanoscale [1]. In Chapter 3, the optical setups of the experiments presented in this work are illustrated and explained in detail.

The investigation of the first localized light phenomenon is then described in Chapter 4. Thin-film silicon solar cells with nanotextured interfaces reveal enhanced absorption of near-infrared light compared to equivalent devices with smooth interfaces. However, the reason for this enhancement has been unclear so far. Here, solar cell devices with smooth and nanotextured interfaces are explored via time-resolved experiments, using ultrashort laser pulses in the near-infrared regime. Coherent backscattering spectroscopy and coherent 2D nanoscopy are utilized to obtain information about the light dynamics within the nanotextured absorber layer and to clarify the mechanism behind the absorption enhancement.

In Chapter 5, a novel hybridized plasmonic device is introduced that consists of two plasmonic nanoantennas located in an elliptcal plasmonic cavity. The goal is to realize a periodic long-range energy transfer between the two nanoantennas on the basis of strong coupling between the localized antenna modes and the spatially extended cavity mode. First, the device is optimized in theory with respect to strong coupling by means of finite-difference time-domain (FDTD) simulations. Then, the evolution of the local electromagnetic field distribution within the optimized device, especially at the antenna positions, is investigated upon pulsed excitation. In order to confirm the theoretical results, fabricated devices are investigated by means of time-resolved correlation measurements, using collinear sequences of two ultrashort laser pulses.

The third localized light phenomenon presented in Chapter 6 of this thesis is about the local enhancement of optical chirality in the vicinity of plasmonic nanostructures. In general, optical chirality is a physical entity that describes the chiral nature of electromagnetic fields and thus co-determines the strength of chiral light-matter interactions. Plasmonic nanostructures are suited to locally enhance optical chirality in their near fields [20–24]. However, the enhancement has solely focused on the design of the nanostructures so far. Here, it is taken into account that the optical near-field response of nanostructures depends on the far-field polarization of the incident light. An analytic function is derived that enables the calculation of the optimal far-field polarization, i.e., that far-field polarization which leads to optimal local optical chirality. In simulations with two different plasmonic nanostructures the optimization of local optical chirality enhancement is exemplariy demonstrated. Furthermore, it is shown how femtosecond polarization pulse shaping can be used to coherently control the optical chirality enhancement over a continuous frequency range.

Finally, the experimental and theoretical results of this work are summarized in Chapter 7.

2 Coherent Two-Dimensional (2D) Nanoscopy

Coherent two-dimensional (2D) nanoscopy was introduced and experimentally implemented for the first time within a collaboration of our research group with the research groups of Walter Pfeiffer and Martin Aeschlimann [1]. This technique combines the concept of coherent two-dimensional (2D) spectroscopy with photoemission electron microscopy (PEEM). It ensures high temporal resolution by using ultrashort laser pulses for excitation, as well as high spatial resolution below the optical diffraction limit due to the detection of electrons. Since 2D nanoscopy was employed for the experiment described in Sect. 4.4, its theoretical background and experimental implementation are explained in detail in this chapter. Starting with the principles of conventional 2D spectroscopy (Sect. 2.1), the main idea of 2D nanoscopy is presented in Sect. 2.2. After that, it is discussed which spectral information about the optical response of investigated samples is obtained via 2D nanoscopy (Sect. 2.3) and how this information is extracted from the total measurement signal via phase-cycling (Sect. 2.4).

2.1 Principles of Coherent Two-Dimensional (2D) Spectroscopy

Coherent 2D spectroscopy is a powerful technique to study ultrafast dynamics, energy transfer, and coupling within quantum systems. In this section, the fundamental principles of this method are presented on the basis of Refs. [25–28].

In conventional 2D spectroscopy, the investigated quantum systems are excited by a sequence of three ultrashort laser pulses, leading to a third-order polarization due to three interactions with the electric field of the incident pulse sequence. The induced third-order polarization gives rise to the emission of an optical signal that depends on the time delays between the pulses. Using perturbation theory, the third-order polarization at time t and one point in space $\mathbf{r}$ is given by [25, 27]

$$P^{(3)}(\mathbf{r},t) = \int_0^\infty \mathrm{d}\tau_3 \int_0^\infty \mathrm{d}\tau_2 \int_0^\infty \mathrm{d}\tau_1 \, S^{(3)}(\tau_1,\tau_2,\tau_3) \times E(\mathbf{r},t-\tau_3)E(\mathbf{r},t-\tau_3-\tau_2)E(\mathbf{r},t-\tau_3-\tau_2-\tau_1)\,, \tag{2.1}$$

wherein $S^{(3)}(\tau_3,\tau_2,\tau_1)$ is the real-valued third-order response function, and the times of the three light-matter interactions are defined by $t-\tau_3-\tau_2-\tau_1$, $t-\tau_3-\tau_2$, and $t-\tau_3$ (see

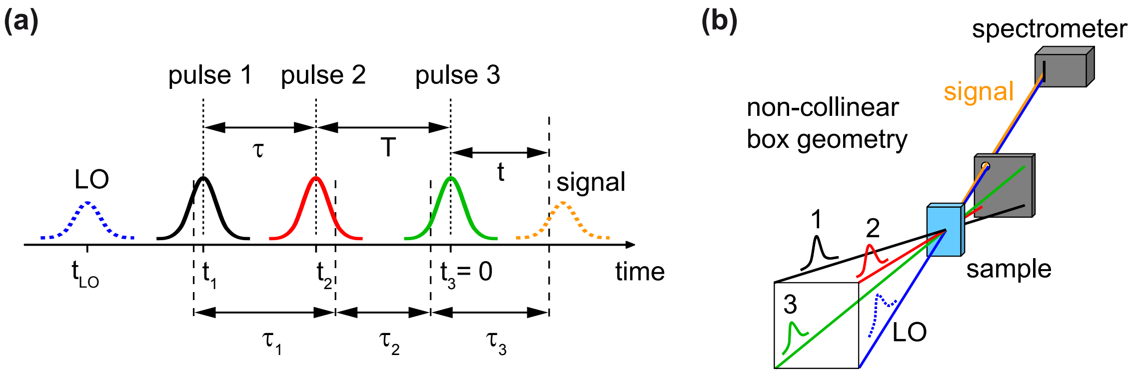

Figure 2.1: Scheme of a coherent 2D spectroscopy experiment. (a) A sequence of three ultrashort laser pulses centered at t_1 (black), t_2 (red), and $t_3 = 0$ (green) with variable time delays τ (between pulse 1 and pulse 2) and T (between pulse 2 and pulse 3) induce a third-order nonlinear polarization in the investigated sample. Each pulse interacts once with the sample at times $t - \tau_1 - \tau_2 - \tau_3$, $t - \tau_2 - \tau_3$, and $t - \tau_3$. Due to the induced polarization an optical signal (dotted orange) is emitted. A reference pulse with known spectral phase, the so-called local oscillator (LO, dotted blue), is used to determine the electric field of the emitted signal via spectral interferometry (SI) [29]. (b) The three excitation pulses are arranged in a non-collinear box geometry. The propagation direction of the pulses is defined by their wave vectors $\mathbf{k}_1$, $\mathbf{k}_2$, and $\mathbf{k}_3$. Due to phase matching the desired optical signal is emitted in direction $\mathbf{k}_s = -\mathbf{k}_1 + \mathbf{k}_2 + \mathbf{k}_3$ and detected via a spectrometer. The LO is spatially overlapped with the emitted signal for characterization via SI. Figure adapted from Ref. [30].

Fig. 2.1a). The real-valued temporal electric field of the incident pulse sequence can be expressed via [27]

$$\begin{aligned} E(\mathbf{r},t) =& \tilde{A}(t-t_1)\,\mathrm{e}^{-\mathrm{i}\omega_0(t-t_1)+\mathrm{i}\mathbf{k}_1\mathbf{r}} + \tilde{A}(t-t_2)\,\mathrm{e}^{-\mathrm{i}\omega_0(t-t_2)+\mathrm{i}\mathbf{k}_2\mathbf{r}} \\ &+ \tilde{A}(t-t_3)\,\mathrm{e}^{-\mathrm{i}\omega_0(t-t_3)+\mathrm{i}\mathbf{k}_3\mathbf{r}} + c.c. \end{aligned} \tag{2.2}$$

with *c.c.* denoting the complex conjugate. The first three terms in Eq. (2.2) represent one pulse each with the center frequency ω_0, the complex envelope function $\tilde{A}(t - t_j)$ with $j = \{1, 2, 3\}$, and the temporal shift t_j. The wave vector $\mathbf{k}_j$ determines the propagation direction of the corresponding pulse. As indicated in Fig. 2.1a, the time delay between the first and the second pulse is called coherence time $\tau = t_2 - t_1$, while the time delay between the second and the third pulse is called population time $T = t_3 - t_2$. Substituting Eq. (2.2) in Eq. (2.1) leads to $6^3 = 216$ terms each of which contain a multiplication of three complex envelope functions and their phase factors including, among other things, the corresponding wave vectors. All these terms contribute to the third-order polarization and lead to the radiation of an optical signal. However, there are terms that arise from interactions with only one or two pulses and thus are independent from the two time delays or depend on only one of them. To extract those terms which originate from one interaction with one pulse each the so-called phase matching is applied. Due to the limited spatial resolution of 2D spectroscopy, a high number of quantum systems is excited simultaneously and the radiated optical signals of each term interfere constructively along the direction that is determined by the addition of the three wave vectors within the phase factor of the term. This effect is exploited by arranging the three pulses in a non-collinear box geometry and detecting only the optical signals that propagate in direction $\mathbf{k}_s = -\mathbf{k}_1 + \mathbf{k}_2 + \mathbf{k}_3$ (see Fig. 2.1b) [31–33]. As a result, the number of terms is reduced from 216 to six which contain all the common phase factor

$$\mathrm{e}^{-\mathrm{i}\omega_0(t+t_1-t_2-t_3)} = \mathrm{e}^{-\mathrm{i}\omega_0(t-\tau)}, \tag{2.3}$$

as well as one of the phase factors

$$\mathrm{e}^{\mathrm{i}\omega_0(\tau_3-\tau_1)},\ \mathrm{e}^{\mathrm{i}\omega_0(\tau_3+\tau_1)},\quad \text{or}\quad \mathrm{e}^{\mathrm{i}\omega_0(\tau_1+2\tau_2+\tau_3)}. \tag{2.4}$$

Note that t_3 is set to zero in Eq. (2.3), i.e., the third pulse is centered at time zero. Applying the rotating wave approximation (RWA) [34] and assuming that the center frequency ω_0 approximately matches the transition frequencies in the investigated quantum systems, the third-order polarization can be simplified to [27]

$$\begin{aligned}
P^{(3)}_{\mathrm{RWA}}(\tau, T, t) = \mathrm{e}^{-\mathrm{i}\omega_0(t-\tau)} \int_0^\infty \mathrm{d}\tau_3 \int_0^\infty \mathrm{d}\tau_2 \int_0^\infty \mathrm{d}\tau_1 \\
\times \Big\{ S^{(3)}_{\mathrm{R}}(\tau_1,\tau_2,\tau_3)\, \mathrm{e}^{\mathrm{i}\omega_0(\tau_3-\tau_1)} \big[\tilde{A}^*(t-t_1-\tau_3-\tau_2-\tau_1)\tilde{A}(t-t_2-\tau_3-\tau_2)\tilde{A}(t-t_3-\tau_3) \\
+ \tilde{A}^*(t-t_1-\tau_3-\tau_2-\tau_1)\tilde{A}(t-t_3-\tau_3-\tau_2)\tilde{A}(t-t_2-\tau_3)\big] \\
+ S^{(3)}_{\mathrm{NR}}(\tau_1,\tau_2,\tau_3)\, \mathrm{e}^{\mathrm{i}\omega_0(\tau_3+\tau_1)} \big[\tilde{A}(t-t_2-\tau_3-\tau_2-\tau_1)\tilde{A}^*(t-t_1-\tau_3-\tau_2)\tilde{A}(t-t_3-\tau_3) \\
+ \tilde{A}(t-t_3-\tau_3-\tau_2-\tau_1)\tilde{A}^*(t-t_1-\tau_3-\tau_2)\tilde{A}(t-t_2-\tau_3)\big] \\
+ S^{(3)}_{\mathrm{DC}}(\tau_1,\tau_2,\tau_3)\, \mathrm{e}^{\mathrm{i}\omega_0(\tau_1+2\tau_2+\tau_3)} \big[\tilde{A}(t-t_2-\tau_3-\tau_2-\tau_1)\tilde{A}(t-t_3-\tau_3-\tau_2)\tilde{A}^*(t-t_1-\tau_3) \\
+ \tilde{A}(t-t_3-\tau_3-\tau_2-\tau_1)\tilde{A}(t-t_2-\tau_3-\tau_2)\tilde{A}^*(t-t_1-\tau_3)\big]\Big\}
\end{aligned} \tag{2.5}$$

with the asterisk ($*$) denoting complex conjugation. Due to the RWA, all contributions to the third-order polarization are neglected whose integrands contain fast oscillating terms with respect to the variables τ_1, τ_2, and τ_3. Thus, the third-order response function of each term in Eq. (2.5) has to fulfill the condition that its included phase factors cancel out the phase factors that originate from the incident electric field and oscillate with the center frequency ω_0. For instance, in the first two terms of Eq. (2.4), the phase factor $\mathrm{e}^{\mathrm{i}\omega_0(\tau_3-\tau_1)}$ has to be canceled out. This enables a classification of the response functions into sums over rephasing (R), non-rephasing (NR) and double-coherence (DC) Liouville-space pathways [27]. In general, Liouville-space pathways determine how the density matrix of a quantum system evolves due to the interactions with an external electric field. In Fig. 2.2, the Liouville-space pathways of the rephasing response function $S^{(3)}_{\mathrm{R}}$ are illustrated by means of a three-level system consisting of a ground state $|g\rangle$, a first-excited state $|e\rangle$, and a second-excited state $|f\rangle$. Both the energy difference between the excited states $E_f - E_e = \hbar\omega_{fe}$ and that between the first-excited state and the ground

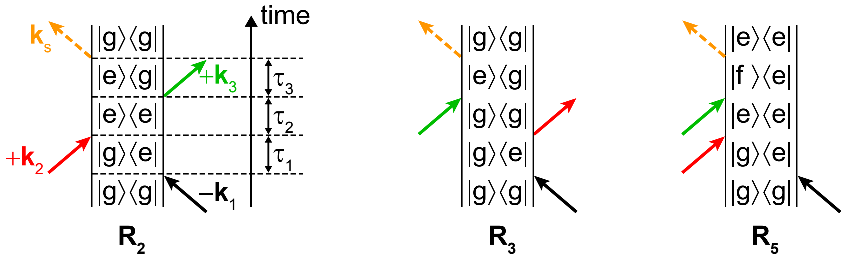

Figure 2.2: Double-sided Feynman diagrams corresponding to the Liouville-space pathways of the rephasing third-order response function $S^{(3)}_{\mathrm{R,RWA}}$ for a three-level system. The temporal evolution of the density matrix is from bottom to top and the interactions with the external field are indicated by the colored arrows. The pathways lead to the emission of an optical signal (orange arrow) into the direction $\mathbf{k}_s = -\mathbf{k}_1 + \mathbf{k}_2 + \mathbf{k}_3$ [25].

state $E_e - E_g = \hbar\omega_{eg}$ are approximately $\hbar\omega_0$. The pathways are depicted as double-sided Feynman diagrams [35, 36]. The vertical axis represents the time evolution of the density matrix starting from the bottom to the top, and each interaction with the electric field is expressed by an arrow [25]. The direction of each arrow is defined by the sign of the wave vector of the corresponding pulse. For a positive sign, the arrow points to the right, and for a negative sign, it points to the left. If the arrow points towards the diagram, the corresponding side of the density matrix is increased. If the arrow points away, the corresponding side is decreased. More detailed information about double-sided Feynman diagrams in coherent 2D spectroscopy is given in Ref. [25]. According to the above-mentioned rules, three different rephasing Liouville-space pathways R$_2$, R$_3$ and R$_5$ are obtained. The labeling of the indices follows the convention used in Refs. [25, 37]. Due to the negative sign of $\mathbf{k}_1$, the first interaction (black arrow) induces a coherence $|g\rangle\langle e|$ in each pathway, leading to a phase factor $\mathrm{e}^{-\mathrm{i}\omega_{eg}\tau_1}$ in the corresponding third-order response function. After the second interaction (red arrow), the quantum system is either in the population $|e\rangle\langle e|$ (R$_2$ and R$_5$) or $|g\rangle\langle g|$ (R$_3$). The third interaction induces a coherence again. In R$_2$ and R$_3$, the coherence $|g\rangle\langle e|$ leads to a phase factor $\mathrm{e}^{\mathrm{i}\omega_{eg}\tau_3}$, whereas R$_5$ contains the phase factor $\mathrm{e}^{\mathrm{i}\omega_{fe}\tau_3}$. Finally, the emission of the optical signal after the third interaction converts the coherence into a population in all pathways and is represented by an orange arrow pointing away from the diagram. It is obvious that in R$_2$ and R$_3$ the phases acquired during τ_1 are canceled out by the phases acquired during τ_3 for the condition $\tau_1 = \tau_3$, since the corresponding phase factors oscillate with the same frequency but opposite sign. This rephasing results in an enhancement of the emitted signal and is called photon echo. For R$_5$ the coherences during τ_1 and τ_3 lead to phase factors that oscillate with opposite sign as well, but not with the same frequency. It has to be mentioned that the time ordering of the interactions in Fig. 2.2 only represents the case that the quantum system interacts first with pulse 1, then with pulse 2, and finally with pulse 3. The identical Liouville-space pathways are obtained, if $+\mathbf{k}_2$ and $+\mathbf{k}_3$ are interchanged, i.e., if the second interaction occurs with pulse 3 and the third interaction with pulse 2. Thus, there are two combinations for the time ordering of interactions which lead to identical pathways and therefore $S^{(3)}_{\mathrm{R}}$ is connected to two specific terms in Eq. (2.5).

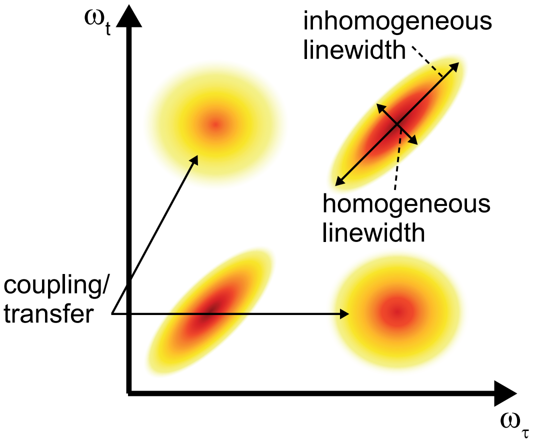

Figure 2.3: Schematic of a 2D spectrum. The horizontal and vertical axis indicate the pump frequency ω_τ and the probe frequency ω_t, respectively. The inhomogeneous and homogeneous line widths of the quantum states can be determined by the shape of the diagonal peaks. Coupling and energy transfers between the states lead to off-diagonal peaks.

The Liouville-space pathways of the other four terms are obtained analogously and can be expressed by two different response functions each. In contrast to the pathways of $S_{\mathrm{R}}^{(3)}$, the pathways of $S_{\mathrm{NR}}^{(3)}$ and $S_{\mathrm{DC}}^{(3)}$ are non-rephasing and describe a free-induction decay. Furthermore, the pathways of the latter contain a double coherence, i.e., a coherence between the ground state and the second-excited state, after the second interaction. Thus, these pathways are only present in systems with more than two energy levels.

In conventional 2D spectroscopy, the electric field of the emitted signal is detected with a spectrometer. Hence, it is not measured as a function of the time t, but as a function of the conjugate frequency ω_t and related to the induced third-order polarization via [27]

$$E_s(\tau, T, \omega_t) \propto \frac{\mathrm{i}\omega_t}{n(\omega_t)} P^{(3)}(\tau, T, \omega_t) \tag{2.6}$$

with the refractive index $n(\omega_t)$. In order to characterize both the spectral amplitude and phase of $E_s(\tau, T, \omega_t)$, the signal is collinearly overlapped with a local oscillator (LO), i.e., a reference pulse with a known spectral phase (see Fig. 2.1b). In a photon-echo experiment, the electric field is measured as a function of the coherence time τ at a fixed population time T. The corresponding two-dimensional (2D) spectrum is then obtained via a Fourier transformation with respect to τ, leading to [27]

$$\begin{aligned} S_{2D}(\omega_\tau, T, \omega_t) &= \int_{-\infty}^{\infty} \mathrm{d}\tau \, \mathrm{i} P^{(3)}(\tau, T, \omega_t) \, \mathrm{e}^{\mathrm{i}\omega_\tau \tau} \\ &\propto \int_{-\infty}^{\infty} \mathrm{d}\tau \frac{E_s(\tau, T, \omega_t) n(\omega_t)}{\omega_t} \, \mathrm{e}^{\mathrm{i}\omega_\tau \tau} \, . \end{aligned} \tag{2.7}$$

Since a 2D spectrum is a complex-valued entity, it can be expressed either as real and imaginary part or as amplitude and phase. However, its absolute phase is not defined unambiguously but can be determined by comparing the 2D spectrum with additional pump-probe measurements [27]. In Fig. 2.3, a schematic 2D spectrum is illustrated and can be interpreted as follows. The investigated quantum systems are pumped with the excitation frequency ω_τ and probed after a waiting time (the population time T) at frequency ω_t. Diagonal peaks indicate the spectral position of the quantum states

Figure 2.4: Comparison between conventional 2D spectroscopy and 2D nanoscopy. In conventional 2D spectroscopy, three ingoing optical waves E_1, E_2, and E_3 are used as input and interact with a quantum system consisting of a ground state $|g\rangle$, a first excited state $|e\rangle$, and a second excited state $|f\rangle$. In the resulting four-wave–mixing (FWM) process, an optical signal E_s is emitted as output. As opposed to this, in coherent 2D nanoscopy, four optical waves E_j with $j = \{1, 2, 3, 4\}$ are used as input. After the FWM process, a non-optical signal is emitted and serves as output. Figure adapted from Ref. [1]. © (2011) American Association for the Advancement of Science.

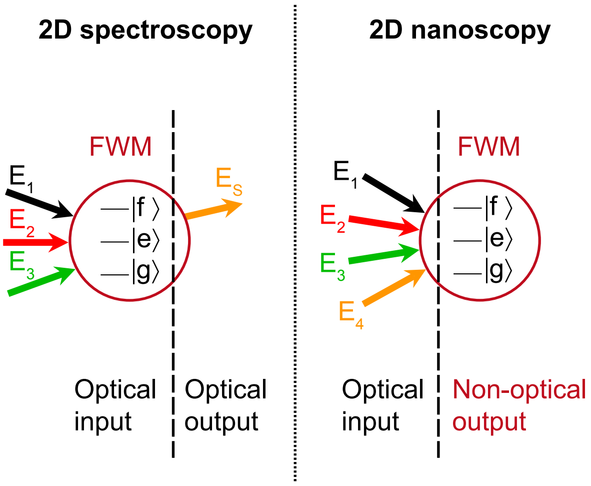

and their shapes provide information about the inhomogeneous and homogeneous line widths of the corresponding states. In addition, couplings and energy transfers between the states are directly visible as off-diagonal peaks. This would not be possible in a linear spectrum, since the spectral properties of the diagonal and off-diagonal peaks would overlap. Furthermore, a linear spectrum would only give information about the inhomogeneous line widths of the quantum states.

2.2 From 2D Spectroscopy to 2D Nanoscopy

In this section, the main idea of coherent 2D nanoscopy is presented on the basis of Ref. [1], starting from the comparison with conventional 2D spectroscopy. Both techniques enable the measurement of four-wave–mixing (FWM) responses but their excitation and detection schemes are different. This is illustrated in Fig. 2.4 by means of the three-level quantum system that was already introduced in Sect. 2.1. In 2D spectroscopy, three incident optical waves interact with the investigated quantum system and induce a third-order polarization. As a result of this polarization a fourth optical wave is radiated by the system and detected as output signal. In contrast to this, 2D nanoscopy uses four incident optical waves to excite the quantum system and the final-state population is probed via photoemission. Due to the detection of a non-optical signal, the spatial resolution is not limited by optical diffraction but by the de Broglie wavelength of the emitted electrons. This means, for instance, that if an electron has a kinetic energy of $E_{\text{kin}} = 1$ eV, a theoretical spatial resolution of

$$\lambda_{\text{dB}} = \frac{h}{\sqrt{2m_e E_{\text{kin}}}} \approx 1 \text{ nm} \tag{2.8}$$

is possible. Note that h and m_e are the Planck constant and the mass of the electron, respectively. By contrast, the wavelength of a photon with the same energy is about 1 μm

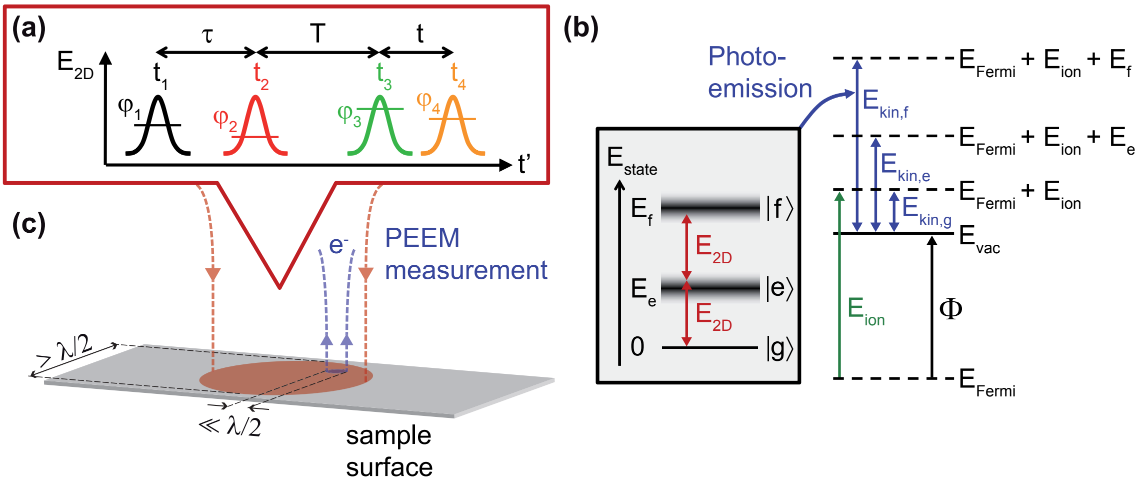

Figure 2.5: Experimental implementation of 2D nanoscopy. (a) A sequence of four femtosecond laser pulses centered at t_j with the phases φ_j ($j = \{1, 2, 3, 4\}$) and the relative time delays τ, T, and t excite the sample. (b) After interaction with the electric field E_{2D} of the four-pulse sequence, the final-state population is probed via photoemission. If the energies $E_g = 0$, E_e, and E_f of the states are below the work function Φ of the system, an additional ionization laser is used to generate photoelectrons after the last interaction with the pulse sequence. The differences between the maximum kinetic energies $E_{\mathrm{kin},\,q}$ ($q = \{e, g, f\}$) of the emitted electrons correspond to the energy differences between the quantum states. (c) The optical excitation spot on the sample is larger than half of the excitation wavelength due to optical diffraction, whereas the emitted photoelectrons are locally detected by a photoemission electron microscope (PEEM) with a high spatial resolution well below the optical diffraction limit. Figure adapted from Ref. [1]. © (2011) American Association for the Advancement of Science.

and thus the achievable spatial resolution is three orders of magnitude worse. Hence, 2D nanoscopy has the potential to obtain the optical response of single quantum systems, whereas in 2D spectroscopy only ensembles of quantum systems can be investigated.

The experimental implementation of 2D nanoscopy is shown in Fig. 2.5. A sequence of four femtosecond laser pulses centered at t_j with $j = \{1, 2, 3, 4\}$ is used for excitation (see Fig. 2.5a). The time delays between the pulses can be varied and are defined as coherence time $\tau = t_2 - t_1$, population time $T = t_3 - t_2$, and signal time $t = t_4 - t_3$. Note that t is the temporal separation between the third and the fourth pulse here, whereas in Sect. 2.1 it represents a given point in time. In addition to the time delays, the relative phases between the pulses defined by $\varphi_\tau = \varphi_2 - \varphi_1$, $\varphi_T = \varphi_3 - \varphi_2$, and $\varphi_t = \varphi_4 - \varphi_3$ can be varied as well. After the interaction with the pulse sequence, the populations $|g\rangle\langle g|$, $|e\rangle\langle e|$, and $|f\rangle\langle f|$ of the quantum states are probed via the emission of photoelectrons (Fig. 2.5b). If the energies of the states do not exceed the work function of the system Φ, an additional ionization laser can be employed to release the electrons from the final-state populations into the vacuum. This can be realized, for instance, via an ionization laser pulse that is temporally delayed with respect to the four-pulse sequence. The maximum kinetic energy of photoelectrons emitted from an energy state at the Fermi level E_{Fermi} is then given by

$$E_{\text{kin}} = E_{\text{ion}} + E_{\text{state}} - (E_{\text{vac}} - E_{\text{Fermi}}) = E_{\text{ion}} + E_{\text{state}} - \Phi \tag{2.9}$$

with the photon energy E_{ion} of the ionization laser, the energy $E_{\text{state}} = \{E_g, E_e, E_f\}$ of the populated quantum state, and the vacuum energy E_{vac}. Note that not only single-particle states, such as electronic transitions in the electronic band structure, but also states of collective nature, such as plasmon polaritons in metallic systems or excitons in molecular aggregates, can be investigated by means of 2D nanoscopy [1]. Since the photoemission always occurs via a single-particle state, the excitation and the probe process have to be treated separately. For this reason, both processes are depicted on separate energy scales in Fig. 2.5b.

In 2D nanoscopy, the emitted photoelectrons are locally detected with a photoemission electron microscope (PEEM) that enables a high spatial resolution at the nanoscale [38], i.e., well below the optical diffraction limit (see Fig. 2.5c). However, due to aberrations, it is higher than the theoretical lower limit defined by the de Broglie wavelength of the photoelectrons. The local photoemission yield is measured as a function of the time delays τ, T, t and the relative phases φ_τ, φ_T, φ_t. If the employed PEEM allows energy-resolved measurements, it is also possible to detect the yield for a particular kinetic energy of the photoelectrons. Otherwise, the measured signal results from the integration over the complete spectrum of the kinetic energies. For a nanoscopy measurement, τ and t are systematically varied, while T is kept constant. The corresponding 2D nanospectra are then obtained by a two-dimensional Fourier transformation with respect to τ and t. Since an incoherent non-optical signal is measured, phase cycling [37, 39, 40] instead of phase matching has to be used to extract coherent signal contributions, e.g., the photon-echo signal. For this purpose, the measurements are repeated for different combinations of the relative phases φ_τ, φ_T, and φ_t, and the signal contributions are received by suitable linear combinations of the measured data sets. A detailed description about phase cycling is given in Sect. 2.4. Since a phase-matching condition is irrelevant, the illumination geometry of the excitation pulses can be chosen collinear and the required four-pulse sequences can be generated by a femtosecond pulse shaper (see Refs. [41–43]).

2.3 Spectral Information in 2D Nanospectra

In the previous section, the main idea of coherent 2D nanoscopy was introduced by means of a three-level quantum system. Here, it is discussed which spectral information about the optical response of a quantum system can be obtained via this technique. In 2D nanoscopy, the final-state population of a quantum system after interaction with an external four-pulse sequence is probed via photoemission and the emitted electrons are detected spatially-resolved with a PEEM. The local time-integrated photoemission yield arising from the final-state population of the i-th quantum state can be described via [30, 44]

$$Y_i^{(4)}(\mathbf{r}) = \int_{-\infty}^{\infty} \mathrm{d}t' \, p_i^{(4)}(\mathbf{r}, t') \,, \tag{2.10}$$

wherein $p_i^{(4)}(\mathbf{r}, t')$ is the local momentary photoemission probability of the i-th quantum state after four light-matter interactions. Note that in this section as well as in Sect. 2.4 the time variable is labeled t', whereas in Sect. 2.1 it was labeled t. This is because, in 2D nanoscopy, the variable t is already defined as signal time, i.e., the time delay between the third and the fourth pulse in the four-pulse sequence. Using perturbation theory, $p_i^{(4)}(\mathbf{r}, t')$ is proportional to the i-th diagonal element of the fourth-order perturbation to the local density matrix $\rho_{ii}^{(4)}(\mathbf{r}, t')$ that is given according to Refs. [25, 37] by

$$\begin{aligned}\rho_{ii}^{(4)}(\mathbf{r}, t') = &\int_0^\infty \mathrm{d}\tau_4 \int_0^\infty \mathrm{d}\tau_3 \int_0^\infty \mathrm{d}\tau_2 \int_0^\infty \mathrm{d}\tau_1 \\ &\times Q^{(4)}(\mathbf{r}, \tau_1, \tau_2, \tau_3, \tau_4) E(\mathbf{r}, t' - \tau_4) E(\mathbf{r}, t' - \tau_4 - \tau_3) \\ &\times E(\mathbf{r}, t' - \tau_4 - \tau_3 - \tau_2) E(\mathbf{r}, t' - \tau_4 - \tau_3 - \tau_2 - \tau_1)\end{aligned} \tag{2.11}$$

with the local correlation function $Q^{(4)}(\mathbf{r}, \tau_1, \tau_2, \tau_3, \tau_4)$. Analogously to the third-order response function $S^{(3)}$ in Eq. (2.1), the correlation function contains information how the density matrix evolves over time due to the interactions with the incident electric field of the four-pulse sequence at times $t' - \tau_4 - \tau_3 - \tau_2 - \tau_1$, $t' - \tau_4 - \tau_3 - \tau_2$, $t' - \tau_4 - \tau_3$, and $t' - \tau_4$. The electric field of the pulse sequence is defined by

$$E(\mathbf{r}, t') = \sum_{j=1}^{N=4} \tilde{A}(t' - t_j)\, \mathrm{e}^{-\mathrm{i}\omega_0(t' - t_j\gamma_0) + \mathrm{i}\mathbf{k}_j\mathbf{r}} \mathrm{e}^{\mathrm{i}\varphi_j} + c.c.\,, \tag{2.12}$$

wherein each of the first four terms represent one pulse each with center frequency ω_0, the complex envelope function $\tilde{A}(t' - t_j)$ with $j = \{1, 2, 3, 4\}$, the temporal shift t_j, and the wave vector $\mathbf{k}_j$. Compared to the electric field of the three-pulse sequence from Eq. (2.2) in Sect. 2.1, the pulses contain additional phases φ_j that are used for phase cycling (see Sect. 2.4). Since the pulse sequence is collinear in 2D nanoscopy, the wave vectors $\mathbf{k}_j$ are identical and therefore the phase factors $\mathrm{e}^{\mathrm{i}\mathbf{k}_j\mathbf{r}}$ are omitted for brevity in the following. Due to the generation of the pulse sequence with a pulse shaper, a dimensionless factor γ_0 [45] can be introduced in Eq. (2.12). It is defined for values between 0 and 1 and determines, how the carrier-envelope phase, i.e., the phase between the envelope function of a pulse and its corresponding carrier oscillations, changes, if the pulse is temporally shifted. For $\gamma_0 = 1$, the carrier oscillations of the pulse are shifted synchronously with its envelope as in a Mach-Zehnder interferometer. In this case, the experiment is done in the laboratory frame. For $\gamma_0 = 0$, only the envelope is shifted and the phase of the carrier oscillations remains unchanged. In this case, the experiment is done in the rotating frame of ω_0, i.e., the center frequency of the laser spectrum. The measured signals then oscillate with difference frequencies $(\omega - \omega_0)$ instead of ω in the time domain. Analogously, if the values of γ_0 are between 0 and 1, a rotating frame with the reference frequency $\omega_{\mathrm{ref}} = \omega_0(1 - \gamma_0)$ is used, and oscillations of the measurement signal correspond to the difference frequencies $(\omega - \omega_{\mathrm{ref}})$. The advantage of measuring in a rotating frame is that temporal signals oscillate slower than in the laboratory frame and therefore can be sampled in larger time steps according to the Shannon-Nyquist criterion [46, 47]. Thus, the measurement time can be significantly reduced. A detailed comparison between the rotating and laboratory frame and a discussion about the corresponding sampling rates are given in Appendix A.1.

Substituting Eq. (2.12) in Eq. (2.11) leads to $8^4 = 4096$ terms each of which contains a multiplication of four complex envelope functions and their corresponding phase factors including the phases φ_j. However, there are many terms that result from interactions with only one, two or three pulses. In contrast to this, terms that describe one interaction with one pulse each depend on all phases φ_j. Moreover, the signs of the phases can be different from term to term. This can be exploited to distinguish between different signal contributions. The photon-echo contribution $P^{(4)}_{\mathrm{PE}}$, for instance, corresponds to the combination $-\varphi_1 + \varphi_2 + \varphi_3 - \varphi_4$. Note that the signs of the first three phases coincide with those of the three wave vectors in the phase-matching condition $\mathbf{k}_s = -\mathbf{k}_1 + \mathbf{k}_2 + \mathbf{k}_3$ that determines the direction of the emitted photon-echo signal in conventional 2D spectroscopy. The phase φ_4 of the last pulse is negative because the density matrix of the investigated system has to end up in a population after the fourth interaction (see Sect. 2.4). Altogether there are 24 terms with the phase combination of the photon-echo contribution. Each term contains the common phase factor

$$\mathrm{e}^{-\mathrm{i}\omega_0\gamma_0(t_1-t_2-t_3+t_4)} = \mathrm{e}^{-\mathrm{i}\omega_0\gamma_0(t-\tau)} \tag{2.13}$$

as well as one of the phase factors

$$\begin{aligned}&\mathrm{e}^{\mathrm{i}\omega_0(\tau_3-\tau_1)},\ \mathrm{e}^{\mathrm{i}\omega_0(\tau_3+\tau_1)},\ \mathrm{e}^{\mathrm{i}\omega_0(\tau_1+2\tau_2+\tau_3)},\\ &\mathrm{e}^{-\mathrm{i}\omega_0(\tau_3-\tau_1)},\ \mathrm{e}^{-\mathrm{i}\omega_0(\tau_3+\tau_1)},\ \text{ or }\ \mathrm{e}^{-\mathrm{i}\omega_0(\tau_1+2\tau_2+\tau_3)}.\end{aligned} \tag{2.14}$$

The first three phase factors in Eq. (2.14) are identical to those obtained for the photon-echo contribution in conventional 2D spectroscopy (confer Eq. (2.4)), and the last three are their complex conjugated ones. Using the RWA and assuming that the center frequency ω_0 approximately matches the transition frequencies in the investigated quantum system, the i-th diagonal element of the fourth-order density matrix that corresponds to the photon-echo contribution can be simplified to

$$\begin{aligned}\rho^{(4)}_{ii,\mathrm{PE}}(\mathbf{r},t') = {}& \mathrm{e}^{\mathrm{i}(-\varphi_1+\varphi_2+\varphi_3-\varphi_4)}\mathrm{e}^{-\mathrm{i}\omega_0\gamma_0(t-\tau)}\int_0^\infty \mathrm{d}\tau_4\int_0^\infty \mathrm{d}\tau_3\int_0^\infty \mathrm{d}\tau_2\int_0^\infty \mathrm{d}\tau_1\\ &\times\Big[Q^{(4)}_{\mathrm{R1}}(\mathbf{r},\tau_1,\tau_2,\tau_3,\tau_4)\,\mathrm{e}^{\mathrm{i}\omega_0(\tau_3-\tau_1)}M_{\mathrm{R1}}(t',t_1,t_2,t_3,t_4,\tau_1,\tau_2,\tau_3,\tau_4)\\ &+Q^{(4)}_{\mathrm{R2}}(\mathbf{r},\tau_1,\tau_2,\tau_3,\tau_4)\,\mathrm{e}^{-\mathrm{i}\omega_0(\tau_3-\tau_1)}M_{\mathrm{R2}}(t',t_1,t_2,t_3,t_4,\tau_1,\tau_2,\tau_3,\tau_4)\\ &+Q^{(4)}_{\mathrm{NR1}}(\mathbf{r},\tau_1,\tau_2,\tau_3,\tau_4)\,\mathrm{e}^{\mathrm{i}\omega_0(\tau_3+\tau_1)}M_{\mathrm{NR1}}(t',t_1,t_2,t_3,t_4,\tau_1,\tau_2,\tau_3,\tau_4)\\ &+Q^{(4)}_{\mathrm{NR2}}(\mathbf{r},\tau_1,\tau_2,\tau_3,\tau_4)\,\mathrm{e}^{-\mathrm{i}\omega_0(\tau_3+\tau_1)}M_{\mathrm{NR2}}(t',t_1,t_2,t_3,t_4,\tau_1,\tau_2,\tau_3,\tau_4)\\ &+Q^{(4)}_{\mathrm{DC1}}(\mathbf{r},\tau_1,\tau_2,\tau_3,\tau_4)\,\mathrm{e}^{\mathrm{i}\omega_0(\tau_1+2\tau_2+\tau_3)}M_{\mathrm{DC1}}(t',t_1,t_2,t_3,t_4,\tau_1,\tau_2,\tau_3,\tau_4)\\ &+Q^{(4)}_{\mathrm{DC2}}(\mathbf{r},\tau_1,\tau_2,\tau_3,\tau_4)\,\mathrm{e}^{-\mathrm{i}\omega_0(\tau_1+2\tau_2+\tau_3)}M_{\mathrm{DC2}}(t',t_1,t_2,t_3,t_4,\tau_1,\tau_2,\tau_3,\tau_4)\Big],\end{aligned} \tag{2.15}$$

wherein each function M_k with $k = \{\text{R1, R2, NR1, NR2, DC1, DC2}\}$ represents a sum over four terms which in turn are products of four complex envelope functions, e.g.,

$$\begin{aligned}
&M_{\text{R1}}(t', t_1, t_2, t_3, t_4, \tau_1, \tau_2, \tau_3, \tau_4) = \\
&\quad \tilde{A}^*(t' - t_1 - \tau_4 - \tau_3 - \tau_2 - \tau_1)\tilde{A}(t' - t_2 - \tau_4 - \tau_3 - \tau_2) \\
&\qquad \times \tilde{A}(t' - t_3 - \tau_4 - \tau_3)\tilde{A}^*(t' - t_4 - \tau_4) \\
&\quad + \tilde{A}^*(t' - t_1 - \tau_4 - \tau_3 - \tau_2 - \tau_1)\tilde{A}(t' - t_3 - \tau_4 - \tau_3 - \tau_2) \\
&\qquad \times \tilde{A}(t' - t_2 - \tau_4 - \tau_3)\tilde{A}^*(t' - t_4 - \tau_4) \\
&\quad + \tilde{A}^*(t' - t_4 - \tau_4 - \tau_3 - \tau_2 - \tau_1)\tilde{A}(t' - t_2 - \tau_4 - \tau_3 - \tau_2) \\
&\qquad \times \tilde{A}(t' - t_3 - \tau_4 - \tau_3)\tilde{A}^*(t' - t_1 - \tau_4) \\
&\quad + \tilde{A}^*(t' - t_4 - \tau_4 - \tau_3 - \tau_2 - \tau_1)\tilde{A}(t' - t_3 - \tau_4 - \tau_3 - \tau_2) \\
&\qquad \times \tilde{A}(t' - t_2 - \tau_4 - \tau_3)\tilde{A}^*(t' - t_1 - \tau_4)\,.
\end{aligned} \tag{2.16}$$

Due to the RWA, all contributions to $\rho^{(4)}_{ii,\text{PE}}$ are neglected whose integrands contain fast oscillating terms with respect to the variables τ_1, τ_2, τ_3, and τ_4. Thus, by analogy with the third-order response functions in Eq. (2.5), the correlation functions of the different terms in Eq. (2.15) have to fulfill the condition that their included phase factors cancel out the phase factors that originate from the incident electric field and contain oscillations with the center frequency ω_0. Hence, they can be assigned to sums over rephasing (R1 and R2), non-rephasing (NR1 and NR2) and double-coherence (DC1 and DC2) Liouville-space pathways. In Fig. 2.6, the pathways of $Q^{(4)}_{\text{R1}}$ are shown for the three-level quantum system that was previously introduced in Sect. 2.1. They are labeled according to Refs. [25, 37] and depicted as double-sided Feynman diagrams. Here, the signs of the corresponding phases φ_j define the directions of the arrows and their time ordering determines the temporal evolution of the density matrix according to the same rules that apply to the Liouville-space pathways in 2D spectroscopy with respect to the wave vectors (see Sect. 2.1). The pathways Q_{2b}, Q_{3b} and Q_{5b} are identical to the pathways R_2, R_3 and R_5 of the third-order response function $R^{(3)}_{\text{R}}$ in Fig. 2.2. The other three pathways labeled with the index "a" show the same temporal evolution of the density matrix, but end up in the energetically higher quantum state after the last interaction. In contrast to Ref. [37], two additional pathways Q_{2a} and Q_{3a} are possible in 2D nanoscopy, if the final-state population is probed via an ionization laser. Note that only those pathways contribute to $\rho^{(4)}_{ii,\text{PE}}$ which end up in the i-th quantum state. For example, the pathways Q_{2a}, Q_{3a}, and Q_{5b} contribute to $\rho^{(4)}_{ee,\text{PE}}$. Furthermore, the time ordering of the phases in Fig. 2.6 represents only the case where the quantum system successively interacts with pulse 1 (black arrow), pulse 2 (red arrow), pulse 3 (green arrow), and finally pulse 4 (orange arrow). The identical pathways are obtained, if the

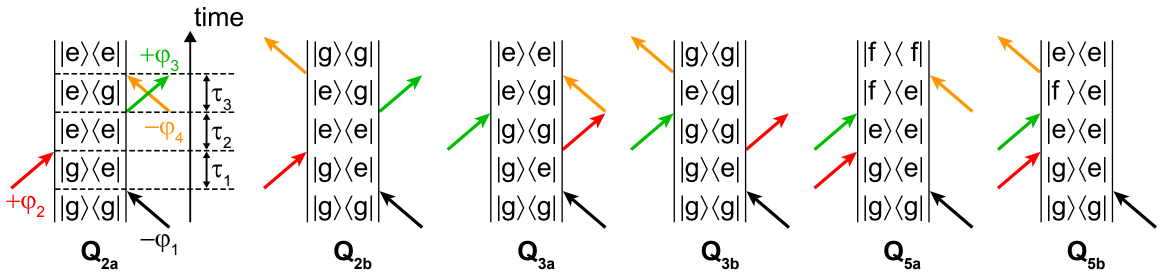

Figure 2.6: Double-sided Feynman diagrams corresponding to the Liouville-space pathways of $Q_{\mathrm{R1}}^{(4)}$ for a three-level quantum system with ground state $|g\rangle$, first-excited state $|e\rangle$, and second-excited state $|f\rangle$. The time evolves from bottom to top and the interactions with the external electric field are indicated by the colored arrows. The signs of the phases φ_j with $j = \{1, 2, 3, 4\}$ and their time ordering determine the temporal evolution of the density matrix.

phases $-\varphi_1$ and $-\varphi_4$ are interchanged, i.e., if the first interaction occurs with pulse 4 and the last interaction with pulse 1. This is also the case, if $+\varphi_2$ and $+\varphi_3$ are interchanged. All in all, this leads to four combinations of the time ordering each of which corresponds to one term in function M_{R1} (confer Eq. (2.16)).

The Liouville-space pathways of the other five correlation functions can be determined analogously to those of the rephasing correlation function $Q_{\mathrm{R1}}^{(4)}$. Note that the pathways of the correlation functions with index "2" are identical to those of the correlation functions with index "1" but complex conjugated. In general, if the four pulses within the sequence temporally overlap, the pathways of all 24 terms contribute to the final-state populations. By contrast, in the case of temporally separated pulses, the number of pathways is reduced due to the different time ordering of the interactions. If the coherence time τ and the signal time t are increased from 0 to positive values beyond the pulse duration of the pulses, the first term in Eq. (2.15) dominates the extracted photon-echo signal contribution. In this case, the spectral information in the resulting 2D nanospectrum is closely related to that in a 2D spectrum obtained via conventional 2D photon-echo spectroscopy due to the identical temporal evolution of the density matrix before the fourth interaction. However, the evolution after the fourth interaction, e.g., an exponential decay of the final-state population, would not be detected via conventional 2D spectroscopy. Therefore, the photoemission should be probed immediately after the fourth interaction. If the investigated quantum states are above the work function of the system, this condition is already fulfilled, since the fourth interaction leads to the photoemission. Otherwise, if an additional ionization laser pulse is employed, it should temporally overlap with the last pulse of the four-pulse sequence.

In this section, the spectroscopic potential of 2D nanoscopy was discussed by means of a three-level quantum system. This system was chosen to illustrate the common features between 2D nanoscopy and conventional 2D spectrosocpy by means of the formalism of Liouville space-pathways. As already mentioned in Sect. 2.2, this technique is not restricted to quantum systems with discrete energy levels. In the first experimental implementation of 2D nanoscopy, for instance, long-lived plasmonic phase coherences of localized excitations on a corrugated silver surface were investigated and explained by the hybridization between localized and propagating plasmons [1]. Hence, coherent

2D nanoscopy can generally be utilized to obtain coherent information about the local response of a sample. However, the total measurement signal is dominated by signal contributions without coherent information, e.g., contributions arising from interactions with only one pulse. Therefore, phase cycling has to be applied to extract the coherent signals, i.e., signals that arise from interactions with all pulses of the pulse sequence.

2.4 Phase-Cycling Scheme Selection

In the previous section, the spectral information content that is included in the total measurement signal of 2D nanoscopy was explained. Here, it is shown how this spectral information can be extracted via phase cycling. Note that the major part of this section is based on Ref. [37]. Phase-cycling scheme selection generally depends on the number of temporally separable pulses within a pulse sequence. In a 2D nanoscopy measurement, a collinear four-pulse sequence with a fixed time delay T (population time) and two varying time delays τ (coherence time) and t (signal time) is employed for excitation. However, for zero population time, i.e., $T = 0$, the second and third pulse temporally overlap and thus the pulse sequence is reduced to a three-pulse sequence. One consequently has to distinguish between 2D nanoscopy measurements with zero and non-zero population time. Hence, phase cycling is first discussed for a collinear three-pulse sequence in Subsect. 2.4.1, and then extended to collinear four-pulse sequences in Subsect. 2.4.2. In the following, the pulses within a sequence are called sub pulses.

2.4.1 Three-Pulse Sequence

In a 2D nanoscopy measurement with zero population time, collinear pulse sequences are used that consist of three temporally separable sub pulses. Analogously to Eq. (2.12), the electric field of such a three-pulse sequence is defined by

$$\begin{aligned} E(t') = {} & \tilde{A}(t'-t_1)\,\mathrm{e}^{-\mathrm{i}\omega_0(t'-t_1\gamma_0)}\mathrm{e}^{\mathrm{i}\varphi_1} + 2\tilde{A}(t'-t_2)\,\mathrm{e}^{-\mathrm{i}\omega_0(t'-t_2\gamma_0)}\mathrm{e}^{\mathrm{i}\varphi_2} \\ & + \tilde{A}(t'-t_3)\,\mathrm{e}^{-\mathrm{i}\omega_0(t'-t_3\gamma_0)}\mathrm{e}^{\mathrm{i}\varphi_3} + c.c.\,, \end{aligned} \tag{2.17}$$

wherein the first three terms describe one sub pulse each. The common phase factor $\mathrm{e}^{\mathrm{i}\mathbf{kr}}$ is omitted for brevity here. The envelope function of the second term is multiplied by 2, since this sub pulse represents two temporally overlapping pulses. As described in Sect. 2.3, the dimensionless factor γ_0 [45] determines the frame of the measurement, and can be chosen between 0 (rotating frame of ω_0) and 1 (laboratory frame). Note that in Ref. [37] the pulse sequence is defined in the rotating frame of ω_0. In the case of a three-pulse sequence, the coherence time is the time delay between the first and the second sub pulse, i.e., $\tau = t_2 - t_1$, while the signal time is the time delay between the second and the third sub pulse, i.e., $t = t_3 - t_2$. The additional phases φ_1, φ_2, and φ_3 of the sub pulses enable the implementation of phase cycling.

In 2D nanoscopy, the total measurement signal corresponds to the electron emission yield Y of the investigated sample. It is composed of signal contributions that arise from a different number of interactions with each sub pulse and are thus proportional to phase factors with different combinations of the phases φ_1, φ_2, and φ_3. The yield can therefore be expressed via [37]

$$Y(\varphi_1, \varphi_2, \varphi_3) = \sum_{\alpha,\beta,\gamma} \widetilde{Y}\left(\alpha, \beta, \gamma\right) \mathrm{e}^{\mathrm{i}(\alpha\varphi_1+\beta\varphi_2+\gamma\varphi_3)}\,, \tag{2.18}$$

wherein the prefactors $\alpha, \beta, \gamma \in \mathbb{Z}$ determine the phase dependency of each contribution $\widetilde{Y}\left(\alpha, \beta, \gamma\right)$. Note that both the yield Y and the contributions $\widetilde{Y}$ also depend on τ and t as well as on the position $\mathbf{r}$. However, since these dependencies are irrelevant for the choice of the phase-cycling scheme, they are omitted for brevity in this section. Assuming that only populations are probed via 2D nanoscopy, the prefactors of each contribution have to meet the condition [37]

$$\alpha + \beta + \gamma = 0\,. \tag{2.19}$$

This can be explained by means of the double-sided Feynman diagrams presented in Fig. 2.6. Starting from the ground state of the quantum system, the number of arrows pointing to the right has to be equal to the number of arrows pointing to the left to generate a population after the fourth interaction. Thus, the sum over the prefactors of the phases, i.e., the sum over α, β, and γ, has to be zero. Applying Eq. (2.19) to Eq. (2.18) leads to [37]

$$Y(\varphi_{21}, \varphi_{31}) = \sum_{\beta,\gamma} \widetilde{Y}\left(\beta, \gamma\right) \mathrm{e}^{\mathrm{i}(\beta\varphi_{21}+\gamma\varphi_{31})} \tag{2.20}$$

with the relative phases $\varphi_{21} = \varphi_2 - \varphi_1$ and $\varphi_{31} = \varphi_3 - \varphi_1$. Since Eq. (2.20) corresponds to a 2D Fourier series, the contributions $\widetilde{Y}(\beta, \gamma)$ represent Fourier coefficients and are obtained via the 2D Fourier transformation [37]

$$\widetilde{Y}(\beta, \gamma) = \frac{1}{4\pi^2} \int_0^{2\pi} \mathrm{d}\varphi_{31} \int_0^{2\pi} \mathrm{d}\varphi_{21}\, Y\left(\varphi_{21}, \varphi_{31}\right) \mathrm{e}^{-\mathrm{i}(\beta\varphi_{21}+\gamma\varphi_{31})}\,. \tag{2.21}$$

In experiments, only a discrete number of relative phases can be sampled. Equation (2.21) is therefore converted to the discrete Fourier transformation [37]

$$\widetilde{Y}(\beta, \gamma) = \frac{1}{LM} \sum_{m=0}^{M-1} \sum_{l=0}^{L-1} Y\left[\varphi_{21}\left(l\right), \varphi_{31}\left(m\right)\right] \mathrm{e}^{-\mathrm{i}\beta\varphi_{21}(l)} \mathrm{e}^{-\mathrm{i}\gamma\varphi_{31}(m)}\,, \tag{2.22}$$

wherein L and M are the number of phase-cycling steps with respect to the relative phases defined by [37]

$$\begin{aligned} \varphi_{21}\left(l\right) &= l \cdot \frac{2\pi}{L} &\qquad &\text{with } l = 0, 1, ..., L-1\,,\\ \varphi_{31}\left(m\right) &= m \cdot \frac{2\pi}{M} &\qquad &\text{with } m = 0, 1, ..., M-1\,. \end{aligned} \tag{2.23}$$

This means that, according to Eq. (2.22), a certain signal contribution, i.e., a certain Fourier coefficient $\widetilde{Y}(\beta, \gamma)$, is extracted by repeating the 2D nanoscopy measurement for every combination of $\varphi_{21}\left(l\right)$ and $\varphi_{31}\left(m\right)$, and summing up the measured signals $Y\left[\varphi_{21}\left(l\right),\varphi_{31}\left(m\right)\right]$ multiplied by the corresponding phase factors $\mathrm{e}^{-\mathrm{i}\beta\varphi_{21}(l)}$ and $\mathrm{e}^{-\mathrm{i}\gamma\varphi_{31}(m)}$. In order to reduce the measurement time, one is often interested in keeping the total number $L\times M$ of phase-cycling steps as low as possible. However, due to the periodic property of the discrete Fourier transformation, aliasing occurs if the number is too low. In this case, there are Fourier coefficients $\widetilde{Y}(\beta+pL,\gamma+qM)$ with $(p,q)\in\mathbb{Z}$ which cannot be separated from $\widetilde{Y}(\beta,\gamma)$ and would also be extracted via the applied $(L\times M)$-step phase-cycling scheme. Therefore, the values of L and M have to be chosen such that only the desired Fourier coefficient is filtered out. Assuming that the total measurement signal contains only fourth- and lower-order contributions, the absolute values of the prefactors α, β, and γ are limited by [37]

$$|\alpha|+|\beta|+|\gamma|\leq 4\,. \tag{2.24}$$

Considering this condition and the condition from Eq. (2.19), one obtains 19 different combinations of the prefactors (see Table 2.1). The choice of the phase-cycling scheme now depends on the phase dependency of the desired signal contribution. This is exemplarily discussed by means of the photon-echo contribution. Analogously to Eq. (2.15), this contribution is proportional to $\mathrm{e}^{\mathrm{i}(-\varphi_1+2\varphi_2-\varphi_3)}$ and thus defined by the combination $\alpha=-1$, $\beta=+2$, and $\gamma=-1$. For its unambiguous extraction from the total measurement signal, the lowest number of phase-cycling steps is given by a (5×2)-step phase-cycling scheme, i.e., for $L=5$ and $M=2$. This can be explained by means of Table 2.1. Since there is no Fourier coefficient $\widetilde{Y}(-2+5p,+1+2q)$ with $(p,q)\in\mathbb{Z}$, aliasing is prevented. In contrast to this, if $L<5$ and/or $M<2$, there is at least one aliased Fourier coefficient that also survives the phase-cycling procedure.

Sometimes it is useful to choose a phase-cycling scheme that allows the extraction of several contributions with only one $(L\times M)$-step phase-cycling measurement. A (4×4)-step phase-cyling scheme, for instance, enables the extraction of not only the photon-echo contribution but also 14 other Fourier coefficients. The different contributions are then calculated by means of Eq. (2.22) with the same data set but different phase factors $\mathrm{e}^{-\mathrm{i}\beta\varphi_{21}(l)}$ and $\mathrm{e}^{-\mathrm{i}\gamma\varphi_{31}(m)}$ due to different values for β and γ. This can be exploited to obtain additional spectral information. For example, if quantum systems are investigated, the so-called third-order 2Q-2D contribution with the combination $\alpha=+2$, $\beta=-1$, and $\gamma=-1$ provides information about Liouville-space pathways with a double coherence during τ, arising from two interactions with the first sub pulse. Note that there are also Liouville-space pathways of the photon-echo contribution which contain a double coherence (see Sect. 2.3). However, if $\tau\geq 0$ and $t\geq 0$, these pathways are only present during the temporal overlap of the sub pulses due to the time ordering of interactions with each sub pulse.

It has to be mentioned that, in the previous sections and in the 2D nanoscopy experiment presented in this work, the relative phases are not defined with respect to the phase of the first sub pulse φ_1 but as relative phases between subsequent sub pulses φ_τ, φ_T, and φ_t. This means that, for $T=0$, the relative phase φ_T is set to zero and Y is measured for different combinations of $\varphi_\tau=\varphi_2-\varphi_1$ and $\varphi_t=\varphi_3-\varphi_2$ instead of φ_{21} and φ_{31}. In order to calculate the desired contribution from the total measurement signal,

$\boldsymbol{\alpha}$	$\boldsymbol{\beta}$	$\boldsymbol{\gamma}$
-2	0	2
-2	2	0
-2	1	1
-1	-1	2
-1	0	1
-1	1	0
$\mathbf{-1}$	$\mathbf{2}$	$\mathbf{-1}$
0	-2	2
0	-1	1
0	0	0
0	1	-1
0	2	-2
1	-2	1
1	-1	0
1	0	-1
1	1	-2
2	-2	0
2	-1	-1
2	0	-2

Table 2.1: Combinations of the prefactors α, β, and γ that fulfill the conditions from Eqs. (2.19) and (2.24). Each combination determines the phase dependency of the corresponding signal contribution, i.e., the Fourier coefficient $\widetilde{Y}(\beta, \gamma)$. The combination in bold represents the phase dependency of the photon-echo contribution. Table adapted from Ref. [37].

Eq. (2.22) is therefore rewritten as follows:

$$\widetilde{Y}(\beta, \gamma) = \frac{1}{LM} \sum_{m=0}^{M-1} \sum_{l=0}^{L-1} Y\left[\varphi_\tau(l), \varphi_t(l,m)\right] \mathrm{e}^{-\mathrm{i}\beta\varphi_\tau(l)} \mathrm{e}^{-\mathrm{i}\gamma[\varphi_t(l,m)+\varphi_\tau(l)]} \tag{2.25}$$

with the relative phases defined by

$$\varphi_\tau(l) = \varphi_{21}(l) = l \cdot \frac{2\pi}{L} \qquad \text{with } l = 0, 1, ..., L-1\,, \tag{2.26}$$

$$\varphi_t(l,m) = \varphi_{31}(m) - \varphi_{21}(l) = m \cdot \frac{2\pi}{M} - l \cdot \frac{2\pi}{L} \qquad \text{with } m = 0, 1, ..., M-1\,. \tag{2.27}$$

2.4.2 Four-Pulse Sequence

In a 2D nanoscopy measurement with population time $T \neq 0$, collinear pulse sequences with four temporally separable sub pulses are used. The temporal electric field of such a four-pulse sequence is defined by Eq. (2.12). Analogously to a measurement with zero population time, the electron emission yield can be described via

$$Y(\varphi_1, \varphi_2, \varphi_3, \varphi_4) = \sum_{\alpha,\beta,\gamma,\delta} \widetilde{Y}\left(\alpha, \beta, \gamma, \delta\right) \mathrm{e}^{\mathrm{i}(\alpha\varphi_1+\beta\varphi_2+\gamma\varphi_3+\delta\varphi_4)} \tag{2.28}$$

with $\alpha, \beta, \gamma, \delta \in \mathbb{Z}$. The prefactor δ determines the dependency of the contribution $\widetilde{Y}\left(\alpha, \beta, \gamma, \delta\right)$ on the phase of the fourth sub pulse φ_4. Using the condition

$$\alpha + \beta + \gamma + \delta = 0 \tag{2.29}$$

and introducing the relative phases φ_{21}, φ_{31}, and $\varphi_{41} = \varphi_4 - \varphi_1$ leads to

$$Y(\varphi_{21}, \varphi_{31}, \varphi_{41}) = \sum_{\beta,\gamma,\delta} \widetilde{Y}\left(\beta, \gamma, \delta\right) \mathrm{e}^{\mathrm{i}(\beta\varphi_{21}+\gamma\varphi_{31}+\delta\varphi_{41})}. \tag{2.30}$$

Hence, the contributions can be obtained via the discrete three-dimensional Fourier transformation

$$\widetilde{Y}(\beta, \gamma, \delta) = \frac{1}{LMN} \sum_{n=0}^{N-1} \sum_{m=0}^{M-1} \sum_{l=0}^{L-1} Y\left[\varphi_{21}\left(l\right), \varphi_{31}\left(m\right), \varphi_{41}\left(n\right)\right] \times \mathrm{e}^{-\mathrm{i}\beta\varphi_{21}(l)} \mathrm{e}^{-\mathrm{i}\gamma\varphi_{31}(m)} \mathrm{e}^{-\mathrm{i}\delta\varphi_{41}(n)}\,. \tag{2.31}$$

In comparison with Eq. (2.22) that was derived for a three-pulse sequence, there is an additional sum over the parameter n due to the additional relative phase $\varphi_{41}\left(n\right)$. The discrete phase-cycling steps with respect to this relative phase are defined by

$$\varphi_{41}\left(n\right) = n \cdot \frac{2\pi}{N} \qquad \text{with } n = 0, 1, ..., N-1\,, \tag{2.32}$$

while those with respect to $\varphi_{21}\left(l\right)$ and $\varphi_{31}\left(m\right)$ are given by Eq. (2.23). Due to the additional sum in Eq. (2.31), the number of total phase-cycling steps is extended to $L \times M \times N$. Assuming [37]

$$|\alpha| + |\beta| + |\gamma| + |\delta| \leq 4 \tag{2.33}$$

and according to the condition from Eq. (2.29), there are 55 contributions with different combinations of the prefactors and thus 36 contributions more than in a 2D nanoscopy measurement with zero population time. As a consequence, the number of phase-cycling steps for the extraction of certain signal contributions is higher as well. For instance, in order to unambiguously extract the photon-echo contribution defined by the combination $\alpha = -1$, $\beta = +1$, $\gamma = +1$, and $\delta = -1$, one has to apply at least a $3 \times 3 \times 3 = 27$ phase-cycling scheme with $L = M = N = 3$.

If the electron emission yield Y is measured for different combinations of the relative phases $\varphi_\tau = \varphi_2 - \varphi_1$, $\varphi_T = \varphi_3 - \varphi_2$, and $\varphi_t = \varphi_4 - \varphi_3$ instead of φ_{21}, φ_{31}, and φ_{41}, Eq. (2.31) has to be rewritten as follows:

$$\begin{aligned}\widetilde{Y}\left[\beta,\gamma,\delta\right] = \frac{1}{LMN}\sum_{n=0}^{N-1}\sum_{m=0}^{M-1}\sum_{l=0}^{L-1} & Y\left[\varphi_\tau\left(l\right),\varphi_T\left(l,m\right),\varphi_t\left(m,n\right)\right] \\ & \times \mathrm{e}^{-\mathrm{i}\beta\varphi_\tau(l)}\mathrm{e}^{-\mathrm{i}\gamma[\varphi_T(l,m)+\varphi_\tau(l)]}\mathrm{e}^{-\mathrm{i}\delta[\varphi_t(m,n)+\varphi_T(l,m)+\varphi_\tau(l)]}\,,\end{aligned} \tag{2.34}$$

wherein the phase steps are given by

$$\begin{aligned}\varphi_\tau\left(l\right) &= \varphi_{21}\left(l\right) = l\cdot\frac{2\pi}{L} && \text{with } l = 0,1,...,L-1\,,\\ \varphi_T\left(l,m\right) &= \varphi_{31}\left(m\right) - \varphi_{21}\left(l\right) = m\cdot\frac{2\pi}{M} - l\cdot\frac{2\pi}{L} && \text{with } m = 0,1,...,M-1\,,\\ \varphi_t\left(m,n\right) &= \varphi_{41}\left(n\right) - \varphi_{31}\left(m\right) = n\cdot\frac{2\pi}{N} - m\cdot\frac{2\pi}{m} && \text{with } n = 0,1,...,N-1\,.\end{aligned} \tag{2.35}$$

3 Experimental Setup

In this chapter, the optical setups that were used for the time-resolved experiments presented in this thesis are described in detail. The setup with the pulse shaper is shown in Sect. 3.1. It was employed for the 2D nanoscopy experiment as well as the two-pulse correlation experiment discussed in Sect. 4.4 and Sect. 5.4, respectively. For the two-pulse correlation experiment that is described in Sect. 5.5, the pulse shaper was replaced by a phase-stabilized Mach-Zehnder interferometer. The corresponding modified setup is shown in Sect. 3.2.

3.1 Setup with the Pulse Shaper

A sketch of the setup with the pulse shaper is depicted in Fig. 3.1. A Ti:sapphire laser oscillator (Newport Spectra-Physics Tsunami) with a repetition rate of 80 MHz enables the generation of linearly polarized laser pulses with a minimum pulse duration of 23 fs (full width at half maximum (FWHM) of temporal intensity). For the experiments with the pulse shaper, the spectral bandwidth of the pulses had to be narrowed to match the usable spectral range of the pulse shaper. Hence, the oscillator was adjusted, leading to output pulses with an increased minimum pulse duration of 60 fs, a center wavelength of 800 nm and a pulse energy of 9.8 nJ. The output beam of the oscillator is stabilized by means of an active stabilization system (Tem Messstechnik Beamlok 4D). This approach reduces beam pointing deviations greatly and thus enhances the quality of the measured signal. A prism compressor consisting of a beam splitter (BS), two prims (PR1 and PR2), and a reflecting mirror (RM) pre-compensates dispersion caused by optical elements in the setup. After dispersion compensation, the beam is coupled into a home-built Fourier-domain pulse shaper [48] with a 128-pixel two-layer liquid-crystal display (LCD) from Cambridge Research & Instrumentation. Before entering the pulse shaper the beam diameter is adjusted by means of a Galilean telescope (T) to 2 mm which corresponds to the LCD pixel height. A pair of glass wedges (GW1) splits the incoming pulse into two parts, one reflected part with very low intensity (4% of incoming intensity), and one transmitted part (96%). The reflected pulse is not shaped and serves as reference for pulse characterization. The transmitted pulse passes a so-called $4f$ setup [41–43] consisting of two holographic gratings (G1 and G2), two cylindrical mirrors (CM1 and CM2), two folding mirrors (FM1 and FM2), and the LCD with two polarizers (P1 and P2). In this configuration, the distance between CM1 and G1 as well as CM2 and G2 is one focal length f, and the length of the optical beam path between CM1 and CM2 $2f$. The LCD is located in the Fourier plane of the

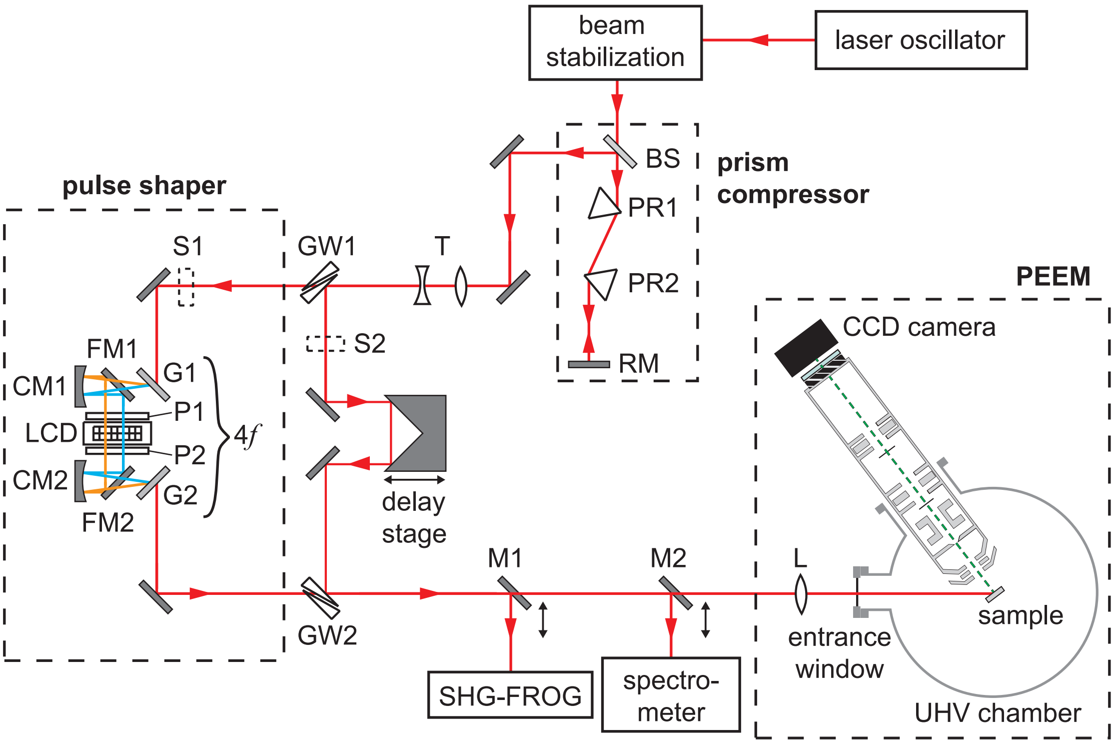

Figure 3.1: Sketch of the experimental setup with the pulse shaper. The output pulses of a Ti:Sapphire oscillator (60 fs pulse duration, 800 nm center wavelength, 9.8 nJ pulse energy) are actively beam stabilized and coupled into a pulse shaper. A prism compressor pre-compensates the dispersion of subsequent optical elements. The beam is split into a transmitted beam (96% of incoming intensity) and a reflected beam (4%) by a pair of glass wedges (GW1). In the pulse shaper, the transmitted beam is shaped via a two-layer LCD located in the Fourier plane of a $4f$ setup. The reflected beam serves as reference for pulse characterization. For the experiment, the shaped beam is weakly focused onto the sample located in the UHV chamber of the PEEM. Two incidence angles with respect to the surface normal of the sample can be chosen, either 65° or 4°, i.e., normal incidence (not shown here). The electron emission is detected spatially resolved with a CCD camera. For pulse characterization, the pulses can be redirected into a SHG-FROG setup and a spectrometer via the mirrors M1 and M2, respectively. The setup was utilized for the 2D nanoscopy experiment as well as the two-pulse experiment discussed in Sect. 4.4 and Sect. 5.4, respectively.

$4f$ setup, i.e., directly in the middle of the optical beam path between CM1 and CM2. The spectral components of the pulse are spatially dispersed by the grating G1 and focused by the cylindrical mirror CM1 via the folding mirror FM1 onto the LCD in the Fourier plane (the beam paths of the two outer spectral components with the longest and shortest wavelength are indicated in Fig. 3.1 by the orange and the blue line, respectively). The polarizer P1 in front of the LCD ensures that the incoming beam is linearly polarized. In the LCD, the spectral components of the pulse are shaped independently from each other. Due to the polarizer P2 behind the LCD, the pulse shaper is in amplitude and phase modulation mode, i.e., the amplitude and phase of each spectral component can be modulated, and the outgoing shaped pulse remains linearly polarized.

The shaped pulse is recollimated by means of the folding mirror FM2, the cylindrical mirror CM2, and the grating G2, and spatially recombined with the reference pulse via a second pair of glass wedges (GW2). The temporal separation between the two pulses can be adjusted by a moveable delay stage in the beam path of the reference pulse. Furthermore, the shaped and the reference pulse can be separately blocked by shutter S1 and S2, respectively. During an experiment, the reference pulse is blocked, and the mirrors M1 and M2 that are mounted on flip holders are removed in order to direct the shaped pulse into the photoemission electron microscope (PEEM) system, a FOCUS NI-PEEM. The beam is weakly focused onto the sample by a lens (L) with a focal length of 200 mm, resulting in a focal spot diameter of about 50 μm (1/e^2 intensity). The sample is located on a holder in the ultrahigh vacuum (UHV) chamber of the PEEM and the emitted electrons are detected spatially resolved with a charge-coupled-device (CCD) camera. The spatial resolution depends on the investigated sample and is limited by aberrations. For the experiments presented in this thesis, the resolution was < 40 nm and thus far below the optical diffraction limit of near-infrared light. The beam impinges on the sample under an incidence angle of 65° with respect to the surface normal and the electric field of the corresponding pulses is linearly polarized parallel to the plane of incidence (p-polarized). In addition, a rhodium mirror (2 mm × 2 mm) positioned in the PEEM enables an incidence angle of 4°, i.e., almost normal incidence (NI). In the case of experiments under NI, the setup directly in front of the PEEM is different from that depicted in Fig. 3.1 (not shown here): The lens L is replaced by two mirrors that redirects the beam through a second entrance window of the UHV chamber onto the rhodium mirror. From there, the beam is reflected onto the sample. An additional lens in front of the second entrance window is used for focusing (200 mm focal length).

For the time-resolved experiments presented in Sects. 4.4 and 5.4, the pulse shaper was used to generate collinear pulse sequences with varying temporal delays and relative phases between the sub pulses. The characterization of the pulse sequences was performed via spectral interferometry (SI) [29] which is a linear measurement technique and provides the possibility to fully reconstruct the temporal electric field of complex shaped pulses, such as the generated pulse sequences. For SI measurements, the pulse sequences are redirected via mirror M2 into a spectrometer and spatially overlapped with the reference pulse by opening shutter S2. The spectral phase of each pulse sequence is then determined by means of the resulting spectral interference pattern, as well as the spectral phase of the reference pulse. Thus, the full spectral and temporal information can be obtained. Before the SI evaluation, the reference pulse has to be characterized. Nonlinear techniques like frequency-resolved optical gating (FROG) [49] or spectral phase interferometry for direct electric-field reconstruction (SPIDER) [50] cannot be used for characterization because the intensity of the reference pulse is too low to generate nonlinear signals. Therefore, the spectral phase is determined via temporal analysis by dispersing a pair of light e-fields (TADPOLE) [51]. This technique represents a combination of SI and FROG. First, the unmodulated pulse, i.e., the pulse that passes the pulse shaper without spectral modulation, is directed via mirror M1 into the setup of a second-harmonic generation (SHG) FROG [49] and fully characterized. After that, the spectral phase of the reference pulse is obtained via SI with the unmodulated pulse as described above.

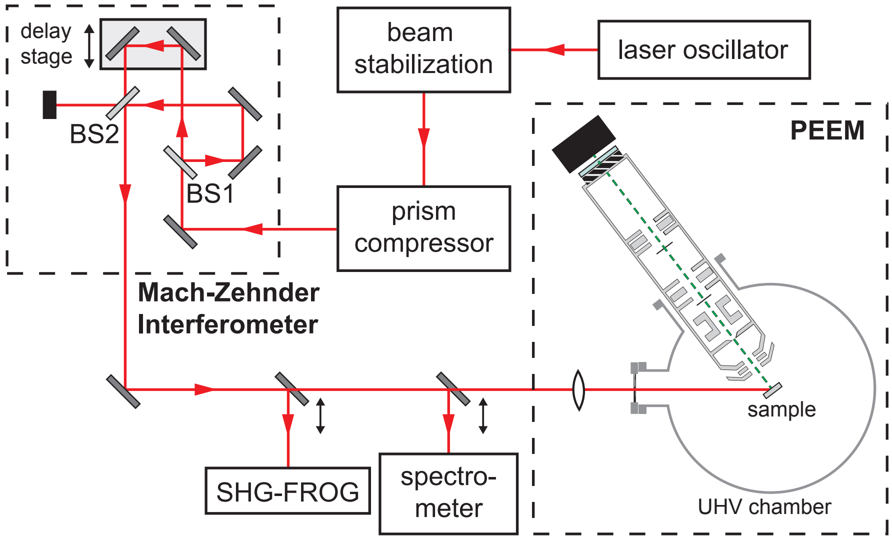

Figure 3.2: Sketch of the modified setup. Compared to the setup described in Sect. 3.1, a phase-stabilized Mach-Zehnder interferometer is used instead of the pulse shaper to generate collinear double-pulse sequences. An electronically-controlled moveable delay stage enables the variation of the time delay T between the two pulses of the sequence. The setup was utilized for the two-pulse experiment presented in Sect. 5.5.

The pulse shaper is also used for dispersion compensation to provide bandwidth-limited (sub) pulses at the sample position. Before each time-resolved measurement, a glass plate is positioned in the beam path directly behind the pulse shaper to reproduce the dispersion caused by the entrance window of the UHV chamber. The spectral phase of the unmodulated pulse is then characterized via SHG-FROG. After removing the glass plate from the experimental setup, the negative spectral phase is added as offset to the spectral phase modulation of the pulse shaper in the subsequent time-resolved measurements.

A detailed description of the utilized PEEM can be found in Refs. [52, 53]. Further information about the employed pulse shaper as well as amplitude and phase shaping of femtosecond laser pulses based on two-layer LCDs is given in Ref. [48] and Refs. [42, 43], respectively. The generation of collinear two- and four-pulse sequences via the pulse shaper is described in Refs. [1, 30].

3.2 Modified Setup with the Phase-Stabilized Mach-Zehnder Interferometer

For the two-pulse experiment presented in Sect. 5.5, the pulse shaper was replaced by a phase-stabilized Mach-Zehnder interferometer. A sketch of the modified setup is illustrated in Fig. 3.2. After the prism compressor, the beam is directed into the interferometer to generate double-pulse sequences. For this purpose, the incoming pulse is split into two pulses via the beamsplitter BS1, and the two pulses are then spatially recombined via the beamsplitter BS2. The temporal delay between the pulses is electronically controlled via a moveable delay stage located in one of the two beam paths between BS1 and BS2. Since the spectrum of the oscillator output is not limited by the interferometer, the maximum spectral bandwidth can be used for the experiments, leading to output pulses with a minimum pulse duration of 23 fs, a center wavelength of 800 nm, and a pulse energy of 8.7 nJ.

4 Anderson Localization of Light in Nanotextured Thin-Film Solar Cells

4.1 Introduction

In the last decades the question arose how energy could be generated in a sustainable way since mankind experienced a huge growth in its energy demand and thus non-renewable resources are being depleted. Therefore, the research about renewable energy sources became more and more important and is nowadays of high interest for science as well as for industry. Especially the solar technology which is based on the direct conversion of sunlight into electricity has successfully emerged over the years and its evolution is still in progress. In this field of research thin-film silicon solar cells are very promising due to their cost-effective fabrication and their environmental compatibility [54]. For this type of solar cells hydrogenated amorphous silicon (a-Si:H) serves as absorbing material. In contrast to crystalline silicon (c-Si), which is employed in traditional silicon solar cells, a long-range order of the silicon atoms in a-Si:H is missing. The structural disorder strongly influences the electronic and optical properties of the material [55]. Instead of the indirect band gap in crystalline silicon a-Si:H has a quasi direct band gap, i.e., for the absorption of a photon no additional phonon is necessary to fulfill the condition of momentum conservation [56]. This leads to considerably higher absorption coefficients in the spectral range of visible light. Hence, the absorber layer can be much thinner than in traditional silicon solar cells to achieve similar absorption in this spectral region.

The main components of an exemplary thin-film silicon solar cell are shown in Fig. 4.1a and are discussed in the following based on Refs. [44, 56, 57]. The a-Si:H layer is basically a p-i-n diode consisting of a very thin n-doped zone on top, an undoped intrinsic zone in the middle and a very thin p-doped zone on the bottom. The diode is embedded between two layers of transparent conductive oxide (TCO) and the complete layer stack is deposited on a glass substrate. An additional metallic layer on the bottom acts as back reflector for light which propagates through the layer stack without being absorbed. The photons of incoming sunlight are transmitted through the glass as well as the upper TCO layer and are absorbed in the a-Si:H layer. The generated electron-hole pairs are then spatially separated by an internal electric field which is caused by the two differently doped zones in the absorber layer. In the n-doped region donor impurity atoms are incorporated which have more valence electrons than silicon. The excess valence electrons are donated to the conduction band (CB) leading to a shift of the Fermi energy E_F towards CB. In the p-doped zone acceptor impurity atoms are added

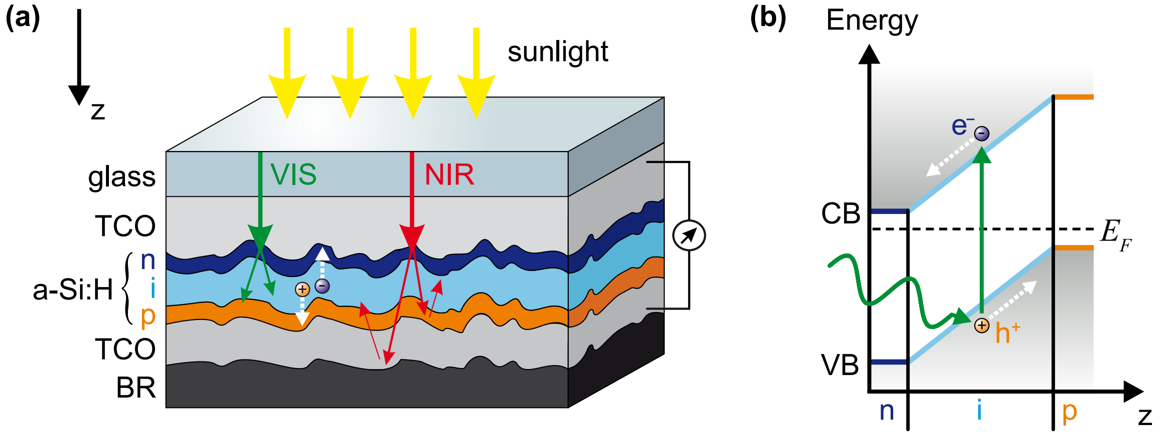

Figure 4.1: Functional principle of thin-film silicon solar cell. (a) Cross section of a thin-film solar cell with hydrogenated amorphous silicon (a-Si:H) as absorbing material. The incoming sunlight is transmitted through a glass substrate and a transparent conductive oxide (TCO) layer into the absorber layer consisting of n-doped (n), intrinsic (i) and p-doped (p) a-Si:H. The absorption coefficient of a-Si:H depends on the wavelength and is higher for the visible region (VIS, green arrow) than for the near-infrared regime (NIR, red arrow). Light that is transmitted through the absorber is reflected by a metallic backreflector (BR). The two TCO layers act as electrodes and enable the current flow. (b) Energy band diagram of the p-i-n-structured a-Si:H layer. An incident photon (green wavy arrow) is absorbed in the intrinsic zone and generates an electron-hole pair. The electron (e^-) in the conduction band (CB) and the hole (h^+) in the valence band (VB) are separated and move in opposite directions due to the potential gradient between the p- and the n-doped zone. Figure adapted from Ref. [44].

which have less valence electrons than silicon. These atoms capture electrons from the valence band (VB) and generate free holes in it. The Fermi energy is consequently shifted towards VB. Since both doped zones are in contact with the undoped intrinsic zone, E_F aligns on the same energy level along all three regions. This gives rise to a bending of the CB as well as the VB and a potential gradient emerges within the intrinsic area. The resulting energy band diagram is depicted in Fig. 4.1b. A photon generates an electron-hole pair in the intrinsic zone. Due to the electric field the electron in the CB moves to the TCO layer above the n-doped zone and the hole in the VB to the TCO layer below the p-doped zone. Since both TCO layers are contacted to an external electric circuit, an electric current is generated [44, 57].

In general, for an improvement of the solar cell efficiency it is crucial to enhance the absorption in the absorber layer for the complete solar spectrum. Although the absorption of visible light is significantly higher in a-Si:H than in c-Si, light in the near-infrared spectral regime is hardly absorbed compared to c-Si due to a drop of the absorption coefficients for wavelengths > 700 nm (see Fig. 4.2). The low absorption of near-infrared light could be enhanced by using thicker a-Si:H layers. However, if the absorber layer is too thick, the solar cell efficiency is reduced because of an increased carrier recombination within the layer. It has turned out that a good tradeoff between high absorption of the solar spectrum in the visible spectral regime and low carrier recombination within the absorber material is achieved by a layer thickness of about

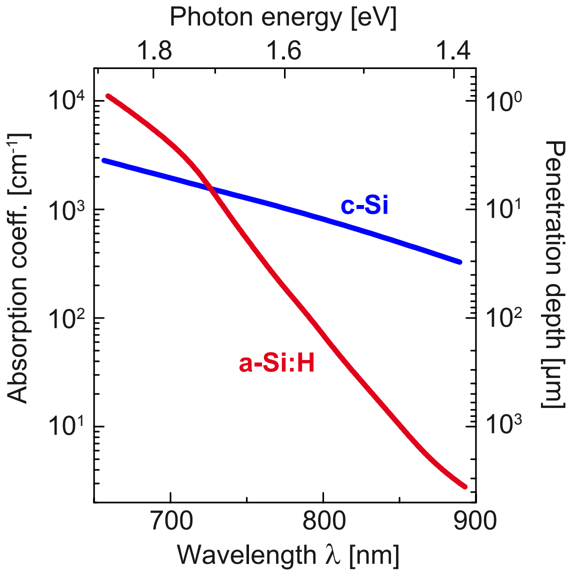

Figure 4.2: Absorption coefficients for hydrogenated amorphous silicon (a-Si:H, red line) and crystalline silicon (c-Si, blue line) as a function of the wavelength and the photon energy, respectively. In the near-infrared spectral region the absorption coefficients of a-Si:H decrease strongly. The penetration depth of the light is inversely related to the absorption coefficients. Figure taken from Ref. [44].

300 nm [55]. Since this value is by more than two orders of magnitude smaller than the penetration depth of near-infrared light, the absorber layer is too thin for an efficient absorption in this spectral range.

Therefore, other enhancement strategies have been suggested and investigated so far: Anti-reflection coatings can be used to reduce the losses due to the reflection at the solar cell surface which leads to an increased transmission into the semiconducting material [58]. Additionally, light-trapping approaches enlarge the effective path length of the incoming light within the absorber layer and can be realized by means of plasmonic nanostructures [59–61], gratings [62], and photonic crystals [63]. Another promising light-trapping concept is based on randomly nanotextured interfaces [64, 65]. In 1982 Yablonovitch *et al.* already investigated the enhancement for absorber layers with corrugated interfaces and predicted a theoretical upper limit of $4n^2$, where n is the refractive index of the absorbing layer [66]. However, their calculations were based on statistical ray optics assuming only thick absorber layers. For thin layers with thicknesses in the range of the wavelength or even smaller, the electromagnetic wave properties of light must be considered. Physical-optics simulations by Yu *et al.* [67] and by Mallick *et al.* [68] have shown enhancements far beyond the limit determined by Yablonovitch confirming the high potential of this light-trapping approach. Though such interfaces are already implemented in commercial devices, the reason for the increased absorption has not been clarified unambiguously. Nevertheless, the understanding of the enhancement mechanism is essential in order to exploit its full potential in future applications.

Two competing mechanisms can be responsible for light trapping by randomly nanotextured interfaces (confer Fig. 4.3): either the propagation length of the light is enlarged by single scattering events and therefore the absorption is increased, or the light is trapped by the formation of photonic modes which are localized within spatially confined areas [69, 70]. In numerical simulations Vynck *et al.* already showed an improved absorption efficiency due to the localization of light in thin nanostructured a-Si films [65]. However, in experiments the direct proof of light localization is still very challenging.

Figure 4.3: Possible mechanisms for enhanced absorption in nanotextured a-Si:H layers. Either the propagation length of the light is enlarged within the absorber layer due to single scattering events (left) or the light is trapped in localized photonic modes caused by multiple scattering (right). Figure taken from Ref. [2].

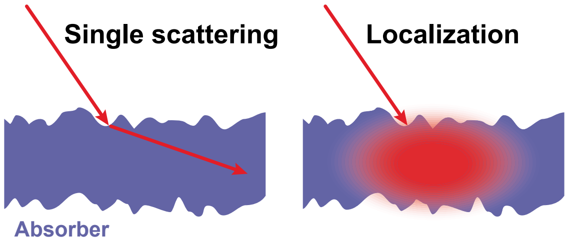

In this chapter, thin-film silicon solar cells with smooth and randomly nanotextured interfaces are investigated by means of optical spectroscopy to clarify the reason for the absorption enhancement in nanotextured a-Si:H layers. First, the preparation and characterization of the employed solar cell devices are presented (Sect. 4.2). In Section 4.3, the coherent backscattered radiation of the samples is analyzed via spectral interferometry, indicating the presence of localized photonic modes in the nanotextured absorber layers. After that, the results of a coherent 2D nanoscopy measurement on a specially modified device with an exposed nanotextured a-Si:H layer are shown which prove the light localization in the a-Si:H layer (Sect. 4.4). Finally, in Section 4.5 the type of localization is identified as strong localization based on the experimental results.

The work that is presented here resulted from a collaboration with the research groups of Walter Pfeiffer (Bielefeld), Martin Aeschlimann (Kaiserslautern), Ulrich Heinzmann (Bielefeld), and with Helmut Stiebig (Bielefeld), and was published in Ref. [2]. The sample fabrication and characterization as well as the linear absorption measurements were done by Florian Lükermann. Dominik Differt performed the coherent backscattering experiments and evaluated the corresponding data. The coherent 2D nanoscopy scans were executed by Christian Strüber, Philip Thielen, Martin Piecuch, Matthias Hensen and myself. My contribution within this collaboration was the implementation of the 2D nanoscopy scheme and the handling of the pulse shaper. The data evaluation of the resulting 2D nanospectra and the fit procedure were done by Christian Strüber. The major part of this chapter is based on the above-mentioned publication [2] and on Christian Strüber's PhD thesis [44].

4.2 Sample Preparation and Characterization

For the experiments described in the following sections three different solar-cell structures were prepared, which are depicted in Fig. 4.4a. The first two samples have the identical layer stack with a p-i-n diode grown by plasma-enhanced chemical vapor deposition (PEVCD) and surrounded by two 1 μm thick TCO layers using zinc oxide (ZnO) as transparent conductive material. The diode is made of hydrogenated amorphous silicon and serves as absorber layer. It consists of a thick intrinsic zone ($\approx$ 250 nm) embedded between a thin p-doped and a thin n-doped zone (both $\approx$ 10–20 nm). For the doping boron and phosphor atoms were incorporated into the p-doped and the n-doped zone, respectively. The layer stacks of both samples are deposited on glass substrates and differ only in their topography. The interface textures of the first sample are smooth, whereas

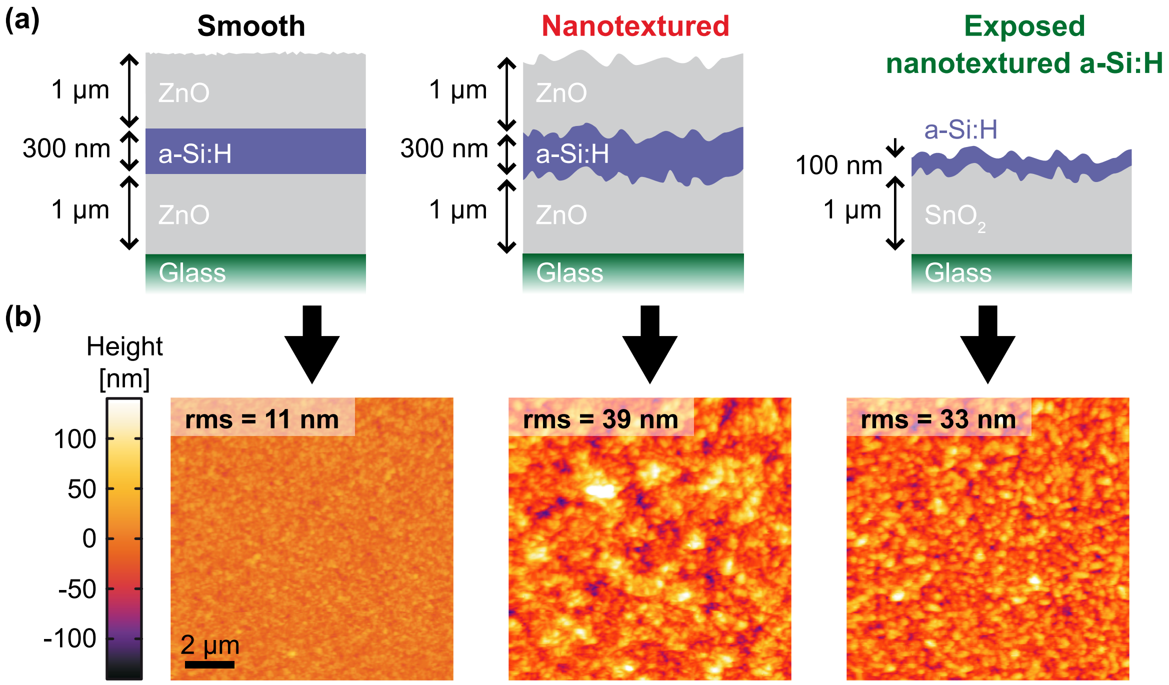

Figure 4.4: Characterization of the prepared thin-film silicon solar cells. (a) Schematic cross sections of the three different samples. The layer stack of the device with the smooth interfaces (left) is identical to that of the nanotextured device in the middle. The third sample is specially modified with a thinner absorber layer and without the second TCO layer (right). (b) Spatial height profiles of the sample surfaces recorded by atomic force microscopy (AFM). The root-mean-square (rms) roughness of the smooth sample (left) is much lower compared to the rms values of the nanotextured (middle) and exposed nanotextured device (right). Figure adapted from Ref. [2].

the interfaces of the second sample are randomly nanotextured. For the 2D nanoscopy experiment (Sect. 4.4) a specially modified sample was prepared. In its layer stack the second TCO layer was omitted so that the absorber layer is exposed at one side and a direct detection of the electrons emitted from its surface is possible. The a-Si:H layer is nanotextured similar to the interfaces of the second sample, but it consists only of a thin n-doped zone (doped with phosphor) and a 100 nm thin intrinsic zone. Furthermore, SnO_2 was used as TCO material instead of ZnO. For all three samples the metallic back reflector is missing to enable an additional optical access from the back side. It has to be mentioned that the third exposed sample is not a fully operative solar cell and its absorber layer is thinner than those in commercial solar cells. However, for the investigation of the light trapping mechanisms within the absorber layer the lack of functionality as a solar cell can be accepted here.

After preparation, the surface topographies of the samples were examined by atomic force microscopy (AFM) using a home-built setup under ambient conditions. In Figure 4.4b spatial height profiles of the sample surfaces are shown. For the first device with the smooth interfaces a relatively flat surface over large areas is observed compared to those of the nanotextured samples. The root-mean-square (rms) values of the

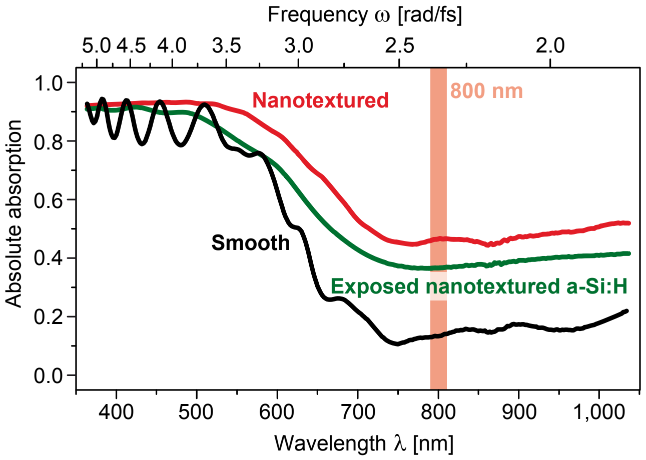

Figure 4.5: Linear UV-VIS absorption spectra for the prepared samples. The nanotextured as well as the exposed nanotextured device show an enhanced absorption in the near-infrared spectral region compared to the smooth sample. The vertical red bar at 800 nm indicates the spectrum of the ultrashort laser pulses used in the time-resolved experiments. Figure taken from Ref. [2].

height profiles which serve as a measure of the surface roughness are much higher for the nanotextured devices (39 nm and 33 nm for the exposed sample) than the rms value of the smooth device (11 nm). In addition, for both nanotextured samples the homogeneity of their nanotexture was investigated by means of cross correlations of their spatial height profiles [2]. Since only a small concentration of nanotexture anomalies ($\approx 1{\times}10^{-2}$ μm^{-2}) was observed, it is assumed that the light trapping mechanism in the nanotextured samples is not caused by local anomalies in the nanotexture.

In order to characterize the optical behavior of the samples absorption spectra were recorded with a Perkin Elmer Lambda 950 UV-VIS spectrometer. The spectrometer collects the transmitted as well as the reflected light and the resulting spectral absorption $A(\omega)$ is calculated via

$$A(\omega) = 1 - T(\omega) - R(\omega) \tag{4.1}$$

with the transmission $T(\omega)$ and the reflection $R(\omega)$ as a function of the frequency ω.

As opposed to the laser pulse experiments described in Sects. 4.3 and 4.4, the light entered the samples from the glass side here. The absorption spectra are depicted in Fig. 4.5. In the wavelength region below 550 nm the absorption of all devices shows high values between 80% and 95%. This strong absorption results from the high photon energies which overcome the optical bandgap (≈ 1.8 eV) of hydrogenated amorphous silicon [55]. The spectral oscillations in the absorption spectrum of the smooth sample are induced by the formation of Fabry-Pérot resonances. Due to the parallel interfaces the incident light beam can be reflected multiple times between the two TCO layers and the reflected beams interfere constructively or destructively as a function of the wavelength. In the second sample such resonances are extinguished by the nanotexturing and the absorption in this spectral region is enhanced compared to that of the smooth sample. For the modified device with the exposed a-Si:H layer the absorption is high, as well, but slightly lower than that of the other nanotextured device due to the thinner absorber layer. In the wavelength range of the interband absorption cutoff (600-700 nm) the values for all devices drop down and remain nearly constant for the near-infrared spectral regime. However, the absorption for the nanotextured sample with values of about 50% is significantly higher than that of the smooth sample with values below 20%. Even for the exposed sample the absorption is enhanced (≈ 40%), although the absorber layer of the smooth sample is three times thicker.

Additionally, for the two solar-cell devices with full functionality the short-circuit current densities were measured under standard solar cell test conditions [2]. Thereby, the effect of the metallic back reflector was imitated by a white sheet. Indeed, the current density of the nanotextured sample (15 mA cm^{-2}) is about 35% enhanced compared to that of the smooth sample (11 mA cm^{-2}). Furthermore, the values of the current densities are similar to those of commercial thin-film solar cells. Hence, the prepared samples are suitable to investigate the light trapping mechanism in optimized thin-film silicon solar cells. A more detailed description of the preparation steps as well as the AFM and linear absorption measurements can be found in Ref. [2].

4.3 Coherent Backscattering Spectroscopy

In order to find the reason for the absorption enhancement that was observed for the nanotextured samples in the near-infrared spectral regime, a detailed insight into the temporal and spectral evolution of the incoming light within the absorber layer is necessary. For this purpose, microscopy experiments with coherent femtosecond laser pulses were performed to analyze the radiation scattered from the absorber layer of each sample. A scheme of the experimental setup is illustrated in Fig. 4.6a. Bandwidth-limited laser pulses with a pulse duration of 25 fs (FWHM) and a center wavelength of 790 nm are focused onto the sample under a small incidence angle of 2° with respect to the surface normal. The diameter of the focal spot on the sample surface is $\approx 15\ \mu$m determined by the 1/e^2 values of the light intensity. Although the major part of the incident pulses is either absorbed, transmitted through the layer stack or reflected in the specular direction, there is a small fraction which is scattered back by the absorber layer. This backscattered light is collected by a focusing mirror and coupled into a spectrometer via a single mode fiber. The entrance aperture of the fiber is located in the focus of a microscope objective such that only the radiation coming from the excitation focal spot is transmitted to the spectrometer. In addition, the sample position can be moved laterally with respect to the focal spot.

For all three samples backscattered spectra were recorded for 25 different positions along a lateral scan of the sample position over 100 μm as depicted in Fig. 4.6b. The spectra obtained for the device with the smooth interfaces are very similar to the spectrum of the incident laser pulse and do not reveal pronounced spectral variations along the scan. However, in the spectra for the device with the nanotextured interfaces a more complex behavior is observed which strongly depends on the lateral position of the sample. A typical spectrum of the scan is shown in Fig. 4.6c. In contrast to the incident spectrum it consists of several narrow peaks confirming the presence of spectral resonances in the investigated region. Since the spectral line width of each resonance peak represents a lower limit of the corresponding resonance lifetime, it was possible to compile a statistical lifetime distribution by calculating the minimum lifetime values for all line widths in the spectra measured along the lateral scan. The result is presented in the inset of Fig. 4.6c. The distribution is centered at ≈ 100 fs containing exceptionless high values higher than 50 fs. Assuming that the lifetimes represent roughly the time

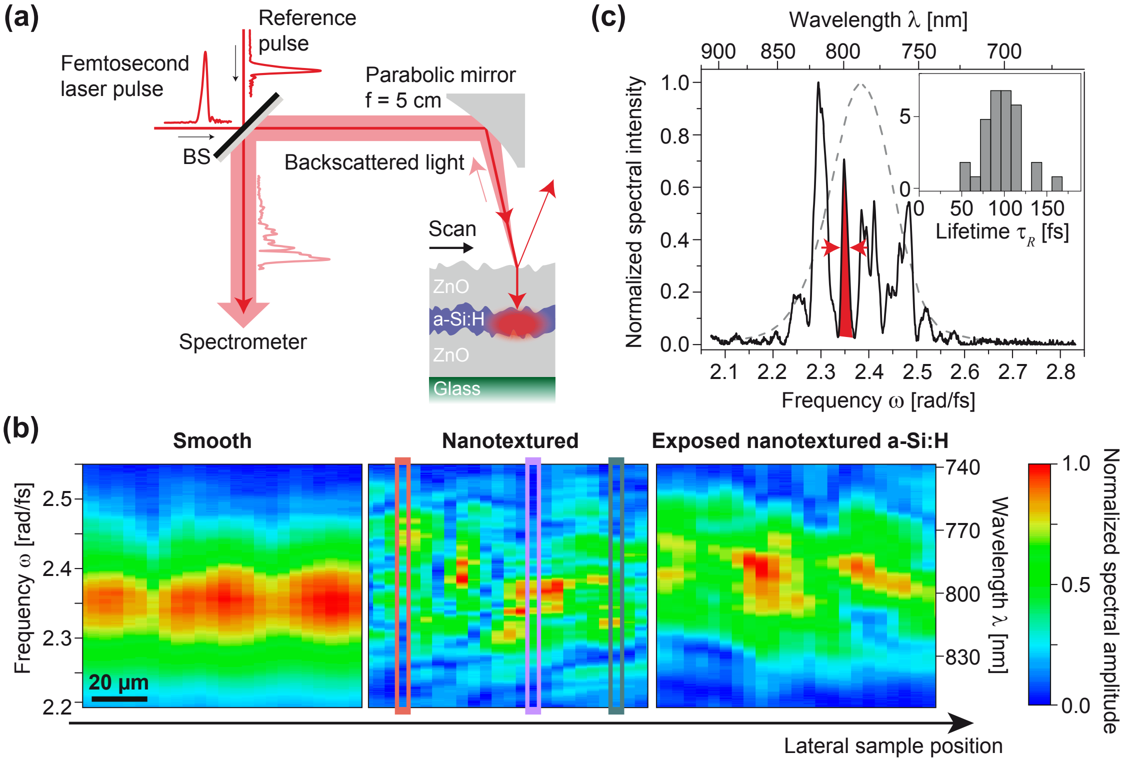

Figure 4.6: Investigation of the coherent backscattered radiation. (a) Scheme of the experimental setup. Femtosecond laser pulses (25 fs pulse duration, 790 nm center wavelength, 80 MHz repetition rate) are focused onto the sample under a small incidence angle. A portion of the coherent backscattered light is redirected by a parabolic mirror and detected via a spectrometer. It can additionally be superimposed with a reference pulse for spectral interferometry (SI). A moveable sample holder (not shown here) enables lateral scans of the sample position. (b) Spatially-resolved spectral field amplitude of the backscattered radiation for all three devices. Each set of spectra was obtained by a unidirectional lateral scan over 100 μm. For the three spectra indicated by the colored boxes in the middle panel the time-domain representation was determined and is illustrated in Fig. 4.7a. (c) Normalized spectral intensity measured at one sample position for the nanotextured device. The gray dashed line indicates the incident laser spectrum. The red marked area exhibits a spectral line with a line width of 0.013 rad/fs corresponding to a minimum coherence lifetime of $\tau_R = 160$ fs. The inset shows a histogram of the lifetime distribution that was received from the resonance peaks in the spectra of the nanotextured sample depicted in b. Figure taken from Ref. [2].

in which the incoming light resides in the device, the backscattered radiation is much longer in the absorber layer than light which would only propagate vertically through the layer stack (≈ 7.5 fs).

The same statistical peak analysis was done for the exposed nanotextured sample. Here, the spectra consist of distinct spectral peaks, as well, but they exhibit a higher background signal and the peaks are slightly broader than those of the nanotextured sample with the two TCO layers. This is explained by the increased diffuse reflection at the amorphous silicon layer due to the stronger change of the refractive index from air to a-Si:H compared to that from ZnO to a-Si:H ($n_{\text{a-Si:H}}/n_{\text{air}} \approx 4$, $n_{\text{a-Si:H}}/n_{\text{ZnO}} \approx 2$, taken from Ref. [56]). Nevertheless, the lifetime values for this structure are comparatively high, as well, with an average value of ≈ 70 fs.

In addition to the statistical analysis of the spectra in the Fourier Domain the temporal evolution of the backscattered radiation was also investigated in detail. Since the temporal fields had to be reconstructed from the spectral fields via Fourier transformation, the information about the spectral phase of each measured spectrum was required to calculate the corresponding temporal field unambiguously. However, nonlinear techniques like frequency resolved optical gating (FROG) [49] or spectral phase interferometry for direct electric-field reconstruction (SPIDER) [50] could not be used to retrieve the spectral phases because the intensities of the backscattered light were too low for the generation of nonlinear signals. Therefore, the so-called spectral interferometry (SI) [29] was applied which enables the full reconstruction of the temporal electric field of laser pulses with low intensities due to the detection of a linear signal. At each position of the lateral scan the backscattered pulses were superimposed with a reference pulse originating from the same laser source as the incident excitation pulse and the resulting spectral interference patterns were recorded by a spectrometer (see Fig. 4.6a). The spectral phases of the backscattered pulses were then received by means of the respective interference spectra as well as the spectral phase of the reference pulse which was previously determined by SPIDER. In Figure 4.7a the temporal field evolution at three different positions on the nanotextured sample with the two TCO layers is shown. After a fast initial increase the temporal amplitudes of all three curves decay slowly with a very complex and unique beating behavior. This beating behavior results from the presence of several resonance peaks which are excited by the incident laser spectrum. The temporal behavior at each sample position depends on the number and the spectral positions of the resonances within the laser spectrum.

For a further insight into the evolution of the temporal field envelope, the temporal backscattered field amplitudes were incoherently averaged over all 25 sample positions, i.e., they were summed up without taking into account the corresponding temporal phases. The resulting normalized signals for the three samples are illustrated in Fig. 4.7b. The averaged field amplitude of the smooth device (black line) follows the electric field amplitude of the incident laser pulse in the first approximation. After reaching the maximum at time zero the signal decreases fast. Since the absorption is spectrally inhomogeneous in the amorphous silicon layer, the duration of the backscattered signal is slightly higher than the pulse duration of the incident pulse. In contrast, the temporal behavior of the nanotextured sample with the two TCO layers (red line) is significantly different. The averaged amplitude shows an exponential decay and decreases much slower than the signal of the smooth sample. For the exposed nanotextured sample (green line) a similar exponential tail is observed, but with a slightly faster decay. An exponential fit of the tails leads to average coherence lifetime values of 70 fs for the exposed nanotextured and 135 fs for the nanotextured device which is in good agreement with the average lifetime values obtained from the statistical analysis of the spectral line widths.

Such long-lived coherence lifetimes confirm that the incoming light is trapped in the nanotextured devices, i.e., it remains in the nanotextured devices much longer than in the smooth device and therefore, the absorption is enhanced. Furthermore, the strong spatial variations of the backscattered spectra within the range of the focal spot size

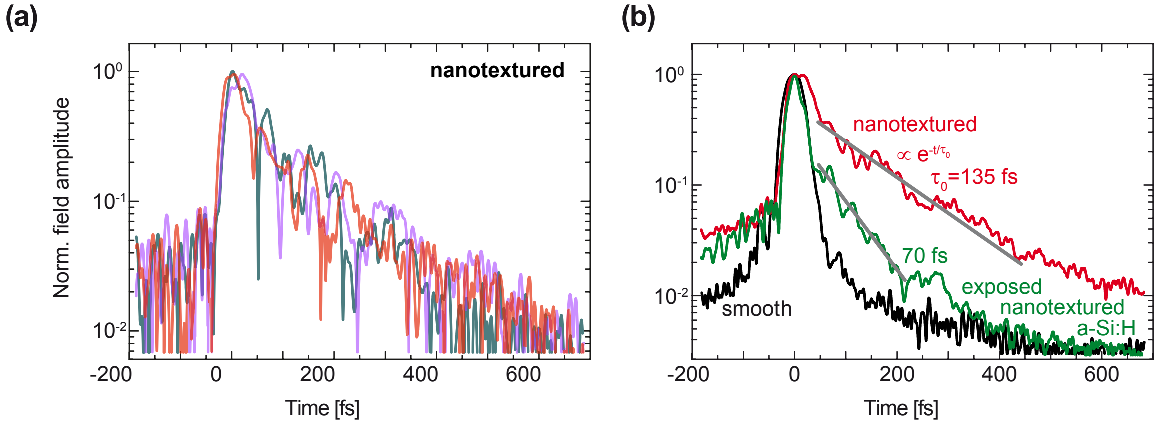

Figure 4.7: Time-domain representation of the coherent backscattered radiation from the investigated thin-film silicon solar cells by using spectral interferometry. (a) Normalized amplitude of the temporal electric field at three different positions on the nanotextured device with the two TCO layers (see colored boxes in Fig. 4.6b). (b) Incoherent average of the temporal backscattered field amplitudes determined from the lateral scans shown in Fig. 4.6b. The amplitude decays of the nanotextured and the exposed nanotextured sample were fitted with a single exponential function (gray solid lines). Figure taken from Ref. [2].

(10–20 μm) indicate that the observed resonances are confined to the volume defined by the thickness of the absorber layer and by the focal spot. The existence of the localized resonances could be explained by the formation of localized standing-wave patterns within the silicon layer. These localized photonic modes are then observable via their leakage radiation. A minor part of the trapped light escapes from the modes, propagates back out of the layer stack and can be detected. However, the spectral peaks in the measured spectra could also be caused by a spectrally selective diffraction of the incoming light into the a-Si:H layer. Thus, additional measurements with a higher spatial resolution are necessary to decide which of the two possible mechanisms is responsible for the observed behavior. Further information about the coherent ultrafast backscattering experiments can be found in Ref. [2] and in Dominik Differt's PhD thesis [71].

4.4 Coherent 2D Nanoscopy on the Exposed Nanotextured a-Si:H Layer

Coherent 2D nanoscopy provides high temporal resolution in the femtosecond regime as well as high spatial resolution below the optical diffraction limit [1]. Hence, it was a suitable technique to clarify the light trapping mechanism in the nanotextured absorber layer. A detailed description of this method is given in Chapter 2 and Ref. [1]. For the experiment presented in this section only the exposed nanotextured sample was used because its modified layer stack allowed a direct detection of the electrons which were emitted from the surface of the a-Si:H layer due to the excitation with ultrashort laser pulses. This was not possible for the other two samples since their absorber layers are covered by a second TCO layer. The experimental setup consisting of a home-

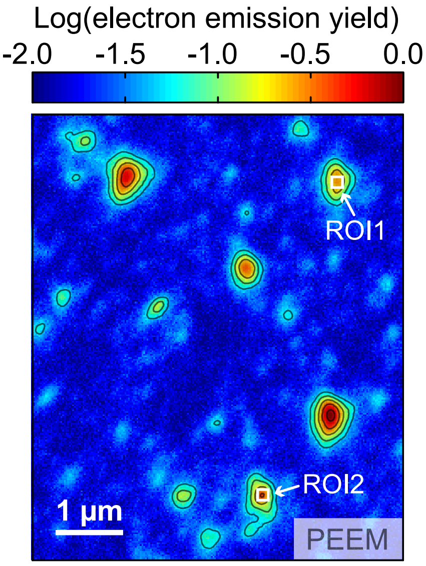

Figure 4.8: Spatially-resolved electron emission of the exposed nanotextured sample. The local electron yield is normalized to the maximum value of the emission pattern and plotted on a logarithmic scale. The image was taken with a normal incidence photoemission electron microscope (NI-PEEM) for the bandwidth-limited laser pulse (60 fs pulse duration, 800 nm center wavelength). The detected electrons originate from the surface of the a-Si:H layer. The spatial distribution of the electron emission is dominated by localized hot spots. Figure adapted from Ref. [2].

built femtosecond pulse shaper and a FOCUS normal incidence photoemission electron microscope (NI-PEEM) is explicitly described in Chapter 3. The collinear four-pulse sequences with the time delays τ, T, and t as well as with the relative phases φ_τ, φ_T, and φ_t were generated by the pulse shaper using the bandwidth-limited laser pulse with a center wavelength of 800 nm and a pulse duration of 60 fs (FWHM of temporal intensity). In the 2D nansocopy measurement T and φ_T were set to zero, such that the second and the third sub pulse of the sequence temporally overlapped. The sample was positioned in the vacuum chamber of the PEEM and the pulse sequences impinged under an incidence angle of 4°, i.e., near normal incidence. The spatial distribution of the time-integrated electron emission was measured by the CCD camera of the PEEM and saved as PEEM image. The field of view (FoV) was set to 30 μm ensuring a high spatial resolution below 40 nm. The exposure time of the camera was adjusted to 1100 ms to exploit the optimal dynamic range of the electron yield. Before performing the 2D nanoscopy measurement, the electron emission pattern was recorded with the excitation of the bandwidth-limited pulse, i.e., for $\tau = T = t = 0$ and $\varphi_\tau = \varphi_T = \varphi_t = 0$. The obtained PEEM image is shown in Fig. 4.8. The emission is not homogeneously distributed over the complete area, but rather dominated by distinct spatially confined hot spots with a significantly higher electron yield. By means of 2D nanoscopy the spectral properties of these hot spots were investigated to prove the existence of localized photonic modes in the a-Si:H layer. The nanoscopy scan was done in the rotating frame of the center frequency of the laser spectrum $\omega_0 = 2.356$ rad/fs. Thus, compared to a scan in the laboratory frame, larger steps of the coherence time τ and the signal time t could be chosen to sample the measurement signal and, with this, the measurement time could be significantly reduced (see Appendix A.1). Both τ and t were varied from 0 to 280 fs in steps of 10 fs and for each time-delay step the spatial distribution of the electron emission was measured. A (4×4)-step phase-cycling scheme [37, 40] was applied to extract the photon-echo signal contribution, i.e., the contribution that arises from the interaction with all sub pulses of the pulse sequence and therefore depends on both relative phases φ_τ and φ_t (see Sect. 2.4). For this purpose, φ_τ and φ_t were varied from 0 to $3\pi/2$ in steps of $\pi/2$ at each time-delay step and the resulting local electron emission $Y(\mathbf{r},\tau,t,\varphi_\tau,\varphi_t)$ was measured for the 16 different combinations of φ_τ and φ_t. Since thermal drifts between the CCD camera and the sample holder occurred during the scan, a drift correction was necessary in order to preserve the high spatial resolution. Therefore, an additional reference PEEM image was acquired per time-delay step using the bandwidth-limited pulse. After the scan the drift was determined by cross-correlations of the single reference images and all PEEM images were shifted back by means of their respective drift vectors [44]. The photon-echo signal contribution was then calculated with the drift-corrected data according to Eqs. (2.25) and (2.26) in Sect. 2.4 via

$$\widetilde{Y}_{\mathrm{PE}}(\mathbf{r},\tau,t) = \frac{1}{16}\sum_{m=0}^{3}\sum_{l=0}^{3} Y\left[\mathbf{r},\tau,t,\varphi_\tau(l),\varphi_t(l,m)\right]\mathrm{e}^{-\mathrm{i}l\cdot\pi}\mathrm{e}^{\mathrm{i}m\cdot\frac{\pi}{2}}\,, \tag{4.2}$$

wherein the relative phases are defined by

$$\begin{aligned} \varphi_\tau(l) &= l\cdot\frac{\pi}{2} && \text{with } l = 0,1,2,3\,,\\ \varphi_t(l,m) &= \begin{cases} m\cdot\frac{\pi}{2} - l\cdot\frac{\pi}{2} + 2\pi & \text{if } \left(m\cdot\frac{\pi}{2} - l\cdot\frac{\pi}{2}\right) < 0\,,\\ m\cdot\frac{\pi}{2} - l\cdot\frac{\pi}{2} & \text{if } \left(m\cdot\frac{\pi}{2} - l\cdot\frac{\pi}{2}\right) \geq 0 \end{cases}\\ & && \text{with } m = 0,1,2,3\,. \end{aligned} \tag{4.3}$$

In contrast to Eq. (2.26) a distinction between two cases was made for $\varphi_t(l,m)$ in Eq. (4.3) to keep the values of the relative phases between 0 and $3\pi/2$ in the measurement. Finally, the local complex-valued 2D nanospectra were obtained via the 2D Fourier transformation

$$S_{\mathrm{PE}}\left(\mathbf{r},\omega_\tau-\omega_0,\omega_t-\omega_0\right) = \int_{-\infty}^{+\infty}\int_{-\infty}^{+\infty} \widetilde{Y}_{\mathrm{PE}}\left(\mathbf{r},\tau,t\right)\mathrm{e}^{-\mathrm{i}\omega_\tau\tau}\mathrm{e}^{-\mathrm{i}\omega_t t}\mathrm{d}\tau\mathrm{d}t. \tag{4.4}$$

Note that a continuous Fourier transformation is described here for the sake of simplicity whereas the experimental 2D spectra were calculated via a discrete Fourier transformation. Furthermore, since the electron yield was measured in the rotating frame of ω_0, S_{PE} depends on the difference frequencies $(\omega_\tau-\omega_0)$ and $(\omega_t-\omega_0)$ instead of the absolute frequencies ω_τ and ω_t (Appendix A.1).

The local electron yield of all pixels within the FoV ($\approx 10^6$) was detected simultaneously such that local 2D nanospectra from different positions could be directly compared to each other. The real parts of two local 2D nanospectra are shown in Fig. 4.9 and illustrate the spatial dependency of the sample response. They originate from two different hot spots marked in Fig. 4.8 as ROI1 and ROI2, respectively, and are averaged over a region of 4×4 pixels corresponding to an area of about 100 nm^2. In Fig. 4.9a the real parts of the 2D spectra without phase cycling are depicted to demonstrate the importance of phase-cycling scheme selection in 2D nanoscopy. They were obtained via a 2D Fourier transformation of the local electron yield measured for the relative phases $\varphi_\tau = \varphi_t = 0$.

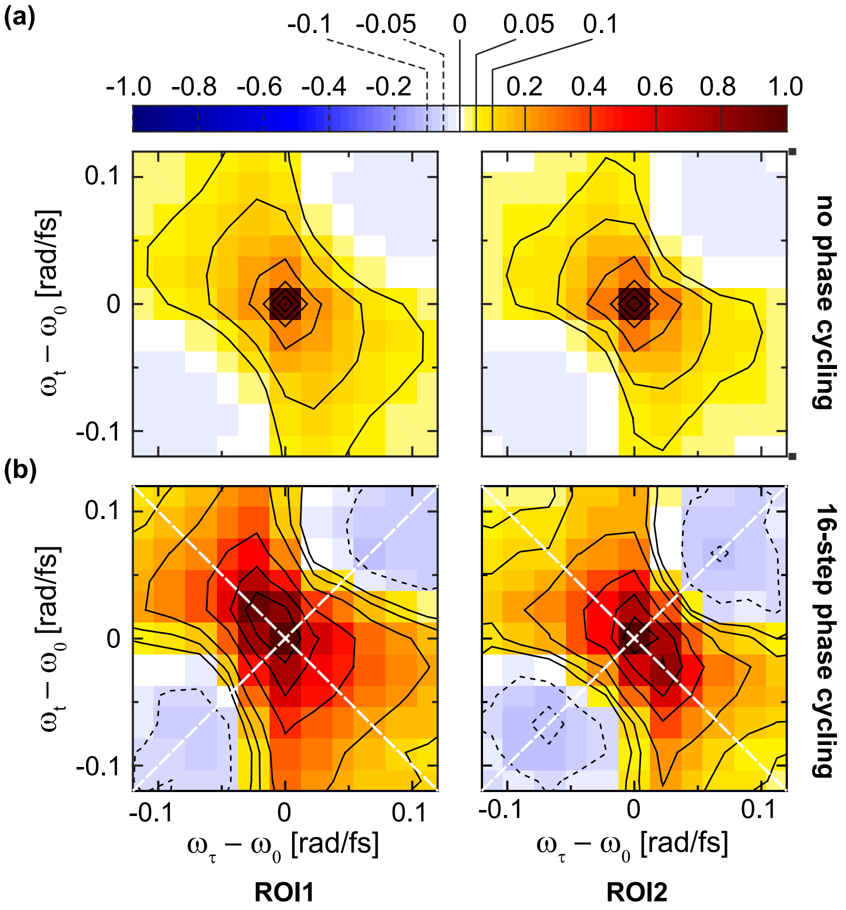

Figure 4.9: Real parts of local 2D nanospectra for two different regions ROI1 (left) and ROI2 (right) of the exposed a-Si:H layer marked with white squares in Fig. 4.8. Each spectrum is normalized to the maximum of its absolute value. Both frequency axes range from -0.12 to +0.12 rad/fs with respect to the center frequency of the laser spectrum $\omega_0 = 2.356$ rad/fs. (a) Real parts obtained without phase cycling for the relative phases $\varphi_\tau = \varphi_t = 0$. The spectra are dominated by the background signal and contributions that arose from interactions with only one pulse of the pulse sequence, leading to a maximum at $(\omega_\tau - \omega_0) = (\omega_t - \omega_0) = 0$. (b) Real parts of the photon-echo contribution obtained with a 16-step phase cycling. The white dashed lines are inserted to facilitate the comparison between both spectra. The peak in the real part of ROI1 is broader and slightly shifted compared to the peak in the real part of ROI2 along the diagonal (from top left corner to bottom right corner).

In each spectrum one peak is observed on the diagonal (defined from top left corner to bottom right corner of the spectrum), but the peaks only differ slightly in comparison with each other. Due to the Fourier transformation of real-valued signals, both 2D spectra fulfill the condition $S\left[-\left(\omega_\tau - \omega_0\right), -\left(\omega_t - \omega_0\right)\right] = S^*\left[\left(\omega_\tau - \omega_0\right), \left(\omega_t - \omega_0\right)\right]$ and therefore their real parts have point symmetry with respect to the central point defined by $(\omega_\tau - \omega_0) = (\omega_t - \omega_0) = 0$. Thus, a spectral shift of the local sample response with respect to ω_0 could not be determined unambiguously because the shift would appear both at lower and higher frequencies in the 2D spectrum. In addition, the 2D spectra are congested by the background signal of the CCD camera and signal contributions that arose from interactions with only one pulse, leading to a very high maximum at the central point of the spectra. Contributions that were generated due to interactions with all pulses of the sequence spectrally overlap with these dominant signals and are hidden in the 2D spectra. Hence, it was necessary to extract the desired signal contribution via phase cycling. In Fig. 4.9b the real parts of the 2D spectra are shown that correspond to the photon-echo signal contribution. They were obtained via the 16-step phase cycling according to Eq. (4.4). Both spectra still contain one peak on the diagonal, but in contrast to the spectra without phase cycling, the peaks differ significantly in their spectral positions and widths. Since the phase-cycled signals $\widetilde{Y}_{\mathrm{PE}}$ are complex-valued in the time domain, the 2D spectra resulting from the Fourier transformation are not restricted to the above-mentioned point-symmetry condition and spectral shifts can be determined unambiguously. The peak of ROI1 is slightly shifted along the diagonal suggesting that a resonance with a frequency $\omega \neq \omega_0$ was excited by the incident laser spectrum at the position of ROI1. In the photon-echo 2D spectrum of a rotating-frame experiment, a resonance with frequency $\omega > \omega_0$ is generally located at the positive $(\omega_t - \omega_0)$ axis and the negative $(\omega_\tau - \omega_0)$ axis. This is due to the fact that the photon-echo contribution contains rephasing signals which oscillate with negative frequencies during the coherence time τ but positive frequencies during the signal time t (confer Sects. 2.1 and 2.3). Thus, the observed peak in the real part of ROI1 corresponds to a resonance with a frequency $\omega > \omega_0$. By contrast, the peak in the real part of ROI2 is closer to ω_0 with a small shift towards lower frequencies. Moreover, the peak of ROI1 is spectrally broader than the peak of ROI2. This indicates that the resonances at the two hot spots differ not only in their resonance frequencies, but also in their coherence lifetimes.

To investigate the spatial distribution of the spectral properties in more detail the full spatial resolution of the technique was exploited and local 2D nanospectra of the photon-echo signal contribution were calculated separately for every single pixel of the area shown in Fig. 4.8. As expected, the nanospectra for pixels outside the hot spots were dominated by noise due to the low electron yield and could not be used for further data analysis. In contrast to this, the spectra within the hot spots contained a distinct peak whose spectral properties depended on the spatial position of the corresponding pixel. Spectra from the same hot spot were very similar whereas spectra from different hot spots could vary significantly with respect to their peak width and their peak position.

However, for a quantitative analysis of the local 2D nanospectra it was necessary to clarify first the underlying electron emission process and, in particular, its nonlinear order. Hence, the local electron emission Y was measured as a function of the power of the incident bandwidth-limited laser pulse W. Additional reference PEEM images were recorded between each measurement step for the drift correction [44]. After the data acquisition the local nonlinearity of the emission process N_j was determined for every spatial pixel j by a fit of the drift-corrected data set with the power law function

$$Y_j(W) = a_j + b_j \cdot W^{N_j} \qquad \text{with } N_j \in \mathbb{R}\,, \tag{4.5}$$

wherein a_j and b_j are the offset parameter and the scaling factor, respectively. A spatial map of the fit results is shown in Fig. 4.10. Pixels with an electron emission $< 5\%$ of the maximum electron yield obtained for the highest laser power were neglected and

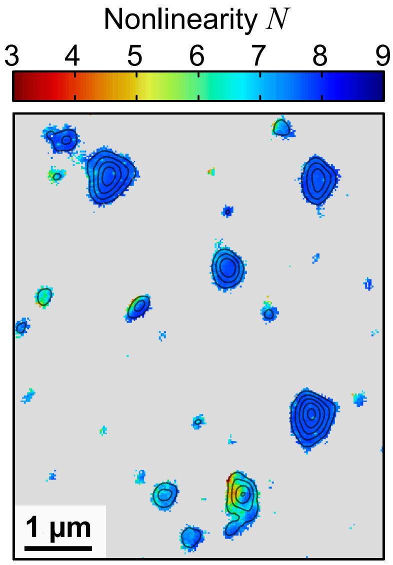

Figure 4.10: Local nonlinearity N of the electron emission pattern shown in Fig. 4.8. For the determination of the nonlinear order the local electron yield was first measured as a function of the excitation pulse power using the bandwidth-limited pulse and then fitted with a power function. In the gray colored areas the yield was too low ($< 5\%$ of the maximum yield) to obtain a reliable fit result. The contour lines indicate the logarithmized electron emission, which are identical to those of Fig. 4.8. Figure taken from [2].

grayed out in the map because the low electron yield did not result in a reliable fit. For most of the hot spots very high values for N_j between 7 and 9 were observed. However, assuming a work function of 5.8 eV for a-Si:H and a photon energy of roughly 1.55 eV corresponding to a wavelength of 800 nm, only four photons would be necessary to excite an electron from the sample surface into the vacuum via a multiphoton photoemission process. Hence, such a process would result in a significantly lower nonlinearity of $N = 4$. Moreover, the high nonlinearities can also not be explained by above-threshold photoemission and strong-field emission processes [72, 73].

In the following section a thermionic emission model is discussed which is based on the heating-up of the electron gas due to the absorption of light. Since this process strongly depends on the absorbed energy, it can be responsible for the high nonlinear order of the measured electron yield.

4.4.1 Thermionic Emission Model

When a metal or a semiconductor is heated up, the electrons inside the material are thermally excited. If some of the electrons gain enough energy to overcome the work function, they escape from the material. This thermally induced electron flow is called thermionic emission and was first reported by Frederick Guthrie in 1872 [74]. After decades of research, among others by Thomas A. Edison and Owen W. Richardson, this phenomenon is nowadays well-known and used for many applications, e.g. for thermionic cathodes in vacuum tubes [75, 76]. If the heating-up of the material is caused by light absorption, the resulting thermionic emission can depend strongly on the absorbed energy and therefore strongly on the power of the incident light.

In the following, a thermionic emission model is introduced to explain the high nonlinearities observed for the localized hot-spot electron emission of the exposed a-Si:H layer in the 2D nanoscopy experiments. The basic idea is illustrated in Fig. 4.11. The light of the incident laser pulse is coupled to photonic modes which are spatially confined in the amorphous silicon layer. Thus, the light is trapped within the modes and absorbed at

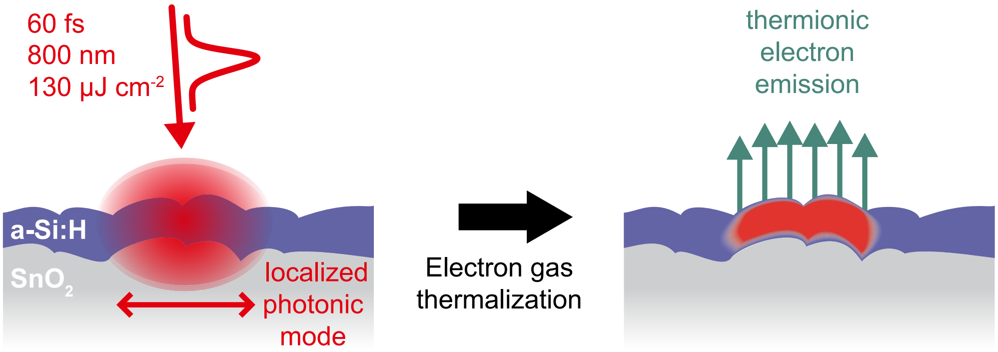

Figure 4.11: Thermionic emission from the nanotextured a-Si:H layer. The incident laser pulse couples to localized photonic modes, leading to an enhanced absorption in the amorphous silicon layer. By means of the absorbed energy the electron gas is locally heated. After its thermalization high-energy electrons can leave the material and thermionic emission occurs. Figure adapted from Ref. [2].

some point. The locally absorbed energy heats the electron gas at the positions of the modes. Finally, electrons can escape from there into the vacuum because of the thermal excitation. However, the thermionic emission only occurs after the light absorption. During the laser-pulse excitation the electron emission is dominated by multiphoton photoemission processes. Due to the simultaneous absorption of multiple photons electrons are transferred into vacuum states and leave the absorber layer. Nevertheless, a large part of the pulse energy is deposited into the electron gas by the absorption of single photons. Hence, the electron gas is highly excited after the light-matter interactions and its electron distribution is not yet thermalized. Via electron-electron scattering the non-thermal distribution evolves then into a thermal Fermi distribution with a maximum electron gas temperature $T_{\mathrm{el}}^{\mathrm{max}}$ which is higher than the inital electron gas temperature $T_{\mathrm{el}}^{\mathrm{init}}$ before the absorption processes. For a sufficiently high $T_{\mathrm{el}}^{\mathrm{max}}$ the tail of the distribution reaches above the work function and electrons which populate states in this tail are emitted into the vacuum. Therefore, the electron emission depends on the final electron gas temperature which in turn depends strongly on the absorbed energy.

Assuming that the thermalization process lasts for 50–100 fs, cooling mechanisms like hot-electron transport in an inhomogeneously excited system, electron-phonon scattering, or the thermionic emission itself can be neglected here because they have either only weak effects on the electron gas temperature or occur on time scales which are considerably larger than 100 fs [2]. Thus, the locally absorbed energy remains mostly in the local electronic system and is given by

$$\begin{aligned} E_{\mathrm{abs}}\left(T_{\mathrm{el}}^{\mathrm{max}}, T_{\mathrm{el}}^{\mathrm{init}}\right) = \int_{-\infty}^{\infty} & \mathrm{EDOS}\left(E\right) \\ & \times \left\{ \frac{1}{1+\exp\left[\frac{E-E_F}{k_b T_{\mathrm{el}}^{\mathrm{max}}}\right]} - \frac{1}{1+\exp\left[\frac{E-E_F}{k_b T_{\mathrm{el}}^{\mathrm{init}}}\right]} \right\} \left(E-E_F\right) \mathrm{d}E \end{aligned} \tag{4.6}$$

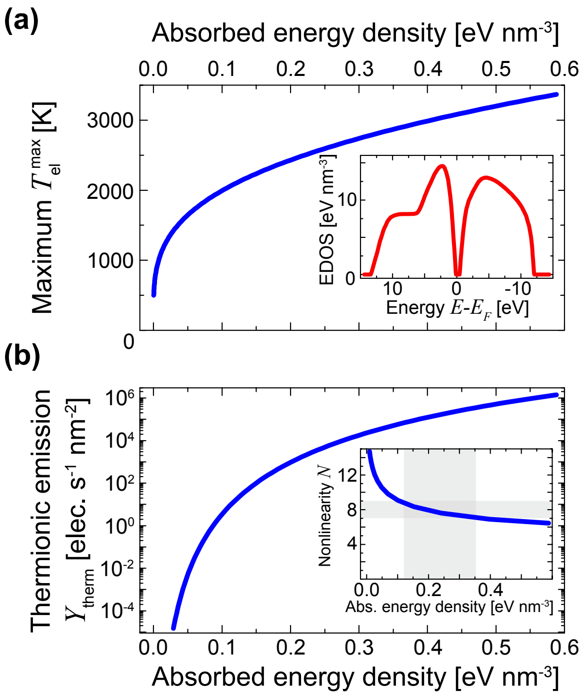

Figure 4.12: Thermionic emission model for a-Si:H. (a) Maximum electron gas temperature $T_{\mathrm{el}}^{\mathrm{max}}$ as a function of the absorbed energy density E_{abs} according to Eq. (4.6). For the calculations the initial temperature of the electron gas was set to room temperature, i.e., $T_{\mathrm{el}}^{\mathrm{init}} = 300$ K. The inset shows the electronic density of states EDOS used for a-Si:H. (b) Thermionic emission yield Y_{therm} as a function of E_{abs} based on Eqs. (4.6) and (4.7). The corresponding nonlinear order of the emission process N is obtained via Eq. (4.8) and shown as inset. The range of the experimentally observed values for N between 7 and 9 and their corresponding theoretical absorbed energy densities are highlighted by the gray rectangles. Figure taken from Ref. [2].

with the Boltzmann constant k_b, the Fermi energy E_F and the electronic density of states EDOS(E) which depends on the energy E. For further calculations the EDOS is taken from a theoretical model of a-Si:H [77] as depicted in the inset of Fig. 4.12a. Its scale is calibrated by using another theoretical model for amorphous silicon [78]. Since the density of states varies significantly with the amount of hydrogen in the amorphous silicon, an uncertainty in the used EDOS is estimated on the order of 10%. The relation between $T_{\mathrm{el}}^{\mathrm{max}}$ and E_{abs} according to Eq. (4.6) is illustrated in Fig. 4.12a. For low absorbed energy densities the temperature increases very fast due to the missing electronic states in the middle of the band gap around E_F, whereas for higher density values the slope of the temperature becomes flatter.

Furthermore, the dependency of the thermionic emission yield Y_{therm} on the electron gas temperature T_{el} is described by the so-called Richardson-Dushman equation

$$Y_{\mathrm{therm}} = A_0 T_{\mathrm{el}}^2 \mathrm{e}^{-\frac{W_{\mathrm{eff}}}{k_b T_{\mathrm{el}}}} \tag{4.7}$$

with the Richardson constant $A_0 = 60\ \mathrm{AK}^{-2}\mathrm{cm}^{-2}$ and the effective work function $W_{\mathrm{eff}} = 4.9$ eV [2]. The relation between Y_{therm} and E_{abs} can then be determined via Eqs. (4.6) and (4.7) using $T_{\mathrm{el}} = T_{\mathrm{el}}^{\mathrm{max}}$ (see Fig. 4.12b). Finally, the corresponding nonlinear order of the emission process N is obtained via

$$N = \frac{\mathrm{dlog}(Y_{\mathrm{therm}})}{\mathrm{dlog}(E_{\mathrm{abs}})}\,. \tag{4.8}$$

The resulting nonlinearities are shown as a function of E_{abs} in the inset of Fig. 4.12b. A nonlinearity between 7 and 9 corresponds to an absorbed energy density between 0.12 and 0.35 eVnm^{-3}. After thermalization the electron gas temperature does not remain

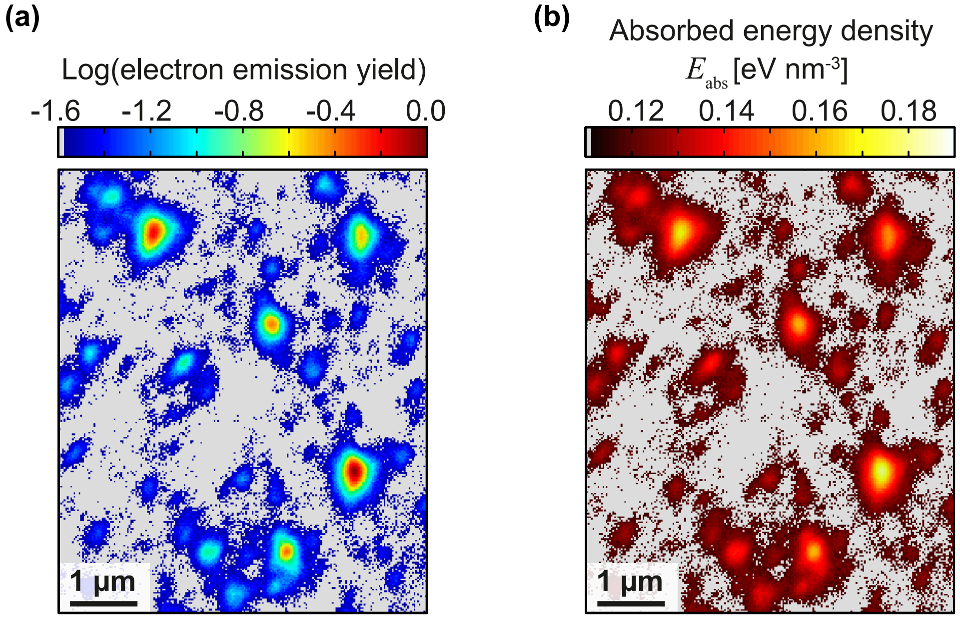

Figure 4.13: Local electron emission and energy absorption in the a-Si:H layer. (a) Spatial distribution of the electron emission normalized to the maximum electron yield and plotted on a logarithmic scale. The area is identical to that in Fig. 4.8. Pixels with an electron yield $< 2.5\%$ of the maximum are grayed out due to their negligible contribution to the absorption density. (b) Locally absorbed energy density based on the electron emission shown in (a). Figure taken from Ref. [2].

constant but decreases rapidly via the above-mentioned cooling mechanisms. At the same time the thermionic emission also vanishes rapidly because of its highly nonlinear dependency on the temperature. Therefore, the measured time-integrated electron yield is dominated by the thermionic emission occurring at $T_{\mathrm{el}}^{\mathrm{max}}$.

Based on the thermionic emission model the locally absorbed energy density in the a-Si:H layer of the exposed nanotextured sample is estimated from the spatial electron yield pattern which is illustrated in Fig. 4.13a. The PEEM image was recorded by excitation with the bandwidth-limited pulse and is identical to that of Fig. 4.8, but pixels with an electron yield $< 2.5\%$ of the maximum value are grayed out. Since the measured yield is only a relative value, it does not exactly represent the thermionic emission yield Y_{therm} [44]. However, the measured power-law dependence could be used to determine the relation between the experimental and the theoretical yield. For the strongest emission hot spots a nonlinear order of $N = 8$ was obtained which corresponds to an absorbed energy density of about 0.2 eVnm^{-3}. Thus, this E_{abs} value was assigned to the pixel with the maximum electron yield and the experimental values of all other pixels were rescaled accordingly. The spatial distribution of the locally absorbed energy density is shown in Fig. 4.13b. A lateral averaging over the complete map results in a mean value of $\overline{E}_{\mathrm{abs}} = 0.06$ eVnm^{-3}. By means of $\overline{E}_{\mathrm{abs}}$ and assuming a homogeneous excitation across the 100 nm thick absorber layer an average absorbed fluence per pulse of 0.1 mJ cm^{-2} is received. Dividing this value by the incident fluence of 0.13 mJ cm^{-2} leads to an absolute absorption of $\approx 75\%$ in the a-Si:H layer. This result differs from the absorption value of 40% which was obtained in the linear absorption spectrum of the exposed nanotextured sample (see Sect. 4.2). Nevertheless, considering the high uncertainties of the assumptions, this rough estimation reflects the enhanced absorption in the nanotextured absorber layer well. Thus, it is concluded that the measured electron yield is dominated by local thermionic electron emission which is caused by the enhanced light absorption within spatially confined photonic modes. Furthermore, the approximate lateral diameter of the localized modes can be obtained via the absorbed energy density pattern in Fig. 4.12b, as well. Since the color scale covers roughly a factor of two (0.11–0.2 eVnm^{-3}), it is possible to estimate the full width at half maximum (FWHM) of the absorption profile for the brightest emission spots. The estimated FWHM values imply mode diameters of roughly 1 μm.

After determining the nonlinear order of the electron yield and after clarifying the origin of the electron emission process, the experimental 2D nanospectra were fitted by means of a Lorentzian oscillator model. The model as well as the results of the fitting process are presented in the following section. Additional information and a more detailed discussion about the thermionic emission model can be found in Ref. [2].

4.4.2 Analysis of 2D Nanospectra with Lorentzian Oscillator Model

In this section, it is described how the experimental 2D nanospectra were analyzed quantitatively. Due to the observed high nonlinear orders of the emission process and the narrow spectral bandwidth of the excitation pulse, exact values for the resonance frequencies and coherence lifetimes of the photonic modes could not be obtained directly from the 2D spectra. Christian Strüber has shown previously by means of numerical simulations in the rotating frame of ω_0 that both the incident laser spectrum and the nonlinear order influence the peak properties in 2D nanospectra considerably [44]. A finite spectral bandwidth of the incident pulse leads to a shift of the resonance peaks in the spectra towards the center frequency of the laser spectrum ω_0. Additionally, a nonlinear order of $N > 2$ causes a broadening of the peak widths and may lead to increased asymmetric peak shapes. This is due to the fact that phase-cycling schemes can only extract signal contributions with a certain dependency on the relative phases between the sub pulses of the incident pulse sequence. For $N = 2$, the photon-echo signal contribution would arise from one interaction with one sub pulse each (see Sect. 2.4). By contrast, for $N > 2$, there are more interactions per sub pulse possible leading to the above-described effects. Since the nonlinear order of the emission process in the experiment is 8, contributions with much more interactions ($2N = 16$) but the same phase dependency are extracted via the applied (4×4)-step phase-cycling scheme. Thus, for a quantitative analysis of the nanospectra a fit model was necessary which took into account the emission process, its nonlinear order, and the spectrum of the incident laser pulse.

The fit procedure was performed by Christian Strüber and is only briefly summarized in the following. A more detailed description is given in Refs. [2, 44]. The fit model is based on the idea that each spatially confined photonic mode can be expressed via a single Lorentzian oscillator with a resonance frequency ω_R and a damping constant γ_R. The local thermionic emission $Y_{\text{therm}}(\mathbf{r})$ at the position of a photonic mode then depends on the two parameters of the respective Lorentzian oscillator. Since the spatial dependency of the thermionic emission is contained in ω_R and γ_R, the local position $\mathbf{r}$ is omitted for brevity in the following equations.

As described in the previous section, Y_{therm} is proportional to the Nth order of the locally absorbed energy density which in turn depends on the local field intensity. The local temporal field intensity is in turn proportional to the square of the local temporal electric field $E_{\text{loc}}(t', \tau, t, \varphi_\tau, \varphi_t, \omega_R, \gamma_R)$. Note that E_{loc} depends not only on the time variable t', but also on the parameters of the local Lorentzian oscillator ω_R and γ_R as well as on the parameters of the incident pulse sequence, i.e., τ, t, φ_τ, and φ_t. Assuming a linear response of the sample and using the convolution theorem [79], the real-valued local temporal electric field is obtained via

$$E_{\text{loc}}(t', \tau, t, \varphi_\tau, \varphi_t, \omega_R, \gamma_R) = 2\,\mathrm{Re}\Big\{\mathcal{F}^{-1}\big[E_{\text{in}}(\omega, \tau, t, \varphi_\tau, \varphi_t)\, A(\omega, \omega_R, \gamma_R)\big]\Big\}\,, \tag{4.9}$$

wherein “ Re” denotes the real part of the inverse Fourier transformation ($\mathcal{F}^{-1}$), and the incident electric field in the frequency domain and the local spectral response function are described by $E_{\text{in}}(\omega, \tau, t, \varphi_\tau, \varphi_t)$ and $A(\omega, \omega_R, \tau_R)$, respectively. For a collinear four-pulse sequence in the rotating frame of ω_0 with fixed population time $T = 0$ and relative phase $\varphi_T = 0$, the incident electric field can be expressed via [1]

$$E_{\text{in}}(\omega, \tau, t, \varphi_\tau, \varphi_t) = \frac{E_0(\omega)}{4}\Big\{\mathrm{e}^{\mathrm{i}[(\omega-\omega_0)\tau-\varphi_\tau]} + 2 + \mathrm{e}^{\mathrm{i}[(\omega-\omega_0)(-t)+\varphi_t]}\Big\} \tag{4.10}$$

with the electric field of the single bandwidth-limited pulse $E_0(\omega)$. The spectral response function $A(\omega, \omega_R, \gamma_R)$ is given by the Lorentzian function

$$A(\omega, \omega_R, \gamma_R) = \frac{1}{\omega_R^2 - \omega^2 + 2\mathrm{i}\gamma_R\omega}\,. \tag{4.11}$$

Using Eq. (4.9), the local electron yield is then related to the incident electric field and the local response function via

$$\begin{aligned} Y_{\text{therm}}(\tau, t, \varphi_\tau, \varphi_t, \omega_R, \gamma_R) &\propto \int_{-\infty}^{\infty} \big[E_{\text{loc}}(t', \tau, t, \varphi_\tau, \varphi_t, \omega_R, \gamma_R)\big]^{2N} \mathrm{d}t \\ &= \int_{-\infty}^{\infty} \Big(2\,\mathrm{Re}\Big\{\mathcal{F}^{-1}\big[E_{\text{in}}(\omega, \tau, t, \varphi_\tau, \varphi_t)\, A(\omega, \omega_R, \gamma_R)\big]\Big\}\Big)^{2N} \mathrm{d}t\,. \end{aligned} \tag{4.12}$$

Equation (4.12) already allows a direct fit of the experimental nanospectra with ω_R and γ_R as fit parameters. However, the number of the spectra was in the range of 10^6 and the fit of one spectrum was very time-consuming because the local electron yield had to be calculated for each combination of the time delays τ and t as well as the relative phases φ_τ and φ_t. Therefore, another fast and reliable fit routine was applied. First, a sufficient number of 2D spectra was simulated for varying parameters (ω_R, γ_R) using

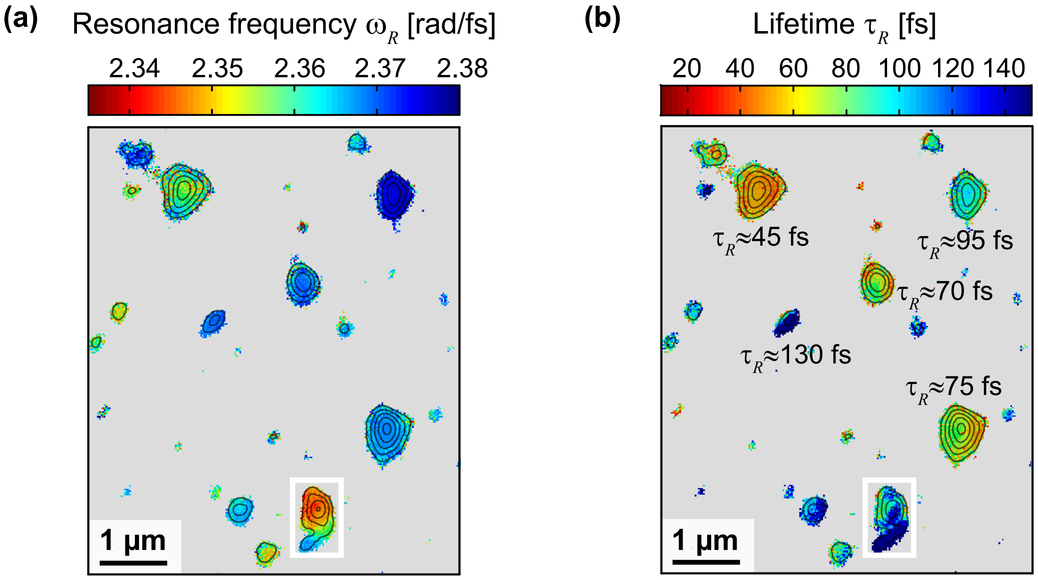

Figure 4.14: Local response parameters of the exposed nanotextured a-Si:H layer obtained by a line-shape analysis of the local 2D nanospectra. The analysis is based on a Lorentzian oscillator model yielding to a spatial distribution of (a) the local resonance frequency ω_R and (b) the local coherence lifetime $\tau_R = \gamma_R^{-1}$. Pixels with an electron yield below 5% of the maximum yield are grayed out. The contour lines indicate the logarithmized electron emission and are identical to those of Fig. 4.8. Figure adapted from Ref. [2].

Eq. (4.12). After that, the simulated spectra were fitted via the 2D Lorentzian line-shape function

$$L(\omega_\tau, \omega_t, \omega'_R, \gamma'_R) = \frac{a}{(\omega'^2_R - \omega^2_\tau - 2i\gamma'_R\omega_\tau)(\omega'^2_R - \omega^2_t - 2i\gamma'_R\omega_t)} \tag{4.13}$$

with the amplitude factor a and the phenomenological parameters ω'_R and γ'_R. Since an unambiguous relation between the parameters (ω'_R, γ'_R) and (ω_R, γ_R) was found, it was finally possible to fit the experimental spectra with the line-shape function and to convert the received phenomenological fit parameters into the corresponding resonance frequencies and damping constants.

The fits were done analogously to this procedure for all experimental nanospectra that had already been calculated for the single spatial pixels of the area shown in Fig. 4.8. Only for pixels with an electron emission $< 5\%$ of the maximum yield the fit procedure was not performed because their spectra were dominated by noise. The spatial distributions of the resulting resonance frequencies ω_R and coherence lifetimes $\tau_R = \gamma_R^{-1}$ are illustrated in Fig. 4.14a and Fig. 4.14b, respectively. It is striking that in both maps the variations of the response parameters within most of the hot spots are small, whereas the variations between different spots are partially very large. One exception to this is the hot spot marked by the white rectangles in Fig. 4.14. It apparently consists of two nearly homogeneous regions which differ significantly in the values for ω_R and τ_R. This is explained with the presence of two localized modes that are in close proximity. In general, when comparing both spatial distributions, no correlation between ω_R and

τ_R is found suggesting that both parameters are independent of each other. For the resonance frequencies (see Fig. 4.14a) only values between 2.32 rad/fs and 2.38 rad/fs were obtained because in this spectral region the intensity of the incident laser spectrum was high enough to drive the observed modes. This does not exclude the existence of additional modes with higher or lower resonance frequencies in the a-Si:H layer, but for the investigation of such modes a broader laser spectrum would be necessary. The values for the coherence lifetimes shown in Fig. 4.14b range mainly from 50 to 130 fs. This agrees very well with the averaged lifetime of 70 fs received from the measurements of the backscattered radiation in Sect. 4.3.

Altogether, the results from the 2D nanoscopy scan confirm the observations from the coherent backscattering experiments and, in addition, give a more detailed insight into the underlying light trapping mechanism. The electron emission of the exposed a-Si:H layer stems mainly from localized hot spots, which can be attributed to distinct spatially-confined resonances with specific lifetimes and resonance frequencies. With this, it is concluded that indeed localized photonic modes are responsible for the enhanced absorption. Hence, propagating modes do not contribute significantly to the total absorption (confer Fig. 4.3). By means of the experimental findings from the 2D nanoscopy measurements it is even possible to decide which type of localization in the absorber layer of the exposed nanotextured sample occurs. The determination of the localization mechanism is described in the following section.

4.5 Anderson Localization in Nanotextured a-Si:H Layers

In disordered media the scattering of waves can lead either to weak localization or to strong localization depending on the degree of disorder and thus on the mean free propagation path length of the waves. Both localization mechanisms are caused by the wave interference between multiple-scattering pathways. In the case of weak scattering, the waves can still propagate over larger distances within the media but pass through self-intersecting scattering paths along their way, leading to a weak localization [80, 81]. If the degree of disorder is so high that the mean free propagation path length is on the order of the wavelength or even shorter, the weak localization will be converted into a strong localization and the waves will be trapped in closed loops due to strong multiple scattering. This effect was first reported by P. W. Anderson in 1958 for electrons in a semiconductor [69], but, as a general wave phenomenon, it can be applied to the transport of electromagnetic waves as well [70, 82]. The strong localization is therefore also referred to as Anderson localization.

In order to classify the type of localization in the exposed nanotextured a-Si:H layer, the localization length ξ and the dimension of the investigated system have to be determined. Since the thickness of the layer (100 nm) matches the fundamental transverse mode for the wavelength of the radiation in the medium ($\lambda_{\text{a-Si:H}} = 800\ \text{nm}/n_{\text{a-Si:H}} \approx 200$ nm with $n_{\text{a-Si:H}} \approx 4$ [56]), the absorber can basically be interpreted as a disordered two-dimensional waveguide with respect to the lateral directions. The diameter of the localized modes was already estimated via the absorbed energy density pattern at about

1 μm (see Subsect. 4.4.1). It has to be mentioned that, in general, the value for ξ can be influenced by absorption. In a non-absorbing material closed loops that arise from strong multiple scattering are not restricted by an absorption length. As opposed to this, in an absorbing material loops with path lengths larger than the absorption length can not be formed because the light is absorbed before such loops are closed. As a result, ξ would become smaller due to absorption and additional propagating waves would appear. However, the spatial extent of the observed localized modes is about ten times smaller than the absorption length in a-Si:H (10 μm for 800 nm wavelength [56]). Furthermore, it was already shown in Subsect. 4.4.1 that the excitation of propagating modes does not contribute considerably to the total absorption. Additional finite-difference time-domain (FDTD) simulations which were performed by Matthias Hensen exhibited identical mode sizes in absorbing as well as in hypothetical non-absorbing nanotextured a-Si:H layers [2]. Hence, it is assumed that ξ is not particularly influenced by the absorption in the a-Si:H layer and that the experimentally determined mode diameter of 1 μm coincides with the localization length. According to scaling theory, ξ is related to the mean free path l^* in a 2D disordered system via [83]

$$\xi = l^* \mathrm{e}^{\frac{\pi k l^*}{2}} \tag{4.14}$$

with the wave vector in the medium k. By means of Equation (4.14), a mean free path of ≈ 60 nm is received, which is significantly smaller than $\lambda_{\text{a-Si:H}}$. This means that photons propagating in the a-Si:H layer with a reduced speed of light $c_{\text{a-Si:H}} = c/n_{\text{a-Si:H}}$ are scattered every $(l^*/c_{\text{a-Si:H}}) \approx 0.8$ fs. Considering the experimentally obtained lifetimes of the localized modes with values of about 100 fs (see Sects. 4.3 and 4.4) the photons undergo more than 100 scattering events. Thus, it is evident from the small localization length and the high number of scattering events within the localized modes that indeed Anderson localization occurs in the a-Si:H layer of the exposed nanotextured sample.

Since the 2D nanoscopy measurements could not be realized for the nanotextured sample with the two TCO layers, the determination of the localization mechanism via a quantitative measure of the locally absorbed energy density is not possible in this case. However, independently from the results of the 2D nanoscopy experiments, the coherent backscattered radiation can also be used to investigate the type of localization in the absorber layer because it contains information about possible localization effects inside the scattering medium. For this purpose, additional measurements were done by Dominik Differt to receive the dimensionless conductance g. This parameter was introduced within the scaling theory to quantitatively classify the localization [84]. If g is smaller than one, the localization in the scattering medium is strong. In the experiment the backscattered radiation was recorded at a large number of different positions on the nanotextured as well as on the exposed nanotextured sample using the setup shown in Fig. 4.6a. The value for g was then derived by analyzing the statistical correlations in the measured spectra. A detailed description of the analysis procedure and the determination of g is given in Ref. [2, 71]. For the nanotextured and the exposed nanotextured sample a dimensionless conductance of $g = (0.82 \pm 0.08)$ and $g = (0.76 \pm 0.07)$, respectively, was obtained. These results confirm that in the absorber layer of the nanotextured sample strong localization occurs.

4.6 Summary and Outlook

Light absorption in a-Si:H thin-film silicon solar cells is improved by using nanotextured absorber layers. In this chapter, solar cell devices with smooth and randomly nanotextured interfaces were investigated to clarify the reason for the absorption enhancement. In linear absorption spectra, it was shown that especially in the near-infrared regime the absorption was significantly higher for the nanotextured devices than for a device with smooth interfaces. Time-resolved experiments with femtosecond laser pulses were performed to determine the underlying enhancement mechanism in this wavelength region. The coherent backscattered radiation from each sample was analyzed via spectral interferometry for lateral scans of the sample position. The recorded spectra of the nanotextured devices revealed sharp resonance peaks which varied strongly with the sample position. A statistical peak analysis led to high average coherence lifetimes of 100 fs for the nanotextured and 70 fs for a modified nanotextured sample with an exposed absorber layer. The experimental findings indicated the presence of spatially-confined photonic modes in the nanotextured absorber layers.

In order to unambiguously identify the localized modes, the exposed nanotextured absorber layer of the modified device was investigated by means of coherent 2D nanoscopy, providing a high spatial resolution below 40 nm. The electron emission pattern from the surface of the absorber layer was dominated by localized hot spots, which showed distinct spectral properties in their local 2D nanospectra. This observation confirmed the assumption that localized photonic modes form in the absorber layer. The nanospectra were fitted with a damped Lorentzian oscillator model, yielding the quantitative information about the resonance frequencies and coherence lifetimes of the localized modes. The resulting lifetime values between 50 fs and 130 fs agreed very well with the 70 fs obtained from the statistical peak analysis of the backscattered spectra. The high nonlinear order of the electron emission process with values between 7 and 9 was attributed to local thermionic electron emission. Using a thermionic emisson model enabled the determination of the locally absorbed energy density and, with this, an estimation of the localization length of the photonic modes at about 1 μm. Moreover, the type of localization in the exposed nanotextured sample was classified as Anderson localization by means of the estimated localization length. Additional data evaluation of the backscattered spectra confirmed that Anderson localization occurs in the absorber layers of both nanotextured samples.

Combining all results, it was demonstrated that the absorption of near-infrared light in nanotextured thin-film silicon solar cells is enhanced due to the formation of strongly localized photonic modes in disordered absorber layers. Incident photons are trapped in such long-living modes and at some point absorbed by the material. The principle of this light trapping mechanism has great potential to significantly improve light absorption in solar cells. The localized modes can be understood as randomly distributed open resonators which are coupled to the incident light. If the losses within the resonators are equal to the losses due to the coupling to external fields, the critical coupling conditions are met and the absorption is strongly enhanced, even for materials which otherwise absorb only weakly. With these considerations in mind, the absorption enhancement via Anderson localization can have a major impact on future designs of absorber layers.

5 Cavity-Assisted Periodic Energy Transfer Between Widely Separated Nanoantennas

5.1 Introduction

Routing and manipulating optical signals enable information transport with superior operational bandwidth and higher operating speed compared to signal transfer in electronic devices [85, 86]. However, due to optical diffraction, the localization of electromagnetic waves in dielectric media is restricted to spatial dimensions in the range of half of their wavelength, that is, several hundred nanometers for light in the visible range. Thus, optical signal-processing devices and integrated circuits cannot be miniaturized down to the nanoscale like modern electronic equivalents [87]. In contrast to this, the wide field of plasmonics provides the opportunity to spatially confine light well below the optical diffraction limit. For instance, the interaction of light with subwavelength metallic nanostructures gives rise to the formation of localized plasmon polaritons (LSPs) with strong local field enhancements [88, 89]. Propagating surface plasmon polaritons (SPPs) enable guiding of electromagnetic waves at metal-dielectric interfaces within cross sections on the nanoscale [86, 87, 90, 91]. Compared to LSP modes, SPP modes do not couple directly to far-field radiation and exhibit only a small overlap with bulk electronic states [1], leading to reduced radiative and Ohmic losses. Furthermore, the propagation velocities of SPPs are maintained close to speed of light in free space [92, 93]. Hence, SPPs might be utilized as a building block for ultrafast on-chip routing of signals and energy [86, 94]. One-dimensional plasmonic waveguides, i.e., specially designed structures that guide SPP waves along one direction, can serve as transmission lines for all-optical nanocircuitry [85]. Moreover, two-wire transmission lines were used to coherently control the transport of SPPs from one input port to different output ports [95], and even the routing of single SPPs in a plasmonic circuit, i.e., the transmission of non-classical fields, was demonstrated [96]. For future applications in plasmonic nanocircuitry, it is of great interest to design devices that enable not only uni-directional but also multi-directional energy transfer between selectively addressable ports.

In this chapter, the investigation of a hybridized plasmonic device is shown that combines the strong local field enhancements of LSPs with the long-range transmission of SPPs. The device consists of two identical plasmonic nanoantennas located in the focal spots of a plasmonic elliptical cavity. The goal was to realize a long-range periodic energy transfer between the antennas on the basis of strong coupling between the spatially extended SPP mode of the cavity and the localized LSP modes of the antennas. The device was investigated in both theory and experiment. First, the single plasmonic components, i.e., the nanoantenna and the cavity, were adjusted separately via finite-difference time domain (FDTD) in order to meet the requirements for strong coupling between their modes. Then, the hybridized device with the adjusted components was explored by means of additional FDTD simulations. Based on the FDTD results, plasmonic cavities with embedded nanoantennas were fabricated and characterized for time-resolved experiments (Sect. 5.3). Two-pulse correlation measurements were performed on the fabricated devices using time-resolved photoemission electron microscopy (TR-PEEM) (Sects. 5.4 and 5.5).

The work that is described in this chapter resulted from a collaboration of our research group with the research groups of Walter Pfeiffer (Bielefeld), Martin Aeschlimann (Kaiserslautern), and Bert Hecht (Würzburg). A publication of this work was already submitted [5]. The FDTD simulations were done by Matthias Hensen. The samples were prepared in two major steps. In a first step, single-crystalline gold microplates with elliptical cavities were fabricated by Enno Krauss in Würzburg. After that, whispering gallery mode (WGM) nanoantennas were written into the cavities via focused-ion-beam milling (FIB) with the support of Thomas Löber in Kaiserslautern. The time-resolved measurement presented in Sect. 5.4 was performed by Benjamin Frisch, Matthias Hensen, Bernhard Huber, Martin Piecuch, Philip Thielen, and myself in Kaiserslautern. The measurement described in Sect. 5.5 was done by Benjamin Frisch. My contribution within this collaboration was the handling of the pulse shaper that was employed in the two-pulse experiment in Sect. 5.4, as well as the evaluation of the experimental data together with Matthias Hensen. The major part of this chapter is based on the above-mentioned publication [5] and on Matthias Hensen's PhD thesis [97].

5.2 Finite-Difference Time-Domain (FDTD) Simulations

For a periodic energy transfer between the two nanoantennas within the cavity, the antenna modes have to couple strongly to the cavity mode. In order to achieve a strong coupling, two basic requirements have to be met. Firstly, the antenna modes and the cavity mode have to spectrally overlap in the frequency domain. Secondly, a high spatial overlap of the cavity mode with each antenna mode is necessary. Hence, the single plasmonic components were adjusted separately in a first step to ensure high spectral overlap of their mode resonances. Then, in a second step, the spatial electric field distributions of the modes were investigated to find appropriate positions for the nanoantennas within the cavity. After that, the hybridized device with the adjusted components was explored in detail. Note that in both the presented FDTD simulations and the subsequent experiments, gold was used as substrate, since it is resistant to oxidation and corrosion. This guaranteed that the structure surface and quality were not affected by the environment on long time scales [97]. For the simulations, the optical parameters of gold were taken from the data of Johnson and Christy [98].

5.2.1 Adjustment of Single Plasmonic Components

The optical response of the single plasmonic components was simulated with FDTD using a pulsed electric dipole with a broad Gaussian spectrum (800 nm center wavelength, 218 nm FWHM, 4.3 fs pulse duration) as local excitation source. First, the response of the elliptical cavity was investigated for varying semi-major axes a and semi-minor axes b of the ellipse, respectively. The dipole was positioned 10 nm directly above the left focal spot of the ellipse and was oscillating perpendicular to the cavity floor. For $a = 1046$ nm and $b = 725$ nm, a cavity resonance at 2.356 rad/fs (800 nm vacuum wavelength) was received — the center frequency of the excitation pulses used in the time-resolved experiments. In Fig. 5.1a, the spatial field distribution of the corresponding mode pattern in the xy plane 10 nm above the cavity floor is shown. Since the mode pattern is dominated by the electric field component parallel to the z axis, i.e., the out-of-plane component, only the amplitude $|E_z|$ is depicted. Note that the values on the left side are higher than those on the right side due to the position of the excitation source above the left focal spot. The distribution of $|E_z|$ reveals a standing wave pattern with several nodes and anti-nodes, resulting from the reflection of the SPPs at the upright cavity walls. The height of the walls was set to 500 nm because this value corresponded roughly to the maximum wall height that could be realized in the fabrication process of the experimental devices. In general, the choice of the height is important, since it determines the reflectance of the walls. High reflectance is desired to prevent the escape of SPPs, i.e., to keep the energy within the cavity. However, for the chosen height, small energy losses at the cavity walls were obtained, since the calculated 1/e-decay of SPP intensity into the vacuum half-space for the permittivity of gold [98] and frequencies around $\omega = 2.356$ rad/fs (800 nm vacuum wavelength) is about 600 nm [97, 99]. Nevertheless, the standing-wave pattern within the cavity is well pronounced with intense anti-nodes. The anti-nodes with the highest values are located at the two focal spots and therefore represent well-suited positions for the nanoantennas.

As a next step the plasmonic nanoantenna was adjusted. For the hybridized device, so-called whispering gallery mode (WGM) resonators served as nanoantennas [100, 101]. In general, WGM resonators simply consist of annular grooves in a metallic substrate and represent circularly closed channel plasmon polariton (CPP) waveguides [91] (see inset in Fig. 5.1b). This kind of nanoantenna was chosen for two major reasons. Firstly, if WGM nanoantennas are located in the cavity floor, their LSPs share the same electrons like the SPPs of the cavity so that coupling between their modes might be facilitated. Secondly, it has been shown previously that the fundamental $m = 0$ (m_0) mode of a WGM nanoantenna is radially symmetric with respect to the surface normal of the substrate, and that its electric field distribution resembles a dipole which oscillates parallel to the surface normal [100, 101]. Hence, radiation into the far field is suppressed and most of the electromagnetic near-field energy of the mode is injected into propagating SPP modes [97]. This favors the interaction with the cavity mode. Further information about WGM resonators and their modes is given in Refs. [97, 100, 101]. For the investigation of the antenna response, the excitation dipole was located inside the antenna and was oscillating perpendicular to the substrate surface. The spectral position of the m_0 mode was tuned by varying the radius R of the antenna and the depth d of the antenna grooves.

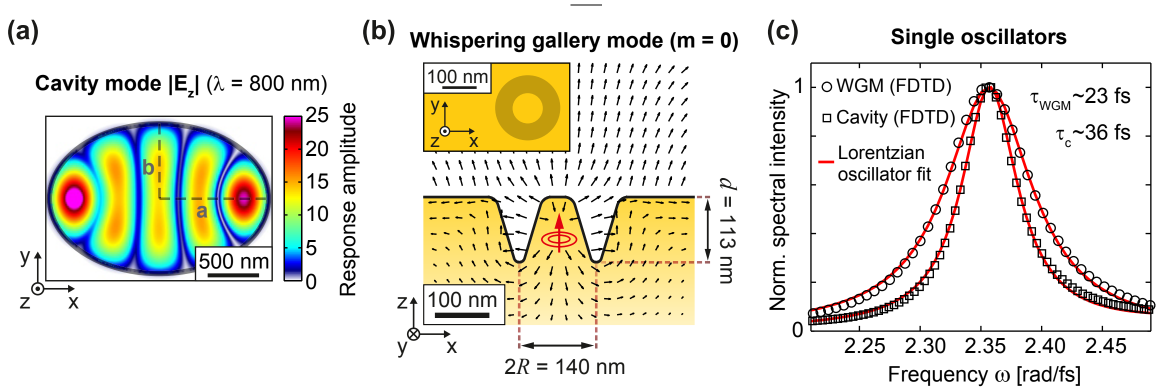

Figure 5.1: FDTD simulations with the single plasmonic components of the hybridized device. (a) Spatial distribution of $|E_z|$ 10 nm above the floor of a elliptical plasmonic cavity with semi-major axis a = 1046 nm and semi-minor axis b = 725 nm (gray dashed lines) at ω = 2.356 rad/fs. The cavity is incorporated in a gold substrate and its contour is indicated by the gray solid line. The excitation dipole was positioned within the xy plane directly above the left focal spot of the ellipse and was oscillating perpendicular to the cavity floor. (b) Cross section through a whispering gallery mode (WGM) nanoantenna with radius R = 70 nm and depth d = 113 nm and electric field distribution of the m_0 mode at ω = 2.356 rad/fs (black arrows with $\log_{10}$-scaled lengths). The excitation dipole (red arrow) was located inside the antenna. The inset shows the nanoantenna from above. (c) Normalized spectral response intensity of the cavity (black squares) and the WGM nanoantenna (black circles). The intensities were obtained via FDTD from $|E_z|^2$ 10 nm above the left focal spot of the cavity ellipse and 10 nm above the center of the WGM antenna, respectively. They were fitted separately with a Lorentzian oscillator function (red solid line), leading to a cavity lifetime of 36 fs and an antenna lifetime of 23 fs. Figure adapted from Ref. [5].

The cross section of the grooves was chosen to be V-shaped to mimic grooves which were written into a substrate via FIB milling. For $d = 113$ nm and $R = 70$ nm, the m_0 mode was resonant at 2.356 rad/fs. In Fig. 5.1b, the cross section through the corresponding WGM nanoantenna as well as the electric field distribution of the m_0 mode are shown. The field distribution reveals a dipole-like behavior as expected. The mode is radially symmetric and has a strong axial field along the symmetry axis of the structure [5]. Thus, the m_0 mode is well suited to couple to the cavity mode, if the nanoantenna is positioned in one of the anti-nodes of the cavity mode, e.g., in one of the focal spots.

Finally, the spectral line shapes of the cavity and the antenna mode were investigated. For this purpose, the spectral intensity of the cavity mode was recorded 10 nm above the left focal spot of the cavity (black squares in Fig. 5.1c). Analogously, the spectral intensity of the m_0 mode was recorded 10 nm above the center of the WGM nanoantenna (black circles in Fig. 5.1c). In both cases, the positions of the exciting dipole source were identical to those which generated the mode pattern in Figs. 5.1a and 5.1b, respectively. The intensities were obtained from the E_z component of the electric field, i.e., $|E_z|^2$, since the other components were negligible small at these positions. The corresponding curves resemble the spectral response of a Lorentzian oscillator with a resonance at 2.356 rad/fs, but different spectral line widths. Thus, both could be fitted separately with the Lorentzian function

$$A_j(\omega) = \frac{1}{\omega_j^2 - \omega^2 + 2\mathrm{i}\gamma_j\omega}\,, \tag{5.1}$$

wherein ω_j and γ_j are the resonance frequency and damping constant, respectively, of the cavity (j = ca) or the WGM nanoantenna (j = WGM). Note that γ_j determines the time $\tau_j = 1/\gamma_j$ in which the electric field amplitudes have decayed to 1/e. In the following, τ_j is called cavity and antenna lifetime, respectively. The results of the two fits (red lines in Fig. 5.2) are in good agreement with the data of the FDTD simulations and indicate a cavity lifetime of $\tau_{\mathrm{ca}} = 36$ fs ($\gamma_{\mathrm{ca}} = 0.028$ fs^{-1}) and an antenna lifetime of $\tau_{\mathrm{WGM}} = 23$ fs ($\gamma_{\mathrm{WGM}} = 0.043$ fs^{-1}).

5.2.2 Spectral Response of Hybridized Plasmonic Device

The hybridized plasmonic device was assembled from the adjusted components. Two identical nanoantennas were placed in the focal spots of the cavity to ensure high spatial overlap between the cavity and the antenna modes (see Fig. 5.2a). Thus, the centers of the antennas were widely separated by 1646 nm, i.e., more than twice the resonant wavelength $\lambda = 800$ nm of the plasmonic components. First, the spectral response at the positions of the two nanoantennas was investigated with FDTD using the same pulsed dipole source like in Subsect. 5.2.1. The dipole was positioned inside the left focal spot of the cavity, i.e., inside the left nanoantenna. Therefore, this antenna is labeled as "excited antenna", whereas the opposite one is labeled as "shaded antenna" in the following. The spectral electric field was recorded directly above the groove of each antenna, as indicated by the red and green crosses in Fig. 5.2a. The spectral intensity (circles) and phase (dashed lines) of the E_x component at the excited (red) and the shaded antenna (green) are shown in Fig. 5.2b. The contribution of the E_y and E_z component, respectively, was rather small at these positions so that these components were neglected here. In contrast to the Lorentzian-shaped response of the isolated nanoantenna with one peak at the resonance frequency, the spectral intensity of the excited antenna in the hybridized plasmonic device reveals three clearly separated peaks within an energy range of about 90 meV (≈ 0.14 rad/fs, 6% of the resonance frequency). This indicates the formation of new hybridized eigenmodes arising from an energy splitting of the modes of the single plasmonic components [97]. In addition, the spectral phase exhibits shifts arising from the resonances as well as small so-called Fano-dips between them [5]. It has been shown previously that Fano resonances occur if a Lorentzian oscillator with a very broad spectral response couples to a Lorentzian oscillator with a narrow spectral response [102]. In the resulting response of such a coupled system, the spectral phase then reveals a typical dip of π and the spectral intensity an asymmetric line shape at the Fano resonance. Since in the case of the hybridized plasmonic device the spectral responses of the isolated single plasmonic components have similar spectral bandwidths, the typical Fano-like line shapes are not observed, but the above-mentioned small dips in the phase. Due to the presence of the three peaks and the small Fano-dips, it was concluded that the modes of the single plasmonic components couple in the hybridized plasmonic device. The spectral intensity and phase of the shaded antenna

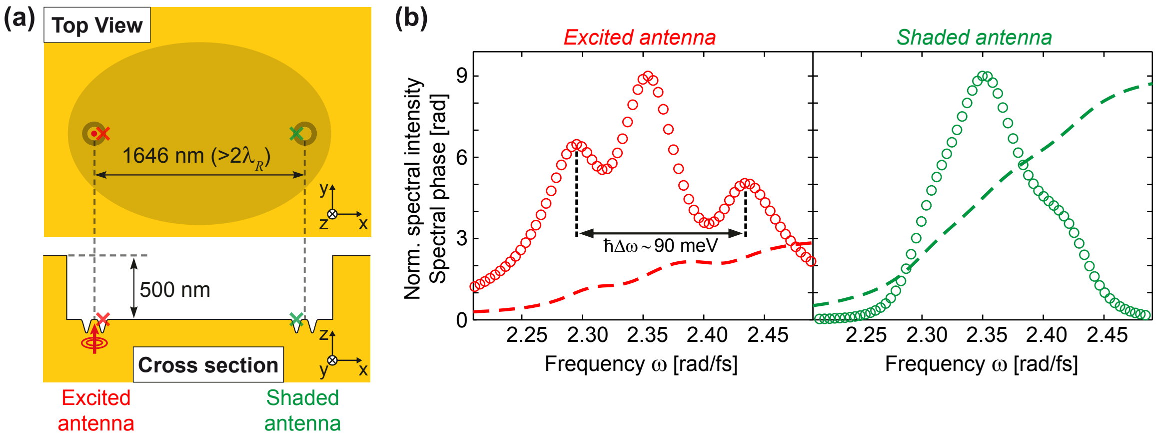

Figure 5.2: Spectral response of the hybridized plasmonic device at the two nanoantennas. (a) Top view of the investigated hybridized plasmonic device (top image) and cross section along the major axis of its elliptical cavity (bottom image). The centers of the WGM antennas are separated by 1646 nm. The exciting dipole source (red arrow and red point, respectively) was positioned inside the left nanoantenna labeled as "excited antenna". The right antenna is not directly excited and labeled as "shaded antenna". (b) Spectral intensities (circles) and phases (dashed lines) at the excited (red) and shaded (green) antenna obtained via FDTD. The data was received via the E_x component of the electric field at the positions marked by the red and green crosses in (a). (b) adapted from Ref. [5].

are modulated, as well. However, the modes spectrally overlap and therefore are not well separated like those of the excited antenna. Note that the spectral phase of the response at the shaded antenna is dominated by a linear term, since this antenna was excited a certain time after the excited antenna.

5.2.3 Coupled-Oscillator Model

For a quantitative analysis of the spectral response at both antennas, a coupled-oscillator model was utilized. It is based on the two-oscillator model of Zhang *et al.* and was extended here to three coupled Lorentzian oscillators, representing the two WGM nanoantennas and the cavity. In this model, the evolution of the temporal electric fields at the excited antenna $E_{\mathrm{ex}}(t)$, the shaded antenna $E_{\mathrm{sh}}(t)$, and the cavity $E_{\mathrm{cav}}(t)$ is described by the following system of differential equations:

$$\begin{aligned} \frac{\mathrm{d}^2}{\mathrm{d}t^2}E_{\mathrm{ex}}(t) + 2\gamma_{\mathrm{ex}}\frac{\mathrm{d}}{\mathrm{d}t}E_{\mathrm{ex}}(t) + \omega_{\mathrm{ex}}^2 E_{\mathrm{ex}}(t) + \kappa E_{\mathrm{ca}}(t) &= E_{\mathrm{in}}(t)\,, \\ \frac{\mathrm{d}^2}{\mathrm{d}t^2}E_{\mathrm{ca}}(t) + 2\gamma_{\mathrm{ca}}\frac{\mathrm{d}}{\mathrm{d}t}E_{\mathrm{ca}}(t) + \omega_{\mathrm{ca}}^2 E_{\mathrm{ca}}(t) + \kappa\big[E_{\mathrm{ex}}(t) + E_{\mathrm{sh}}(t)\big] &= 0, \\ \frac{\mathrm{d}^2}{\mathrm{d}t^2}E_{\mathrm{sh}}(t) + 2\gamma_{\mathrm{sh}}\frac{\mathrm{d}}{\mathrm{d}t}E_{\mathrm{sh}}(t) + \omega_{\mathrm{sh}}^2 E_{\mathrm{sh}}(t) + \kappa E_{\mathrm{ca}}(t) &= 0, \end{aligned} \tag{5.2}$$

wherein ω_{ex}, ω_{sh}, and ω_{ca} are the resonance frequencies of the single plasmonic components, and γ_{ex}, γ_{sh}, and γ_{ca} are the corresponding damping constants. The incident electric field is defined by $E_{\mathrm{in}}(t)$ and exclusively drives the electric field at the excited antenna to match the local excitation used in the FDTD simulation (confer Fig. 5.2). The coupling between the WGM nanoantennas and the cavity is described by the coupling constant κ. Note that there is no direct coupling between the excited and the shaded nanoantenna. Assuming a δ-pulse excitation, i.e., $E_{\mathrm{in}}(t) = \delta(t)$, and applying the Fourier transformation to Eq. (5.2) leads to

$$\begin{aligned} -\omega^2 A_{\mathrm{ex}}(\omega) + 2\mathrm{i}\gamma_{\mathrm{ex}}\omega A_{\mathrm{ex}}(\omega) + \omega_{\mathrm{ex}}^2 A_{\mathrm{ex}}(\omega) + \kappa A_{\mathrm{ca}}(\omega) &= 1, \\ -\omega^2 A_{\mathrm{ca}}(\omega) + 2\mathrm{i}\gamma_{\mathrm{ca}}\omega A_{\mathrm{ca}}(\omega) + \omega_{\mathrm{ca}}^2 A_{\mathrm{ca}}(\omega) + \kappa\left[A_{\mathrm{ex}}(\omega) + A_{\mathrm{sh}}(\omega)\right] &= 0, \\ -\omega^2 A_{\mathrm{sh}}(\omega) + 2\mathrm{i}\gamma_{\mathrm{sh}}\omega A_{\mathrm{sh}}(\omega) + \omega_{\mathrm{sh}}^2 A_{\mathrm{sh}}(\omega) + +\kappa A_{\mathrm{ca}}(\omega) &= 0, \end{aligned} \tag{5.3}$$

for a given frequency ω. Since the Fourier transformation of the incident δ-pulse $\mathcal{F}[\delta(t)] = 1$, the local electric fields in the frequency domain $E_{\mathrm{ex}}(\omega)$, $E_{\mathrm{ca}}(\omega)$, and $E_{\mathrm{sh}}(\omega)$ coincide with the local spectral response functions $A_{\mathrm{ex}}(\omega)$, $A_{\mathrm{ca}}(\omega)$, and $A_{\mathrm{sh}}(\omega)$. Equation (5.3) can then be rewritten as

$$\begin{pmatrix} \omega_{\mathrm{ex}}^2 - \omega^2 + 2\mathrm{i}\gamma_{\mathrm{ex}}\omega & \kappa & 0 \\ \kappa & \omega_{\mathrm{ca}}^2 - \omega^2 + 2\mathrm{i}\gamma_{\mathrm{ca}}\omega & \kappa \\ 0 & \kappa & \omega_{\mathrm{sh}}^2 - \omega^2 + 2\mathrm{i}\gamma_{\mathrm{sh}}\omega \end{pmatrix} \begin{pmatrix} A_{\mathrm{ex}}(\omega) \\ A_{\mathrm{ca}}(\omega) \\ A_{\mathrm{sh}}(\omega) \end{pmatrix} = \begin{pmatrix} 1 \\ 0 \\ 0 \end{pmatrix}, \tag{5.4}$$

and solving Eq. (5.4) for the local spectral response functions leads to

$$\begin{pmatrix} A_{\mathrm{ex}}(\omega) \\ A_{\mathrm{ca}}(\omega) \\ A_{\mathrm{sh}}(\omega) \end{pmatrix} = \begin{pmatrix} \omega_{\mathrm{ex}}^2 - \omega^2 + 2\mathrm{i}\gamma_{\mathrm{ex}}\omega & \kappa & 0 \\ \kappa & \omega_{\mathrm{ca}}^2 - \omega^2 + 2\mathrm{i}\gamma_{\mathrm{ca}}\omega & \kappa \\ 0 & \kappa & \omega_{\mathrm{sh}}^2 - \omega^2 + 2\mathrm{i}\gamma_{\mathrm{sh}}\omega \end{pmatrix}^{-1} \begin{pmatrix} 1 \\ 0 \\ 0 \end{pmatrix}. \tag{5.5}$$

The spectral response functions of the excited and the shaded nanoantenna $A_{\mathrm{ex}}(\omega)$ and $A_{\mathrm{sh}}(\omega)$, respectively, were calculated by means of Eq. (5.5) and compared to those from the FDTD simulations. The resonance frequencies and damping constants were set to the values obtained for the single plasmonic components from the fits with the Lorentzian function, i.e., $\omega_{\mathrm{ex}} = \omega_{\mathrm{sh}} = \omega_{\mathrm{ca}} = 2.356$ rad/fs, $\gamma_{\mathrm{ex}} = \gamma_{\mathrm{sh}} = 0.043\ \mathrm{fs}^{-1}$, and $\gamma_{\mathrm{ca}} = 0.028\ \mathrm{fs}^{-1}$. The coupling constant κ served as free parameter and was adjusted by hand to match the amount of mode splitting in the FDTD response [97]. For $\kappa = 0.22\ \mathrm{rad}^2/\mathrm{fs}^2$, a good agreement with the FDTD data was observed (see black lines in Fig. 5.3). The three clearly separated peaks in the spectral amplitude of the excited antenna, the reduced spectral modulation of the shaded antenna, and the Fano-dips in the spectral phases were well reproduced by means of the coupled-oscillator model. Note that, in this simple model, the spatial dependency of the electric field distribution is ignored. However, the intensities of the modes obtained from the FDTD simulations revealed spatial variations. In addition, the vector character of the electric fields was omitted. Nevertheless, the still excellent reproduction of the FDTD response at the positions of

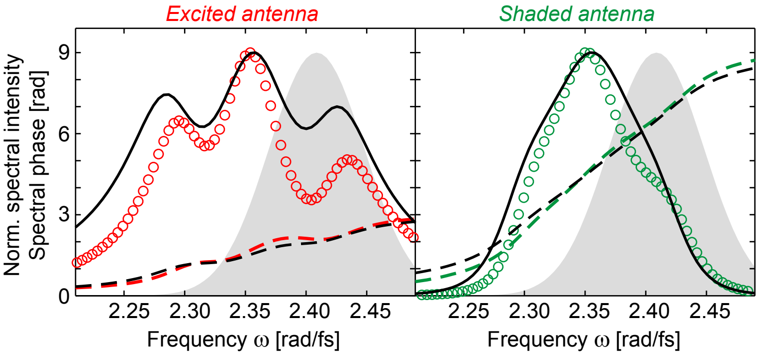

Figure 5.3: Comparison between the spectral response obtained via FDTD and the coupled-oscillator model. The black lines correspond to the spectral intensities (solid) and phases (dashed) calculated with the model. The colored circles and dashed lines are the spectral intensities and phases, respectively, at the excited (red) and shaded (green) antenna obtained via FDTD. They are identical to those of Fig. 5.2b. The gray-shaded area depicts the excitation spectrum of the laser pulse used in the FDTD simulation in Subsect. 5.2.4. Figure adapted from Ref. [5].

the nanoantennas demonstrates that the hybridized plasmonic device can be described via the coupled-oscillator model. Thus, this model represents a suitable tool for studying the coupling effects in the hybridized device.

5.2.4 Investigation of Energy Transfer between Nanoantennas

After retrieving the optical response of the hybridized device in the frequency domain, the device was investigated in the time domain. For this purpose, the spectral bandwidth, i.e., the pulse duration, and the center frequency of the exciting dipole source located inside the excited nanoantenna were varied, and the respective temporal electric field distribution was calculated via the FDTD response of the device. In Fig. 5.4a, the logarithmized temporal electric field envelope along the major axis of the ellipse, 10 nm below the cavity floor, is shown for a Gaussian dipole source with a pulse duration of 30 fs (FWHM of temporal intensity) and the center frequency $\omega_0 = 2.41$ rad/fs (782 nm). The corresponding excitation spectrum is depicted by the gray shaded area in Fig. 5.3. Due to the narrow bandwidth, it covers only partially the spectral response of the antennas and is located between the outer high-frequency and the middle resonance peak of the response functions. In addition to the temporal evolution of the field envelope in Fig. 5.4a, Fig. 5.4b illustrates the normalized temporal electric field at two positions within the grooves of the excited (red) and shaded (green) nanoanntena until 130 fs after excitation. The positions are marked by the red and green dashed lines in Fig. 5.4a. First, the electric field envelope, i.e., the square root of the field energy, at the excited antenna is increasing due to the excitation. After reaching a maximum value, it is decreasing, while a portion of the energy is transferred to the shaded antenna leading to a maximum at about 40 fs. Then, at the excited antenna, an energy minimum is observed after 50 fs, whereas some energy is still located near the shaded antenna. After that, the energy at the excited antenna is increasing again, while that at the shaded antenna

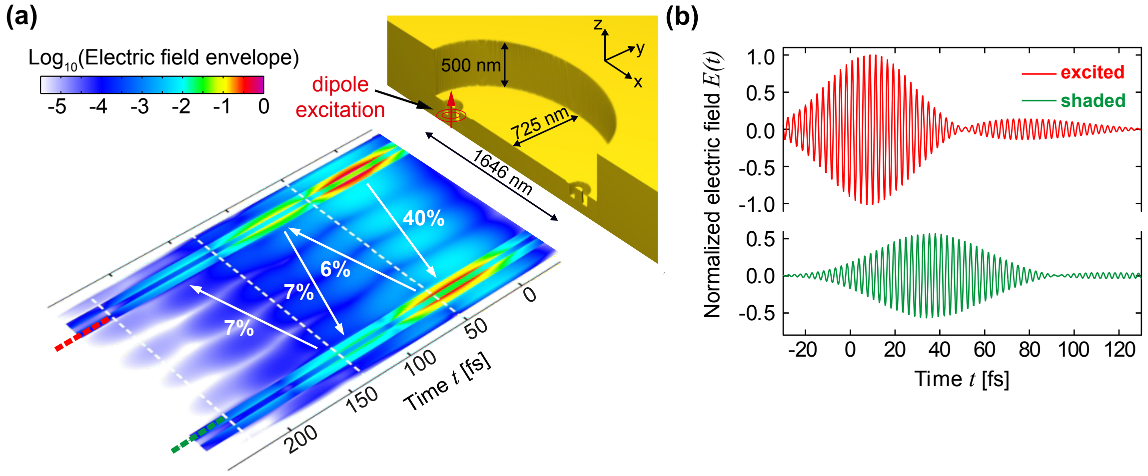

Figure 5.4: Coherent energy transfer within the hybridized plasmonic system. (a) Cross section of the hybridized plasmonic device and temporal evolution of the electric field envelope 10 nm below the cavity floor along the major axis of the ellipse. The envelope is plotted on a logarithmic scale and normalized to the maximum. The exciting dipole source (red arrow) was a Gaussian pulse (30 fs pulse duration, 2.41 rad/fs center frequency) located inside the left antenna (excited antenna). The excitation spectrum is depicted as gray shaded area in Fig. 5.3. (b) Normalized temporal electric field $E(t)$ at two positions within the grooves of the excited and shaded antenna, respectively. The positions are marked by the red (excited antenna) and green (shaded antenna) dashed lines. (a) and (b) adpated from Ref. [97] and Ref. [5], respectively.

is decreasing and so forth. This demonstrates that a periodic long-range energy transfer between both antennas within the hybridized plasmonic device is possible. Nearly 40% of the electromagnetic energy are transferred from the excited to the shaded antenna in the initial transfer process, and about 7% are transferred between both antennas in subsequent re-emission processes within periods of 86 fs [5, 97]. The energy transfer efficiency of the initial process is significantly higher, since the dipole source additionally excites the cavity mode directly.

Note that the behavior of the temporal field envelope in Fig. 5.4a is a consequence of the similar lifetimes (damping constants) of the single plasmonic components ($\tau_{\mathrm{ca}} = 36$ fs and $\tau_{\mathrm{WGM}} = 23$ fs). Additional FDTD simulations for devices with higher cavity walls and thus higher cavity lifetimes due to reduced cavity leakage lead to different temporal electric field dynamics without a periodic energy transfer [97]. This observation was confirmed via the coupled-oscillator model by calculating the temporal electric fields at the antennas for different damping constants of the cavity [5, 97]. Thus, it was concluded that only if the dissipation of the cavity and the antennas are roughly matched, an oscillatory energy exchange between both antennas can be achieved. This behavior is very similar to impedance matching, which is well-known from electrical engineering. Besides the dissipation of the single plasmonic components, the bandwidth and center frequency of the excitation spectrum can also influence the temporal field evolution within the device significantly. For instance, it was observed via FDTD that if the excitation spectrum overlaps with all three hybridized eigenmodes, the beating of the electric field at the antenna positions is only weak with small modulation depths and seems to appear synchronized in time [97]. A detailed discussion about the influence of the cavity and antenna damping as well as the excitation spectrum onto the electric field dynamics within the device can be found in Matthias Hensen's PhD thesis [97].

In order to show this energy transfer experimentally, samples with hybridized plasmonic devices were fabricated and investigated via time-resolved PEEM measurements. This is described in the following sections.

5.3 Sample Fabrication and Characterization

In this section, it is explained how the hybridized plasmonic devices were fabricated and characterized. Single-crystalline gold microplates [103] were used as material for the devices. In general, these micrometer sized single crystals are chemically grown and free from random crystal grains in contrast to vapor-deposited multi-crystalline gold layers [104]. This enabled the fabrication of smooth and well-defined nanostructures with improved plasmonic performance [105] because scattering and dephasing of surface plasmons were significantly reduced due to the absence of roughness and small grain boundaries [106]. Moreover, the atomically flat surface of the microplates (< 1 nm over an area of 1 μm^2) [105] is very well suited to serve as floors of the elliptical cavities. A synthesis procedure was applied that allowed the growth of the microplates directly on the substrate [104]. Hence, imperfections like gold particle contamination or plate aggregation were prevented and strain during the growth process was avoided [104].

For the fabrication of the hybridized plasmonic devices, two microplates were stacked on top of each other. The upper one was perforated with elliptical holes in order to provide the cavity walls, whereas the lower one served as floor for the cavities and as substrate for the WGM anntenas. The single steps of the fabrication process are shown in Fig. 5.5a. First, a single-crystalline gold microplate was grown on a glass substrate, covered with polymethyl methacrylate (PMMA), and transferred with the PMMA from the glass onto a hard silicon substrate with a silicon nitride (Si_3N_4) layer for focused-ion-beam (FIB) structuring. The transfer onto the Si_3N_4 layer was necessary to avoid a welding of the structures and the substrate during the FIB processing [107]. After removing the PMMA, elliptical holes were written into the microplate via FIB milling. The perforated microplate was then stacked by means of another PMMA-transfer onto a second microplate that was also grown on glass. In order to prevent charging effects during the time-resolved PEEM measurements, the stacked microplates were transferred onto a conductive indium tin oxide (ITO) substrate using PMMA again. Finally, two WGM antennas of identical size were written into each cavity floor, i.e., through the elliptical holes into the lower microplate.

In order to assure matched resonance frequencies of the WGM antennas and the elliptical cavity for at least one device, different devices with varying geometrical parameters of both the cavity and the WGM antennas were fabricated. For the variation of the cavity ellipse, the parameters of the theoretical device that was introduced in Sect. 5.2 served as reference, i.e., $a = 1046$ nm and $b = 725$ nm, since the resonance frequency of its cavity corresponds to the center frequency $\omega_0 = 2.356$ rad/fs of the laser pulses

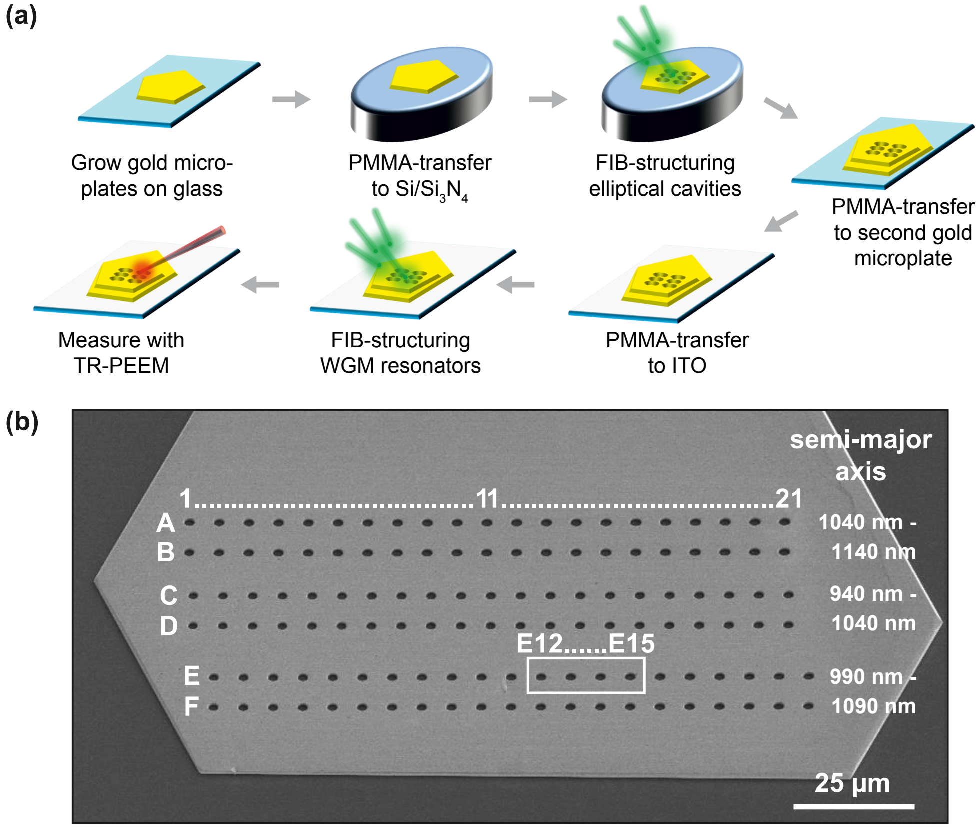

Figure 5.5: Sample preparation of hybridized plasmonic devices with single-crystalline gold microplates. (a) Single steps of the sample preparation. Two microplates were used for the fabrication of the devices. The first microplate was perforated with elliptical holes via focused-ion-beam (FIB) milling and put onto the second microplate that served as floor of the elliptical cavities. The height of the cavity walls were given by the thickness of the upper microplate. In the last fabrication step, two WGM antennas were written into the floor of each elliptical cavity via FIB milling. (b) SEM image of the upper microplate. An array of elliptical holes was written via FIB milling into the microplate with varying semi-major axes a and constant semi-minor axis $b = 725$ nm. In each row, a was increased from column 1 to column 21 in steps of 5 nm. The starting and end values of a are denoted on the right. Every second row is a copy of the previous one, i.e., rows A and B, rows C and D as well as rows E and F contain identical elliptical holes. (a) and (b) adapted from Ref. [5] and Ref. [97], respectively.

used in the time-resolved PEEM experiments. Furthermore, previous FDTD simulations done by Matthias Hensen were taken into account. In these simulations it was shown that a variation of the semi-major axis a of the ellipse leads to a factor of 3.5 stronger shift of the resonance frequency than a variation of the semi-minor axis b [97]. Hence, it was decided to vary only a, whereas b was kept constant at 725 nm. In Fig. 5.5b, a scanning electron microscope (SEM) image of a perforated upper microplate is depicted. It was recorded after the FIB structuring of the elliptical holes, i.e., after the third step in Fig. 5.5a. The thickness of the microplate was roughly 450 nm which is slightly lower than the cavity walls of the theoretical device. Six rows with 21 holes each were milled into the microplate. The rows are labeled by the capital letters A to F and the columns

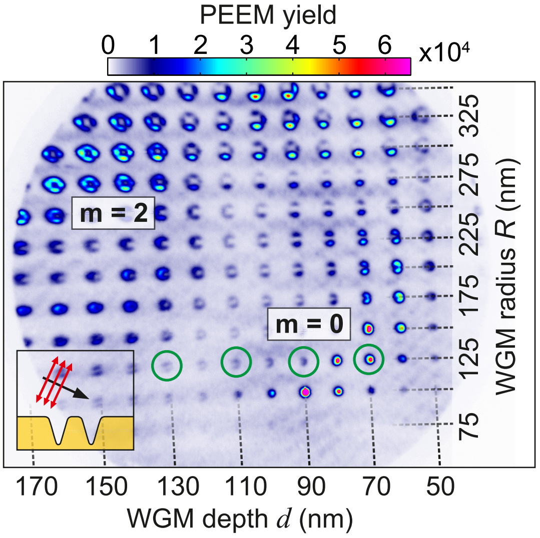

Figure 5.6: Spatial electron emission of an antenna array with varying groove depths d and radii R of the WGM nanoantennas. The antennas were written into a single gold microplate via FIB milling. The emission pattern was measured with the PEEM using the bandwidth-limited laser pulse. The pulse impinged on the sample under 65° to provide a high electric field component perpendicular to the substrate surface (see inset). Regions of resonant $m = 0$ and $m = 2$ excitation were observed. The four green circles indicate the antennas that were used for the fabrication of the hybridized devices. Figure adapted from Ref. [97].

are numbered consecutively from 1 to 21. In each row, a was increased in steps of 5 nm. In row A and B, it was varied from 1040 nm to 1140 nm, in row C and D from 940 nm to 1040 nm, and in row E and F from 990 nm to 1090 nm. Note that every second row is a copy of the previous one. According to the above-mentioned FDTD simulations, the chosen step size of 5 nm leads to a relatively small shift of the resonance frequency of about ±0.01 rad/fs between neighboring cavities [97].

After stacking the perforated microplate onto a second microplate, the suitable positions of the WGM antennas within the cavities, i.e., the positions of the outer anti-nodes of the cavity modes, were determined. For this purpose, the sample with the stacked microplates was transferred into the vacuum chamber of the PEEM and excited with the ultrashort laser pulse that was also used in the following time-resolved experiments (see experimental setup in Sect. 3.1). The resulting electron emission was then detected spatially resolved with the CCD camera of the PEEM. Unfortunately, due to the weak coupling of SPPs to incident far-field radiation, the electron yield from the cavity floors was very low. In some of the cavities, the electron emission seemed to reveal a standing wave pattern with nodes and anti-nodes (not shown here), similar to the spatial mode pattern obtained via FDTD. However, it could not be unambiguously clarified, whether four or five anti-nodes were present within these cavities. Thus, it was estimated that the outer anti-nodes within a cavity were located $\pm a \cdot (3/4.5)$ away from the center of the ellipse on the major axis [97]. The factor 4.5 was chosen due to the ambiguous number of anti-nodes.

Finally, the sample was removed from the PEEM and transferred into the FIB system in order to write the WGM antennas into the cavities. The geometrical parameters of the antennas, i.e., the groove depth and the antenna radius, were chosen on the basis of experimental results from a previous PEEM measurement performed on another single microplate. A detailed description about this measurement is given in Matthias Hensen's PhD thesis [97] and is only briefly outlined here: A large array of WGM antennas with increasing groove depths d along the columns and increasing radii R along the

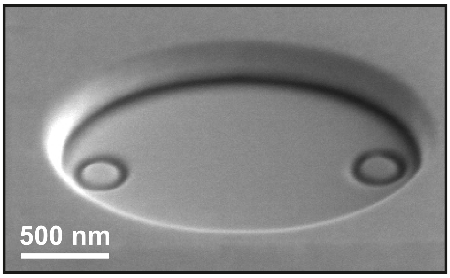

Figure 5.7: SEM image of an exemplary hybridized plasmonic device consisting of two WGM nanoantennas in an elliptical cavity. The fabricated device has a flat cavity floor and well-defined WGM nanoantennas. Figure adapted from Ref. [5].

rows was written into the single microplate via FIB milling. After that, the electron emission of this array was investigated with the PEEM, using the bandwidth-limited laser pulse (60 fs pulse duration, 800 nm center wavelength). The incidence angle of the pulse was 65° with respect to the surface normal of the sample because, for the excitation of the m_0 mode, the incident electric field has to contain a sufficiently high component perpendicular to the antenna surface (see inset of Fig. 5.6). The resulting electron emission is shown in Fig. 5.6. For WGM antennas with low groove depth and small antenna radius, e.g., for $R = 125$ nm and $d = 70$ nm, a resonant m_0 mode pattern, i.e., a circular electron emission along the groove edges of the antennas, was observed. In contrast to this, for antennas with larger radii and depths, e.g., for $R = 300$ nm and $d = 150$ nm, an antenna emission pattern with four lobes around the groove was visible, indicating a quadrupole resonance ($m = 2$).

According to the electron emission pattern of the antenna array and considering possible deviations of the FIB structuring from microplate to microplate, four different groove depths from 70 nm to 130 nm in steps of 20 nm and a constant diameter of $R = 125$ nm were selected for the fabrication of the hybridized devices. The corresponding antennas are marked by green circles in Fig. 5.6. The antennas were milled into the cavities in an alternating order. Two WGM antennas with the first groove depth $d = 70$ nm were written into cavity $A1$, two with $d = 90$ nm into $A2$, two with $d = 110$ nm into $B1$, and two with $d = 130$ nm into $B2$. This ordering of the antennas was repeated for the subsequent cavities in rows A and B. Analogously, the WGM antennas were milled into the cavities of rows C and D as well as E and F. In each cavity, the WGM antennas were centered at the estimated positions of the outer anti-nodes, i.e., $\pm a \cdot (3/4.5)$ away from the center of the ellipse along its major axis. Figure 5.7 shows a scanning electron microscope (SEM) image of an exemplary hybridized plasmonic device. It looks very smooth with a flat cavity floor and well-defined WGM nanoantennas. Furthermore, the cavity walls are perpendicular to the floor without a tilt. Due to the crescent-shaped shadow at the interface of the microplates, it appears that there is a gap between them. Since such a shadow was also observed in tilted-view SEM images of elliptical plasmonic arena cavities, each of which was built from a single crystal pellet of gold via FIB milling by Schoen *et al.* [108], it is assumed that the shadow is an artifact arising from the SEM geometry [97].

After fabrication, the sample with the hybridized plasmonic devices was transferred into the vacuum chamber of the PEEM for two-pulse correlation measurements. The experiments, their results and the corresponding data evaluation are described in the following sections.

5.4 Two-Pulse Experiment with the Pulse Shaper

The hybridized plasmonic devices were first investigated with respect to their temporal electric field dynamics via time-resolved measurements with the pulse shaper. The goal was to experimentally prove the coherent energy transfer between the two WGM nanoantennas within the elliptical cavity due to strong coupling. For this purpose, two-pulse correlation measurements were performed (Subsect. 5.4.1) and the experimental results were compared to the coupled-oscillator model (Subsect. 5.4.2).

5.4.1 Correlation Measurements with the Pulse Shaper

The experimental setup that was used for the measurements is explicitly described in Chapter 3 and identical to that used in Sect. 4.4. The excitation scheme is depicted in Fig. 5.8a. The hybridized plasmonic devices were excited by collinear double-pulse sequences consisting of two bandwidth-limited pulses (60 fs pulse duration, 800 nm center wavelength) with varying time delay T and relative phase φ_T. The resultant electron emission was detected spatially resolved with the CCD camera of the PEEM. The p-polarized pulse sequences impinged on the cavities at an incidence angle of 65°. Furthermore, the projection of their propagation direction onto the plane of the sample surface was parallel to the major axes of the cavities. In this excitation geometry, only one of the two WGM antennas in each cavity was directly excited by the pulses, while the second antenna was shielded by the cavity walls. Thus, the directly excited WGM antenna is called “excited”, and the opposite antenna is called “shaded” in the following (see Sect. 5.2). Moreover, as mentioned in Sect. 5.3, the tilted incidence angle and the orientation of the linear polarization ensured the excitation of the m_0 mode of the WGM antennas.

Before conducting the time-resolved experiments, the local electron yield of each hybridized plasmonic device was investigated upon excitation with a single bandwidth-limited pulse. The corresponding local electron emission of the ellipctial cavities from $E12$ to $E15$ is shown in Fig. 5.8b on a logarithmic scale. The semi-major axes of the cavities increase from 1045 nm ($E12$) to 1060 nm ($E15$) in steps of 5 nm. The WGM antennas of cavities $E12$ and $E14$ have identical geometrical parameters, i.e., groove depth $d = 70$ nm and radius $R = 125$ nm (denoted as A^{70}_{125}). The cavities $E13$ and $E15$ are equipped with WGM antennas of the same diameter but with groove depth $d = 90$ nm (denoted as A^{90}_{125}). Only the cavities $E12$ and $E14$ exhibit an enhanced emission at both antennas A^{70}_{125}, whereas in the other two cavities the yield at the excited antennas is low and vanishingly small at the shaded ones. Analogously to $E12$–$E15$, the local electron emission of all other devices on the sample was investigated (not shown here). In most cavities, the directly excited antenna showed a slightly increased electron emission, but no significant yield was observed at the shaded antenna. By contrast, the devices in row E, which contained the antennas A^{70}_{125} and were located in the vicinity of $E12$ and $E14$, also revealed an enhanced electron yield at both WGM antennas. Assuming that the electron emission is caused by a resonant response instead of an enhanced light intensity at sharp metallic edges, only for cavities with specific major axes and antennas A^{70}_{125} a resonant excitation of both antennas was observed. In these cavities,

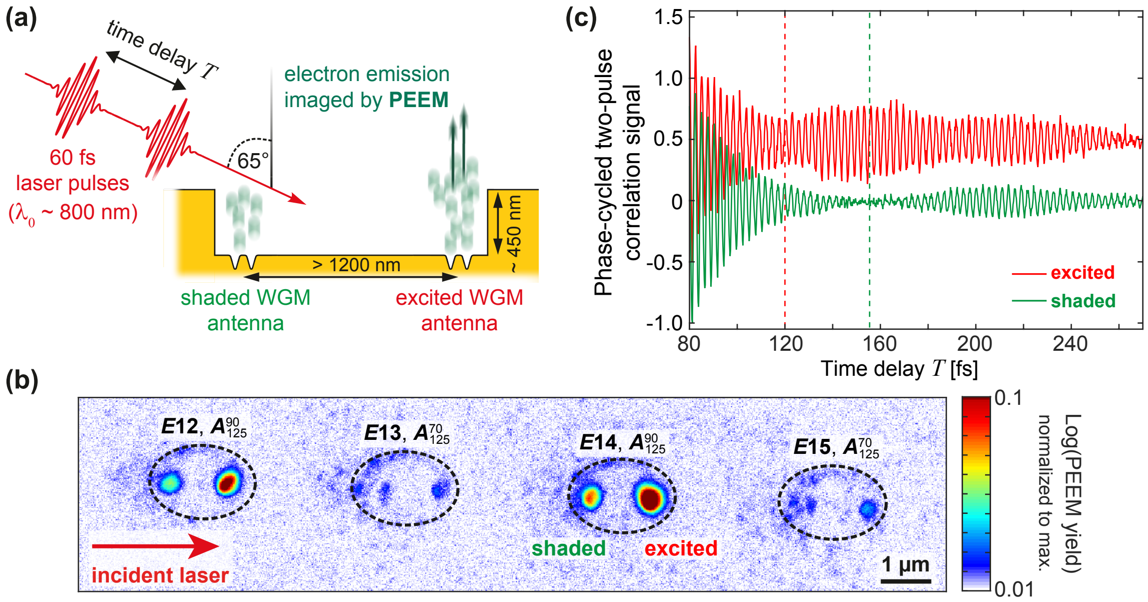

Figure 5.8: Two-pulse PEEM experiment with the pulse shaper on hybridized plasmonic devices. (a) Excitation scheme of the experiment. The double-pulse sequences with varying time delay T and relative phase φ_T were generated by the pulse shaper and impinged onto the sample at an incidence angle of 65° with respect to its surface normal. Each pulse of the sequence was bandwidth-limited (60 fs pulse duration, 800 nm center wavelength). Only the right WGM antenna is excited directly, while the left one is shielded by the cavity walls (height of the walls $\approx$ 450 nm). The emitted electrons (blurred green circles) were detected spatially-resolved with the PEEM. (b) Logarithmic local electron emission yield of the cavities $E12$–$E15$ (white rectangle in Fig. 5.5b) obtained for the excitation with the single bandwidth-limited pulse. $E12$ and $E14$ contain identical WGM antennas A_{125}^{90} (groove depth $d = 90$ nm, radius $R = 125$ nm). The antennas A_{125}^{70} in $E13$ and $E15$ are identical as well, but with $d = 70$ nm. Only in $E12$ and $E14$ both antennas revealed an enhanced electron yield. (c) Phase-cycled two-pulse correlation signals at the excited (red solid line) and the shaded (green solid line) antenna in $E12$ from $T = 80$ fs to $T = 270$ fs. A 2-step phase cycling was applied to extract the coherent signal contribution from the total yield. For both signals a distinct minimum of their envelopes is observed. The signal at the excited antenna exhibits the minimum at roughly $T = 120$ fs (red dashed line). The minimum of the shaded antenna is observed for a significantly higher delay $T \approx 156$ fs (green dashed line), where the envelope of the signal of the excited antenna has a maximum. (a) adapted from Ref. [97].

energy was apparently transferred from the excited to the shaded antenna. This already indicates that the resonance frequencies of the single plasmonic components were roughly matched, leading to an energy transfer between the antennas due to coupling [5].

As a next step two pulse correlation measurements were performed on the cavities in row E with an enhanced electron emission at both nanoantennas. The pulse shaper was used to generate double-pulse sequences with varying T and φ_T in the laboratory frame (see Appendix A.1), i.e., both the envelopes and the carrier oscillations of the pulses were synchronously shifted in the time domain. For the correlation measurement, T was scanned and the spatial distribution of the time-integrated local electron emission, i.e., a PEEM image, was recorded with the CCD camera at each scan step. Since the signal was dominated by the correlation signal of the incident double-pulse sequence for delays smaller than the temporal duration of the bandwidth-limited pulse, the scan was started at $T = 80$ fs, i.e., beyond the temporal overlap of the two pulses. The exposure time of the camera was then adjusted to 1100 ms such that for $T = 80$ fs the highest value of the electron yield within the corresponding PEEM image was slightly below the saturation value of the CCD pixels. This enabled a better resolution of the yield for larger delay times $T > 80$ fs where differences between the signals of the excited and the shaded nanoantenna became obvious. During the scan, T was increased in steps of 0.2 fs to 270 fs. In addition, a 2-step phase cycling (2pc) was applied to extract the coherent signal contribution, i.e., the signal that arises from interactions with both pulses and thus depends on T and, in particular, on φ_T, from the total PEEM signal. For this purpose, one PEEM image was acquired per time step for $\varphi_T = 0$ and $\varphi_T = \pi$, respectively. In order to correct thermal drifts that can occur between the CCD camera and the sample holder during the measurement, an additional reference PEEM image was recorded at each time step using the double-pulse sequence with $T = 80$ fs and $\varphi_T = 0$ (confer PEEM measurement in Sect. 4.4). After data acquisition and drift correction, the local phase-cycled correlation signal was obtained from the drift-corrected data via

$$\widetilde{Y}_{2\mathrm{pc}}(\mathbf{r}, T) = Y(\mathbf{r}, T, \varphi_T = 0) - Y(\mathbf{r}, T, \varphi_T = \pi)\,. \tag{5.6}$$

In Fig. 5.8c, the phase-cycled two-pulse correlation signals of the excited (red) and the shaded antenna (green) of cavity $E12$ are shown. For this measurement, the field of view (FoV) was set to ≈ 10 μm, leading to a spatial resolution below 40 nm. The correlation signals were obtained via the spatial integration over the areas of the respective antennas and were normalized to their corresponding maximum values. Furthermore, the signal of the excited antenna is shifted vertically by 0.5 to improve visibility. Due to phase cycling, the signals oscillate symmetrically between values of -1 and $+1$ as well as -0.5 and $+1.5$ in the case of the shifted curve. For $T < 160$ fs, both correlation signals reveal a dip in their envelopes instead of a continuous decay, i.e., the amplitudes of their oscillations decrease until a minimum is reached and come up again with increasing time delay. However, the positions of the minima differ significantly in the signals. For the excited antenna, the minimum is observed at 120 fs, while the minimum at the shaded antenna is reached at 156 fs. At this time delay, the envelope of the signal at the excited antenna has increased again. Between the shifted minima, the correlation signals oscillate with a delay-dependent phase shift to each other. For $T > 160$ fs, the envelope of the signal at the excited antenna exhibits another slight dip at about 180 fs. After this time delay, both correlation signals oscillate in phase again. Similar results, i.e., shifted minima of the excited and shaded antenna at small time delays and synchronous oscillations at large time delays, were observed for those neighboring devices in row E which were equipped with antennas A_{250}^{70}.

In addition to the time-resolved measurements, the local nonlinear order of the electron emission at the positions of the nanoantennas was determined via a power-law measurement in order to investigate the underlying emission process. For this purpose, a neutral density wheel was positioned in front of the vacuum chamber of the PEEM and the local electron yield was recorded with the single bandwidth-limited pulse as a function of the laser power. Using the power-law function defined in Eq. (4.5), local nonlinear orders of about 4 were obtained. Assuming a photon energy of 1.55 eV ($\lambda = 800$ nm) and a work function of gold between 4.8 and 5.4 eV, this value agrees well with the number of photons that are theoretically necessary for a multiphoton photoemission process in gold. This means that the measured electron yield is driven by the local field intensity. Thus, the minima in the correlation signals indicate that the field intensities, i.e., the electromagnetic energy, at the respective antennas first decreased and then increased again with increasing T. However, a more detailed investigation of the signals with respect to a possible energy transfer between the antennas was difficult: The local field intensities depended on the complex electric-field distributions that arose from the excitation with both pulses of the double-pulse sequence [97]. Therefore, the correlation signals could not be directly compared to the temporal electric-field distribution that was obtained for the single-pulse excitation in the FDTD simulation (see Fig. 5.4 in Sect. 5.2). Hence, for a further interpretation of the experimental results, the coupled-oscillator model presented in Sect. 5.2 was used to calculate two-pulse correlation signals at the nanoantennas and to compare them to the experimental data.

5.4.2 Analysis of Experimental Data with Coupled-oscillator Model

In order to simulate two-pulse correlation signals, the coupled-oscillator model was combined with a model for plasmon-assisted multiphoton photoemission that was introduced by Merschdorf *et al.* [109]. According to the latter model, the local time-integrated photoelectron yield is connected to the local temporal electric field $E_{\mathrm{loc}}(\mathbf{r}, t)$ via

$$Y(\mathbf{r}) \propto \int_{-\infty}^{\infty} \left[E_{\mathrm{loc}}(\mathbf{r}, t)\right]^{2N} \mathrm{d}t \tag{5.7}$$

with the nonlinear order N of the photoemission process. Assuming a linear response and using the convolution theorem [79], the real-valued local electric field in the time domain is given by

$$E_{\mathrm{loc}}(\mathbf{r}, t) = 2\,\mathrm{Re}\Big\{\mathcal{F}^{-1}\left[A(\mathbf{r}, \omega)\, E_{\mathrm{in}}(\omega)\right]\Big\}, \tag{5.8}$$

wherein $A(\mathbf{r}, \omega)$ and $E_{\mathrm{in}}(\omega)$ are the spectral response function and the incident electric field in the frequency domain, respectively. In the coupled-oscillator model, the response functions at the nanoantennas, $A_{\mathrm{ex}}(\omega)$ and $A_{\mathrm{sh}}(\omega)$, are defined via Eq. (5.5). Note that the spatial dependency of these response functions is indicated by the indices "ex" and "sh" and therefore the local position $\mathbf{r}$ is omitted in the following. Both response functions depend on the parameters of the single plasmonic components, i.e., ω_j and γ_j with $j = \{\mathrm{ex}, \mathrm{sh}, \mathrm{cav}\}$, as well as on the coupling constant κ. In the frequency domain, the incident electric field of a collinear double-pulse sequence can be expressed via [1, 45]

$$E_{\mathrm{in}}(\omega, T, \varphi_T) = \frac{E_0(\omega)}{2}\left(1 + \mathrm{e}^{\mathrm{i}\omega T - \mathrm{i}\varphi_T}\right) \tag{5.9}$$

with the electric field of the single bandwidth-limited pulse $E_0(\omega)$. Note that the double-pulse sequence is defined in the laboratory frame here. Combining the equations of both models, the phase-cycled two-pulse correlation signals of the excited and the shaded antenna can be calculated via

$$\begin{aligned}\widetilde{Y}_{k,2\mathrm{pc}}(T) &= Y_k(T,\varphi_T=0) - Y_k(T,\varphi_T=\pi)\\ &\propto \int\limits_{-\infty}^{\infty}\left(2\,\mathrm{Re}\Big\{\mathcal{F}^{-1}\big[A_k(\omega)\,E_{\mathrm{in}}(\omega,T,\varphi_T=0)\big]\Big\}\right)^{2N}\mathrm{d}t\\ &\quad-\int\limits_{-\infty}^{\infty}\left(2\,\mathrm{Re}\Big\{\mathcal{F}^{-1}\big[A_k(\omega)\,E_{\mathrm{in}}(\omega,T,\varphi_T=\pi)\big]\Big\}\right)^{2N}\mathrm{d}t \qquad (5.10)\end{aligned}$$

with $k = \{\mathrm{ex}, \mathrm{sh}\}$. However, a fit of the experimental data using Eq. (5.10) with the coupling constant, the resonance frequencies, and the damping constants as fit parameters was not successful with respect to convergence. Nevertheless, a qualitative comparison between simulated and measured correlation signals was possible. For this purpose, the correlation signals were first calculated for the spectral response functions that were already used to mimic the FDTD response in Sect. 5.2, i.e., for the parameters $\omega_{\mathrm{ex}} = \omega_{\mathrm{sh}} = \omega_{\mathrm{ca}} = 2.356$ rad/fs, $\gamma_{\mathrm{ex}} = \gamma_{\mathrm{sh}} = 0.043\ \mathrm{fs}^{-1}$, $\gamma_{\mathrm{ca}} = 0.028\ \mathrm{fs}^{-1}$, and $\kappa = 0.22\ \mathrm{rad}^2/\mathrm{fs}^2$. In this case, the resonance frequencies of the single plasmonic components are equal to ω_0, i.e., the center frequency of the excitation spectrum. The spectral intensity (solid lines) and phase (dashed lines) of the response functions at the excited (top graph, dark-red) and the shaded nanoantenna (bottom graph, dark-green) are illustrated in Fig. 5.9a. They are denoted as intensity and phase of “COM I” (coupled-oscillator model I) and are identical to the intensity and phase of the response functions in Fig. 5.2d. In addition, the excitation spectrum that was measured with a spectrometer and corresponds to $|E_0(\omega)|^2$, i.e., the squared absolute value of the electric field of the single bandwidth-limited laser pulse, is depicted as gray-shaded area. The resulting phase-cycled two-pulse correlation signals are shown in Fig. 5.9b. Additionally, the time delays at which the minima occurred in the experimental signals are marked by the vertical red (excited antenna) and green (shaded antenna) dashed lines for comparison. Each curve is normalized to its maximum value and the signal of the excited antenna is vertically shifted by 0.5 to improve visibility. Both calculated signals look very similar and reveal an almost continuous decay of their envelopes with only a slight beating behavior in their envelope. This is explained by the excitation spectrum and its spectral position with respect to the response functions. Due to the narrow spectral bandwidth, the excitation spectrum only covers a small part of the broad response functions. Furthermore, since ω_0 is identical to the resonance frequencies of the single plasmonic systems, the maximum of the excitation spectrum coincides with the maximum of the intensity peak in the middle of the response functions. Hence, the complex spectral properties of the response functions are not probed and the resultant local electric field is similar to that of a single Lorentzian oscillator. Considering the FDTD simulations in Sect. 5.2, the coherent energy transfer between both antennas was clearly visible in the local temporal electric field for the excitation with a Gaussian pulse whose center frequency was blue-shifted with respect to the resonance frequencies of the plasmonic components (see

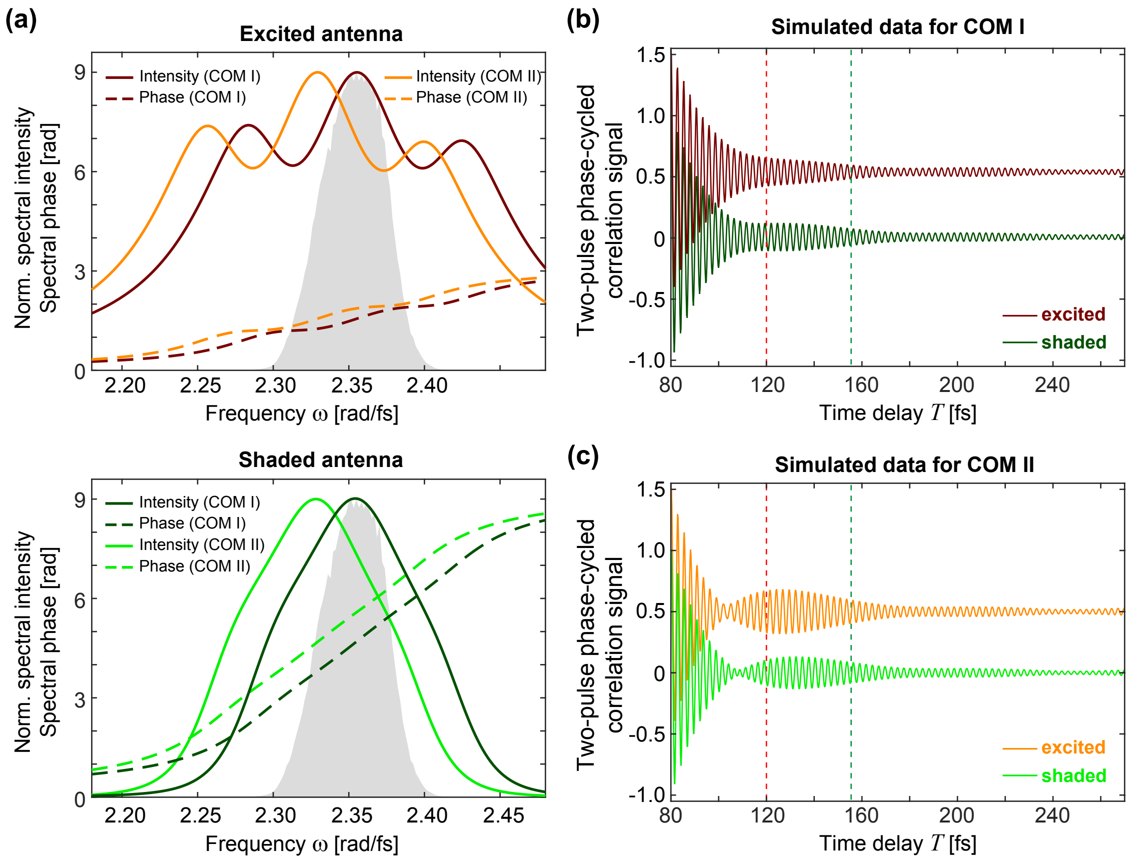

Figure 5.9: Simulation of phase-cycled two-pulse correlation signals via the coupled-oscillator model introduced in Sect. 5.2. (a) Spectral intensities (solid lines) and phases (dashed lines) of the response functions of the excited (top graph) and shaded (bottom graph) antenna for coupled oscillators (COM I) with resonance frequencies $\omega_{\mathrm{cav,ex,sh}} = 2.356$ rad/fs (dark red and dark green, respectively) and for coupled oscillators (COM II) with $\omega_{\mathrm{cav,ex,sh}} = 2.33$ rad/fs (orange and bright green, respectively). The remaining parameters of COM I and COM II were identical with $\gamma_{\mathrm{ex,sh}} = 0.043\ \mathrm{fs}^{-1}$, $\gamma_{\mathrm{ca}} = 0.028\ \mathrm{fs}^{-1}$ and $\kappa = 0.22\ \mathrm{rad}^2/\mathrm{fs}^2$. (b) Two-pulse phase-cycled correlation signals of the excited (dark red) and shaded (dark green) antenna for COM I. (c) Two-pulse phase-cycled correlation signals of the excited (orange) and shaded (bright green) antenna for COM II. The vertical dashed lines in (b) and (c) indicate the time delays at which the minima in the experimental correlation signals of the excited (red) and shaded (green) occurred (confer Fig. 5.8c).

Fig. 5.3). Therefore, the calculations were repeated for a coupled-oscillator system with resonance frequencies that were red-shifted with respect to ω_0. In Fig. 5.9a, the response functions of the excited (top graph, orange) and shaded (bottom graph, bright-green) are shown for $\omega_{\mathrm{ex}} = \omega_{\mathrm{sh}} = \omega_{\mathrm{ca}} = 2.33$ rad/fs and denoted as “COM II” (coupled-oscillator model II). The remaining parameters, i.e., the damping constants as well as the coupling constant, are identical to those of COM I. Due to the red-shifted resonance frequencies, the excitation spectrum is now between the outer high-frequency and the middle resonance peak of the response functions. The corresponding correlation signals are illustrated in Fig. 5.9c. Analogously to the experimental data, each calculated signal exhibits a beating behavior of its envelope with a distinct minimum at small time delays. The positions of the two minima are shifted with respect to each other as well. The minimum at the excited antenna is at $T \approx 100$ fs, whereas the minimum at the shaded antenna is at $T \approx 110$ fs. Between these two minima, the signal amplitudes oscillate with a delay-dependent phase shift to each other. However, compared to the minima in the experimental data (confer vertical dashed lines), those of the calculated signals occur at earlier time delays and are much closer to each other. Furthermore, for $T > 160$ fs, both correlation signals oscillate in phase again, but their envelopes reveal tiny dips. This slight beating of the envelopes at large time delays is also observed in the signals of COM I and arises from the shape of the excitation spectrum that is distorted by small wiggles and not symmetrically distributed with respect to ω_0. Using a smooth Gaussian excitation spectrum with a center frequency and spectral bandwidth similar to those of the measured excitation spectrum, the small dips at large time delays completely disappears (COM I) or becomes negligibly small (COM II), while the features at small time delays, i.e., the minima in the signals of COM I and the continuous decrease of the signals of COM II, are still present (not shown here). Hence, it was concluded that the behavior of the experimentally measured correlation signals for delay times $T > 160$ fs might also result from the spectral shape of the excitation spectrum rather than the spectral response of the investigated device.

Altogether, the important features of the experimental two-pulse correlation signals at small time delays could be qualitatively reproduced by means of the coupled-oscillator model. However, due to the narrow excitation spectrum, only a small spectral region of the expected broad response at the antenna positions was probed. This made a comparison of the experimental data with the calculated data difficult, since the calculated correlation signals strongly depended on the position of the excitation spectrum with respect to the spectral response. Therefore, the two-pulse correlation measurements were repeated with a spectrally broader excitation spectrum. However, the usable spectral range of the pulse shaper was limited by the geometry of its $4f$ setup. Hence, the phase-stabilized Mach-Zehnder interferometer shown in Sect. 3.2 was employed instead of the pulse shaper. The corresponding experiment and its results are described in the following section.

5.5 Two-pulse Experiment with the Mach-Zehnder Interferometer

For the measurements with the phase-stabilized Mach-Zehnder interferometer, the experimental setup used in Sect. 5.4 was modified. The beam was not coupled into the pulse shaper any more but redirected into the interferometer. In addition, the Ti:sapphire oscillator was adjusted so that its output provided spectrally broader pulses with a bandwidth-limited pulse duration of 23 fs and a center wavelength of 800 nm. A detailed description of the setup is given in Sect. 3.2. The two-pulse correlation measurements are described in Subsect. 5.5.1 and a discussion of the experimental results by means of the coupled-oscillator model is presented in Subsect. 5.5.2.

5.5.1 Correlation Measurements with the Mach-Zehnder Interferometer

Before conducting time-resolved measurements with the interferometer, the work function of the sample was further reduced by vapor deposition of caesium to increase the photoemission yield [110]. After vapor deposition, the local nonlinear order N of the photoemission at the antennas in the cavities $E12$ and $E14$ was determined via a power-law measurement. Fitting the measured data with a power-law function according to Eq. (4.5) resulted in nonlinear orders of about 2. The two-pulse correlation measurements were then performed on $E12$ and $E14$ simultaneously. For this purpose, the FoV was set to $\approx 30\ \mu$m so that the local photoemission at the antennas was well separated in the recorded PEEM images. During the measurement, the time delay T was scanned from 22 fs to 270 fs in steps of 0.1 fs and the time-integrated local photoelectron yield was measured with the CCD camera (1100 ms exposure time). Analogously to the measurement with the pulse shaper, the starting value of the time delay was set beyond the temporal overlap of the pulses. Since the double-pulse sequences were generated by a Mach-Zehnder interferometer, a variation of the relative phase between the pulses was not possible and therefore phase cycling could not be applied. Thus, in contrast to the two-pulse measurements with the pulse shaper, only two PEEM images were recorded with the camera at each time delay. The first image served as correlation signal, whereas the second one served as reference image for the drift correction and was recorded for the double-pulse sequence with $T = 22$ fs.

In Fig. 5.10a, the two-pulse correlation signals of the excited (red solid line) and shaded (green solid line) antenna of cavity $E14$ are illustrated. Each signal was obtained via the spatial integration of the local photoelectron yield over the complete area of the respective antenna. Since phase cycling was not applied, the decay of the signals with increasing T is determined by the nonlinear order of the photoemission process and thus is more strongly than the decay of the phase-cycled correlation signals obtained with the pulse shaper (confer Fig. 5.8c). Furthermore, the signals converge to a non-zero baseline for large delay times. This baseline resulted from delay-independent contributions to the photoemission, i.e., contributions that arose from the interactions with only one of the two pulses. At small delay times, the two correlation signals differ significantly. The signal at the excited antenna reveals a distinct dip of its envelope at 40 fs, i.e., the envelope of the oscillations decreases first and then comes up again. After reaching a maximum at 50 fs, the signal decays to the baseline. In contrast to this, the correlation signal at the shaded antenna does not exhibit such a distinct dip but decreases continuously to the baseline. In the correlation signals of $E12$, a similar behavior was observed, i.e., a dip in the signal at the excited antenna and a continuous decay of the signal at the shaded antenna (not shown here). Compared to the measurement with the pulse shaper, a broader part of the spectral response functions was probed due to the broader spectral bandwidth of the excitation spectrum. The correlation signals could therefore not be directly compared to the phase-cycled correlation signals shown in Fig. 5.8c of the previous section. Nevertheless, a further interpretation of the experimental data was possible via the coupled-oscillator model.

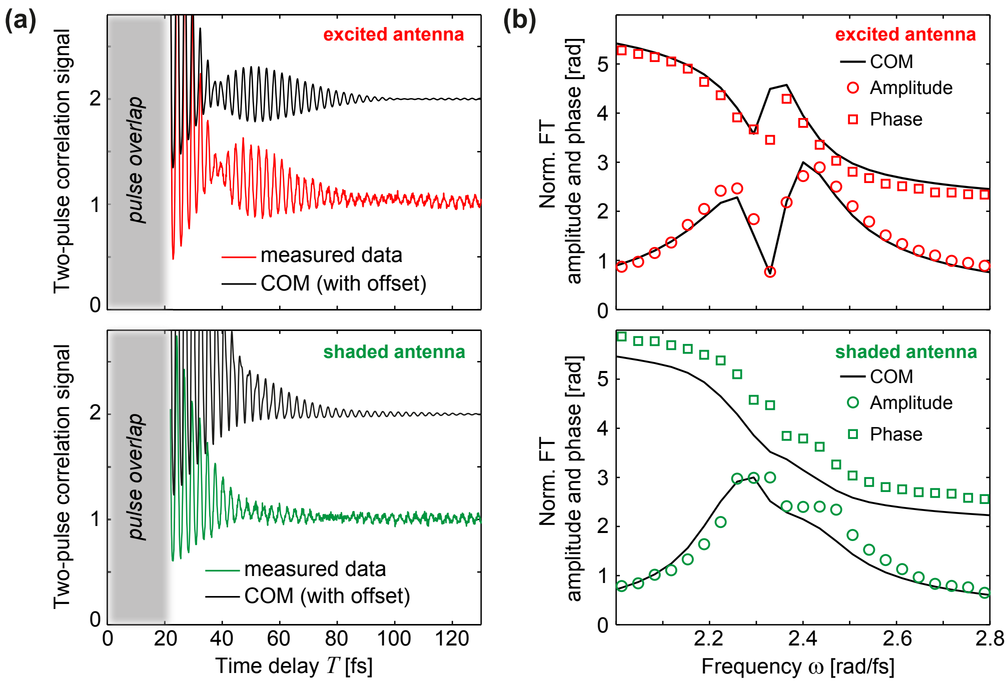

Figure 5.10: Two-pulse PEEM experiment with the phase-stabilized Mach-Zehnder interferometer on cavity $E14$. (a) Two-pulse correlation signals at the excited (top graph) and shaded (bottom graph) antenna. The measured data (red and green solid lines) could be reproduced by the coupled-oscillator model (COM, black solid lines). (b) Normalized Fourier transformation (FT) of the data shown in (a). The FT of the measured signals at the excited (top graph, red) and shaded (bottom graph, green) antenna are depicted as amplitude (circles) and phase (squares). The black lines correspond to the coupled-oscillator model (COM). Figure adapted from Ref. [5].

5.5.2 Analysis of Experimental Data with Coupled-Oscillator Model

For the interpretation of the experimental correlation signals, the coupled-oscillator model introduced in Subsect. 5.4.2 was slightly adapted. According to Eq. (5.2) of the model, only one of the antennas is excited by the incident electric field. This assumption was made since one of the antennas was located in the geometrical shadow of the cavity walls with respect to the incident light. However, due to diffraction of the incident light at the cavity edges, this “shaded” antenna might be weakly excited as well. Hence, Eq. (5.2) was extended to

$$\frac{\mathrm{d}^2}{\mathrm{d}t^2}E_{\mathrm{ex}}(t) + 2\gamma_{\mathrm{ex}}\frac{\mathrm{d}}{\mathrm{d}t}E_{\mathrm{ex}}(t) + \omega_{\mathrm{ex}}^2 E_{\mathrm{ex}}(t) + \kappa E_{\mathrm{ca}}(t) = (1-\alpha)\,E_{\mathrm{in}}(t)\,,$$

$$\frac{\mathrm{d}^2}{\mathrm{d}t^2}E_{\mathrm{ca}}(t) + 2\gamma_{\mathrm{ca}}\frac{\mathrm{d}}{\mathrm{d}t}E_{\mathrm{ca}}(t) + \omega_{\mathrm{ca}}^2 E_{\mathrm{ca}}(t) + \kappa\big[E_{\mathrm{ex}}(t) + E_{\mathrm{sh}}(t)\big] = 0,$$

$$\frac{\mathrm{d}^2}{\mathrm{d}t^2}E_{\mathrm{sh}}(t) + 2\gamma_{\mathrm{sh}}\frac{\mathrm{d}}{\mathrm{d}t}E_{\mathrm{sh}}(t) + \omega_{\mathrm{sh}}^2 E_{\mathrm{sh}}(t) + \kappa E_{\mathrm{ca}}(t) = \alpha\,\mathrm{e}^{\mathrm{i}\phi_\alpha}E_{\mathrm{in}}(t)\,, \qquad (5.11)$$

wherein $\alpha \in [0,1]$ is an amplitude ratio that determines how much field strength of the incident electric field $E_{\mathrm{in}}(t)$ arrives at the shaded antenna. The additional phase ϕ_α was introduced to allow a phase difference between the incident light at the excited antenna and that at the shaded antenna due to diffraction at the cavity edges and/or due to the optical path difference. Both new parameters were assumed to be constant throughout the spectrum in order to keep the model as simple as possible. Assuming a δ-pulse excitation $(E_{\mathrm{in}}(t) = \delta(t))$ and applying the Fourier transformation to Eq. (5.11), the spectral response functions were obtained via

$$\begin{pmatrix} A_{\mathrm{ex}}(\omega) \\ A_{\mathrm{ca}}(\omega) \\ A_{\mathrm{sh}}(\omega) \end{pmatrix} = \begin{pmatrix} \omega_{\mathrm{ex}}^2 - \omega^2 + 2\mathrm{i}\gamma_{\mathrm{ex}}\omega & \kappa & 0 \\ \kappa & \omega_{\mathrm{ca}}^2 - \omega^2 + 2\mathrm{i}\gamma_{\mathrm{ca}}\omega & \kappa \\ 0 & \kappa & \omega_{\mathrm{sh}}^2 - \omega^2 + 2\mathrm{i}\gamma_{\mathrm{sh}}\omega \end{pmatrix}^{-1} \begin{pmatrix} 1-\alpha \\ 0 \\ \alpha\, \mathrm{e}^{\mathrm{i}\phi_\alpha} \end{pmatrix} . \tag{5.12}$$

According to Eqs. (5.7) and (5.8), the two-pulse correlation signals at the antennas were then calculated via

$$Y_k(T) = \int_{-\infty}^{\infty} \left(2\,\mathrm{Re}\left\{ \mathcal{F}^{-1}\left[A_k(\omega)\, E_{\mathrm{in}}(\omega, T) \right] \right\} \right)^{2N} \mathrm{d}t \tag{5.13}$$

with $k = \{\mathrm{ex}, \mathrm{sh}\}$ and the incident electric field of the double-pulse sequence

$$E_{\mathrm{in}}(\omega, T) = \frac{E_0(\omega)}{2} \left(1 + \mathrm{e}^{\mathrm{i}\omega T} \right) . \tag{5.14}$$

Note that compared to Eq. (5.9), i.e., the electric field of the double-pulse sequence generated by the pulse shaper, the relative phase φ_T between the two pulses was omitted in Eq. (5.14), since it could not be varied by the interferometer and was zero for every time delay T. Similarly to the two-pulse measurements with the pulse shaper, a fit of the measured data by means of Eq. (5.13) was not successful with respect to convergence. Nevertheless, correlation signals were calculated via this equation for varying parameters of the coupled-oscillator model (COM) and compared to the experimental data. In Fig. 5.10a, the correlation signals are shown that were obtained for the parameters $\omega_{\mathrm{cav}} = \omega_{\mathrm{ex}} = \omega_{\mathrm{sh}} = 2.33$ rad/fs, $\gamma_{\mathrm{ex}} = \gamma_{\mathrm{sh}} = 0.078\ \mathrm{fs}^{-1}$, $\gamma_{\mathrm{cav}} = 0.066\ \mathrm{fs}^{-1}$, $\kappa = 0.16\ \mathrm{rad}^2/\mathrm{fs}^2$, $\alpha = 0.89$, and $\phi_\alpha = \pi/10$. They are plotted as black solid lines and vertically shifted by $+1$ to improve visibility. Both calculated signals are in good agreement with the measured data. Especially the dip in the envelope of the signal at the excited antenna is reproduced well. In order to investigate the spectral response of the device, a discrete Fourier transformation (FT) was applied to the measured and calculated signals. The resulting normalized amplitudes and phases are illustrated in Fig. 5.10b. The FT data obtained from the model is represented by the black solid lines, whereas the FT amplitude and phase of the signals measured at the excited (red) and shaded (green) antenna are marked as circles and squares, respectively. In the signal of the excited antenna, the dip in the phase at about 2.28 rad/fs and that in the amplitude at about 2.33 rad/fs is well reproduced via the model. Furthermore, in both amplitudes of the shaded antenna, a

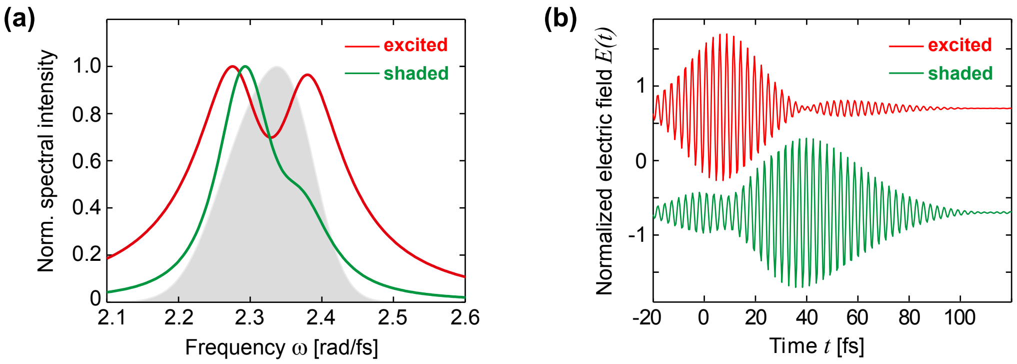

Figure 5.11: (a) Normalized spectral intensities of the response functions $|A_{\mathrm{ex}}(\omega)|^2$ (red) and $|A_{\mathrm{sh}}(\omega)|^2$ (green) at the excited and shaded antenna, respectively. (b) Normalized temporal electric field $E(t)$ at the excited (red) and shaded (green) antenna for single-pulse excitation, reconstructed via the response functions $A_{\mathrm{ex}}(\omega)$ and $A_{\mathrm{sh}}(\omega)$ of the coupled-oscillator model. The curves were shifted to improve visibility. The excitation spectrum of the incident pulse is depicted as gray shaded area in (a). Figure adapted from Ref. [97].

shoulder at about 2.45 rad/fs is observed. In the calculated signal, this shoulder arises from the values of the two parameters α and ϕ_α. For $\alpha = 1$ and $\phi_\alpha = 0$, i.e., in the case that the shaded antenna is not directly excited, the shoulder disappears, while the other spectral features in the FT data of the excited and shaded antenna are still present (not shown here).

The good agreement between the calculated and measured signals indicates that the coupled-oscillator model is suitable to describe the response of the investigated device. In Fig. 5.11a, the normalized spectral intensity of the response functions $|A_{\mathrm{ex}}(\omega)|^2$ (red) and $|A_{\mathrm{sh}}(\omega)|^2$ (green) are shown. It was calculated via Eq. (5.12) of the model and the above-mentioned parameters. Similarly to the FT amplitudes of the measured data depicted in Fig. 5.10b, the intensity of the excited and shaded antenna reveals a dip and a shoulder, respectively. However, their spectral positions do not perfectly coincide with the ones in the FT amplitudes. This is explained by the finite spectral bandwidth of the excitation spectrum (gray shaded area in Fig. 5.11a). The peaks in the response of the excited antenna are more clearly separated than those of the shaded antenna. This was also observed for the response functions that were obtained in Subsect. 5.2.3 to mimic the FDTD response. However, compared to those, only two instead of three peaks are visible. This is because the central peak is obscured by the two outer peaks due to the lower coupling constant κ and the lower cavity lifetime $\tau_{\mathrm{cav}} = 1/\gamma_{\mathrm{cav}}$.

By means of the response functions, the temporal electric field evolution at both antennas was reconstructed for single-pulse excitation via Eq. (5.8) and $E_{\mathrm{in}}(\omega) = E_0(\omega)$. The resulting normalized temporal electric fields are illustrated in Fig. 5.11b. The curves of the excited and shaded antenna are vertically shifted to improve visibility. First, the envelope of the electric field and, with this, the electromagnetic energy increases at both antennas. After a few femtoseconds, the energy at the excited antenna reaches a maximum, while the energy at the shaded antenna has slightly decreased. Then, a huge increase of the envelope is observed at the shaded antenna leading to a maximum at around 40 fs. During this time, the envelope at the excited antenna is continuously decreasing and reaches a minimum. After that, the energy reoccurs at the excited antenna with another maximum at about 60 fs, whereas that at the shaded antenna decays. Hence, for $t < 60$ fs, the energy is transferred between the excited and the shaded antenna back and forth once. Since the ratio between the first and second maximum at the excited antenna is about 0.1, an energy transfer efficiency of roughly $\sqrt{0.1} = 10\%$ for a full period of energy exchange is achieved [5] and agrees well with the value obtained from the FDTD simulations with the theoretical device ($\approx 7\%$). However, instead of a continuing periodic energy transfer, the electric-field evolution at both antennas synchronizes for $t > 60$ fs in the experimental device. The difference of the temporal field evolution in the theoretical and experimental device at later times mainly result from the different shapes of the corresponding spectral response functions, which in turn can be explained by the parameters of the coupled-oscillator model. Compared to the device that was used in the FDTD simulations, the coupling constant of the experimental device is slightly lower, which strongly influences the temporal field dynamics between the antennas. In addition to the different response functions, the excitation of both devices was not identical as well. On the one hand, the spectral bandwidths of the excitation spectra did not coincide. On the other hand, in contrast to the excitation spectrum used in the FDTD simulations, the experimental excitation spectrum was not perfectly Gaussian-shaped. Furthermore, the spectral positions of the excitation spectra with respect to the response functions were different. Nevertheless, despite the above-mentioned differences against the simulations with the theoretical device, the reconstructed electric-field evolution in the experimental device demonstrates a back-and-forth energy exchange between the antennas. Hence, considering the experimental results and the successful comparison with the coupled-oscillator model, it was concluded that indeed each antenna mode strongly couples to the cavity mode, leading to the observed energy transfer between the two nanoantennas.

5.6 Summary and Outlook

In this chapter, a hybridized plasmonic device consisting of two WGM nanoantennas in an elliptical cavity was introduced and investigated with respect to energy distribution dynamics between the antennas in both simulations and experiments. First, the device was optimized in theory via FDTD to achieve strong coupling between the localized antenna modes and the spatially extended cavity mode. The geometrical parameters of the components were adjusted separately to achieve a resonance of both the cavity mode and the m_0 antenna mode at $\lambda = 800$ nm. This guaranteed a high spectral overlap of the modes. After that, two antennas were positioned in the focal spots of the cavity, leading to a high spatial overlap of the modes. The FDTD response of the optimized device revealed three hybridized eigenmodes that were clearly separated within an energy range of about 90 meV. They resulted from the splitting of the cavity mode and the antenna modes due to strong coupling. Moreover, the FDTD response was well reproduced by a simple model based on three consecutively coupled oscillators. In FDTD simulations with single-pulse excitation, an oscillatory energy exchange between the two antennas was observed with a period of 86 fs and an energy transfer efficiency of about 7%, although the antennas were well separated by about twice the excitation wavelength (1646 nm distance between the antenna centers). Additional calculations with the coupled-oscillator model and FDTD revealed that, besides strong coupling, impedance matching, i.e., similar damping of the cavity mode and the antenna modes, is required to achieve a back-and-forth energy transfer between the antennas over several periods. Then, hybridized plasmonic devices were fabricated for time-resolved experiments via FIB milling by using two stacked single-crystalline gold microplates. The upper microplate served as substrate for the cavity walls, whereas the lower one was used as substrate for the cavity floor and the nanoantennas. This fabrication technique ensured smooth and well-defined structures with reduced ohmic losses within the cavities. In the experiments, only one antenna was directly excited by the incident pulses, while the opposite one was shielded by the cavity walls. Two-pulse PEEM measurements with high spatial and high temporal resolution were performed on cavities in which both nanoantennas revealed an enhanced electron emission. The coupled-oscillator model allowed a reconstruction of the measured data and thus a reconstruction of the local antenna response. The obtained response functions confirmed the formation of hybridized eigenmodes in the investigated experimental device due to strong coupling. In addition, the electric-field evolution at both antennas was calculated for single-pulse excitation by means of the response functions. In the resulting temporal electric fields, an energy transfer from one antenna to the other back and forth was observed with an energy transfer efficiency of $\approx 10\%$.

Combining all results, it was demonstrated that the plasmonic device presented here enables a long-range periodic energy transfer between two widely separated nanoantennas due to strong coupling. Furthermore, it was shown that the coupled-oscillator model provides the opportunity to further analyze the impact of device properties on the complex electric field evolution at the nanoantennas. Tuning the dissipation of the involved plasmonic resonances, e.g., the dissipation of the cavity mode via the height of the cavity walls, can be exploited to specifically tailor the energy flow dynamics [5]. Different applications of the device are possible depending on the choice of the excitation spectrum. In the case of broadband excitation, i.e., if the utilized pulses are short in the time domain and excite at least two of the hybridized eigenmodes, the device is suited for ultrafast plasmonic nanocircuitry. By contrast, in the case of excitation pulses with narrow spectral bandwidth, the device can be used to enhance the radiative coupling between two quantum emitters located in the vicinity of the nanoantennas. For this purpose, the quantum emitters have to couple strongly to a specific eigenmode of the device which in turn spectrally overlaps with the narrow excitation spectrum. In additional FDTD simulations done by Matthias Hensen, it was shown that, in the presence of the plasmonic device, the energy transfer between two widely separated quantum emitters can be enhanced up to seven orders of magnitude [5, 97, 111]. This enhancement is two orders of magnitude higher than that obtained for one-dimensional plasmonic waveguides [112]. Hence, the device has great potential to realize SPP-mediated strong coupling between single quantum emitters [113, 114], and thus could become interesting for future quantum optical applications.

6 Analytic Optimization of Local Optical Chirality Enhancement

6.1 Introduction

Chirality is a geometric property that is of relevance throughout a wide field of natural and artificial entities and materials. For example, many biomolecules like aminoacids or sugars are chiral, i.e., they cannot be superimposed onto their mirror images. Such molecules interact differently with left- and right-handed circularly polarized light (LCPL and RCPL, respectively), leading to chiroptical effects, e.g., optical rotatory dispersion (ORD) and circular dichroism (CD) [115]. The latter is caused by the difference in absorption between LCPL and RCPL, and is exploited in CD spectroscopy. However, molecular CD signals are typically weak and thus difficult to measure with high fidelity, especially in variants where additional time resolution is desired [116–122] or where concentrations are low, such as in sensing applications. Hence, for practical purposes, the question arises whether chiroptical signals can be enhanced with respect to the conventional measurement techniques. This also leads to a deeper fundamental question: Which electromagnetic field is actually most sensitive to chirality? Traditionally, circular polarization is employed. But can one do better? Is it possible to enhance chiroptical effects by using suitably "tailored" light fields, independent from the investigated specimen?

Formally, the absorption A of an electromagnetic field by a chiral molecule at frequency ω can be expressed via [123–125]

$$A \propto \omega \left(\alpha^{''} U_e + \frac{\chi^{''}}{c^2} U_b \right) - G^{''} C \,, \tag{6.1}$$

wherein c is the speed of light in free space, U_e and U_b are the electric and magnetic energy density, respectively, and the imaginary parts of the electric and magnetic polarizability are defined by $\alpha^{''}$ and $\chi^{''}$. The imaginary part of the so-called mixed electric-magnetic dipole polarizability is described by $G^{''}$ and the optical chirality C introduced by Lipkin [123] quantifies the chiral nature of the electromagnetic field. A precise definition of C and its discussion will follow in Sect. 6.2. The sign of $G^{''}$ depends on the handedness of the chiral molecule [126], whereas the sign of C depends on the handedness of the electromagnetic field. Considering Eq. (6.1), the difference in the absorption of light of opposite handedness results from the last term, which is proportional to the optical chirality. Hence, analogously to conventional CD spectroscopy, arbitrary pairs of electromagnetic field distributions with opposite optical chirality but identical U_e as well as U_b can be used for CD-like measurements. Thus, the difference in absorption of such enantiomorphic fields can in principle be enhanced by increasing the magnitude of C. For propagating plane waves, the largest optical chirality is achieved for CPL. Tang and Cohen have introduced an experimental scheme where they superimposed two counterpropagating circularly polarized beams of opposite handedness and slightly different amplitudes leading to a standing wave pattern [127]. They observed an enhanced optical response of chiral molecules with respect to their relative differential absorption, i.e., the difference in absorption of light with opposite handedness normalized to the absolute (chirality-independent) absorption, which is proportional to C/U_e. However, this relative signal was enhanced due to the reduction of U_e at the nodes of the standing waves and not due to an increased optical chirality. An option for the enhancement of absolute instead of relative chiroptical signals is provided by the wide-field of chiral plasmonics [128–136]. Geometrically chiral plasmonic nanostructures with large chiroptical far-field responses have been developed [137–147]. Furthermore, the interaction between chiral molecules and plasmonic nanostructures was investigated in theory [148–153] and experiments [154–160]. In recent years, it has been demonstrated that the near-fields of plasmonic nanostructures can be utilized to locally enhance the optical chirality [20, 21]. By means of specially tailored chiral nanostructures local optical chirality values greater than that of CPL in free space were achieved [22–24]. Enhanced optical chirality was even found at distinct local positions near achiral nanostructures [161–163]. Additionally, an enhancement in a large volume region was demonstrated [164].

In all approaches of optical chirality enhancement mentioned above, either linearly or circularly polarized excitation light has been used. However, besides the composition and geometry of the nanostructures, the modification of the far-field polarization of the exciting radiation offers another degree of freedom to increase local optical chirality. It has been shown previously, both theoretically and experimentally, that using femtosecond polarization pulse shaping it is possible to coherently control the localization of near fields on a nm spatial and fs temporal scale [165–171].

In this chapter, it is demonstrated how the local optical chirality can be enhanced by tuning the far-field polarization of the external light. First, it is shown how analytic expressions for the optimal external field were derived (Sect. 6.2). For an exemplary illustration (Sect. 6.4), the principle was then applied to an achiral (Subsect. 6.4.2) and a chiral nanostructure assembly (Subsect. 6.4.3). The numerical results confirmed that local optical chirality can be enhanced both with respect to free space as well as with respect to circular input polarization. Moreover, the temporal electric and magnetic near-field evolution for optimal and circular far-field polarization were compared to each other to illustrate the control mechanism (Sect. 6.5). Finally, the potential for enhancing the “local dissymmetry factor” is discussed in Sect. 6.6 before summarizing the theoretical findings and providing an outlook for future applications in Sect. 6.7.

The work that is presented here resulted from a collaboration with the research group of Harald Giessen (Stuttgart) and Thomas Weiss (Stuttgart) and was published in Ref. [4]. My contribution within this collaboration was the derivation of the analytic expressions, the numerical illustration of the local optical chirality enhancement by means of the achiral and chiral nanostructure, the investigation of the temporal

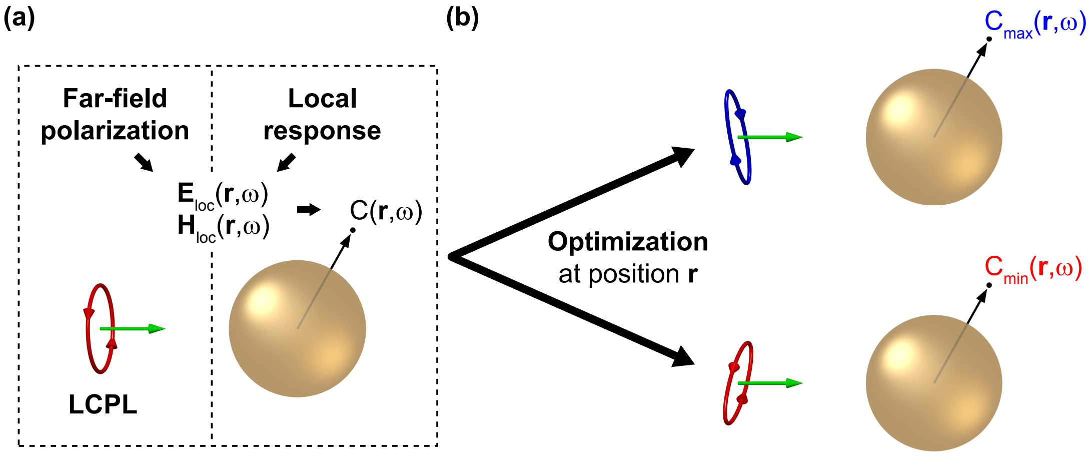

Figure 6.1: Basic idea of local optical chirality enhancement. (a) Far-field illumination of a gold sphere with left-handed circularly polarized light (LCPL, red circle) induces the local electric and magnetic fields $\mathbf{E}_{\text{loc}}(\mathbf{r},\omega)$ and $\mathbf{H}_{\text{loc}}(\mathbf{r},\omega)$, respectively, at position $\mathbf{r}$ and frequency ω. Both local fields determine the local optical chirality $C(\mathbf{r},\omega)$ according to Eq. (6.2). Since they depend not only on the local response of the nanostructure, but also on the far-field polarization of the external light, $C(\mathbf{r},\omega)$ can be optimized by tuning the far-field polarization. The propagation direction of the external light is indicated by the green arrow. (b) By means of optimization, far-field polarizations (blue/red ellipse) can be found that lead to maximum/minimum local optical chirality $C_{\max}(\mathbf{r},\omega)/C_{\min}(\mathbf{r},\omega)$. Figure adapted from Ref. [4]. © (2017) American Chemical Society.

near-field evolution regarding this enhancement, and the discussion about the local dissymmetry factor. For the numerical simulations, the spectral response functions of the utilized nanostructures were calculated by Martin Schäferling via MESME (multiple elastic scattering of multipole expansions) [172]. This chapter is mainly based on the above-mentioned publication [4].

6.2 Analytic Derivation of Optimal Local Optical Chirality

6.2.1 One Given Position

The basic idea of local optical chirality enhancement is illustrated in Fig. 6.1. If a plasmonic nanostructure, e.g., a gold sphere, is illuminated by external light, the local electric and magnetic near fields in the vicinity of the nanostructre are generated. The local optical chirality $C(\mathbf{r},\omega)$ at position $\mathbf{r}$ and frequency ω can then be calculated via [123, 124]

$$C(\mathbf{r},\omega) = -\frac{\epsilon_0\mu_0\omega}{2}\,\operatorname{Im}\left[\mathbf{E}^*_{\text{loc}}(\mathbf{r},\omega)\cdot\mathbf{H}_{\text{loc}}(\mathbf{r},\omega)\right], \tag{6.2}$$

wherein ϵ_0 is the vacuum permittivity, μ_0 is the vacuum permeability, and the complex-valued vectors $\mathbf{E}_{\text{loc}}$ and $\mathbf{H}_{\text{loc}}$ are the local electric and magnetic fields, respectively, with the asterisk (*) denoting complex conjugation. Both local fields depend on the local response of the nanostructure as well as on the far-field polarization of the external light. In Fig. 6.1a, the far-field polarization is circular, leading to a certain value for $C(\mathbf{r},\omega)$. However, there are possibly far-field polarizations for which the optical chirality value at this position is higher or lower. This can be understood because the local response of the nanostructure crucially depends on the incident polarization. Additionally, interference between incident and scattered fields influences the local optical chirality. The goal is now to find the optimal far-field polarizations, i.e., the far-field polarizations that lead to maximum (i.e., the highest positive) local optical chirality $C_{\mathrm{max}}(\mathbf{r},\omega)$ and minimum (i.e., the highest negative) optical chirality $C_{\mathrm{min}}(\mathbf{r},\omega)$ (Fig. 6.1b). In the case of external plane-wave illumination, the electromagnetic field is transverse and thus the electric field consists of two orthogonal far-field polarization components, $\alpha = \{1,2\}$, that can be expressed by [173]

$$E_\alpha^{\mathrm{ext}}(\omega) = \sqrt{\frac{I_\alpha(\omega)}{2\epsilon_0 c}}\mathrm{e}^{\mathrm{i}\varphi_\alpha(\omega)} \tag{6.3}$$

with the intensity $I_\alpha(\omega)$ and the phase $\varphi_\alpha(\omega)$. Assuming a linear response of the nanostructure, the local electric and magnetic fields can then be obtained via the linear superpositions

$$\begin{aligned}\mathbf{E}_{\mathrm{loc}}(\mathbf{r},\omega) &= \sum_{\alpha=1,2}\mathbf{S}_\alpha^e(\mathbf{r},\omega)\,E_\alpha^{\mathrm{ext}}(\omega)\\ &= \begin{pmatrix} S_{1x}^e(\mathbf{r},\omega)\\ S_{1y}^e(\mathbf{r},\omega)\\ S_{1z}^e(\mathbf{r},\omega)\end{pmatrix}\sqrt{\frac{I_1(\omega)}{2\epsilon_0 c}}\mathrm{e}^{\mathrm{i}\varphi_1(\omega)} + \begin{pmatrix} S_{2x}^e(\mathbf{r},\omega)\\ S_{2y}^e(\mathbf{r},\omega)\\ S_{2z}^e(\mathbf{r},\omega)\end{pmatrix}\sqrt{\frac{I_2(\omega)}{2\epsilon_0 c}}\mathrm{e}^{\mathrm{i}\varphi_2(\omega)}\end{aligned} \tag{6.4}$$

and

$$\begin{aligned}\mathbf{H}_{\mathrm{loc}}(\mathbf{r},\omega) &= \sum_{\alpha=1,2}\mathbf{S}_\alpha^h(\mathbf{r},\omega)\,\frac{1}{\mu_0 c}E_\alpha^{\mathrm{ext}}(\omega)\\ &= \begin{pmatrix} S_{1x}^h(\mathbf{r},\omega)\\ S_{1y}^h(\mathbf{r},\omega)\\ S_{1z}^h(\mathbf{r},\omega)\end{pmatrix}\sqrt{\frac{I_1(\omega)}{2\mu_0 c}}\mathrm{e}^{\mathrm{i}\varphi_1(\omega)} + \begin{pmatrix} S_{2x}^h(\mathbf{r},\omega)\\ S_{2y}^h(\mathbf{r},\omega)\\ S_{2z}^h(\mathbf{r},\omega)\end{pmatrix}\sqrt{\frac{I_2(\omega)}{2\mu_0 c}}\mathrm{e}^{\mathrm{i}\varphi_2(\omega)}\end{aligned} \tag{6.5}$$

with the complex-valued local electric and magnetic response functions $\mathbf{S}_\alpha^e(\mathbf{r},\omega)$ and $\mathbf{S}_\alpha^h(\mathbf{r},\omega)$ of the corresponding far-field polarization components, respectively. The local response functions are dimensionless vectors and characteristics of the nanostructure. Furthermore, they depend on the illumination geometry, e.g., the incidence angle and the focusing parameters of the external light, but they are independent from the far-field polarization state that is defined by the amplitudes $\sqrt{I_\alpha(\omega)}$ and the phases $\varphi_\alpha(\omega)$ [171]. Note that the electric field of the external light is sufficient to obtain both the local electric and local magnetic fields. Inserting Eqs. (6.4) and (6.5) into Eq. (6.2) leads to

$$\begin{aligned}C(\mathbf{r},\omega) = -\frac{\epsilon_0\mu_0\omega}{4}\ \mathrm{Im}\Big[&\mathbf{S}_1^{e*}(\mathbf{r},\omega)\cdot\mathbf{S}_1^{h}(\mathbf{r},\omega)\,I_1(\omega)\\ &+\mathbf{S}_1^{e*}(\mathbf{r},\omega)\cdot\mathbf{S}_2^{h}(\mathbf{r},\omega)\,\sqrt{I_1(\omega)\,I_2(\omega)}\mathrm{e}^{\mathrm{i}[\varphi_2(\omega)-\varphi_1(\omega)]}\\ &+\mathbf{S}_2^{e*}(\mathbf{r},\omega)\cdot\mathbf{S}_1^{h}(\mathbf{r},\omega)\,\sqrt{I_1(\omega)\,I_2(\omega)}\mathrm{e}^{\mathrm{i}[\varphi_1(\omega)-\varphi_2(\omega)]}\\ &+\mathbf{S}_2^{e*}(\mathbf{r},\omega)\cdot\mathbf{S}_2^{h}(\mathbf{r},\omega)\,I_2(\omega)\Big]\,.\end{aligned} \tag{6.6}$$

Since the goal is to enhance the local optical chirality for a given incident spectrum, this relation is rewritten in terms of the total intensity $I(\omega) = I_1(\omega) + I_2(\omega)$ and the relative phase between the two external electric-field components $\varphi(\omega) = [\varphi_2(\omega) - \varphi_1(\omega)]$,

$$\begin{aligned}C(\mathbf{r},\omega) = -\frac{\epsilon_0\mu_0\omega}{4}\Bigg(&I_1(\omega)\left[C_{S_1}(\mathbf{r},\omega) - C_{S_2}(\mathbf{r},\omega)\right] + I(\omega)\,C_{S_2}(\mathbf{r},\omega)\\ &+\sqrt{I_1(\omega)\left[I(\omega)-I_1(\omega)\right]}\Big\{C_{S_\mathrm{p}}(\mathbf{r},\omega)\cos\left[\varphi(\omega)\right] + C_{S_\mathrm{m}}(\mathbf{r},\omega)\sin\left[\varphi(\omega)\right]\Big\}\Bigg)\,,\end{aligned} \tag{6.7}$$

with the abbreviations

$$C_{S_1}(\mathbf{r},\omega) = \ \mathrm{Im}\left[\mathbf{S}_1^{e*}(\mathbf{r},\omega)\cdot\mathbf{S}_1^{h}(\mathbf{r},\omega)\right], \tag{6.8}$$

$$C_{S_\mathrm{p}}(\mathbf{r},\omega) = \ \mathrm{Im}\left[\mathbf{S}_1^{e*}(\mathbf{r},\omega)\cdot\mathbf{S}_2^{h}(\mathbf{r},\omega) + \mathbf{S}_2^{e*}(\mathbf{r},\omega)\cdot\mathbf{S}_1^{h}(\mathbf{r},\omega)\right], \tag{6.9}$$

$$C_{S_\mathrm{m}}(\mathbf{r},\omega) = \ \mathrm{Re}\left[\mathbf{S}_1^{e*}(\mathbf{r},\omega)\cdot\mathbf{S}_2^{h}(\mathbf{r},\omega) - \mathbf{S}_2^{e*}(\mathbf{r},\omega)\cdot\mathbf{S}_1^{h}(\mathbf{r},\omega)\right], \tag{6.10}$$

$$C_{S_2}(\mathbf{r},\omega) = \ \mathrm{Im}\left[\mathbf{S}_2^{e*}(\mathbf{r},\omega)\cdot\mathbf{S}_2^{h}(\mathbf{r},\omega)\right]. \tag{6.11}$$

Parameters $C_{S_1}(\mathbf{r},\omega)$ and $C_{S_2}(\mathbf{r},\omega)$ are proportional to the local optical chirality of the independent response functions, while $C_{S_\mathrm{p}}(\mathbf{r},\omega)$ and $C_{S_\mathrm{m}}(\mathbf{r},\omega)$ mix the electric and magnetic response of the two orthogonal far-field polarizations. Additional relations arising under specific symmetry conditions are discussed in Sect. 6.3. It can be seen from Eq. (6.7) that the local optical chirality depends on the intensities of the two far-field components $I_1(\omega)$ and $I_2(\omega) = [I(\omega) - I_1(\omega)]$ as well as on their relative phase $\varphi(\omega)$, i.e., on the polarization state of the external light for a given total intensity $I(\omega)$. Hence, tuning of the external far-field polarization enables the control of local optical chirality.

In order to classify the enhancement of $C(\mathbf{r},\omega)$, the optical chirality of CPL in free space, $C_\mathrm{CPL}^\mathrm{free}(\omega)$, is calculated and used as reference for all later results. Assuming that circularly polarized light propagates in free space along the z direction with time dependency $\mathrm{e}^{-\mathrm{i}\omega t}$ of its temporal electric and magnetic fields, the corresponding fields in the frequency domain can be defined via

$$\mathbf{E}_\mathrm{CPL}^\mathrm{free}(\omega) = \sqrt{\frac{I(\omega)}{4\epsilon_0 c}}\begin{pmatrix}1\\ \pm\mathrm{i}\\ 0\end{pmatrix} \quad \text{and} \quad \mathbf{H}_\mathrm{CPL}^\mathrm{free}(\omega) = \sqrt{\frac{I(\omega)}{4\mu_0 c}}\begin{pmatrix}\mp\mathrm{i}\\ 1\\ 0\end{pmatrix}. \tag{6.12}$$

Note that, according to the definition of LCPL and RCPL from the observer's point of view, the light is left-circularly polarized, if the phase difference between the x and y components of the fields is $(\varphi_y - \varphi_x) = +\pi/2$, and right-circularly polarized, if the phase difference is $-\pi/2$. Inserting Eq. (6.12) into Eq. (6.2) leads to the optical chirality of CPL in free space:

$$C_{\mathrm{CPL}}^{\mathrm{free}}(\omega) = -\frac{\epsilon_0 \mu_0 \omega}{2} \operatorname{Im}\left\{\mathbf{E}_{\mathrm{CPL}}^{\mathrm{free}*}(\omega) \cdot \mathbf{H}_{\mathrm{CPL}}^{\mathrm{free}}(\omega)\right\} = \pm\frac{\epsilon_0 \mu_0 \omega I(\omega)}{4}\,. \tag{6.13}$$

Using this result, the normalized local optical chirality is then given by

$$\begin{aligned}\hat{C}(\mathbf{r},\omega) =& \frac{C(\mathbf{r},\omega)}{|C_{\mathrm{CPL}}^{\mathrm{free}}(\omega)|} \\ =& -\Bigg(\hat{I}_1(\omega)\left[C_{S_1}(\mathbf{r},\omega) - C_{S_2}(\mathbf{r},\omega)\right] + C_{S_2}(\mathbf{r},\omega) \\ & + \sqrt{\hat{I}_1(\omega) - \hat{I}_1^2(\omega)}\Big\{C_{S_\mathrm{p}}(\mathbf{r},\omega)\cos\left[\varphi(\omega)\right] + C_{S_\mathrm{m}}(\mathbf{r},\omega)\sin\left[\varphi(\omega)\right]\Big\}\Bigg)\end{aligned} \tag{6.14}$$

with the normalized intensity $\hat{I}_1(\omega) = I_1(\omega)/I(\omega)$. In consequence, the normalized optical chirality of CPL in free space is $\hat{C}_{\mathrm{CPL}}^{\mathrm{free}}(\omega) = \pm 1$. The sign indicates the handedness of the chiral electromagnetic field.

By means of Eq. (6.14), it is possible to find that far-field polarization which leads to either the highest positive or negative values of local optical chirality, i.e., maximum local optical chirality with opposite handedness. In order to determine extremal values for $\hat{C}(\mathbf{r},\omega)$, Eq. (6.14) is differentiated with respect to $\hat{I}_1(\omega)$ and $\varphi(\omega)$, for any given frequency ω independently, and the resulting derivatives are set to zero. Solving for $\hat{I}_1(\omega)$ and $\varphi(\omega)$ lead to two different solutions which can be identified as global maximum and minimum (see Appendix A.2). The corresponding far-field polarization parameters are expressed by

$$\hat{I}_{1,{\max \atop \min}}(\mathbf{r},\omega) = \frac{1}{2} \mp \frac{C_{S_1}(\mathbf{r},\omega) - C_{S_2}(\mathbf{r},\omega)}{2\left\{C_{S_\mathrm{p}}^2(\mathbf{r},\omega) + C_{S_\mathrm{m}}^2(\mathbf{r},\omega) + \left[C_{S_1}(\mathbf{r},\omega) - C_{S_2}(\mathbf{r},\omega)\right]^2\right\}^{\frac{1}{2}}}\,, \tag{6.15}$$

$$\varphi_{\max \atop \min}(\mathbf{r},\omega) = \mp 2\arctan\left[\frac{\pm C_{S_\mathrm{p}}(\mathbf{r},\omega) + \sqrt{C_{S_\mathrm{p}}^2(\mathbf{r},\omega) + C_{S_\mathrm{m}}^2(\mathbf{r},\omega)}}{C_{S_\mathrm{m}}(\mathbf{r},\omega)}\right], \tag{6.16}$$

with $\varphi_{\max}(\mathbf{r},\omega)$ and $\varphi_{\min}(\mathbf{r},\omega) \in [-\pi,\pi]$. Equations (6.15) and (6.16) constitute a first major result, as they enable an analytic calculation of the external field for optimal local optical chirality.

Due to the linear response of the nanostructure, the optimal external polarizations for different frequencies are independent from each other. Therefore, the result is not restricted to a monochromatic wave as external light source. Laser pulses, i.e., the superposition of monochromatic waves, can also be used to optimize the local optical chirality for a continuous frequency range simultaneously. Note that in general the far-field polarization parameters $\hat{I}_{1,\mathrm{opt}}(\mathbf{r},\omega)$ and $\varphi_{\mathrm{opt}}(\mathbf{r},\omega)$ with opt $=\{\max,\min\}$ can strongly vary for different locations near the nanostructure, so they depend on the local position $\mathbf{r}$. Combining Eqs. (6.15) and (6.16) with Eq. (6.14) leads to the maximum and minimum normalized local optical chirality

$$\begin{aligned}\hat{C}_{\substack{\max\\\min}}(\mathbf{r},\omega) = -\frac{1}{2}\Bigg(& C_{S_1}(\mathbf{r},\omega) + C_{S_2}(\mathbf{r},\omega) \\ & \mp \left\{C_{S_\mathrm{p}}^2(\mathbf{r},\omega) + C_{S_\mathrm{m}}^2(\mathbf{r},\omega) + \left[C_{S_1}(\mathbf{r},\omega) - C_{S_2}(\mathbf{r},\omega)\right]^2\right\}^{\frac{1}{2}}\Bigg) . \end{aligned} \tag{6.17}$$

As a next step, these optimal chirality values are compared with those obtained by CPL as external input. In that case, using $\hat{I}_1(\omega) = 1/2$ and $\varphi(\omega) = \pi/2$ for LCPL and $\varphi(\omega) = -\pi/2$ for RCPL the normalized local chirality is

$$\hat{C}_{\substack{\mathrm{LCPL}\\\mathrm{RCPL}}}(\mathbf{r},\omega) = -\frac{1}{2}\left[C_{S_1}(\mathbf{r},\omega) + C_{S_2}(\mathbf{r},\omega) \pm C_{S_\mathrm{m}}(\mathbf{r},\omega)\right] . \tag{6.18}$$

Comparing Eqs. (6.17) and (6.18), CPL is the optimal far-field polarization only if either

$$C_{S_1}(\mathbf{r},\omega) = C_{S_2}(\mathbf{r},\omega) = C_{S_\mathrm{p}}(\mathbf{r},\omega) = 0 \tag{6.19}$$

or if

$$C_{S_1}(\mathbf{r},\omega) = C_{S_2}(\mathbf{r},\omega) \quad \text{and} \quad C_{S_\mathrm{p}}(\mathbf{r},\omega) = 0 . \tag{6.20}$$

In all other cases, circular input polarization is not optimal, and Eqs. (6.15) and (6.16) provide room for enhancement.

6.2.2 Region of Interest (ROI)

For practical purposes, one is often interested in enhanced optical chirality over a finite volume of space, rather than just at an isolated point. In particular, this is relevant for potential experiments in chiral sensing or chiral spectroscopy where, for example, chiral interactions between molecules and light play a key role for the measured signal. In CD-like measurements with pairs of electromagnetic field distributions with opposite handedness, an enhanced local optical chirality throughout the sample volume of the investigated molecules would lead to an enhanced difference in absorption. Therefore, the averaged normalized optical chirality $\overline{C}(\omega)$ of a certain region of interest (ROI) is defined and investigated by integrating the normalized local optical chirality over the complete ROI and normalizing the result to the volume V:

$$\overline{C}(\omega) = \frac{1}{V}\int_V \hat{C}(\mathbf{r},\omega)\,\mathrm{d}\mathbf{r} . \tag{6.21}$$

Using Eq. (6.14), i.e., the definition of the normalized local optical chirality, one obtains

$$\overline{C}(\omega) = -\Bigg(\hat{I}_1(\omega)\left[\overline{C}_{S_1}(\omega) - \overline{C}_{S_2}(\omega)\right] + \overline{C}_{S_2}(\omega) + \sqrt{\hat{I}_1(\omega) - \hat{I}_1^2(\omega)}\Big\{\overline{C}_{S_\mathrm{p}}(\omega)\cos\left[\varphi(\omega)\right] + \overline{C}_{S_\mathrm{m}}(\omega)\sin\left[\varphi(\omega)\right]\Big\}\Bigg) \tag{6.22}$$

by replacing in Eq. (6.14) the local parameters $C_{S_j}(\mathbf{r},\omega)$ with $j = \{1, 2, \mathrm{p}, \mathrm{m}\}$ from Eqs. (6.8)–(6.11) with their ROI averages

$$\overline{C}_{S_j}(\omega) = \frac{1}{V}\int\limits_V C_{S_j}(\mathbf{r},\omega)\,\mathrm{d}\mathbf{r}\,. \tag{6.23}$$

As a consequence, the optimal optical chirality within the ROI, $\overline{C}_\mathrm{opt}(\omega)$, and the required far-field polarizations defined by $\hat{I}_{1,\mathrm{opt}}(\omega)$ and $\varphi_\mathrm{opt}(\omega)$ are obtained via Eqs. (6.15) and (6.16) as well, using the averaged parameters $\overline{C}_{S_j}(\omega)$ instead of the local ones $C_{S_j}(\mathbf{r},\omega)$. Note that the optimal results do not depend explicitly on $\mathbf{r}$ any more because of the volume integration, but an implicit dependence on the spatial location is retained via the choice of the ROI.

6.2.3 Relation between Optimal Far-Field Polarizations

The two far-field polarizations for maximum and minimum local optical chirality $\hat{C}_\mathrm{max}$ and $\hat{C}_\mathrm{min}$, respectively, are not independent from each other. In the following, their relations are determined for a given position $\mathbf{r}$ and frequency ω.

The normalized intensities $\hat{I}_{1,\mathrm{max}}$ and $\hat{I}_{1,\mathrm{min}}$ of the two optimal far-field polarizations are defined by Eq. (6.15). If both intensities are summed up, one obtains the relation

$$\hat{I}_{1,\mathrm{max}}(\mathbf{r},\omega) + \hat{I}_{1,\mathrm{min}}(\mathbf{r},\omega) = 1\,. \tag{6.24}$$

Analogously, a relation between $\varphi_\mathrm{max}(\mathbf{r},\omega)$ and $\varphi_\mathrm{min}(\mathbf{r},\omega)$ can be derived. According to Eq. (6.16), the two relative phases are given by

$$\varphi_\mathrm{max}(\mathbf{r},\omega) = -2\arctan\left[\frac{C_{S_\mathrm{p}}(\mathbf{r},\omega) + \sqrt{C_{S_\mathrm{p}}^2(\mathbf{r},\omega) + C_{S_\mathrm{m}}^2(\mathbf{r},\omega)}}{C_{S_\mathrm{m}}(\mathbf{r},\omega)}\right] \in [-\pi,\pi]\,, \tag{6.25}$$

$$\varphi_\mathrm{min}(\mathbf{r},\omega) = 2\arctan\left[\frac{-C_{S_\mathrm{p}}(\mathbf{r},\omega) + \sqrt{C_{S_\mathrm{p}}^2(\mathbf{r},\omega) + C_{S_\mathrm{m}}^2(\mathbf{r},\omega)}}{C_{S_\mathrm{m}}(\mathbf{r},\omega)}\right] \in [-\pi,\pi]\,. \tag{6.26}$$

Dividing both sides of Eqs. (6.25) and (6.26) by 2, applying the tangent, and using

$$\tan[\varphi] = \frac{2\tan\left[\frac{\varphi}{2}\right]}{1 - \tan\left[\frac{\varphi}{2}\right]^2} \tag{6.27}$$

result in

$$\tan\left[\varphi_{\max}\left(\mathbf{r},\omega\right)\right] = \frac{-\frac{2C_{S_\mathrm{p}}(\mathbf{r},\omega)+2\sqrt{C^2_{S_\mathrm{p}}(\mathbf{r},\omega)+C^2_{S_\mathrm{m}}(\mathbf{r},\omega)}}{C_{S_\mathrm{m}}(\mathbf{r},\omega)}}{1-\frac{2C^2_{S_\mathrm{p}}(\mathbf{r},\omega)+C^2_{S_\mathrm{m}}(\mathbf{r},\omega)+2C_{S_\mathrm{p}}(\mathbf{r},\omega)\sqrt{C^2_{S_\mathrm{p}}(\mathbf{r},\omega)+C^2_{S_\mathrm{m}}(\mathbf{r},\omega)}}{C^2_{S_\mathrm{m}}(\mathbf{r},\omega)}} = \frac{C_{S_\mathrm{m}}\left(\mathbf{r},\omega\right)}{C_{S_\mathrm{p}}\left(\mathbf{r},\omega\right)}\,, \quad (6.28)$$

$$\tan\left[\varphi_{\min}\left(\mathbf{r},\omega\right)\right] = \frac{\frac{-2C_{S_\mathrm{p}}(\mathbf{r},\omega)+2\sqrt{C^2_{S_\mathrm{p}}(\mathbf{r},\omega)+C^2_{S_\mathrm{m}}(\mathbf{r},\omega)}}{C_{S_\mathrm{m}}(\mathbf{r},\omega)}}{1-\frac{2C^2_{S_\mathrm{p}}(\mathbf{r},\omega)+C^2_{S_\mathrm{m}}(\mathbf{r},\omega)-2C_{S_\mathrm{p}}(\mathbf{r},\omega)\sqrt{C^2_{S_\mathrm{p}}(\mathbf{r},\omega)+C^2_{S_\mathrm{m}}(\mathbf{r},\omega)}}{C^2_{S_\mathrm{m}}(\mathbf{r},\omega)}} = \frac{C_{S_\mathrm{m}}\left(\mathbf{r},\omega\right)}{C_{S_\mathrm{p}}\left(\mathbf{r},\omega\right)}\,. \quad (6.29)$$

This leads to the condition that

$$\tan\left[\varphi_{\max}\left(\mathbf{r},\omega\right)\right] = \tan\left[\varphi_{\min}\left(\mathbf{r},\omega\right)\right] \quad (6.30)$$

which is fulfilled for

$$\varphi_{\max}\left(\mathbf{r},\omega\right) = \varphi_{\min}\left(\mathbf{r},\omega\right) + n\pi \quad (6.31)$$

with $n \in \mathbb{Z}$, and thus, considering $\varphi_{\max}\left(\mathbf{r},\omega\right) \neq \varphi_{\min}\left(\mathbf{r},\omega\right)$ and that values for $\varphi_{\max}\left(\mathbf{r},\omega\right)$ and $\varphi_{\min}\left(\mathbf{r},\omega\right)$ are between $-\pi$ and π, to

$$\left|\varphi_{\max}\left(\mathbf{r},\omega\right) - \varphi_{\min}\left(\mathbf{r},\omega\right)\right| = \pi\,. \quad (6.32)$$

According to Eq. (6.32), the relative phases $\varphi_{\max}\left(\mathbf{r},\omega\right)$ and $\varphi_{\min}\left(\mathbf{r},\omega\right)$ differ by a constant offset of $\pm\pi$. An analogous "π rule" was derived previously for coherent control of energy localization [169] and experimentally confirmed in gold nanotriangles [170]. This means that an optimal optical chirality contrast, i.e., maximally different local optical chirality, is achieved by applying a π shift to the far-field phase difference φ.

For a direct and more intuitive interpretation of the relations between the optimal far-field polarizations defined in Eqs. (6.24) and (6.32), the polarization parameters are transformed into elliptical parameters. In this representation, any possible polarization state can be generally assigned to an ellipse with a given ellipticity ϵ and orientation angle θ [174]. In Fig. 6.2a, exemplary polarization states are depicted in the two-dimensional (θ-ϵ) plane. The parameter ϵ is defined for values between $-\pi/4$ and $+\pi/4$, while θ is defined for values between $-\pi/2$ and $+\pi/2$. The sign of ϵ determines the handedness of the ellipse. If $\epsilon > 0$, the polarization is left-handed, and if $\epsilon < 0$, the polarization is right-handed. Circularly polarized light is described via $\epsilon = +\pi/4$ (LCPL) and $\epsilon = -\pi/4$ (RCPL). In the case of $\epsilon = 0$, the polarization state is linear. It is shown in Appendix A.3 that, according to the conditions from Eqs. (6.24) and (6.32), the ellipticities of the two optimal far-field polarizations differ only in their sign, i.e., in their handedness, and that the angle between their orientations, i.e., between the principal axes of their ellipses, is $\pm\pi/2$. These conditions are illustrated via the projection of the (θ-ϵ) plane onto a sphere, the so-called Poincaré sphere [175], in Fig. 6.2b. The latitude and longitude of each point on the surface of the sphere correspond to the values 2ϵ and 2θ, respectively. Due to the relations $\epsilon_{\max} = -\epsilon_{\min}$ and $\theta_{\max} = \theta_{\min} \pm \pi/2$, the points of the far-field polarizations for minimum optical chirality are the antipodal points of the

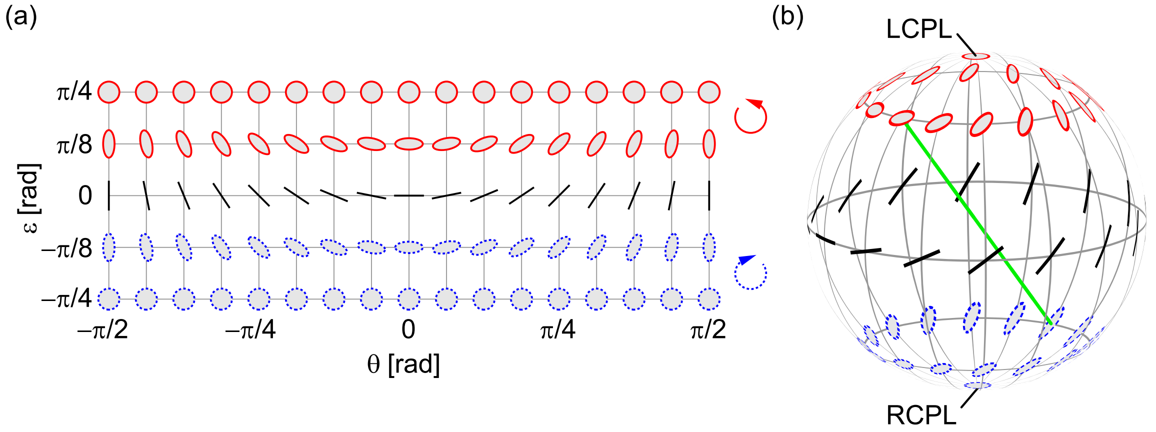

Figure 6.2: Relation between optimal far-field polarizations with respect to their elliptical parameters [174]. (a) Representation of the polarization via elliptical parameters. Each polarization state can be described via an ellipse with a given ellipticity ϵ and orientation angle θ. For $\epsilon > 0$, the polarization is left-handed (red solid ellipses), and for $\epsilon < 0$, it is right-handed (blue dashed ellipses). If $\epsilon = 0$, the polarization is linear (black lines). LCPL and RCPL correspond to $\epsilon = +\pi/4$ and $\epsilon = -\pi/4$, respectively. (b) Relation between exemplary optimal far-field polarizations on the surface of the Poincaré sphere [175]. Each point of the surface represents a polarization state determined by ϵ and θ. The latitude and longitude of the surface correspond to the values 2ϵ and 2θ, respectively. In the upper hemisphere the polarization states are left elliptical ($\epsilon > 0$) with the pole representing LCPL, in the lower hemisphere right elliptical ($\epsilon < 0$) with the pole representing RCPL. The polarization states at the equator are linear ($\epsilon = 0$). The two points of ôptimal far-field polarization are connected by a green line through the origin. The point of the far-field polarization for minimum optical chirality is the antipodal point of the corresponding far-field polarization for maximum optical chirality. (b) taken from Ref. [4]. © (2017) American Chemical Society.

corresponding far-field polarizations for maximum optical chirality, i.e., “maximally different external polarization states” lead to “maximally different local optical chirality”. In the example of Fig. 6.2b, the green line through the origin of the Poincaré sphere connects external polarization states leading to maximum and minimum local optical chirality.

In this subsection, the relations between the optimal far-field polarizations have been determined by means of the local parameters $C_{S_j}(\mathbf{r}, \omega)$ with $j = \{1, 2, \mathrm{p}, \mathrm{m}\}$ and thus for one given position $\mathbf{r}$. For a ROI, the optimal far-field polarizations are also calculated via Eqs. (6.15) and (6.16), with the sole difference that the averaged parameters $\overline{C}_{S_j}$ instead of the local ones are used. Hence, these relations are valid in the case of ROIs as well.

6.3 Consequences of Symmetry

The optimal far-field polarization for a ROI generally depends on its averaged parameters $\overline{C}_{S_j}$ with $j = \{1, 2, \mathrm{p}, \mathrm{m}\}$. Analogously to Eqs. (6.19) and (6.20), circularly polarized light is optimal as input polarization, if the condition

$$\overline{C}_{S_1}(\omega) = \overline{C}_{S_2}(\omega) = \overline{C}_{S_p}(\omega) = 0 \tag{6.33}$$

or

$$\overline{C}_{S_1}(\omega) = \overline{C}_{S_2}(\omega) \quad \text{and} \quad \overline{C}_{S_p}(\omega) = 0\,. \tag{6.34}$$

is met. In this subsection, it is exemplarily demonstrated how symmetry properties of a nanostructure with respect to the illumination geometry can be exploited in order to deduce, which ROIs fulfill one of these two conditions and thus have CPL as optimal far-field polarization.

A golden truncated square pyramid is chosen as nanostructure for illustration purposes (see Fig. 6.3a). It is centered around the z axis of a Cartesian coordinate system with the two parallel planes perpendicular to this axis. The truncated square pyramid is illuminated by external light that propagates along its normalized wave vector $\mathbf{e}_k$ parallel to the z axis either as a plane wave or as a Gaussian beam whose center axis goes through the center of the nanostructure. The far-field polarization components 1 and 2 of the external light are parallel to the x and y axis, respectively. Their directions are defined via the unit vectors $\mathbf{e}_1$ and $\mathbf{e}_2$. In this geometry, the nanostructure has four mirror-symmetry planes with the principle axis parallel to $\mathbf{e}_k$ and thus is C_{4v} symmetric with respect to the propagation direction of the external light.

Now the conditions from Eqs. (6.33) and (6.34) are analyzed with respect to the symmetry by using the definitions from Eqs. (6.8)–(6.11) and (6.23) in terms of the response functions $\mathbf{S}^e_\alpha(\mathbf{r},\omega)$ and $\mathbf{S}^h_\alpha(\mathbf{r},\omega)$ with $\alpha = \{1,2\}$. In the following, the local position $\mathbf{r}$ is expressed by the coordinates (x,y,z) and the dependency on ω is omitted for brevity, i.e., $\mathbf{S}^{e,h}_\alpha(\mathbf{r},\omega) \equiv \mathbf{S}^{e,h}_\alpha(x,y,z)$. Due to the symmetry of the nanostructure the response-function components $S^e_{\alpha q}(x,y,z)$ and $S^h_{\alpha q}(x,y,z)$ with $q = \{x,y,z\}$ can be classified as either even or odd functions with respect to x and y. For example, component $S^e_{1z}(x,y,z)$ is odd with respect to x and even with respect to y:

$$S^e_{1z}(x,y,z) = -S^e_{1z}(-x,y,z) = +S^e_{1z}(x,-y,z)\ . \tag{6.35}$$

Analogously, the symmetry properties of all response-function components can be derived and are shown in Table 6.1. Note that in general, under the same illumination conditions, these properties would be also valid for plasmonic nanostructures that are only C_{2v}-symmetric with the xz and the yz plane as mirror symmetry planes. The stronger C_{4v} symmetry, however, enables that the response functions of far-field polarization 2 can be expressed by those of far-field polarization component 1 because they only differ from each other in a rotation by $\pi/2$ with respect to the z axis. This leads to the following relations:

$$\mathbf{S}^{e,h}_1(x,y,z) = \mathbb{R}_z(-\pi/2)\,\mathbf{S}^{e,h}_2(-y,x,z)\ , \tag{6.36}$$

$$\mathbf{S}^{e,h}_2(x,y,z) = \mathbb{R}_z(+\pi/2)\,\mathbf{S}^{e,h}_1(y,-x,z)\ . \tag{6.37}$$

Here, $\mathbb{R}_z$ denotes a rotation around the z axis. For example, the response-function

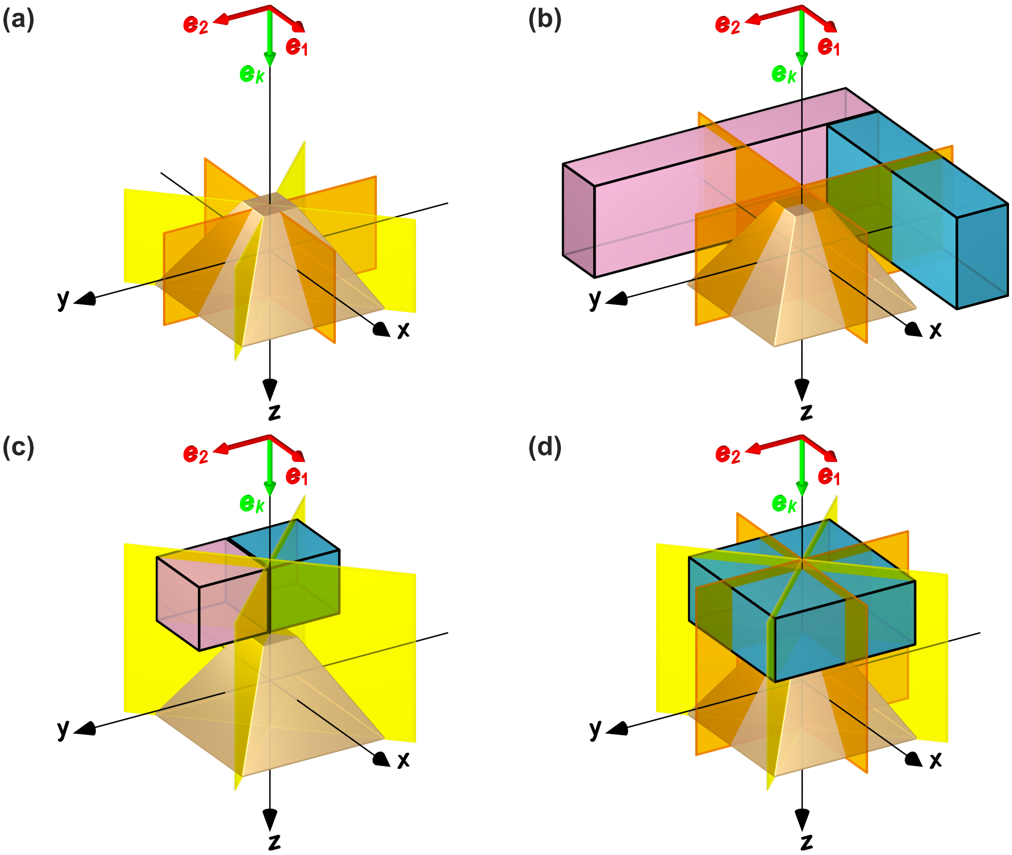

Figure 6.3: Golden truncated square pyramid illuminated by external light with the normalized wave vector $\mathbf{e}_k$ (green arrows) and the far-field polarization components 1 and 2 along the unit vectors $\mathbf{e}_1$ and $\mathbf{e}_2$, respectively (red arrows). (a) The truncated square pyramid has mirror symmetry to the xz and yz plane (orange cuts) as well as to the $x = y$ and $x = -y$ plane (yellow cuts). (b) The blue-colored ROI has mirror symmetry with respect to the yz plane and the pink-colored ROI with respect to the xz plane. For both ROIs the parameters $\overline{C}_{S_1}$ and $\overline{C}_{S_2}$ are zero. (c) The blue-colored ROI has mirror symmetry with respect to the plane $x = y$ and the pink-colored ROI with respect to the plane $x = -y$. For both ROIs $\overline{C}_{S_\mathrm{p}}$ is zero. (d) The blue-colored ROI has mirror symmetry to all four planes. Due to the vanishing parameters $\overline{C}_{S_1}$, $\overline{C}_{S_2}$, and $\overline{C}_{S_\mathrm{p}}$, the optimal external polarization for maximum and minimum optical chirality within this ROI is CPL. Figure taken from Ref. [4]. © (2017) American Chemical Society.

components of $\mathbf{S}_1^e(x, y, z)$ are connected to those of response function $\mathbf{S}_2^e(-y, x, z)$ via

$$\begin{aligned}\begin{pmatrix} S_{1x}^e(x,y,z) \\ S_{1y}^e(x,y,z) \\ S_{1z}^e(x,y,z) \end{pmatrix} &= \begin{pmatrix} \cos(-\pi/2) & -\sin(-\pi/2) & 0 \\ \sin(-\pi/2) & \cos(-\pi/2) & 0 \\ 0 & 0 & 1 \end{pmatrix} \begin{pmatrix} S_{2x}^e(-y,x,z) \\ S_{2y}^e(-y,x,z) \\ S_{2z}^e(-y,x,z) \end{pmatrix} \\ &= \begin{pmatrix} 0 & 1 & 0 \\ -1 & 0 & 0 \\ 0 & 0 & 1 \end{pmatrix} \begin{pmatrix} S_{2x}^e(-y,x,z) \\ S_{2y}^e(-y,x,z) \\ S_{2z}^e(-y,x,z) \end{pmatrix} = \begin{pmatrix} S_{2y}^e(-y,x,z) \\ -S_{2x}^e(-y,x,z) \\ S_{2z}^e(-y,x,z) \end{pmatrix} .\end{aligned} \tag{6.38}$$

The symmetry properties of the response functions are now exploited to determine which

Response-function component $\boldsymbol{S^{e,h}_{\alpha q}} \in \mathbb{C}$ $\left[\alpha = \{1,2\}, q = \{x,y,z\}\right]$	**Symmetry with respect to $\boldsymbol{x}$ $(\boldsymbol{x \rightarrow -x})$**	**Symmetry with respect to $\boldsymbol{y}$ $(\boldsymbol{y \rightarrow -y})$**
$S^e_{1x}(x,y,z)$	even	even
$S^e_{1y}(x,y,z)$	odd	odd
$S^e_{1z}(x,y,z)$	odd	even
$S^h_{1x}(x,y,z)$	odd	odd
$S^h_{1y}(x,y,z)$	even	even
$S^h_{1z}(x,y,z)$	even	odd
$S^e_{2x}(x,y,z)$	odd	odd
$S^e_{2y}(x,y,z)$	even	even
$S^e_{2z}(x,y,z)$	even	odd
$S^h_{2x}(x,y,z)$	even	even
$S^h_{2y}(x,y,z)$	odd	odd
$S^h_{2z}(x,y,z)$	odd	even

Table 6.1: Symmetry properties of response functions for plasmonic nanostructures that have mirror symmetry with respect to the xz and the yz plane. The external light propagates along the z axis, and the far-field polarization components 1 and 2 are parallel to the x and y axis, respectively. Table taken from Ref. [4]. © (2017) American Chemical Society.

symmetry properties a ROI must have in order to fulfill Eqs. (6.33) and (6.34). For a ROI with volume V, the parameter $\overline{C}_{S_1}$ is obtained via Eqs. (6.8) and (6.23) as

$$\overline{C}_{S_1} = \frac{1}{V}\iiint\limits_V \mathrm{Im}\Big[\underbrace{\overbrace{S^{e*}_{1x}(x,y,z)}^{\substack{\text{even for } \pm x \\ \text{even for } \pm y}}\,\overbrace{S^{h}_{1x}(x,y,z)}^{\substack{\text{odd for } \pm x \\ \text{odd for } \pm y}}}_{\text{odd for } \pm x \text{ and } \pm y} + \underbrace{\overbrace{S^{e*}_{1y}(x,y,z)}^{\substack{\text{odd} \\ \text{odd}}}\,\overbrace{S^{h}_{1y}(x,y,z)}^{\substack{\text{even} \\ \text{even}}}}_{\text{odd for } \pm x \text{ and } \pm y}$$

$$+ \underbrace{\overbrace{S^{e*}_{1z}(x,y,z)}^{\substack{\text{odd} \\ \text{even}}}\,\overbrace{S^{h}_{1z}(x,y,z)}^{\substack{\text{even} \\ \text{odd}}}}_{\text{odd for } \pm x \text{ and } \pm y}\Big]\,\mathrm{d}x\,\mathrm{d}y\,\mathrm{d}z\,. \tag{6.39}$$

Since, according to Table 6.1, each term of the sum in Eq. (6.39) is a product of an odd and an even function with respect to x and y, all three terms are odd functions with respect to both x and y. Analogously, the three terms of parameter $\overline{C}_{S_2}$ are odd functions with respect to x and y as well. Thus, if a ROI has mirror-symmetry with respect to the xz and/or yz plane, i.e., the plane that is spanned by $\mathbf{e}_k$ and $\mathbf{e}_1$ and/or the plane that is spanned by $\mathbf{e}_k$ and $\mathbf{e}_2$, respectively, then $\overline{C}_{S_1} = \overline{C}_{S_2} = 0$. In Fig. 6.3b, two exemplary box-shaped ROIs are shown that are mirror-symmetric with respect to the xz (pink-colored) and yz plane (blue-colored), respectively. Note that a fusion of both ROIs would also lead to vanishing parameters $\overline{C}_{S_1}$ and $\overline{C}_{S_2}$, although the fused ROI does not meet the mirror-symmetry condition. Therefore, it is concluded that if a ROI lacks this mirror symmetry, but can be decomposed into ROIs which are mirror-symmetric separately from each other, then $\overline{C}_{S_1}$ and $\overline{C}_{S_2}$ are zero as well.

As opposed to the parameters $\overline{C}_{S_1}$ and $\overline{C}_{S_2}$, parameter $\overline{C}_{S_\mathrm{p}}$ contains response functions of both far-field polarization components. It is defined by Eqs. (6.9) and (6.23) as

$$\overline{C}_{S_\mathrm{p}} = \underbrace{\frac{1}{V}\iiint\limits_V \mathrm{Im}\Big[\mathbf{S}_1^{e*}(x,y,z)\cdot\mathbf{S}_2^{h}(x,y,z)\Big]\mathrm{d}x\,\mathrm{d}y\,\mathrm{d}z}_{\overline{C}_{S_\mathrm{p1}}}$$
$$+\underbrace{\frac{1}{V}\iiint\limits_V \mathrm{Im}\Big[\mathbf{S}_2^{e*}(x,y,z)\cdot\mathbf{S}_1^{h}(x,y,z)\Big]\mathrm{d}x\,\mathrm{d}y\,\mathrm{d}z}_{\overline{C}_{S_\mathrm{p2}}}\,. \tag{6.40}$$

Since all terms of both scalar products in Eq. (6.40) are even functions with respect to x and y, they would not vanish for a ROI with mirror symmetry with respect to the xz and/or xy plane. Nevertheless, $\overline{C}_{S_\mathrm{p1}}$ and $\overline{C}_{S_\mathrm{p2}}$ can cancel out each other so that $\overline{C}_{S_\mathrm{p}}$ becomes zero. Applying Eqs. (6.36) and (6.37) to $\overline{C}_{S_\mathrm{p1}}$ leads to

$$\begin{aligned}\overline{C}_{S_\mathrm{p1}} &= \frac{1}{V}\iiint\limits_V \mathrm{Im}\Big[\mathbb{R}_z(-\pi/2)\,\mathbf{S}_2^{e*}(-y,x,z)\cdot\mathbb{R}_z(\pi/2)\,\mathbf{S}_1^{h}(y,-x,z)\Big]\mathrm{d}x\,\mathrm{d}y\,\mathrm{d}z\\ &= \frac{1}{V}\iiint\limits_V \mathrm{Im}\Big[-S_{2y}^{e*}(-y,x,z)\,S_{1y}^{h}(y,-x,z) - S_{2x}^{e*}(-y,x,z)\,S_{1x}^{h}(y,-x,z)\\ &\qquad + S_{2z}^{e*}(-y,x,z)\,S_{1z}^{h}(y,-x,z)\Big]\mathrm{d}x\,\mathrm{d}y\,\mathrm{d}z\,.\end{aligned} \tag{6.41}$$

Using the relations from Table 6.1 on these terms one obtains

$$\begin{aligned}\overline{C}_{S_\mathrm{p1}} &= \frac{1}{V}\iiint\limits_V \mathrm{Im}\Big[-S_{2y}^{e*}(y,x,z)\,S_{1y}^{h}(y,x,z) - S_{2x}^{e*}(y,x,z)\,S_{1x}^{h}(y,x,z)\\ &\qquad - S_{2z}^{e*}(y,x,z)\,S_{1z}^{h}(y,x,z)\Big]\mathrm{d}x\,\mathrm{d}y\,\mathrm{d}z\\ &= -\frac{1}{V}\iiint\limits_V \mathrm{Im}\Big[\mathbf{S}_2^{e*}(y,x,z)\cdot\mathbf{S}_1^{h}(y,x,z)\Big]\mathrm{d}x\,\mathrm{d}y\,\mathrm{d}z\,.\end{aligned} \tag{6.42}$$

It is seen that for a ROI with mirror symmetry to the plane $x = y$, $\overline{C}_{S_\mathrm{p1}}$ is equal to $\overline{C}_{S_\mathrm{p2}}$ with opposite sign, and thus, $\overline{C}_{S_\mathrm{p}} = 0$. In addition, it can be shown by means of the relations from Table 6.1 and Eq. (6.42) that for a ROI with mirror symmetry to the plane $x = -y$, $\overline{C}_{S_\mathrm{p}}$ is zero as well. Hence, it is concluded that if a ROI has mirror symmetry with respect to the plane $x = y$ and/or with respect to the plane $x = -y$, i.e., the plane that is spanned by $\mathbf{e}_k$ and $1/\sqrt{2}(\mathbf{e}_1 + \mathbf{e}_2)$ and/or the plane that is spanned by $\mathbf{e}_k$ and $1/\sqrt{2}(\mathbf{e}_1 - \mathbf{e}_2)$, respectively, then $\overline{C}_{S_\mathrm{p}} = 0$ (compare blue- and pink-colored ROIs in Fig. 6.3c). In addition, if a ROI lacks this mirror symmetry, but can be decomposed into single ROIs which have the required mirror symmetry separately from each other, then $\overline{C}_{S_\mathrm{p}}$ becomes zero as well.

According to Eqs. (6.33) and (6.34), the optimal external polarization is circular not only for the condition $\overline{C}_{S_1} = \overline{C}_{S_2} = \overline{C}_{S_\mathrm{p}} = 0$, but also for the condition $\overline{C}_{S_1} = \overline{C}_{S_2}$ and $\overline{C}_{S_\mathrm{p}} = 0$. Therefore, it is analyzed in which case the parameters $\overline{C}_{S_1}$ and $\overline{C}_{S_2}$ are equal. The parameter $\overline{C}_{S_1}$ can be expressed via Eqs. (6.8) and (6.23) and by means of Eqs. (6.36) and (6.37) as

$$\begin{aligned}\overline{C}_{S_1} &= \frac{1}{V}\iiint\limits_V \operatorname{Im}\Big[\mathbb{R}_z\left(-\pi/2\right)\mathbf{S}_2^{e*}\left(-y,x,z\right)\cdot\mathbb{R}_z\left(-\pi/2\right)\mathbf{S}_2^{h}\left(-y,x,z\right)\Big]\mathrm{d}x\,\mathrm{d}y\,\mathrm{d}z\\ &= \frac{1}{V}\iiint\limits_V \operatorname{Im}\Big[S_{2y}^{e*}\left(-y,x,z\right)S_{2y}^{h}\left(-y,x,z\right)+S_{2x}^{e*}\left(-y,x,z\right)S_{2x}^{h}\left(-y,x,z\right)\\ &\qquad + S_{2z}^{e*}\left(-y,x,z\right)S_{2z}^{h}\left(-y,x,z\right)\Big]\mathrm{d}x\,\mathrm{d}y\,\mathrm{d}z\,. \end{aligned} \tag{6.43}$$

Using the symmetry properties from Table 6.1 leads to

$$\begin{aligned}\overline{C}_{S_1} = \frac{1}{V}\iiint\limits_V \Bigg(&\operatorname{Im}\Big\{-S_{2y}^{e*}\left(y,x,z\right)S_{2y}^{h}\left(y,x,z\right)\\ &- S_{2x}^{e*}\left(y,x,z\right)S_{2x}^{h}\left(y,x,z\right)\\ &- S_{2z}^{e*}\left(y,x,z\right)S_{2z}^{h}\left(y,x,z\right)\Big\}\Bigg)\mathrm{d}x\,\mathrm{d}y\,\mathrm{d}z\,. \end{aligned} \tag{6.44}$$

It is obvious by comparing Eq. (6.44) with the definition of $\overline{C}_{S_2}$,

$$\begin{aligned}\overline{C}_{S_2} = \frac{1}{V}\iiint\limits_V \operatorname{Im}\Big[&S_{2x}^{e*}\left(x,y,z\right)S_{2x}^{h}\left(x,y,z\right)+S_{2y}^{e*}\left(x,y,z\right)S_{2y}^{h}\left(x,y,z\right)\\ &+ S_{2z}^{e*}\left(x,y,z\right)S_{2z}^{h}\left(x,y,z\right)\Big]\mathrm{d}x\,\mathrm{d}y\,\mathrm{d}z\,, \end{aligned} \tag{6.45}$$

that $\overline{C}_{S_1} = -\overline{C}_{S_2}$ for a ROI with mirror symmetry to the plane $x = y$. Furthermore, it can be demonstrated by means of the symmetry properties from Table 6.1 and Eq. (6.44) that this is the case for a ROI with mirror symmetry to the plane $x = -y$ as well. These results coincide with the result obtained for $\overline{C}_{S_\mathrm{p}} = 0$. Thus, if a ROI has mirror symmetry with respect to the plane $x = y$ and/or with respect to $x = -y$, i.e., the plane that is spanned by $\mathbf{e}_k$ and $1/\sqrt{2}(\mathbf{e}_1 + \mathbf{e}_2)$ and/or the plane that is spanned by $\mathbf{e}_k$ and $1/\sqrt{2}(\mathbf{e}_1 - \mathbf{e}_2)$, then not only $\overline{C}_{S_\mathrm{p}} = 0$, but also $\overline{C}_{S_1} = -\overline{C}_{S_2}$. However, for $\overline{C}_{S_1} = \overline{C}_{S_2}$ only the trivial solution $\overline{C}_{S_1} = \overline{C}_{S_2} = 0$ exists.

Combining all results the parameters $\overline{C}_{S_1}$, $\overline{C}_{S_2}$ and $\overline{C}_{S_\mathrm{p}}$ are zero if the ROI has mirror symmetry with respect to the four mirror-symmetry planes of the nanostructure. As a consequence, ROIs with these symmetry properties are centered around the principle axis of the nano̴structure (compare blue-colored ROI in Fig. 6.3d). Finally, it is concluded that if a nanostructure has at least C_{4v} symmetry with the principal axis parallel to e_k, then for any ROI that is also C_{4v} symmetric with identical principal axis and mirror-symmetry planes, circularly polarized light is the optimal external polarization to achieve either the highest positive ($\overline{C}_\mathrm{max}$) or negative ($\overline{C}_\mathrm{min}$) optical chirality within the ROI.

Note that there are ROIs possible which do not have these symmetry properties, but nevertheless fulfill the condition $\overline{C}_{S_1} = \overline{C}_{S_\mathrm{p}} = \overline{C}_{S_2} = 0$ and thus, $\overline{C}_\mathrm{CPL} = \overline{C}_\mathrm{opt}$ with $\mathrm{opt} = \{\mathrm{max}, \mathrm{min}\}$. For instance, the fusion of the blue- and pink-colored ROI in Fig. 6.3c would also lead to vanishing parameters $\overline{C}_{S_1}$, $\overline{C}_{S_2}$, and $\overline{C}_{S_2}$, since the fused ROI is mirror-symmetric with respect to the xz plane and can be decomposed into two ROIs with mirror symmetry with respect to the planes $x = y$ and $x = -y$, respectively.

6.4 Numerical Illustration

Based on the analytic derivations from Sect. 6.2, the optimization of the local optical chirality is numerically illustrated in this section using an achiral and a chiral nanostructure. First, it is described in Subsect. 6.4.1 how the numerical calculations are performed. Then, the results of the optimizations for the achiral and chiral nanostructure are discussed in Subsect. 6.4.2 and Subsect. 6.4.3, respectively.

6.4.1 Calculation Technique

The local optical chirality is optimized by tuning the far-field polarization of the external light that propagates in positive z direction along its normalized wave vector $\mathbf{e}_k$ either as a monochromatic plane wave with frequency ω or as a superposition of monochromatic plane waves, i.e., a laser pulse with a defined spectral bandwidth. In the latter case the following optimization procedure is done for each frequency component separately. The two orthogonal far-field polarization components 1 and 2 of the external light are parallel to the x axis along the unit vector $\mathbf{e}_1$ and parallel to the y axis along $\mathbf{e}_2$, respectively. The corresponding far-field polarization state for a given total intensity $I(\omega)$ is then defined by the normalized intensity $\hat{I}_1(\omega)$ and the relative phase between the two components $\varphi(\omega)$. In the first step the local response functions $\mathbf{S}^e_\alpha(\mathbf{r}, \omega)$ and $\mathbf{S}^h_\alpha(\mathbf{r}, \omega)$ with $\alpha = \{1, 2\}$ are determined for both far-field polarization components. This is done for each component separately by means of multiple elastic scattering of multipole expansions (MESME), introduced by García de Abajo [172]. First, the local electric and magnetic fields $\mathbf{E}_\mathrm{loc}(\mathbf{r}, \omega)$ and $\mathbf{H}_\mathrm{loc}(\mathbf{r}, \omega)$ are simulated for external light with a linear polarization along the x axis and field amplitude of unity, i.e., $E^\mathrm{ext}_1(\omega) = 1$ and $E^\mathrm{ext}_2(\omega) =$

0. The resulting local electric field is then identified as response function $\mathbf{S}_1^e(\mathbf{r},\omega)$ and the local magnetic field as $\frac{1}{\mu_0 c}\mathbf{S}_1^h(\mathbf{r},\omega)$. After that, the simulations are repeated for external light under the same illumination conditions, but with linear polarization along the y axis, i.e., $E_1^{\text{ext}}(\omega) = 0$ and $E_2^{\text{ext}}(\omega) = 1$, to obtain the response functions $\mathbf{S}_2^e(\mathbf{r},\omega)$ and $\mathbf{S}_2^h(\mathbf{r},\omega)$. For any given ROI the parameters $\overline{C}_{S_j}(\omega)$ with $j = \{1, 2, \mathrm{p}, \mathrm{m}\}$ are then calculated using Eqs. (6.8)–(6.11) and (6.23) in order to obtain the optimal optical chiraliy values $\overline{C}_{\text{opt}}(\omega)$ with opt $= \{\max, \min\}$ via Eq. (6.17). In addition, the optimal far-field polarizations defined by $\hat{I}_{1,\text{opt}}(\omega)$ and $\varphi_{\text{opt}}(\omega)$ are calculated via Eqs. (6.15) and (6.16). Note that considering the averaged quantities reduces the risk of artifacts resulting from numerical inaccuracies at singular points in the local fields for single positions $\mathbf{r}$.

6.4.2 Single Gold Sphere

The first investigated nanostructure is a single gold sphere in vacuum with a radius of 50 nm located at the origin of the coordinate system (Fig. 6.4a). The electric and magnetic response functions of far-field polarization components 1 and 2 are calculated for the resonance frequency of the sphere, $\omega_R = 3.65$ rad/fs, as described in Subsect. 6.4.1. The optimization of optical chirality is performed for several cubic ROIs (edge length of 20 nm) that differ only in their positions with respect to the gold sphere. The center of the first ROI is located at $(0, 0, 70)$ nm. From there, the positions of subsequent ROIs are obtained by shifting the cube in steps of 10 nm in positive y direction, until its center is at $(0, 70, 70)$ nm. This scan of the ROI position is called pathway I in the following and indicated by the symbol “I” in Fig. 6.4a. After that, the scan is proceeded by shifting the cube from $(0, 70, 70)$ nm in steps of 10 nm in negative z direction to the position at $(0, 70, 0)$ nm (pathway II indicated by “II” in Fig. 6.4a). The results for $\overline{C}_{\text{opt}}$ as well as $\overline{C}_{\text{LCPL}}$ and $\overline{C}_{\text{RCPL}}$ are shown in Fig. 6.4b as a function of the ROI center position, and the optimal far-field polarization parameters $\hat{I}_{1,\text{opt}}$ and φ_{opt} are depicted in Fig. 6.4c. For the first ROI with its center at $(0, 0, 70)$ nm the far-field polarizations for $\overline{C}_{\max}$ and $\overline{C}_{\min}$ are equal to LCPL and RCPL, respectively, with $\hat{I}_{1,\max}(\omega) = 1/2$ and $\varphi_{\max}(\omega) = \pi/2$ as well as $\hat{I}_{1,\min}(\omega) = 1/2$ and $\varphi_{\min}(\omega) = -\pi/2$. This can be explained by the symmetry of the nanostructure with respect to $\mathbf{e}_k$ as well as by the position and the symmetry properties of the ROI. In Sect. 6.3, it was shown that, in general, for a C_{4v}-symmetric nanostructure with the principal axis parallel to $\mathbf{e}_k$ the parameters $\overline{C}_{S_1}$, $\overline{C}_{S_2}$, and $\overline{C}_{S_\text{p}}$ of a ROI are simultaneously zero if the shape of the ROI is also C_{4v}-symmetric with identical principal axis and mirror-symmetry planes. Since both the sphere and the first ROI fulfill these symmetry conditions, $\overline{C}_{S_1} = \overline{C}_{S_2} = \overline{C}_{S_\text{p}} = 0$ and therefore the optimal far-field polarization is CPL at this ROI position. In contrast to the first ROI, the subsequent ROIs along pathways I and II do not share their principle axis with the nanostructure. Nevertheless, they still have mirror symmetry with the yz plane, i.e., the mirror-symmetry plane of the nanostructure parallel to $\mathbf{e}_2$ and $\mathbf{e}_k$. This also leads to vanishing parameters $\overline{C}_{S_1}$ and $\overline{C}_{S_2}$, but parameter $\overline{C}_{S_\text{p}}$ is non-zero and thus the optimal far-field polarizations for these ROIs are different from CPL (see Sect. 6.3). Note that $\overline{C}_{S_1}$ and $\overline{C}_{S_2}$ would also vanish if the ROIs had mirror symmetry with respect to the xz plane, i.e., the mirror-symmetry plane of the nanostructure parallel to $\mathbf{e}_1$ and $\mathbf{e}_k$. In

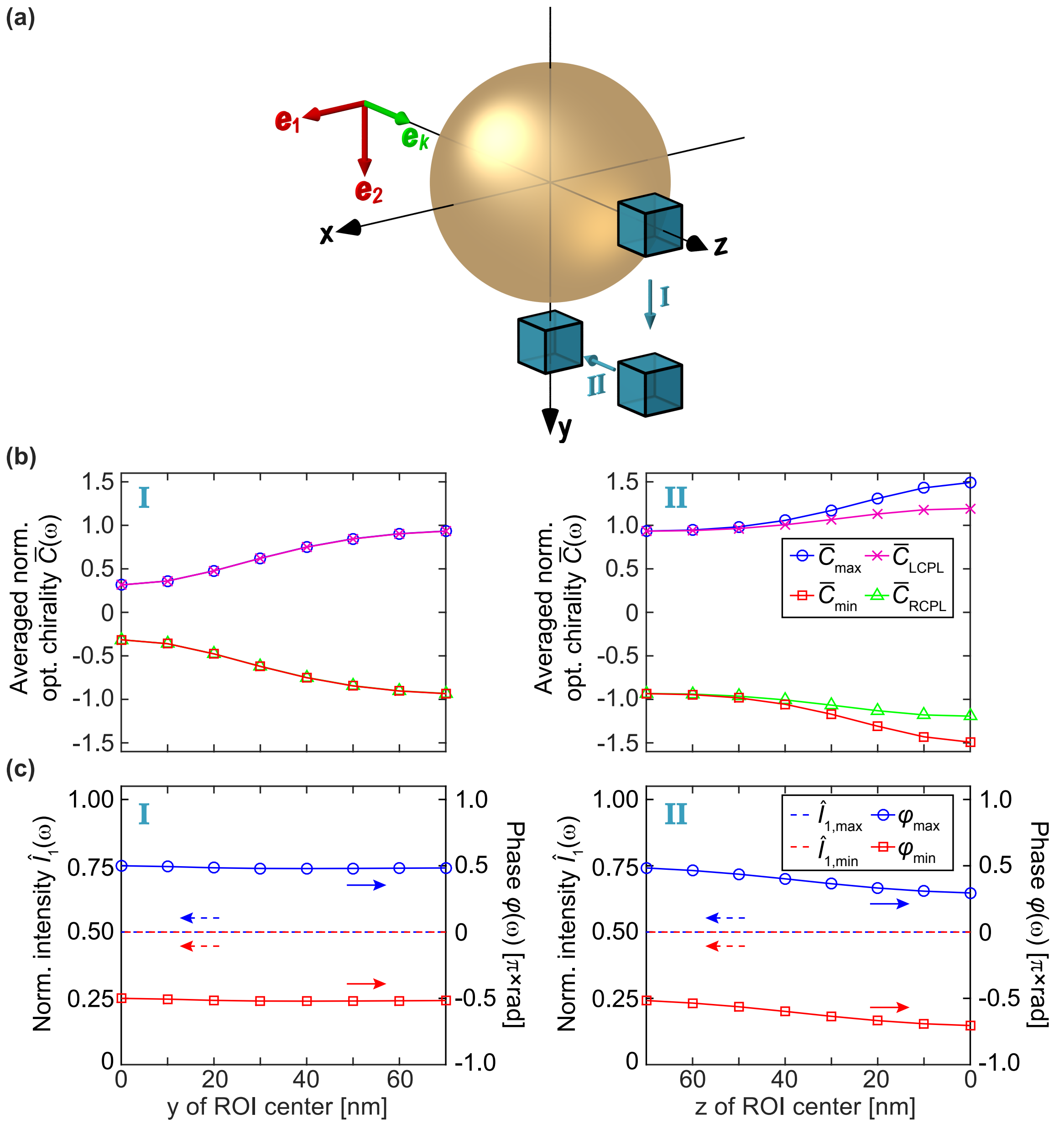

Figure 6.4: First structure for optical chirality control. (a) Different cubic regions of interest (ROIs, blue boxes, 20 nm edge length) are investigated in the vicinity of a gold sphere with a radius of 50 nm. The external light propagates in positive z direction along its normalized wave vector $\mathbf{e}_k$ (green arrow). Its two orthogonal far-field polarization components 1 and 2 are parallel to the x axis along unit vector $\mathbf{e}_1$ and to the y axis along $\mathbf{e}_2$, respectively (red arrows). The ROI positions are scanned in steps of 10 nm along the y axis (pathway I) as well as along the z axis (pathway II). (b) Normalized optical chirality values $\overline{C}_{\text{max}}$ (blue circles), $\overline{C}_{\text{min}}$ (red squares), $\overline{C}_{\text{LCPL}}$ (pink crosses), and $\overline{C}_{\text{RCPL}}$ (green triangles) as a function of the ROI center position at the resonance frequency $\omega_R = 3.65$ rad/fs of the sphere. (c) Far-field polarization for maximum (blue) and minimum optical chirality (red) defined by the normalized intensities $\hat{I}_{1,\text{max}}$ and $\hat{I}_{1,\text{min}}$ (dashed lines) as well as the relative phases φ_{max} and φ_{min} (solid lines with circles, squares) as a function of the ROI center position. For all ROIs both $\hat{I}_{1,\text{max}}$ and $\hat{I}_{1,\text{min}}$ remain constant at 1/2. Figure taken from Ref. [4]. © (2017) American Chemical Society.

the case of $\overline{C}_{S_1} = \overline{C}_{S_2} = 0$, $\overline{C}_{\max}$ and $\overline{C}_{\min}$ as well as $\overline{C}_{\text{LCPL}}$ and $\overline{C}_{\text{RCPL}}$ differ only in their sign according to Eqs. (6.17) and (6.18). Therefore, it is sufficient to discuss the relation between $\overline{C}_{\max}$ and $\overline{C}_{\text{LCPL}}$ for all ROIs along both pathways.

We observe that, for the first ROI, $\overline{C}_{\max}$ is lower than +1, the normalized optical chirality value for LCPL in free space $\hat{C}^{\text{free}}_{\text{LCPL}}$. For the subsequent ROIs along pathway I, the values for $\overline{C}_{\max}$ rise up from 0.32 to 0.94, but the difference $\left(\overline{C}_{\max} - \overline{C}_{\text{LCPL}}\right)$ increases only up to about 10^{-3} and the optimal far-field polarization is only slightly different from LCPL. For the ROIs along pathway II, however, a further rise of $\overline{C}_{\max}$ up to 1.5 is observed, significantly larger than $\hat{C}^{\text{free}}_{\text{LCPL}}$. Simultaneously, this value also exceeds $\overline{C}_{\text{LCPL}}$ by 0.3, indicating that optical chirality can be increased significantly with respect to circular input polarization. Along pathways I and II the optimal far-field polarization changes from LCPL to more and more elliptically polarized light. This is achieved by a variation of the relative phase $\varphi_{\max}$, whereas the intensity $\hat{I}_{1,\max}$ remains constant at 1/2. This can be explained by considering Eq. (6.15): Due to the vanishing parameters $\overline{C}_{S_1}$ and $\overline{C}_{S_2}$, the intensity $\hat{I}_{1,\max}$ has to be 1/2 for each ROI. Note that the intensity $\hat{I}_{1,\min}$ is constant at 1/2 for the same reason. In contrast to the parameters $\overline{C}_{S_1}$ and $\overline{C}_{S_2}$, parameters $\overline{C}_{S_{\text{p}}}$ and $\overline{C}_{S_{\text{m}}}$ vary along pathways I and II such that the relative phase $\varphi_{\max}$ decreases from $\pi/2$ to about 0.3π. According to Eq. (6.32), the relative phase $\varphi_{\min}$ shows the same behavior as $\varphi_{\max}$ with a constant phase offset of π.

6.4.3 Chiral Nanostructure Assembly

In the preceding subsection, the optical chirality enhancement was demonstrated for a single frequency. In general, the far-field polarizations required for optimum local optical chirality can vary for different frequencies. This variation is especially strong in more complex nanostructure assemblies with several resonance frequencies and reduced symmetry. This effect is illustrated on a nanostructure consisting of six single gold spheres with a radius of 70 nm each, arranged in a chiral configuration (Fig. 6.5a). The structure is composed of two L shapes, each of which contains three gold spheres within the same xy plane at $z = +80$ nm for the upper and $z = -80$ nm for the lower L shape, respectively. The gap between the neighboring spheres is 20 nm in x, y, and z direction such that the near fields of the single spheres are coupled. The upper L shape is directly above the lower L shape and rotated by $\pi/2$ with respect to the z axis. Thus, the nanostructure is left-handed with respect to $\mathbf{e}_k$. Note that from a geometrical point of view, the structure is achiral itself, but it can be classified as chiral under the given illumination geometry. The response functions of the nanostructure are determined in the same way as for the single sphere of Subsect. 6.4.2, but now calculated for 16 equidistant frequencies ω in a range of 2.28 to 3.80 rad/fs. As a first ROI (ROI1), a cube with an edge length of 48 nm is chosen whose center is located at $(x = -80, y = 0, z = -80)$ nm, i.e., exactly between the centers of two spheres of the lower L shape (blue box in Fig. 6.5a). Points of the ROI that are positioned within the spheres or on their surfaces are omitted in the calculations of the averaged optical chirality.

The resulting chirality values $\overline{C}_{\max}$ and $\overline{C}_{\min}$ as well as $\overline{C}_{\text{LCPL}}$ and $\overline{C}_{\text{RCPL}}$ are shown in Fig. 6.5b. The maximum optical chirality $\overline{C}_{\max}$ rises up to more than a factor of 4 for low frequencies, then drops down at about 2.8 rad/fs and increases again followed by a decay

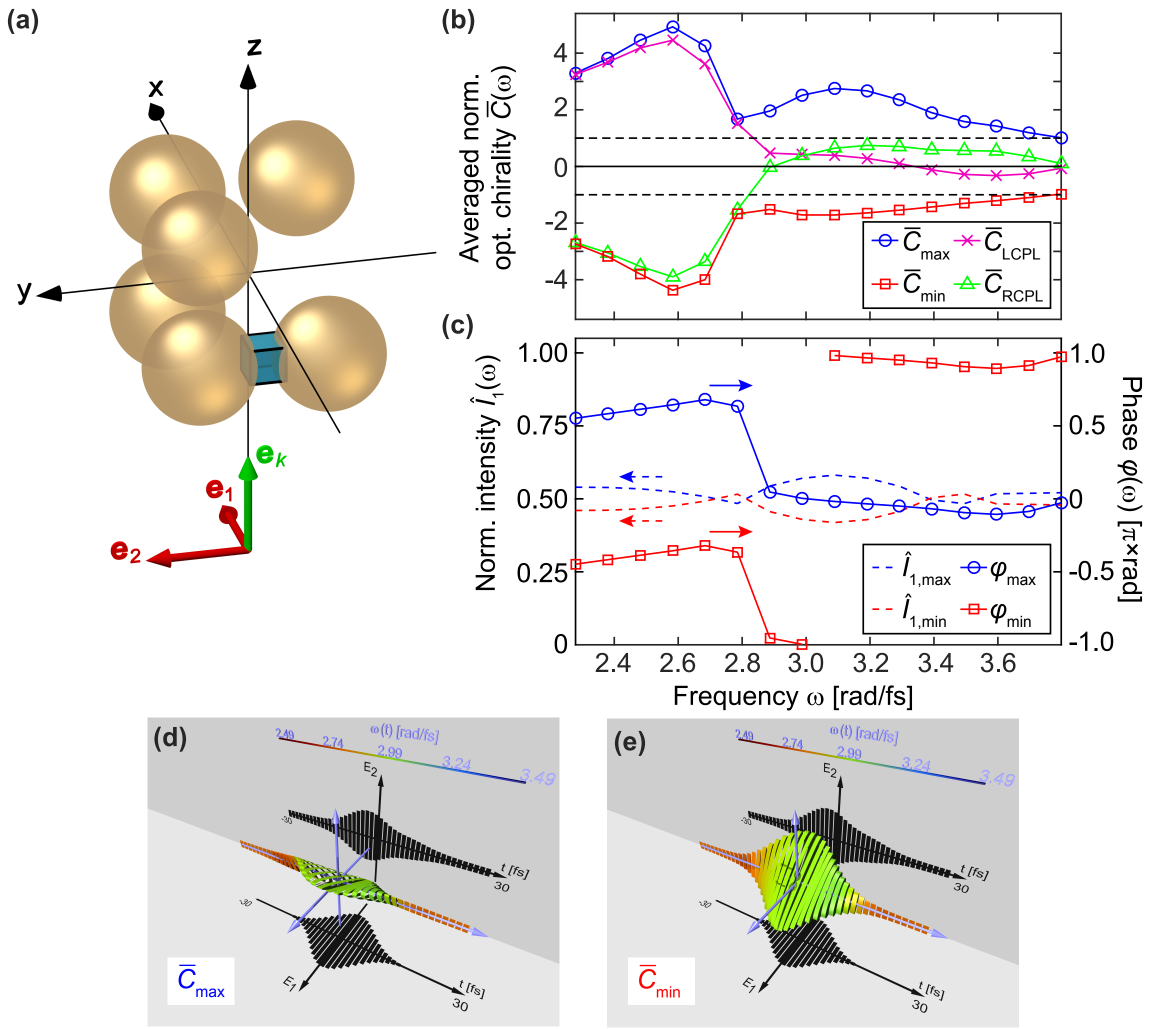

Figure 6.5: Second structure for optical chirality control. (a) Nanostructure composed of two twisted L shapes, each of which contains three gold spheres within the same xy planes. The radius of the spheres is 70 nm and the gap between the neighboring spheres in x, y, and z direction is 20 nm. The external light propagates in positive z direction along its normalized wave vector $\mathbf{e}_k$ (green arrow). Its far-field polarization components 1 and 2 are parallel to the x axis along unit vector $\mathbf{e}_1$ and parallel to the y axis along $\mathbf{e}_2$, respectively (red arrows). The ROI (ROI1, blue box) is a cube with an edge length of 48 nm and located between two spheres of the lower L shape. (b) Normalized optical chirality values $\overline{C}_{\mathrm{max}}$ (blue circles), $\overline{C}_{\mathrm{min}}$ (red squares), $\overline{C}_{\mathrm{LCPL}}$ (pink crosses), and $\overline{C}_{\mathrm{RCPL}}$ (green triangles) as a function of the angular frequency ω. The black dashed lines show the values for $\hat{C}^{\mathrm{free}}_{\mathrm{CPL}} = \pm 1$. (c) Far-field polarization for maximum (blue) and minimum optical chirality (red) defined by the normalized intensities $\hat{I}_{1,\mathrm{max}}$ and $\hat{I}_{1,\mathrm{min}}$ (dashed lines) as well as the relative phases φ_{max} and φ_{min} (solid lines with circles, squares) as a function of ω. (d, e) Examples for polarization-shaped laser pulses in the time domain leading to $\overline{C}_{\mathrm{max}}$ (d) and $\overline{C}_{\mathrm{min}}$ (e) within ROI1. The temporal polarization states are shown in quasi-three-dimensional representations as cylinders with corresponding orientations and ellipticities. The amplitudes of the electric far-field components 1 and 2 are indicated by shadows. The momentary frequency $\omega(t)$ is made visible by means of the color. Zero padding in the frequency domain is used to obtain a smoother behavior in the time domain. Figure taken from Ref. [4]. © (2017) American Chemical Society.

for higher frequencies. Compared to the chirality values obtained for CPL the values for $\overline{C}_{\mathrm{max}}$ are slightly higher in the low-frequency range and significantly enhanced in the high-frequency range. Moreover, $\overline{C}_{\mathrm{max}}$ exceeds +1, the chirality value of $\hat{C}^{\mathrm{free}}_{\mathrm{LCPL}}$, for every frequency component. In contrast to this, $\overline{C}_{\mathrm{LCPL}}$ as well as $\overline{C}_{\mathrm{RCPL}}$ are well below +1 in the high-frequency range. Hence, for this spectral range the optical chirality in ROI1 is enhanced with respect to free space by using the optimal far-field polarization, whereas for CPL it would be considerably reduced to values $< +1$. It is noteworthy that both $\overline{C}_{\mathrm{LCPL}}$ and $\overline{C}_{\mathrm{RCPL}}$ change their sign for higher frequencies. If chiral molecules were located in the ROI, chiroptical effects arising from the light-matter interaction, e.g., handedness-dependent absorption, would also have opposite sign for high and low frequencies. As opposed to this, the optimal chirality values lead to either positive or negative $\overline{C}$ values throughout all frequencies and thus, a mutually opposite behavior of the chiroptical effects would be prevented. Compared to $\overline{C}_{\mathrm{max}}$, the values for $\overline{C}_{\mathrm{min}}$ are similar, but have the opposite sign. However, since $\overline{C}_{S_1} \neq 0$ and $\overline{C}_{S_2} \neq 0$ as well as $\overline{C}_{S_1} \neq -\overline{C}_{S_2}$, the magnitudes of $\overline{C}_{\mathrm{max}}$ and $\overline{C}_{\mathrm{min}}$ are slightly different according to Eq. (6.17). For the same reason, $|\overline{C}_{\mathrm{LCPL}}| \neq |\overline{C}_{\mathrm{RCPL}}|$ according to Eq. (6.18). This results from the reduced symmetry of the nanostructure and the position of the ROI. Since there is no plane of mirror symmetry parallel to $\mathbf{e}_k$, the response functions of far-field polarization components 1 and 2 cannot be expressed by each other and thus, the parameters $\overline{C}_{S_1}$ and $\overline{C}_{S_2}$ are not related as they were for the single sphere from Subsect. 6.4.2.

The optimal far-field polarizations are depicted in Fig. 6.5c as a function of frequency. It is obvious that the far-field polarization for $\overline{C}_{\mathrm{max}}$ depends on ω and is different from circularly polarized light. Both, the normalized intensity $\hat{I}_{1,\mathrm{max}}$ and the relative phase φ_{max} vary for different frequencies. In the low-frequency range the external polarization is elliptical with intensities slightly larger than 1/2 and relative phases near $\pi/2$, i.e., close to LCPL. On the other hand, due to a strong decrease of the relative phase by roughly $\pi/2$ within the frequency region at about 2.8 rad/fs, the values of φ_{max} are near zero in the high-frequency range, and therefore close to the relative phase of linear polarization. The behavior of $\hat{I}_{1,\mathrm{min}}$ is symmetric to $\hat{I}_{1,\mathrm{max}}$ with respect to $\hat{I}_1 = 1/2$ (confer Eq. (6.24)) and the behavior of φ_{min} connected to that of φ_{max} by a phase offset of π (confer Eq. (6.32)). Thus, the present example illustrates that for optimal local optical chirality far-field polarizations different from circular and linear are required.

If one wants to fulfill the optimal chirality condition simultaneously for all frequencies, this requires tuning of the external polarization state independently throughout the optical spectrum. Such a technique is available via femtosecond laser polarization pulse shaping that was developed first for two independent degrees of freedom (the spectral phases of the two transverse polarization components) [176–179]. Recently it has become possible to manipulate all four external degrees of freedom (amplitude and phase for both polarization components separately) [180–185]. The latter technique is also called vector-field pulse shaping. The temporal electric fields of the two pulses leading to maximum and minimum optical chirality are shown in Figs. 6.5d and 6.5e, respectively. Here a Gaussian spectrum is utilized with center frequency $\omega_0 = 2.99$ rad/fs and a bandwidth-limited pulse duration of 10 fs. Since the absolute phases φ_1 and φ_2 of the far-field polarization components are not determined by Eqs. (6.15) and (6.16), one of these can be chosen arbitrarily. This means that for the polarization-shaping only three degrees of freedom — $I_1(\omega)$, $I_2(\omega)$ and either $\varphi_1(\omega)$ or $\varphi_2(\omega)$ — are necessary to enhance the local optical chirality. The additional fourth degree of freedom, $\varphi_1(\omega)$ or $\varphi_2(\omega)$, can be used, e.g., for the manipulation of the temporal evolution of the local near fields, for the generation of spectroscopic pulse sequences or for pulse compression [171]. For the depicted pulses, $\varphi_1(\omega)$ is set to zero and thus, $\varphi(\omega) = \varphi_2(\omega)$. Both the pulse for $\overline{C}_{\text{max}}$ and the one for $\overline{C}_{\text{min}}$ are clearly different from circular and linear polarization and vary with time.

The calculation of optical chirality enhancement is repeated for a second ROI (ROI2) of identical size located at $(x = 0, y = +80, z = +80)$ nm, i.e., directly between the centers of the two spheres of the upper L shape (blue box in Fig. 6.6a). Analogously to ROI1, points of ROI2 that are positioned within the spheres or on their surfaces are omitted in the calculations. The chirality values obtained for optimal far-field polarization and CPL are shown in Fig. 6.6b as a function of ω. Similarly to ROI1, the optimal chirality values are significantly enhanced in the complete frequency range compared to the values obtained for CPL as input polarization. Moreover, for $\omega < 3.39$ rad/fs, the magnitudes of $\overline{C}_{\text{max}}$ and $\overline{C}_{\text{min}}$ are up to two times higher than those obtained for ROI1 and therefore a stronger enhancement with respect to the optical chirality for CPL in free space ($|\hat{C}^{\text{free}}_{\text{CPL}}| = 1$) is achieved. Only for $\omega > 3.39$ rad/fs, the magnitudes are lower than those of ROI1 and decrease below 1. As above mentioned, the slightly lower magnitudes of $\overline{C}_{\text{min}}$ compared to $\overline{C}_{\text{max}}$ can be explained by the reduced symmetry of the nanostructure and the position of the ROI.

The corresponding optimal far-field polarizations are depicted in Fig. 6.6c and reveal a clearly different behavior in the investigated frequency range compared to those of ROI1. This is due to the different properties of the response functions at both ROI positions. In contrast to ROI1, the normalized intensity $\hat{I}_{1,\text{max}}$ of ROI2 is closer to 1/2 and for low as well as for high frequencies $< 1/2$. The relative phase φ_{max} continuously increases from about 0.6π in the low-frequency range to values near π for high frequencies, whereas for φ_{max} of ROI1 a strong decrease of roughly $\pi/2$ was observed within the frequency range at about 2.8 rad/fs. According to Eqs. (6.24) and (6.32), $\hat{I}_{1,\text{min}}$ is symmetric to $\hat{I}_{1,\text{max}}$ with respect to $\hat{I}_1 = 1/2$ and the behavior of φ_{min} is identical to that of φ_{max} with a phase offset of π.

The temporal electric fields of two pulses that lead to maximum and minimum optical chirality are shown in Figs. 6.6d and 6.6e, respectively. For the calculations of the electric fields, the same Gaussian spectrum is used as for the optimal pulses of ROI1 with center frequency $\omega_0 = 2.99$ rad/fs and a bandwidth-limited pulse duration of 10 fs. The phase of far-field polarization component 1, $\varphi_1(\omega)$, is set to zero and thus, $\varphi(\omega) = \varphi_2(\omega)$. In contrast to the pulses of ROI1, the two pulses of ROI2 are nearly linearly polarized in the time domain and thus differ significantly from the temporal polarization of the pulses of ROI1. This is explained by the behavior of the optimal external polarization parameters within the spectral overlap with the Gaussian laser spectrum. Since for the highest intensities of the Gaussian spectrum around the center frequency the optimal external polarization is close to linear, the temporal polarization of the pulses in the time domain is nearly linear as well. As opposed to this, the optimal far-field polarizations for ROI1 are partially linear and, in addition, elliptical within the high-intensity range

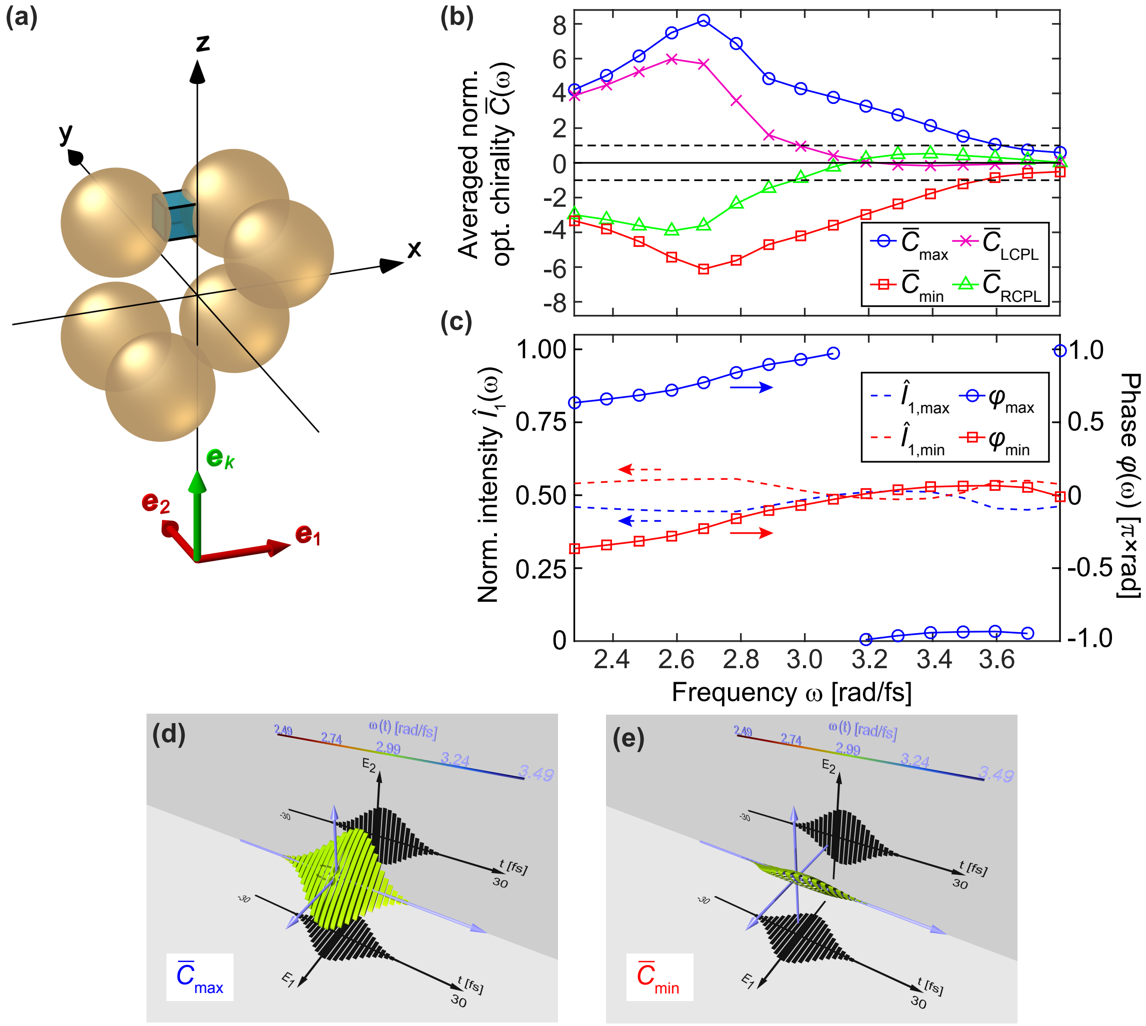

Figure 6.6: Example of optical chirality control for a second ROI in the vicinity of the chiral nanostructure. (a) Chiral nanostructure assembly identical to that shown in Fig. 6.5a. The external light propagates in positive z direction along its normalized wave vector $\mathbf{e}_k$ (green arrow). Its far-field polarization components 1 and 2 are parallel to the x axis along unit vector $\mathbf{e}_1$ and parallel to the y axis along $\mathbf{e}_2$, respectively (red arrows). The ROI (blue box, ROI2) is a cube with an edge length of 48 nm and located between two spheres of the upper L shape. (b) Normalized optical chirality values $\overline{C}_{\mathrm{max}}$ (blue circles), $\overline{C}_{\mathrm{min}}$ (red squares), $\overline{C}_{\mathrm{LCPL}}$ (pink crosses), and $\overline{C}_{\mathrm{RCPL}}$ (green triangles) as a function of the angular frequency ω. The black dashed lines show the values for $\hat{C}^{\mathrm{free}}_{\mathrm{CPL}} = \pm 1$. (c) Far-field polarization for maximum (blue) and minimum optical chirality (red) defined by the normalized intensities $\hat{I}_{1,\mathrm{max}}$ and $\hat{I}_{1,\mathrm{min}}$ (lines) as well as the relative phases φ_{max} and φ_{min} (dashed lines with circles, squares) as a function of ω. (d, e) Examples for polarization-shaped laser pulses in the time domain leading to $\overline{C}_{\mathrm{max}}$ (d) and $\overline{C}_{\mathrm{min}}$ (e) within the ROI. The temporal polarization states are shown in quasi-three-dimensional representations as cylinders with corresponding orientations and ellipticities, and the amplitudes of the electric far-field components 1 and 2 are indicated by shadows. The momentary frequency $\omega(t)$ is made visible by means of the color. Zero padding in the frequency domain is used to obtain a smoother behavior in the time domain. Figure taken from Ref. [4]. © (2017) American Chemical Society.

of the Gaussian spectrum. Thus, the corresponding pulses in the time domain reveal a more complex behavior.

6.5 Electric and Magnetic Near-Field Evolution

In the previous sections, it was demonstrated that the local optical chirality in the vicinity of plasmonic nanostructures can be enhanced by far-field polarizations different from CPL. In this section, the control mechanism is illustrated. In general, considering Eq. (6.2), the local optical chirality is maximal (minimal) if the scalar product of $\mathbf{E}^*_{\text{loc}}$ and $\mathbf{H}_{\text{loc}}$, respectively, contains a minimal (maximal) imaginary part. This is the case if the amplitudes of the components $\mathrm{E}_{\text{loc},q}$ and $\mathrm{H}_{\text{loc},q}$ with $q = \{x, y, z\}$ are maximal and the corresponding phases between the components are shifted by $\pm\pi/2$, due to the complex conjugation of the electric near field in Eq. (6.2). This general finding is now exemplified by means of the exemplary temporal field evolutions shown in Fig. 6.7.

For light in free space, circular polarization leads to extremal optical chirality. Figure 6.7a[1] shows the temporal evolution of the electric (blue) and magnetic (red) field vectors at position $(x, y, z) = (0, 0, 0)$ nm without any nanostructure for LCPL propagating along the z axis with $\omega = 2.89$ rad/fs. The blue and the red little spheres denote the momentary tips of the field vectors with respect to the chosen position, and the blue and red solid lines illustrate the temporal traces. In addition, the projections onto the xy, xz, and yz planes facilitate the investigation of individual polarization components. The vectors of both fields are always perpendicular to each other as expected for a transverse wave and rotate around $(0, 0, 0)$ nm on a circle in the xy plane. Since the oscillations of the components E_x and H_x as well as E_y and H_y have a phase shift of $\pi/2$ with respect to each other, maximal optical chirality is achieved. For any given intensity, circular polarization is thus optimal.

In the vicinity of plasmonic nanostructures, the situation is more complex, because the associated light modes do not constitute propagating transverse waves, and thus all three polarization components are available [186]. Increased optical chirality is possible via near-field enhancement of the amplitudes. For optimum chirality, however, one also has to fulfill the phase requirement. If circular far-field polarization is employed, near-field enhancement occurs, but the phases do not necessarily fulfill the optimal criterion. This is seen in Fig. 6.7b[2] which shows the temporal near-field evolution of the chiral nanostructure assembly from Subsect. 6.4.3 at position $(6, 78, 66)$ nm and $\omega = 2.89$ rad/fs obtained for LCPL as input polarization. The illumination geometry is identical to that in Fig. 6.6a. The chosen position is located within ROI2 from Subsect. 6.4.3, i.e., between two spheres of the upper L-shape. The snapshot indicates a momentary maximal electric field (blue) along the x direction (compare field projection in the xy plane). At this instant, the magnetic field (red) also reaches its (albeit smaller) maximum amplitude along x. Thus the two fields are in phase and the $\pi/2$ optimality condition is not fulfilled.

The corresponding movies are provided by ACS Photonics:

[1] `http://pubs.acs.org/doi/suppl/10.1021/acsphotonics.6b00887/suppl_file/ph6b00887_si_002.avi`, © (2017) American Chemical Society.

[2] `http://pubs.acs.org/doi/suppl/10.1021/acsphotonics.6b00887/suppl_file/ph6b00887_si_003.avi`, © (2017) American Chemical Society.

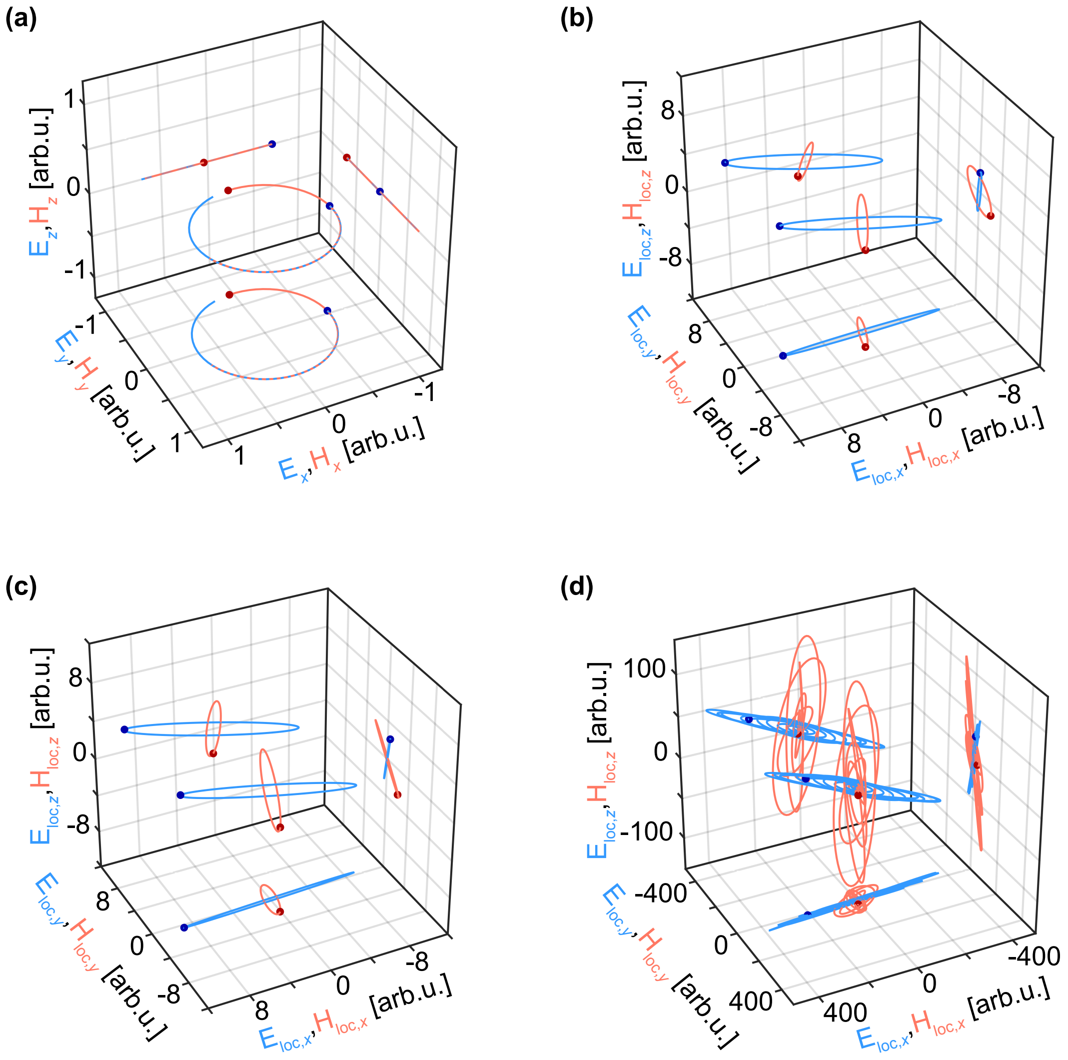

Figure 6.7: Snapshots of movies showing the temporal evolution of electric (blue) and magnetic (red) fields obtained for different far-field polarizations (links to the movie files are given in the footnotes of the running text). The little spheres indicate the tips of the momentary field vectors and the solid lines their temporal traces. (a) Electric and magnetic field of LCPL in free space without a nanostructure at position $(0, 0, 0)$ nm and $\omega = 2.89$ rad/fs. (b) Temporal near fields at $(6, 78, 66)$ nm in the vicinity of the chiral nanostructure assembly from Subsect. 6.4.3 for $\omega = 2.89$ rad/fs and LCPL as input polarization. The electric and magnetic field components parallel to the x axis oscillate nearly in phase. (c) Temporal near fields at the same position and frequency as in (b) obtained for the optimal far-field polarization leading to $C_{\max}$. The phases of the electric and magnetic field components parallel to the x axis are shifted by roughly $\pi/2$. (d) Temporal near fields at the same position as in (b) under excitation with the optimal far-field pulse leading to $C_{\max}$ for the frequency range from 2.28 to 3.80 rad/fs. Figure taken from Ref. [4]. © (2017) American Chemical Society.

On the other hand, for optimal far-field excitation, the corresponding local fields shown in Fig. 6.7c[3] behave differently. Now the snapshot reveals that while the electric field is maximal, the magnetic field passes through zero (along the x direction) indicating a $\pi/2$ phase shift. Analogous analysis can be carried out for the other polarization directions, but it has to be kept in mind that the optimization reaches the global optimum as resulting from a sum (due to the scalar product) of three field-component multiplications. For the chosen position, the contributions to the local optical chirality of the local field components along the y and z directions are negligible for both LCPL and the optimal far-field polarization, because the amplitude of $\mathrm{E}_{\mathrm{loc},y}$ is very small and the phase between $\mathrm{E}_{\mathrm{loc},z}$ and $\mathrm{H}_{\mathrm{loc},z}$ is shifted by π. Thus it may be most important to fulfill the phase condition for that component with the highest amplitude product.

Figure 6.7d[4] shows the temporal electric and magnetic fields that are obtained for an optimal polarization-shaped laser pulse as input and lead to maximum local optical chirality values in the frequency range from 2.28 to 3.80 rad/fs at this position. Since the optimal far-field polarizations differ with frequency and therefore consist of different elliptical polarization states in the frequency domain, the behavior in the time domain is much more complex after Fourier transformation. In particular, the orientation of the temporal ellipses strongly changes over time.

6.6 Optimization of the Local Dissymmetry Factor

Up to here, the optimization of the local optical chirality $C(\mathbf{r}, \omega)$ has been discussed. The optical chirality is proportional to the absolute chirality-induced signal in a spectroscopy experiment, i.e., C is responsible for the absolute signal difference between measurements of systems with opposite chirality according to Eq. (6.1). In some cases, one may be interested in the relative, rather than the absolute, signal difference, in which case one has to normalize the obtained signal difference with respect to the absolute (chirality-independent) absorption signal. The resulting quantity, often called dissymmetry factor g, is responsible for the signal contrast. Using CPL for excitation, the dissymetry factor is given by [124]

$$g_{\mathrm{CPL}} = \frac{A_{\mathrm{LCPL}} - A_{\mathrm{RCPL}}}{\frac{1}{2}\left(A_{\mathrm{LCPL}} + A_{\mathrm{RCPL}}\right)} \tag{6.46}$$

with the absorption of LCPL A_{LCPL} and that of RCPL A_{RCPL}. Tang and Cohen defined a generalized dissymmetry factor g_{TC} including pairs of arbitrary enantiomorphic electromagnetic fields that is expressed via [124, 127]

$$g_{\mathrm{TC}} = g_{\mathrm{CPL}} \frac{cC}{2U_e\omega}\,, \tag{6.47}$$

wherein g_{CPL} is the dissymmetry factor from Eq. (6.46), i.e., the dissymmetry factor obtained for CPL in free space. Considering Eq. (6.47) it is obvious that for an opti-

---

The corresponding movies are provided by ACS Photonics:

[3] http://pubs.acs.org/doi/suppl/10.1021/acsphotonics.6b00887/suppl_file/ph6b00887_si_004.avi, © (2017) American Chemical Society.

[4] http://pubs.acs.org/doi/suppl/10.1021/acsphotonics.6b00887/suppl_file/ph6b00887_si_005.avi, © (2017) American Chemical Society.

mization of g_{TC}, the fraction C/U_e is important instead of the optimization of C alone such that $|g_{\mathrm{TC}}/g_{\mathrm{CPL}}| > 1$. Since an enhanced local optical chirality $C(\mathbf{r}, \omega)$ is often accompanied by an increased electric field amplitude $|\mathbf{E}_{\mathrm{loc}}(\mathbf{r}, \omega)|$, the corresponding local electric energy density

$$U_e\left(\mathbf{r}, \omega\right) = \frac{\epsilon_0}{4} |\mathbf{E}_{\mathrm{loc}}(\mathbf{r}, \omega)|^2 \tag{6.48}$$

is enhanced mostly as well. Thus, the optimal far-field polarization for $C(\mathbf{r}, \omega)$ does usually not coincide with that for $g_{\mathrm{TC}}(\mathbf{r}, \omega)$. Nevertheless, analogously to the optimization of $C(\mathbf{r}, \omega)$ it should be possible to optimize the local normalized dissymmetry factor $\hat{g}_{\mathrm{TC}}(\mathbf{r}, \omega) = g_{\mathrm{TC}}(\mathbf{r}, \omega)/g_{\mathrm{CPL}}$ by means of the far-field polarization. One has to consider in this case, however, that increasing $\hat{g}_{\mathrm{TC}}$ can be carried out by significantly decreasing U_e such that in effect the overall absorption is strongly reduced and small signals result. For practical reasons, therefore, one has to decide carefully whether the absolute or the relative signal is the relevant quantity. Hence, for applications of molecular chiral sensing or spectroscopy, one should analyze in addition signal-to-noise ratios to find "optimal" external driving fields, and very likely one should be interested in the right balance between absolute chiral signal strength, i.e., optimization of C, and contrast, i.e., optimization of $\hat{g}_{\mathrm{TC}}$.

It has to be mentioned that in Eq. (6.47) the magnetic energy density U_b is neglected. A more precise equation was introduced by Choi and Cho via [125]

$$g_{\mathrm{CC}} = g_{\mathrm{CPL}} \frac{cC}{2\omega\left(U_e + \gamma U_b\right)}\,, \tag{6.49}$$

wherein the parameter $\gamma \propto \chi''/\alpha''$ depends on the investigated specimen and is typically in the range $\approx 10^{-6}$–10^{-4} [125]. Hence, Eq. (6.47) is only valid in the case that $U_e \gg \gamma U_b$ or, independently from the specimen, $U_e \gg 10^{-2} U_b$. This leads to a limitation of the maximal/minimal value of the generalized dissymmetry factor and should be taken into account in an analytic derivation for the optimization of $\hat{g}_{\mathrm{TC}}$.

In this section, the definitions of the dissymmetry factor are based on the electric and magnetic dipole approximation of matter. However, if the electromagnetic fields vary strongly across chiral molecules located in the vicinity of a nanostructure, higher multipoles might be included in the calculation of g [187]. Nevertheless, an optimization of the chiral response in the near field of nanostructures via tuning the far-field polarization should be possible.

6.7 Summary and Outlook

In this chapter, it was investigated in theory, how the local optical chirality enhancement in the near field of plasmonic nanostructures can be controlled by tuning the far-field polarization of the external light field. An analytic expression for the two optimal far-field polarizations that lead to highest positive and negative local optical chirality was derived as a function of the local position $\mathbf{r}$ and frequency ω. The ellipticities of the two optimal far-field polarizations differ only in their sign, i.e., in their direction of rotation in the time domain, and the principal axes of their ellipses are rotated by $\pm\pi/2$. The handedness of optimal local optical chirality can be switched by switching the optimal far-field polarization. It was demonstrated on the basis of numerical simulations for two specific nanostructure assemblies that the local optical chirality can be improved significantly in comparison with the optical chirality of circularly polarized light in free space. Optimal enhancement was achieved by using far-field polarizations different from linear or circular. Femtosecond polarization pulse shaping can be employed in order to coherently control the local optical chirality simultaneously over a continuous frequency range. Moreover, it was shown that the symmetry properties of nanostructures can be exploited to determine the optimal far-field polarization. For a nanostructure that is at least C_{4v}-symmetric with respect to the propagation direction of the external light, circularly polarized light is the optimal far-field polarization to enhance optical chirality in near-field regions whose shapes are C_{4v}-symmetric as well, with the same principle axis and mirror-symmetry planes like those of the nanostructure. Finally, it was discussed, how the local dissymmetry factor g — an entity that quantifies the relative chirality-induced difference in absorption — can be improved by means of the far-field polarization.

In conclusion, tuning the far-field polarization can be utilized to control local optical chirality for any given nanostucture geometry. This should enable enhanced chirally specific interactions of light with molecular and other quantum systems in the vicinity of specially-designed nanostructures. Applications are envisioned in chiral sensing of adsorbed molecules, time-resolved chirality-sensitive spectroscopy, and chiral quantum control. For the latter two cases it is of relevance that the time structure of the optimal field can still be varied by means of the spectral phase of one polarization component, while nevertheless retaining the optimality conditions derived above that depend on the relative phase only.

7 Summary

In recent years, the interaction of light with subwavelength structures, i.e., structures that are smaller than the optical wavelength, became more and more interesting to scientific research, since it provides the opportunity to manipulate light-induced dynamics below the optical diffraction limit. Specifically designed nanomaterials can be utilized to tailor the temporal evolution of electromagnetic fields at the nanoscale. For the investigation of strongly localized processes, it is essential to resolve both their spatial and their temporal behavior. This is often very challenging, since the spatial resolution of conventional optical spectroscopy is limited due to optical diffraction. The aim of this thesis was to study and/or control the temporal evolution of three nanostructure-induced localized light phenomena by using ultrafast laser spectroscopy with high spatial resolution.

In Chapter 4, the absorption of near-infrared light in thin-film a-Si:H solar cells was investigated. Using nanotextured instead of smooth interfaces for such devices leads to an increase of absorption from $< 20\%$ to more than 50% in the near-infrared regime. Time-resolved experiments with femtosecond laser pulses were performed to clarify the reason for this enhancement. The coherent backscattered radiation from nanotextured solar cell devices was measured as a function of the sample position and evaluated via spectral interferometry. Spatially varying resonance peaks in the recorded spectra indicated the formation of localized photonic modes within the nanotextured absorber layers. In a statistical peak analysis of the spectra, high averaged coherence lifetimes > 60 fs were obtained for the modes. In order to identify the modes separately from each other, coherent two-dimensional (2D) nanoscopy was utilized, providing a high spatial resolution < 40 nm. In a nanoscopy measurement on a modified device with an exposed nanotextured a-Si:H absorber layer, hot-spot electron emission was observed and confirmed the presence of localized modes. Fitting the local 2D nanospectra at the hot-spot positions enabled the determination of the resonance frequencies and coherence lifetimes of the modes. The obtained lifetime values varied between 50 fs and 130 fs and agreed well with the averaged lifetimes determined via the peak analysis of the coherent backscattered radiation. The high nonlinearity of the observed electron-emission process between 7 and 9 was explained with a thermionic emission model. This model allowed the calculation of the locally absorbed energy density and, with this, an estimation of the localization length of the photonic modes (≈ 1 μm). The localization could be classified by means of the estimated localization length and additional data evaluation of the backscattered spectra as strong localization — the so-called Anderson localization.

Based on the experimental results, it was concluded that the enhanced absorption of near-infrared light in thin-film silicon solar cells with nanotextured interfaces is caused by the formation of strongly localized photonic modes within the disordered absorber layers. The incoming near-infrared light is trapped in these long-living modes until absorption occurs. The understanding of this light-trapping mechanism can help to further enhance the absorption in nanotextured absorber layers. Tuning their disorder provides the opportunity to optimize absorption throughout the complete solar spectrum and therefore to improve their total efficiency. Hence, studying light localization in disordered systems can have a major impact on future designs of absorber layers and, regarding the solar cell technology, can pave the way for the development of more efficient solar-cell devices.

In Chapter 5, a novel hybridized plasmonic device was introduced and investigated in both theory and experiment. It consists of two widely separated whispering gallery mode (WGM) nanoantennas located in an elliptical plasmonic cavity. The goal was to realize a periodic long-range energy transfer between the nanoantennas. In finite-difference time-domain (FDTD) simulations, the device was first optimized with respect to strong coupling between the localized antenna modes and the spatially-extended cavity mode. The geometrical parameters of the antennas and the cavity were adjusted separately so that the $m = 0$ antenna mode and the cavity mode were resonant at 800 nm — the center wavelength of the laser pulses used in the experiments. A high spatial overlap of the modes was achieved by positioning the two antennas in the focal spots of the cavity, leading to a distance between the antenna centers of 1646 nm and thus more than twice the resonant wavelength of the modes. The spectral response of the optimized device revealed an energy splitting of the antenna and the cavity mode into three separated hybridized eigenmodes within an energy range of about 90 meV due to strong coupling. It could be well reproduced by a simple model of three coupled Lorentzian oscillators. In the time domain, an oscillatory energy transfer between both antennas with a period of 86 fs and an energy transfer efficiency of about 7% was observed for single pulse excitation. Besides strong coupling, impedance matching, i.e., similar damping of the cavity mode and the antenna modes, is necessary to achieve such a back-and-forth energy transfer over several periods. For the experiments, devices with cavities and antennas of varying size were fabricated by means of focused-ion-beam (FIB) milling. Using two stacked single-crystalline gold microplates — the upper one as substrate for the cavity walls and the lower one as substrate for the cavity floors and nanoantennas — enabled the fabrication of smooth and well-defined structures with reduced ohmic losses within the devices. Time-resolved correlation measurements were performed with high spatial and temporal resolution by using sequences of two femtosecond laser pulses for excitation and photoemission electron microscopy (PEEM) for detection. Local correlation traces at antennas in resonant devices, i.e., devices with enhanced electron emission at both antenna positions, were investigated and reconstructed by means of the coupled-oscillator model. The corresponding spectral response revealed separated peaks, confirming the formation of hybridized eigenmodes due to strong coupling. In a subsequent simulation for single-pulse excitation, one back-and-forth energy transfer between both antennas with an energy transfer efficiency of about 10% was observed.

Based on the theoretical and experimental results, it was demonstrated that in the presented plasmonic device a periodic long-range energy transfer between the two nanoantennas is possible. Furthermore, the coupled-oscillator model enables one to study in depth how specific device properties impact the temporal electric-field dynamics, i.e., the energy redistribution dynamics, within the device. This can be exploited to further optimize energy transfer efficiency of the device. Future applications are envisioned in ultrafast plasmonic nanocircuitry. Moreover, the presented device can be employed to realize efficient SPP-mediated strong coupling between widely separated quantum emitters. In this case, the quantum emitters have to be positioned close to the nanoantennas and have to couple strongly to a specific eigenmode of the device.

In Chapter 6, it was investigated in theory how the local optical chirality enhancement in the near field of plasmonic nanostructures can be optimized by tuning the far-field polarization of the incident light. An analytic expression was derived that enables the calculation of the optimal far-field polarizations, i.e., the two far-field polarizations which lead to the highest positive and negative local optical chirality, for any given nanostructure geometry. The two optimal far-field polarizations depend on the local optical response of the respective nanostructure and thus are functions of both the frequency ω and the position $\mathbf{r}$. Their ellipticities differ only in their sign, i.e., in their direction of rotation in the time domain, and the angle between their orientations, i.e., the angle between the principal axes of their ellipses, is $\pm\pi/2$. The handedness of optimal local optical chirality can be switched by switching between the optimal far-field polarizations. In numerical simulations, it was exemplarily shown for two specific nanostructure assemblies that the optimal local optical chirality can significantly exceed the optical chirality values of circularly polarized light in free space — the highest possible values in free space. The corresponding optimal far-field polarizations were different from linear and circular and varied with frequency. Using femtosecond polarization pulse shaping provides the opportunity to coherently control local optical chirality over a continuous frequency range. Furthermore, symmetry properties of nanostructures can be exploited to determine which far-field polarization is optimal. For instance, if a nanostructure is at least C_{4v}-symmetric with respect to the propagation direction of the incident light, circularly polarized light is the optimal far-field polarization to enhance optical chirality in near-field regions whose shapes are C_{4v}-symmetric as well, with the same principle axis and mirror-symmetry planes like those of the nanostructure.

The theoretical findings can have impact on future experimental studies about local optical chirality enhancement. Tuning the far-field polarization of the incident light offers a promising tool to enhance chirally specific interactions of local electromagnetic fields with molecular and other quantum systems in the vicinity of plasmonic nanostructures. The presented approach can be utilized for applications in chiral sensing of adsorbed molecules, time-resolved chirality-sensitive spectroscopy, and chiral quantum control.

In conclusion, each of the localized light phenomena that were investigated in this thesis — the enhanced local absorption of near-infrared light due to the formation of localized photonic modes, the periodic long-range energy transfer between two nanoantennas within an elliptical plasmonic cavity, and the optimization of local optical chirality enhancement by tuning the far-field polarization of the incident light — can open up new perspectives for a variety of future applications.

Zusammenfassung

In den vergangenen Jahren rückte die Wechselwirkung von Licht mit Strukturen, deren Größe kleiner als die optische Wellenlänge ist, immer mehr in den Fokus der wissenschaftlichen Forschung, da sie die Möglichkeit bietet, lichtinduzierte Dynamiken unterhalb des optischen Beugungslimits zu manipulieren. Speziell hergestellte Nanomaterialien können verwendet werden, um die zeitliche Entwicklung von elektromagnetischen Feldern auf der Nanoskala zu steuern. Für die Untersuchung von stark lokalisierten Prozessen ist es essentiell, sowohl ihr räumliches als auch ihr zeitliches Verhalten aufzulösen. Dies stellt jedoch oftmals eine große Herausforderung da, weil die räumliche Auflösung der konventionellen optischen Spektroskopie aufgrund der optischen Beugung begrenzt ist. Das Ziel dieser Dissertation war es, die zeitliche Entwicklung von drei lokalisierten Lichtphänomenen, hervorgerufen durch drei unterschiedliche nanostrukturierte Materialien, mit Hilfe von Ultrakurzzeitspektroskopie unter hoher räumlicher Auflösung zu untersuchen und/oder zu kontrollieren.

In Kapitel 4 dieser Arbeit wurde die Absorption von Nahinfrarotlicht in a-Si:H Dünnschicht-Solarzellen untersucht. Durch die Verwendung von nanotexturierten statt glatten Grenzschichten erreicht man bei solchen Solarzellen einen Anstieg der Absorption von < 20 % auf über 50% im Nahinfrarotbereich. Um der Ursache dieser Verstärkung auf den Grund zu gehen, wurden zeitaufgelöste Experimente mit Femtosekundenlaserpulsen durchgeführt. Zunächst wurde die kohärente zurückgestreute Strahlung von nanotexturierten Solarzellen in Abhängigkeit der Probenposition gemessen und mit Hilfe von spektraler Interferometrie ausgewertet. Räumlich variierende Resonanzpeaks in den aufgenommenen Spektren deuteten auf die Bildung von lokalisierten photonischen Moden innerhalb der nanotexturierten Absorberschichten hin. Über eine statistische Peak-Analyse der Spektren wurden für die Moden hohe Durchschnitts-Kohärenzlebenszeiten > 60 fs ermittelt. Um die Moden räumlich getrennt voneinander identifizieren zu können, wurde anschließend die Methode der kohärenten zweidimensionalen (2D) Nanoskopie angewandt, die eine hohe räumliche Auflösung < 40 nm ermöglichte. In einer Nanoskopie-Messung an einer modifizierten Solarzellen-Probe mit einer freiliegenden nanotexturierten a-Si:H Absorberschicht wurde eine Elektronemission beobachtet, die von räumlich begrenzten Hot Spots dominiert war und das Vorhandensein von lokalisierten Moden bestätigte. Über das Fitten der lokalen 2D Nanospektren an den Positionen der Hot Spots wurden die Resonanzfrequenzen und die Kohärenzlebenszeiten der Moden bestimmt. Die ermittelten Werte für die Lebenszeiten lagen zwischen 50 fs und 130 fs und stimmten sehr gut mit den Durchschnitts-Lebenszeiten überein, die mit Hilfe der Peak-Analyse der kohärenten zurückgestreuten Strahlung bestimmt wurden. Die ho-

he Nichtlinearität des beobachteten Elektronenemission-Prozesses (zwischen 7 und 9) wurde mit Hilfe eines Modells für thermionische Elektronenemission erklärt. Dieses Modell ermöglichte die Bestimmung der lokal absorbierten Energiedichte und damit eine Abschätzung der Lokalisierungslänge der photonischen Moden auf etwa 1 μm. Zudem konnte die Lokalisierung über die abgeschätzte Lokalisierungslänge und eine zusätzliche Datenauswertung der zurückgestreuten Spektren als starke Lokalisierung, die sogenannte Anderson-Lokalisierung, klassifiziert werden. Auf der Basis der experimentellen Ergebnisse wurde daher geschlussfolgert, dass die verstärkte Absorption von Nahinfrarotlicht in Silizium-Dünnschicht-Solarzellen mit nanotexturierten Grenzschichten durch die Bildung von stark lokalisierten photonischen Moden innerhalb der ungeordneten Absorberschichten verursacht wird. Das einfallende Nahinfrarotlicht wird in diesen langlebigen Moden gefangen und schließlich irgendwann absorbiert.

Die Erkenntnis über diesen Lichteinfang-Mechanismus kann dabei helfen, die Absorption in nanotexturierten Absorberschichten weiter zu verstärken. Das Einstellen der Absorberschicht-Unordnung bietet die Möglichkeit, die Absorption für das komplette Sonnenlichtspekrum zu optimieren und damit die Gesamteffizienz der Absorberschicht zu erhöhen. Deshalb kann die Untersuchung von Lichtlokalisation in ungeordneten Systemen einen großen Einfluss auf das zukünftige Design von Absorberschichten haben und, hinsichtlich der Solarzellen-Technologie, den Weg ebnen für die Entwicklung von effizienteren Solarzellen.

In Kaptiel 5 wurde eine neuartige plasmonische Struktur vorgestellt und sowohl in der Theorie als auch experimentell untersucht. Die Struktur besteht aus einer elliptischen Kavität, in der sich zwei räumlich getrennte whispering gallery mode (WGM) Nanoantennen befinden. Das Ziel war es nun, einen periodischen langreichweitigen Energietransfer zwischen beiden Nanoantennen zu realisieren. Zuerst wurde die Struktur mit Hilfe von finite-difference time-domain (FDTD) Simulationen darauf optimiert, eine starken Kopplung zwischen den lokalisierten Antennenmoden und der räumlich ausgedehnten Kavitätsmode zu erreichen. Die geometrischen Parameter der Antennen und der Kavität wurden getrennt voneinander so eingestellt, dass sowohl die $m = 0$ Antennenmode als auch die Kavitätsmode bei 800 nm resonant waren — der Zentralwellenlänge der Laserpulse, die in den Experimenten verwendet wurden. Ein hoher räumlicher Modenüberlapp wurde dadurch erzielt, dass die beiden Antennen jeweils in die Brennpunkte der elliptischen Kavität positioniert wurden. Die daraus resultierende Distanz zwischen den Antennenzentren betrug 1646 nm und war damit mehr als doppelt so hoch wie die Resonanzwellenlänge der Moden ($\lambda = 800$ nm). Aufgrund starker Kopplung war in der spektralen Antwort der optimierten Struktur eine Energieaufspaltung der Antennen- und der Kavitätsmode in drei getrennte hybridisierte Eigenmoden innerhalb eines Energiebereichs von ca. 90 meV zu sehen. Die Antwortfunktionen konnten sehr gut mit Hilfe eines einfachen Modells aus drei gekoppelten Lorentz-Oszillatoren reproduziert werden. Im Zeitraum wurde für eine Einfach-Puls-Anregung der Struktur ein ozillatorischer Antennen-Energietransfer mit einer Periode von 86 fs und einer Energietransfer-Effizienz von ungefähr 7% beobachtet. Neben der starken Kopplung ist vor allem auch Impedanzanpassung, also eine ähnliche Dämpfung von Kavitäts- und Antennenmode, nötig, um einen oszillatorischen Energietransfer über mehrere Perioden zu ermöglichen. Für die Experimente wurden Strukturen mit Kavitäten und Antennen unterschiedlicher Größe über focused-ion-beam (FIB) milling hergestellt. Dazu wurden zwei einkristalline Gold-Mikroplättchen übereinandergestapelt, wobei das obere als Substrat für die Kavitätswände und das untere als Substrat für die Kavitätsböden und Nanoantennen diente. Diese Methode ermöglichte die Herstellung von wohldefinierten und glatten Strukturen mit reduzierten Ohmschen Verlusten innerhalb der Kavitäten. Es wurden zeitaufgelöste Korrelationsmessungen durchgeführt, wobei zwei Femtosekundenlaserpulsen zur Anregung und Photoemissionselektronen-Mikroskopie (PEEM) für die Detektion verwendet wurden. Dies ermöglichte sowohl eine hohe zeitliche als auch eine hohe räumliche Auflösung. In den Messungen wurden lokale Korrelationssignale an Antennen in resonanten Strukturen, sprich, Strukturen mit deutlich erhöhter Photoemission an beiden Antennenpositionen, untersucht und mit Hilfe des gekoppelten Lorentz-Oszillatormodells rekonstruiert. Die daraus ermittelte spektrale Antwort zeigte getrennte Peaks und bestätigte damit die Bildung hybridisierter Eigenmoden aufgrund starker Kopplung. In einer nachfolgenden Simulation für Einfach-Puls-Anregung wurde ein einmaliger Hin-und-Her-Energietransfer zwischen den Antennen mit einer Energietransfereffizienz von ca. 10% beobachtet.

Ausgehend von den theoretischen und experimentellen Ergebnissen wurde gezeigt, dass in der hier vorgestellten Struktur ein periodischer langreichweitiger Energietransfer zwischen den zwei Nanoanntenen möglich ist. Zudem ermöglicht es das gekoppelte Oszillatoren-Modell, im Detail zu untersuchen, wie spezifische Eigenschaften der Struktur die Dynamik des zeitlichen elektrischen Feldes bzw. der Energieumverteilung innerhalb der Struktur beeinflussen. Dies kann dazu genutzt werden, die Energietransfer-Effizienz der Struktur noch weiter zu optimieren. Zukünftige Anwendungsmöglichkeiten finden sich im Bereich der ultraschnellen plasmonischen Nanoschaltkreise. Darüberhinaus kann die Struktur genutzt werden, um eine effiziente SPP-vermittelte starke Kopplung zwischen weit voneinder entfernten Quantenemittern zu erreichen. Für diesen Fall müssen die Quantenemitter in der Nähe der Nanoantennen positioniert werden und zusätzlich stark zu einer der spezifischen Eigenmoden der Struktur koppeln.

In Kapitel 6 wurde untersucht, wie die lokale Verstärkung der optischen Chiralität im Nahfeld plasmonischer Nanostrukturen durch das Einstellen der Fernfeld-Polarisation des einfallenden Lichts optimiert werden kann. Zu diesem Zweck wurde ein analytischer Ausdruck hergeleitet, welcher die Berechnung der optimalen Fernfeld-Polarisationen für jede beliebige Nanostruktur-Geometrie ermöglicht. Dabei versteht man unter den optimalen Fernfeld-Polarisationen diejenigen zwei, welche zur höchsten positiven und negativen lokalen optischen Chiralität führen. Da diese von der lokalen optischen Antwort der jeweiligen Nanostruktur abhängig sind, lassen sie sich sowohl als Funktion der Frequenz ω als auch als Funktion der Position $\mathbf{r}$ beschreiben. Die Elliptizitäten der beiden optimalen Fernfeld-Polarisationen unterscheiden sich nur in ihrem Vorzeichen, also ihrer Rotationsrichtung im Zeitraum, und der Winkel zwischen ihren Orientierungen (entspricht dem Winkel zwischen den Hauptachsen ihrer Ellipsen) beträgt $\pm\pi/2$. Die Händigkeit der optimalen lokalen optischen Chiralität kann über das Schalten zwischen den optimalen Fernfeld-Polarisationen hin und her gewechselt werden. Mit Hilfe von numerischen Simulationen wurde für zwei konkrete Nanostrukturen beispielhaft demonstriert, dass für die lokale optische Chiralität Werte erreicht werden können, die deutlich höher sind als die optischen Chiralitätswerte von zirkular polarisiertem Licht im freien Raum — die höchstmöglichen Werte für optische Chiralität im freien Raum. Die entsprechenden optimalen Fernfeld-Polarisationen haben sich dabei von linearer und zirkularer Polarisation unterschieden und variierten mit der Frequenz. Die Anwendung von Femtosekunden-Polarisationspulsformung bietet die Möglichkeit, die lokale optische Chiralität kohärent über einen kontinuierlichen Frequenzbereich zu kontrollieren. Außerdem können Symmetrieeigenschaften der Nanostrukturen genutzt werden, um zu bestimmen, welche Fernfeld-Polarisation optimal ist. Beispielsweise stellt für eine Nanostruktur, die mindestens C_{4v}-symmetrisch in Bezug auf die Propagationsrichtung des einfallenden Lichts ist, zirkulare Polarisation genau dann die optimale Fernfeld-Polarisation dar, wenn die optische Chiralität in einem Nahfeld-Bereich verstärkt werden soll, dessen Form ebenfalls C_{4v}-Symmetrie aufweist mit einer Hauptachse und Spiegelsymmetrie-Ebenen, welche mit denen der Nanostruktur identisich sind.

Die theoretischen Erkenntnisse können zukünftige experimentelle Studien über die lokale Verstärkung der optischen Chiralität beeinflussen. Das Einstellen der Fernfeld-Polarisation des einfallenden Lichts stellt ein vielversprechendes Hilfsmittel dar, um chiral-spezifische Wechselwirkungen von lokalen elektromagnetischen Feldern mit molekularen und anderen Quantensystemen in der Nähe plasmonischer Nanostrukturen zu verstärken. Die hier gezeigte Methode kann Anwendung finden in der chiralen Erkennung adsorbierter Moleküle, in der zeitaufgelösten chiral-sensitiven Spektroskopie und in der chiralen Quantenkontrolle.

Abschließend lässt sich festhalten, dass jedes der lokalisierten Lichtphänomene, die in dieser Arbeit untersucht wurden — die verstärkte lokale Absorption von Nahinfrarotlicht aufgrund der Bildung von lokalisierten photonischen Moden, der periodische langreichweitige Energietransfer zwischen zwei Nanoantennen in einer plasmonischen elliptischen Kavität und die Optimierung der lokalen Verstärkung der optischen Chiralität über das Einstellen der Fernfeld-Polarisation des einfallenden Lichts — neue Perspektiven eröffnen kann für eine Vielzahl von zukünftigen Anwendungsmöglichkeiten.

A Appendix

A.1 Comparison between Rotating and Laboratory Frame

In the 2D nanoscopy experiment presented in Sect. 4.4 of Chapter 4, collinear sequences of four bandwidth-limited laser pulses were employed to obtain information about the investigated sample. The sequences were generated by a pulse shaper in the rotating frame of the center frequency ω_0 of the laser spectrum. By contrast, the two-pulse experiment that is described in Sect. 5.4 of Chapter 5 was also performed with the pulse shaper but in the laboratory frame. In this section, the laboratory and rotating frame are compared to each other with respect to their influence onto measurement signals in time-resolved experiments (Subsect. A.1.1). Additionally, it is discussed how the sampling rate depends on the choice of the frame (Subsect. A.1.2).

A.1.1 Measurement Signals in Time-Resolved Experiments

In the following, the differences between time-resolved experiments in the rotating and laboratory frame are explained by means of a double-pulse sequence. Note that switching between measurements in different frames, i.e., frames with different frequencies as reference, can generally be realized with a pulse shaper [45]. According to Ref. [45], the real-valued temporal electric field of a collinear double pulse is given via

$$E(t,t_1,t_2) = \tilde{A}\,(t-t_1)\ \mathrm{e}^{\mathrm{i}\omega_0(t-\gamma_0 t_1)} + \tilde{A}\,(t-t_2)\ \mathrm{e}^{\mathrm{i}\omega_0(t-\gamma_0 t_2)} + c.c.\,, \tag{A.1}$$

wherein the first two terms correspond to one sub pulse each with the center frequency ω_0, the envelope function $\tilde{A}(t-t_j)$, and the temporal shift t_j with $j=\{1,2\}$. The real-valued dimensionless factor γ_0 in Eq. (A.1) is defined for values between 0 and 1, and determines the frame of the measurement [45]. The reference frequency ω_{ref} of a frame is related to γ_0 via

$$\omega_{\mathrm{ref}} = \omega_0(1-\gamma_0)\,. \tag{A.2}$$

For $\gamma_0 = 0$, the measurement is done in the rotating frame of ω_0, i.e., the center frequency of the laser spectrum. By contrast, for $\gamma_0 = 1$, ω_{ref} becomes zero in Eq. (A.2) and the measurement is done in the laboratory frame. Assuming that only the second sub pulse is temporally shifted during the double-pulse measurement, whereas the first one is fixed at $t_1 = 0$, Eq. (A.1) can be rewritten as follows:

$$E(t,T) = \tilde{A}\,(t)\;\mathrm{e}^{\mathrm{i}\omega_0 t} + \tilde{A}\,(t-T)\;\mathrm{e}^{\mathrm{i}\omega_0 (t-\gamma_0 T)} + c.c. \tag{A.3}$$

with the time delay $T = t_2 - t_1$ between the sub pulses. The envelope functions of the sub pulses can generally contain an additional temporal phase and thus can be complex-valued. However, in the time-resolved experiments presented in this thesis, bandwidth-limited sub pulses were used without an additional temporal phase. Assuming Gaussian-shaped sub pulses, the envelope functions can then be described via the real-valued Gaussian function [188]

$$\tilde{A}(t) = \frac{A_0}{2}\,\mathrm{e}^{-2\ln 2\frac{t^2}{\tau_p^2}} \tag{A.4}$$

with the amplitude A_0 and the temporal pulse duration τ_p. Note that the pulse duration of each sub pulse is determined by the full width at half maximum (FWHM) of its temporal intensity. In Fig. A1a, the temporal electric fields of two exemplary double-pulse sequences in the laboratory frame (red dashed line) and in the rotating frame of the center frequency (blue solid line) are illustrated. The time delay T between the sub pulses is 24 fs for both sequences. Each sub pulse has an amplitude of $A_0 = 1$ and a pulse duration of $\tau_p = 5$ fs. The first sub pulse (sub pulse 1) is centered at $t = 0$ fs, while the second one (sub pulse 2) is temporally shifted by 24 fs. The double-pulse sequences of the two frames differ only in the carrier-envelope phase (CEP) [188] of sub pulse 2, i.e., the phase between the envelope and the carrier oscillations of the second sub pulse. In the laboratory frame, the maximum of the envelope of sub pulse 2 coincides with a maximum of the corresponding carrier oscillations. By contrast, in the rotating frame, the carrier oscillations of sub pulse 2 are shifted with respect to the envelope but are in phase with the oscillations $\cos\omega_0 t$ (gray solid line). In general, if a pulse is temporally shifted in the rotating frame of ω_0, only the envelope is shifted, while the phase of the carrier oscillations remains unchanged, i.e., the carrier oscillations always have a maximum at $t = 0$ fs. As opposed to this, if a pulse is temporally shifted in the laboratory frame, the carrier oscillations are shifted together with the envelope such that the maximum of the envelope always coincide with a maximum of the carrier oscillations. This can also be considered via Eq. (A.1). For $\gamma_0 = 0$, the phase factors of the first two terms become $\mathrm{e}^{-\mathrm{i}\omega_0 t}$ leading to oscillations with a maximum at $t = 0$ fs. In the case of $\gamma_0 = 1$, these phase factors change to $\mathrm{e}^{-\mathrm{i}\omega_0 (t-t_j)}$ with $j = \{1,2\}$ and thus the carrier oscillations have a maximum at t_j.

The effects of different γ_0 values on time-resolved measurements are shown in Fig. A1b by means of linear autocorrelation traces calculated in the laboratory frame (red dashed line) and in the rotating frame of ω_0 (blue solid line) for two Gaussian sub pulses with $A_0 = 1$ and $\tau_p = 5$ fs. The time delay T was scanned from -25 fs to 25 fs in steps of 0.01 fs and the corresponding time-integrated signal $I_{\mathrm{AC}}(T)$ was calculated via [188]

$$I_{\mathrm{AC}}(T) = \int_{-\infty}^{\infty} |E(t,T)|^2 dt \tag{A.5}$$

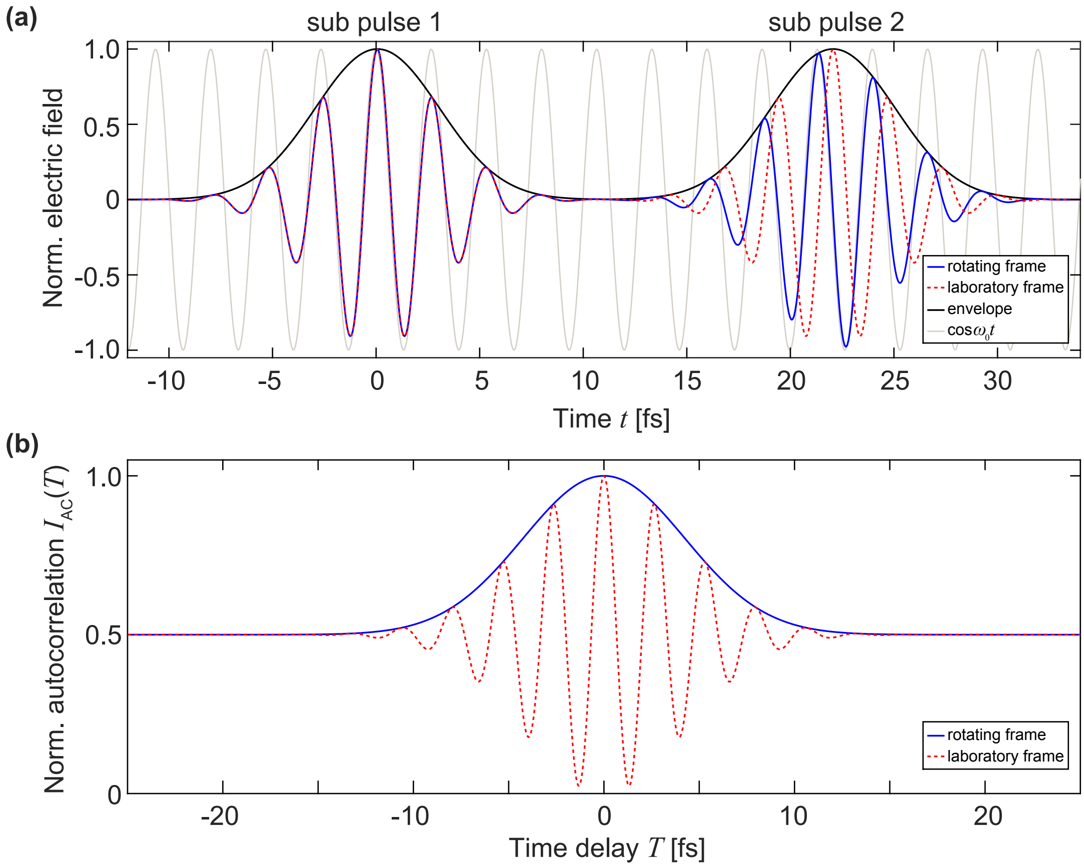

Figure A1: Difference between laboratory frame ($\gamma_0 = 1$) and rotating frame of ω_0 ($\gamma_0 = 0$). (a) Temporal electric fields of two double-pulse sequences with Gaussian-shaped sub pulses 1 and 2 ($A_0 = 1$, $\tau_p = 5$ fs) for a time delay $T = 24$ fs in the laboratory frame (red dashed line) and in the rotating frame of the center frequency $\omega_0 = 2.36$ fs (blue solid line) according to Eqs. (A.3) and (A.4). In the laboratory frame, the maximum of the envelope (black solid line) of each sub pulse coincides with a maximum of its corresponding carrier oscillations. In the rotating frame, this is only the case for the sub pulse centered at $t = 0$ fs. For the delayed sub pulse, the carrier oscillations are shifted with respect to the maximum of the envelope but are in phase with the oscillations arising from $\cos\omega_0 t$ (gray solid line). (b) Linear autocorrelation signals calculated in the laboratory frame (red dashed line) and rotating frame of ω_0 (blue solid line) by means of Eqs. (A.3) and (A.5). The signal in the laboratory frame oscillates with ω_0, whereas a non-oscillating decay is observed for the signal in the rotating frame.

with the electric field $E(t,T)$ defined in Eq. (A.3). In the laboratory frame, the signal oscillates with ω_0 due to constructive and destructive interferences of the two sub pulses. In contrast to this, in the rotating frame of ω_0, only a non-oscillating decay is observed that coincides with the envelope of the signal obtained in the laboratory frame. Thus, a Fourier transformation of the signal in the laboratory frame would lead to peaks at $\pm\omega_0$, whereas a Fourier transformation of the signal in the rotating frame would only lead to a peak at zero frequency. In general, temporal measurement signals, which oscillate with frequencies ω in the laboratory frame, would oscillate with difference frequencies $(\omega - \omega_{\text{ref}})$ in the rotating frame of a reference frequency ω_{ref}. As a consequence, after

Fourier transformation, the corresponding signals in the frequency domain are pushed together around the zero frequency, depending on the choice of ω_{ref} and, with this, on the choice of γ_0. Hence, signal contributions with finite spectral line widths can spectrally overlap in the rotating frame, especially for $\gamma_0 = 0$, i.e., in the rotating frame of ω_0, whereas they would be well separated in the laboratory frame. This drawback can be compensated by using phase cycling that enables the extraction of desired signal contributions from congested spectra (see Sect. 2.4).

A.1.2 Choice of the Sampling Rate

The sampling rate ν_s of a time-resolved measurement has to be chosen carefully in order to correctly reconstruct the oscillation frequencies of the measurement signals. For a correct reconstruction, ν_s has generally to fulfill the Shannon-Nyquist criterion [46, 47]

$$\nu_s \geq 2\nu_{\text{max}}\,, \tag{A.6}$$

wherein $\nu_{\text{max}} = \omega_{\text{max}}/2\pi$ is the maximum frequency of the measurement signal. For equality in Eq. (A.6) the frequency $2\nu_{\text{max}}$ is called Nyquist frequency and corresponds to the smallest possible sampling rate. In a two-pulse experiment, the time delay is scanned from a starting value T_{start} in N discrete steps of constant step size ΔT, i.e.,

$$T_j = T_{\text{start}} + j\Delta T \qquad\qquad \text{with } j = 1, 2, 3, ..., N\,, \tag{A.7}$$

and the corresponding sampling rate is defined by

$$\nu_s = \frac{1}{\Delta T}\,. \tag{A.8}$$

In the laboratory frame, signals oscillate with frequencies ω and thus, according to Eqs. (A.6) and (A.8), the maximum step size ΔT_{max} is given by

$$\Delta T^{\text{lab}}_{\text{max}} = \frac{1}{2\nu_{\text{max}}} = \frac{\pi}{\omega_{\text{max}}}\,. \tag{A.9}$$

By contrast, in the rotating frame of a reference frequency ω_{ref}, signals oscillate with difference frequencies $(\omega - \omega_{\text{ref}})$ and therefore the maximum step size is obtained via

$$\Delta T^{\text{rot}}_{\text{max}}\,(\gamma_0) = \frac{\pi}{|\omega - \omega_{\text{ref}}\,(\gamma_0)\,|_{\text{max}}} = \frac{\pi}{|\omega - \omega_0(1-\gamma_0)|_{\text{max}}}\,. \tag{A.10}$$

Note that $\Delta T^{\text{rot}}_{\text{max}}\,(\gamma_0 = 1)$ is equal to $\Delta T^{\text{lab}}_{\text{max}}$. Since the denominator in Eq. (A.10) represents the maximum absolute value of the difference $[\omega - \omega_0(1-\gamma_0)]$, one has first to consider both the maximum and minimum frequency ω_{max} and ω_{min}, respectively. The maximum step size is then determined by the higher value of $|\omega_{\text{max}} - \omega_0(1-\gamma_0)|$ and $|\omega_{\text{min}} - \omega_0(1-\gamma_0)|$. According to Eq. (A.10), the largest maximum step size is obtained for $\gamma_0 = 0$, i.e., the rotating frame of the center frequency ω_0 of the excitation spectrum.

The laser spectrum that was utilized for the experiments in Sects. 4.4 and 5.4 ranged from $\omega_{\text{min}} = 2.28$ rad/fs to $\omega_{\text{max}} = 2.44$ rad/fs with a center frequency of $\omega_0 =$

2.356 rad/fs. For these values, the maximum step sizes in the laboratory frame and the rotating frame of ω_0 are

$$\Delta T_{\mathrm{max}}^{\mathrm{lab}} \approx 1.29\ \mathrm{fs} \quad \text{and} \quad \Delta T_{\mathrm{max}}^{\mathrm{rot}}\left(\gamma_0 = 0\right) \approx 37.40\ \mathrm{fs}\,. \tag{A.11}$$

This example demonstrates that the step size in a rotating-frame experiment can be chosen significantly higher than the step size in an equivalent laboratory-frame experiment. Thus, the measurement time can be substantially reduced if the time delays are scanned between the same starting and end values in both frames. As mentioned above, in rotating-frame measurements, phase cycling [37, 39, 40] has often to be applied to remove undesired signal contributions and to extract the desired signal contribution unambiguously (see Sect. 2.4). This means that measurements have to be repeated for different phase-cycling steps. Nevertheless, the total measurement time can still be reduced compared to equivalent measurements in the laboratory frame.

A.2 Determination of Optimal Far-Field Polarizations

In Chapter 6, the enhancement of the normalized local optical chirality $\hat{C}\left(\mathbf{r},\omega\right)$ in the vicinity of plasmonic nanostructures by tuning the far-field polarization is investigated. In this section, those far-field polarizations are determined which lead to optimal local optical chirality values. For this purpose, Eq. (6.14) is differentiated with respect to $\hat{I}_1\left(\omega\right)$ and $\varphi\left(\omega\right)$, for any given frequency ω independently, and the resultant derivatives

$$\begin{aligned}\frac{\partial \hat{C}\left(\mathbf{r},\omega\right)}{\partial \hat{I}_1\left(\omega\right)} = -\Bigg(& C_{S_1}\left(\mathbf{r},\omega\right) - C_{S_2}\left(\mathbf{r},\omega\right) \\ & + \frac{\left\{1 - 2\hat{I}_1\left(\omega\right)\right\}\left\{C_{S_\mathrm{p}}\left(\mathbf{r},\omega\right)\cos\left[\varphi\left(\omega\right)\right] + C_{S_\mathrm{m}}\left(\mathbf{r},\omega\right)\sin\left[\varphi\left(\omega\right)\right]\right\}}{2\sqrt{\hat{I}_1\left(\omega\right) - \hat{I}_1^2\left(\omega\right)}}\Bigg)\,,\end{aligned} \tag{A.12}$$

$$\begin{aligned}\frac{\partial \hat{C}\left(\mathbf{r},\omega\right)}{\partial \varphi\left(\omega\right)} = -\Bigg(& \sqrt{\hat{I}_1\left(\omega\right) - \hat{I}_1^2\left(\omega\right)} \\ & \times\left\{-C_{S_\mathrm{p}}\left(\mathbf{r},\omega\right)\sin\left[\varphi\left(\omega\right)\right] + C_{S_\mathrm{m}}\left(\mathbf{r},\omega\right)\cos\left[\varphi\left(\omega\right)\right]\right\}\Bigg)\,,\end{aligned} \tag{A.13}$$

are set equal to zero,

$$\frac{\partial \hat{C}\left(\mathbf{r},\omega\right)}{\partial \hat{I}_1\left(\omega\right)} \overset{!}{=} 0\,, \tag{A.14}$$

$$\frac{\partial \hat{C}\left(\mathbf{r},\omega\right)}{\partial \varphi\left(\omega\right)} \overset{!}{=} 0\,. \tag{A.15}$$

Solving for $\hat{I}_1(\omega)$ and $\varphi(\omega)$ leads to two critical points, i.e., two different solutions for the far-field polarization. The first critical point $P1$ is at

$$\hat{I}_1^{P1}(\mathbf{r},\omega) = \frac{1}{2} - \frac{C_{S_1}(\mathbf{r},\omega) - C_{S_2}(\mathbf{r},\omega)}{2\left\{C_{S_\mathrm{p}}^2(\mathbf{r},\omega) + C_{S_\mathrm{m}}^2(\mathbf{r},\omega) + \left[C_{S_1}(\mathbf{r},\omega) - C_{S_2}(\mathbf{r},\omega)\right]^2\right\}^{\frac{1}{2}}}\,, \tag{A.16}$$

$$\varphi^{P1}(\mathbf{r},\omega) = -2\arctan\left[\frac{C_{S_\mathrm{p}}(\mathbf{r},\omega) + \sqrt{C_{S_\mathrm{p}}^2(\mathbf{r},\omega) + C_{S_\mathrm{m}}^2(\mathbf{r},\omega)}}{C_{S_\mathrm{m}}(\mathbf{r},\omega)}\right], \tag{A.17}$$

whereas the second critical point $P2$ is at

$$\hat{I}_1^{P2}(\mathbf{r},\omega) = \frac{1}{2} + \frac{C_{S_1}(\mathbf{r},\omega) - C_{S_2}(\mathbf{r},\omega)}{2\left\{C_{S_\mathrm{p}}^2(\mathbf{r},\omega) + C_{S_\mathrm{m}}^2(\mathbf{r},\omega) + \left[C_{S_1}(\mathbf{r},\omega) - C_{S_2}(\mathbf{r},\omega)\right]^2\right\}^{\frac{1}{2}}}\,, \tag{A.18}$$

$$\varphi^{P2}(\mathbf{r},\omega) = 2\arctan\left[\frac{-C_{S_\mathrm{p}}(\mathbf{r},\omega) + \sqrt{C_{S_\mathrm{p}}^2(\mathbf{r},\omega) + C_{S_\mathrm{m}}^2(\mathbf{r},\omega)}}{C_{S_\mathrm{m}}(\mathbf{r},\omega)}\right]. \tag{A.19}$$

The nature of each critical point is determined separately via the Hessian matrix of the normalized local optical chirality,

$$\mathbb{H}_{\hat{C}}\left[\hat{I}_1(\omega), \varphi(\omega)\right] = \begin{pmatrix} \frac{\partial^2 \hat{C}(\mathbf{r},\omega)}{\partial^2 \hat{I}_1(\omega)} & \frac{\partial^2 \hat{C}(\mathbf{r},\omega)}{\partial \hat{I}_1(\omega)\partial\varphi(\omega)} \\ \frac{\partial^2 \hat{C}(\mathbf{r},\omega)}{\partial\varphi(\omega)\partial \hat{I}_1(\omega)} & \frac{\partial^2 \hat{C}(\mathbf{r},\omega)}{\partial^2\varphi(\omega)} \end{pmatrix}, \tag{A.20}$$

where the frequency ω is just a parameter. Hence, the dependency on ω can be neglected for the following derivations. Calculating the eigenvalues λ^{P1} of Eq. (A.20) for the first critical point,

$$\det\left[\mathbb{H}_C\left(\hat{I}_1^{P1}, \varphi^{P1}\right) - \lambda^{P1}\mathbb{1}\right] \overset{!}{=} 0\,, \tag{A.21}$$

with the identity matrix $\mathbb{1}$, leads to

$$\begin{aligned} &\lambda_1^{P1}\left[\hat{I}_1^{P1}(\mathbf{r},\omega), \varphi^{P1}(\mathbf{r},\omega)\right] \\ &= -\frac{2\left\{\left[C_{S_1}(\mathbf{r},\omega) - C_{S_2}(\mathbf{r},\omega)\right]^2 + C_{S_\mathrm{p}}^2(\mathbf{r},\omega) + C_{S_\mathrm{m}}^2(\mathbf{r},\omega)\right\}^{\frac{3}{2}}}{\left[C_{S_\mathrm{p}}^2(\mathbf{r},\omega) + C_{S_\mathrm{m}}^2(\mathbf{r},\omega)\right]} \leq 0\,, \end{aligned} \tag{A.22}$$

$$\begin{aligned} &\lambda_2^{P1}\left[\hat{I}_1^{P1}(\mathbf{r},\omega), \varphi^{P1}(\mathbf{r},\omega)\right] \\ &= -\frac{C_{S_\mathrm{p}}^2(\mathbf{r},\omega) + C_{S_\mathrm{m}}^2(\mathbf{r},\omega)}{2\left\{\left[C_{S_1}(\mathbf{r},\omega) - C_{S_2}(\mathbf{r},\omega)\right]^2 + C_{S_\mathrm{p}}^2(\mathbf{r},\omega) + C_{S_\mathrm{m}}^2(\mathbf{r},\omega)\right\}^{\frac{1}{2}}} \leq 0\,. \end{aligned} \tag{A.23}$$

Since both eigenvalues λ_1^{P1} and λ_2^{P1} are negative, the Hessian matrix is negative definite and thus, the critical point $P1$ is a local maximum. Due to the constraints $0 \leq \hat{I}_1(\omega) \leq 1$ and $-\pi \leq \varphi(\omega) < \pi$ the critical point is even a global maximum.

The eigenvalues of the critical point $P2$ are

$$\lambda_1^{P2}\left[\hat{I}_1^{P2}(\mathbf{r},\omega), \varphi^{P2}(\mathbf{r},\omega)\right] = \frac{2\left\{\left[C_{S_1}(\mathbf{r},\omega) - C_{S_2}(\mathbf{r},\omega)\right]^2 + C_{S_\mathrm{p}}^2(\mathbf{r},\omega) + C_{S_\mathrm{m}}^2(\mathbf{r},\omega)\right\}^{\frac{3}{2}}}{\left[C_{S_\mathrm{p}}^2(\mathbf{r},\omega) + C_{S_\mathrm{m}}^2(\mathbf{r},\omega)\right]} \geq 0\,, \tag{A.24}$$

$$\lambda_2^{P2}\left[\hat{I}_1^{P2}(\mathbf{r},\omega), \varphi^{P2}(\mathbf{r},\omega)\right] = \frac{C_{S_\mathrm{p}}^2(\mathbf{r},\omega) + C_{S_\mathrm{m}}^2(\mathbf{r},\omega)}{2\left\{\left[C_{S_1}(\mathbf{r},\omega) - C_{S_2}(\mathbf{r},\omega)\right]^2 + C_{S_\mathrm{p}}^2(\mathbf{r},\omega) + C_{S_\mathrm{m}}^2(\mathbf{r},\omega)\right\}^{\frac{1}{2}}} \geq 0\,. \tag{A.25}$$

In this case, both eigenvalues are positive and therefore the definiteness of the Hessian matrix is positive as well. Thus, the corresponding critical point represents a local minimum and, due to the above-mentioned constraints, even a global minimum.

Taking all results together leads to the assignment of maximum and minimum in Eqs. (6.15), (6.16), and (6.17). Since both extrema are global within the range of the far-field polarization parameters $\hat{I}_1(\omega)$ and $\varphi(\omega)$, there is one unambiguous far-field polarization for which the local optical chirality is maximal and one for which it is minimal (for every frequency).

A.3 Relation between Ellipticities/Orientations of Optimal Far-Field Polarizations

In Appendix A.2, it is explained in detail, how the optimal far-field polarizations for maximum and minimum local optical chirality were determined. In this section, the relation between the two optimal far-field polarizations with respect to their ellipticies and orientations is derived by means of the relations defined in Eqs. (6.24) and (6.32). For this purpose, the polarization parameters $I_1(\omega)$, $I_2(\omega)$, $\varphi_1(\omega)$, and $\varphi_2(\omega)$ are transformed into elliptical parameters [174].

An arbitrary ellipse perpendicular to the propagation direction of the external light $\mathbf{e}_k$ can be described via its amplitudes $\widetilde{A}_1(\omega)$ and $\widetilde{A}_2(\omega)$ along its principal axes $\widetilde{T}_1$ and $\widetilde{T}_2$, respectively (see Figure A2). In general, these amplitudes are different from the amplitudes $A_1(\omega)$ and $A_2(\omega)$ that are oriented along the axes T_1 and T_2, respectively, and are given according to Eq. (6.3) as

$$A_\alpha(\omega) = \sqrt{\frac{I_\alpha(\omega)}{2\epsilon_0 c}} \tag{A.26}$$

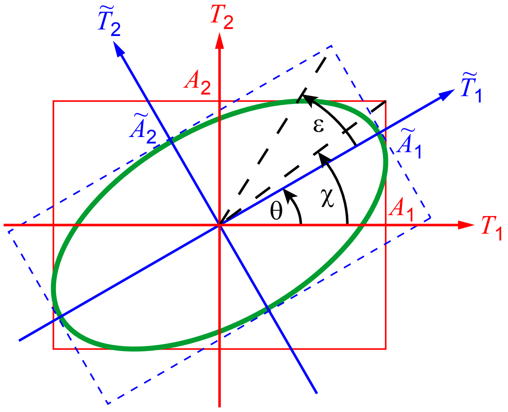

Figure A2: Definition of elliptical parameters [174]. The polarization ellipse (green) is defined by its amplitudes $\widetilde{A}_1$ and $\widetilde{A}_2$ that are oriented along the axes $\widetilde{T}_1$ and $\widetilde{T}_2$ (blue), respectively, and that determine the angle of ellipticity ϵ. The orientation angle θ is the angle between the ellipse-inherent $\widetilde{T}_1$–$\widetilde{T}_2$ coordinate system with respect to the laboratory-frame T_1–T_2 coordinate system with the amplitudes A_1 and A_2 (red). The angle χ is given by the tangent of A_2/A_1. Figure taken from [4]. © (2017) American Chemical Society.

with $\alpha = \{1, 2\}$. The ellipticity of the polarization state is defined by the angle of ellipticity $\epsilon(\omega)$ and its orientation by the orientiation angle $\theta(\omega)$, which is the angle between $\widetilde{T}_1$ and T_1. It has been shown previously [174] that these two elliptical parameters can be expressed via

$$\epsilon(\omega) = \frac{1}{2}\arcsin\Big\{\sin\big[2\chi(\omega)\big]\sin\big[\varphi(\omega)\big]\Big\} \qquad \in [-\pi/4, \pi/4] \tag{A.27}$$

and

$$\theta(\omega) = \begin{cases} \tilde{\theta}(\omega) & \in [-\pi/4, \pi/4] \quad \text{if } \chi(\omega) \leq \pi/4\,, \\ \tilde{\theta}(\omega) + \pi/2 & \in [\pi/4, \pi/2] \quad \text{if } \chi(\omega) > \pi/4 \wedge \tilde{\theta}(\omega) < 0\,, \\ \tilde{\theta}(\omega) - \pi/2 & \in [-\pi/2, -\pi/4] \quad \text{if } \chi(\omega) > \pi/4 \wedge \tilde{\theta}(\omega) \geq 0\,, \end{cases} \tag{A.28}$$

wherein

$$\tilde{\theta}(\omega) = \frac{1}{2}\arctan\Big\{\tan\big[2\chi(\omega)\big]\cos\big[\varphi(\omega)\big]\Big\} \qquad \in [-\pi/4, \pi/4]\,, \tag{A.29}$$

and

$$\chi(\omega) = \arctan\left[\frac{A_2(\omega)}{A_1(\omega)}\right] \qquad \in [0, \pi/2]\ . \tag{A.30}$$

The relative phase is defined as

$$\varphi(\omega) = \varphi_2(\omega) - \varphi_1(\omega) \qquad \in [-\pi, \pi]\ . \tag{A.31}$$

With these relations, both $\epsilon(\omega)$ and $\theta(\omega)$ can be calculated from the polarization parameters $A_1(\omega)$, $A_2(\omega)$, and $\varphi(\omega)$.

Using the definitions $\hat{I}_2(\omega) = [I(\omega) - I_1(\omega)]/I(\omega)$ and $\hat{I}_1(\omega) = I_1(\omega)/I(\omega)$ as well as Eq. (A.26) the angle χ of the far-field polarization for maximum local optical chirality is then given by

$$\chi_{\max}(\mathbf{r}, \omega) = \arctan\left[\sqrt{\frac{1 - \hat{I}_{1,\max}(\mathbf{r}, \omega)}{\hat{I}_{1,\max}(\mathbf{r}, \omega)}}\right] \tag{A.32}$$

and that for minimum local optical chirality by

$$\chi_{\text{min}}(\mathbf{r},\omega) = \arctan\left[\sqrt{\frac{1-\hat{I}_{1,\text{min}}(\mathbf{r},\omega)}{\hat{I}_{1,\text{min}}(\mathbf{r},\omega)}}\right] = \arctan\left[\sqrt{\frac{\hat{I}_{1,\text{max}}(\mathbf{r},\omega)}{1-\hat{I}_{1,\text{max}}(\mathbf{r},\omega)}}\right]. \tag{A.33}$$

In the last step in Eq. (A.33) the relation from Eq. (6.24) was applied. Using the relation

$$\arctan\frac{1}{x} = \frac{\pi}{2}\operatorname{sign}x - \arctan x \tag{A.34}$$

and Eqs. (A.32) and (A.33) leads to

$$\chi_{\text{max}}(\mathbf{r},\omega) + \chi_{\text{min}}(\mathbf{r},\omega) = \pi/2\,. \tag{A.35}$$

Equation (A.35) and Eq. (6.32) can be exploited to compare the ellipticities of the optimal far-field polarizations:

$$\begin{aligned}\epsilon_{\text{max}}(\mathbf{r},\omega) &= \frac{1}{2}\arcsin\Big\{\sin\big[2\chi_{\text{max}}(\mathbf{r},\omega)\big]\sin\big[\varphi_{\text{max}}(\mathbf{r},\omega)\big]\Big\}\\ &= \frac{1}{2}\arcsin\Big\{\sin\big[\pi-2\chi_{\text{min}}(\mathbf{r},\omega)\big]\sin\big[\varphi_{\text{min}}(\mathbf{r},\omega)\pm\pi\big]\Big\}\\ &= -\frac{1}{2}\arcsin\Big\{\sin\big[2\chi_{\text{min}}(\mathbf{r},\omega)\big]\sin\big[\varphi_{\text{min}}(\mathbf{r},\omega)\big]\Big\}\\ &= -\epsilon_{\text{min}}(\mathbf{r},\omega)\,. \end{aligned}\tag{A.36}$$

Analogously, a relation between the angles $\tilde{\theta}$ of the optimal far-field polarizations can be found via

$$\begin{aligned}\tilde{\theta}_{\text{max}}(\mathbf{r},\omega) &= \frac{1}{2}\arctan\Big\{\tan\big[2\chi_{\text{max}}(\mathbf{r},\omega)\big]\cos\big[\varphi_{\text{max}}(\mathbf{r},\omega)\big]\Big\}\\ &= \frac{1}{2}\arctan\Big\{\tan\big[\pi-2\chi_{\text{min}}(\mathbf{r},\omega)\big]\cos\big[\varphi_{\text{min}}(\mathbf{r},\omega)\pm\pi\big]\Big\}\\ &= \frac{1}{2}\arctan\Big\{\tan\big[2\chi_{\text{min}}(\mathbf{r},\omega)\big]\cos\big[\varphi_{\text{min}}(\mathbf{r},\omega)\big]\Big\}\\ &= \tilde{\theta}_{\text{min}}(\mathbf{r},\omega)\,. \end{aligned}\tag{A.37}$$

Considering Eq. (A.35), there are three cases for $\chi_{\text{max}}(\mathbf{r},\omega)$ and $\chi_{\text{min}}(\mathbf{r},\omega)$:

$$\chi_{\text{max}}(\mathbf{r},\omega) > \pi/4 \quad \wedge \quad \chi_{\text{min}}(\mathbf{r},\omega) < \pi/4\,, \tag{A.38}$$

$$\chi_{\text{max}}(\mathbf{r},\omega) < \pi/4 \quad \wedge \quad \chi_{\text{min}}(\mathbf{r},\omega) > \pi/4 \tag{A.39}$$

and

$$\chi_{\text{max}}(\mathbf{r},\omega) = \chi_{\text{min}}(\mathbf{r},\omega) = \pi/4\,. \tag{A.40}$$

According to Eqs. (A.28) and (A.38), the orientation angles of the optimal far-field polarizations are in the first case

$$\theta_{\text{max}}(\mathbf{r},\omega) = \tilde{\theta}_{\text{max}}(\mathbf{r},\omega) \pm \pi/2 \qquad \text{and} \qquad \theta_{\text{min}}(\mathbf{r},\omega) = \tilde{\theta}_{\text{min}}(\mathbf{r},\omega) \tag{A.41}$$

and, according to Eqs. (A.28) and (A.39), in the second case

$$\theta_{\text{max}}(\mathbf{r},\omega) = \tilde{\theta}_{\text{max}}(\mathbf{r},\omega) \qquad \text{and} \qquad \theta_{\text{min}}(\mathbf{r},\omega) = \tilde{\theta}_{\text{min}}(\mathbf{r},\omega) \pm \pi/2\,. \tag{A.42}$$

In the third case, Eq. (A.37) is not valid because the tangents of $2\chi_{\text{max}}(\mathbf{r},\omega) = \pi/2$ and $2\chi_{\text{min}}(\mathbf{r},\omega) = \pi/2$ are not defined due to a pole of the function for this value. Nevertheless, the relation between $\tilde{\theta}_{\text{max}}(\mathbf{r},\omega)$ and $\tilde{\theta}_{\text{min}}(\mathbf{r},\omega)$ can be obtained in this case by the limits

$$\begin{aligned}
\lim_{\chi_{\text{max}}\to\frac{\pi}{4}\pm} \tilde{\theta}_{\text{max}}(\mathbf{r},\omega) &= \lim_{\chi_{\text{max}}\to\frac{\pi}{4}\pm} \frac{1}{2}\arctan\Big\{\tan\big[2\chi_{\text{max}}(\mathbf{r},\omega)\big]\cos\big[\varphi_{\text{max}}(\mathbf{r},\omega)\big]\Big\} \\
&= \mp\frac{\pi}{4}\,\text{sign}\Big\{\cos\big[\varphi_{\text{max}}(\mathbf{r},\omega)\big]\Big\} \\
&= \mp\frac{\pi}{4}\,\text{sign}\Big\{\cos\big[\varphi_{\text{min}}(\mathbf{r},\omega)\pm\pi\big]\Big\} \\
&= \pm\frac{\pi}{4}\,\text{sign}\Big\{\cos\big[\varphi_{\text{min}}(\mathbf{r},\omega)\big]\Big\} \\
&= \lim_{\chi_{\text{min}}\to\frac{\pi}{4}\mp} \tilde{\theta}_{\text{min}}(\mathbf{r},\omega)\ .
\end{aligned} \tag{A.43}$$

The corresponding orientation angles of the optimal far-field polarizations are then received by means of Eqs. (A.28) and (A.43):

$$\begin{aligned}
\lim_{\chi_{\text{max}}\to\frac{\pi}{4}+} \theta_{\text{max}}(\mathbf{r},\omega) &= \lim_{\chi_{\text{max}}\to\frac{\pi}{4}+} \tilde{\theta}_{\text{max}}(\mathbf{r},\omega) \pm \pi/2, \\
\lim_{\chi_{\text{min}}\to\frac{\pi}{4}-} \theta_{\text{min}}(\mathbf{r},\omega) &= \lim_{\chi_{\text{min}}\to\frac{\pi}{4}-} \tilde{\theta}_{\text{min}}(\mathbf{r},\omega)\ ,
\end{aligned} \tag{A.44}$$

as well as

$$\begin{aligned}
\lim_{\chi_{\text{max}}\to\frac{\pi}{4}-} \theta_{\text{max}}(\mathbf{r},\omega) &= \lim_{\chi_{\text{max}}\to\frac{\pi}{4}-} \tilde{\theta}_{\text{max}}(\mathbf{r},\omega)\,, \\
\lim_{\chi_{\text{min}}\to\frac{\pi}{4}+} \theta_{\text{min}}(\mathbf{r},\omega) &= \lim_{\chi_{\text{min}}\to\frac{\pi}{4}+} \tilde{\theta}_{\text{min}}(\mathbf{r},\omega) \pm \pi/2\,.
\end{aligned} \tag{A.45}$$

Finally, applying Eq. (A.37) to Eqs. (A.41) and (A.42), and Eq. (A.43) to Eqs. (A.44) and (A.45) leads to the relation

$$\theta_{\text{max}}(\mathbf{r},\omega) = \theta_{\text{min}}(\mathbf{r},\omega) \pm \pi/2\,. \tag{A.46}$$

The results from Eqs. (A.36) and (A.46) determine the relation between the optimal far-field polarizations. The ellipticity of the far-field polarization for $\hat{C}_{\text{max}}(\mathbf{r},\omega)$ is the same as for $\hat{C}_{\min}(\mathbf{r}, \omega)$ but with opposite sign, i.e., the shape of the ellipse is the same, but in one case the field is left elliptically polarized, and in the other case it is right elliptically polarized. Furthermore, its orientation is rotated by $\pm\pi/2$ with respect to $\mathbf{e}_k$ compared to the orientation of the far-field polarization for $\hat{C}_{\min}(\mathbf{r}, \omega)$.

It is worth noting that the calculations performed in this section were done in the frequency domain. For pulses in the time domain, the temporal polarization states defined by $\epsilon(t)$ and $\theta(t)$ result from the superposition of the monochromatic waves with the corresponding polarization states in the frequency domain, i.e., after performing a Fourier transformation. Thus, the relations (A.36) and (A.46) are not directly seen in the three-dimensional temporal pulse representations of Figs. 6.5 and 6.6 in Section 6.4.

Bibliography

[1] M. Aeschlimann, T. Brixner, A. Fischer, C. Kramer, P. Melchior, W. Pfeiffer, C. Schneider, C. Strüber, P. Tuchscherer, and D. V. Voronine.
Coherent two-dimensional nanoscopy.
Science **333**, 1723–1726, (2011).

[2] M. Aeschlimann, T. Brixner, D. Differt, U. Heinzmann, M. Hensen, C. Kramer, F. Lükermann, P. Melchior, W. Pfeiffer, M. Piecuch, C. Schneider, H. Stiebig, C. Strüber, and P. Thielen.
Perfect absorption in nanotextured thin films via Anderson-localized photon modes.
Nature Photonics **9**, 663–668, (2015).

[3] M. Aeschlimann, T. Brixner, A. Fischer, M. Hensen, B. Huber, D. Kilbane, C. Kramer, W. Pfeiffer, M. Piecuch, and P. Thielen.
Determination of local optical response functions of nanostructures with increasing complexity by using single and coupled Lorentzian oscillator models.
Applied Physics B, 122:199, (2016).

[4] C. Kramer, M. Schäferling, T. Weiss, H. Giessen, and T. Brixner.
Analytic Optimization of Near-Field Optical Chirality Enhancement.
ACS Photonics **4**, 396–406, (2017).

[5] M. Aeschlimann, T. Brixner, B. Frisch, B. Hecht, M. Hensen, B. Huber, C. Kramer, E. Krauss, T. Löber, W. Pfeiffer, M. Piecuch, and P. Thielen.
Cavity-Assisted Ultrafast Long-Range Periodic Energy Transfer between Plasmonic Nanoantennas.
submitted for publication (2017).

[6] M. Aeschlimann, T. Brixner, M. Cinchetti, N. Haag, M. Hensen, B. Huber, C. Kramer, J. Kollamana, W. Pfeiffer, M. Piecuch, C. Schneider, B. Stadtmüller, and P. Thielen.
Long-Lived Coherence at a Ferromagnet-Organic Interface.
in preparation (2017).

[7] M. Pollard.
The Light Bulb: And How It Changed the World.
Facts on File, New York, (1995).

[8] J. F. Waymouth.
Electric Discharge Lamps.
The MIT Press, Cambridge, MA, (1971).

[9] N. Holonyak Jr. and S. F. Bevacqua.
Coherent (visible) light emission from Ga(As1-xPx) junctions.
Applied Physics Letters **1**, 82–83, (1962).

[10] N. Zheludev.
The life and times of the LED — a 100-year history.
Nature Photonics **1**, 189–192, (2007).

[11] A. L. Schawlow and C. H. Townes.
Infrared and Optical Masers.
Physical Review **112**, 1940–1949, (1958).

[12] T. H. Maiman.
Stimulated Optical Radiation in Ruby.
Nature **187**, 493–494, (1960).

[13] A. H. Zewail.
Femtochemistry. Past, present, and future.
Pure and Applied Chemistry **72**, 2219–2231, (2000).

[14] A. H. Zewail.
Femtochemistry: atomic-scale dynamics of the chemical bond.
The Journal of Physical Chemistry A **104**, 5660–5694, (2000).

[15] A. Assion, T. Baumert, M. Bergt, T. Brixner, B. Kiefer, V. Seyfried, M. Strehle, and G. Gerber.
Control of chemical reactions by feedback-optimized phase-shaped femtosecond laser pulses.
Science **282**, 919–922, (1998).

[16] T. Brixner, N. H. Damrauer, G. Krampert, P. Niklaus, and G. Gerber.
Femtosecond learning control of quantum dynamics in gases and liquids: Technology and applications.
Journal of Modern Optics **50**, 539–560, (2003).

[17] E. Abbe.
Beiträge zur Theorie des Mikroskops und der mikroskopischen Wahrnehmung.
Archiv für Mikroskopische Anatomie **9**, 413–418, (1873).

[18] E. Ozbay, K. Guven, K. Aydin, and M. Bayindir.
Physics and applications of photonic nanocrystals.
International Journal of Nanotechnology **1**, 379–398, (2004).

[19] W. A. Murray and W. L. Barnes.
Plasmonic Materials.
Advanced Materials **19**, 3771–3782, (2007).

[20] E. Hendry, R. V. Mikhaylovskiy, L. D. Barron, M. Kadodwala, and T. J. Davis.
Chiral Electromagnetic Fields Generated by Arrays of Nanoslits.
Nano Letters **12**, 3640–3644, (2012).

[21] N. Meinzer, E. Hendry, and W. L. Barnes.
Probing the chiral nature of electromagnetic fields surrounding plasmonic nanostructures.
Physical Review B **88**, 041407, (2013).

[22] M. Schäferling, D. Dregely, M. Hentschel, and H. Giessen.
Tailoring Enhanced Optical Chirality: Design Principles for Chiral Plasmonic Nanostructures.
Physical Review X **2**, 031010, (2012).

[23] M. Schäferling, X. Yin, N. Engheta, and H. Giessen.
Helical Plasmonic Nanostructures as Prototypical Chiral Near-Field Sources.
ACS Photonics **1**, 530–537, (2014).

[24] M. Schäferling, N. Engheta, H. Giessen, and T. Weiss.
Reducing the Complexity: Enantioselective Chiral Near-Fields by Diagonal Slit and Mirror Configuration.
ACS Photonics **3**, 1076–1084, (2016).

[25] S. Mukamel.
Principles of nonlinear optical spectroscopy.
First edition. Oxford University Press, New York, (1995).

[26] D. M. Jonas.
Two-dimensional femtosecond spectroscopy.
Annual Review of Physical Chemistry **54**, 425–463, (2003).

[27] T. Brixner, T. Mančal, I. V. Stiopkin, and G. R. Fleming.
Phase-stabilized two-dimensional electronic spectroscopy.
The Journal of Chemical Physics **121**, 4221–4236, (2004).

[28] M. Cho.
Two-Dimensional Optical Spectroscopy.
CRC Press, Boca Raton, FL, (2009).

[29] L. Lepetit, G. Chériaux, and M. Joffre.
Linear techniques of phase measurement by femtosecond spectral interferometry for applications in spectroscopy.
Journal of the Optical Society of America B: Optical Physics **12**, 2467–2474, (1995).

[30] P. Tuchscherer.
A Route to Optical Spectroscopy on the Nanoscale.
Dissertation, Universität Würzburg, (2012).

[31] J. D. Hybl, A. Albrecht Ferro, and D. M. Jonas.
Two-dimensional Fourier transform electronic spectroscopy.
The Journal of Chemical Physics **115**, 6606, (2001).

[32] O. Golonzka, M. Khalil, N. Demirdöven, and A. Tokmakoff.
Vibrational Anharmonicities Revealed by Coherent Two-Dimensional Infrared Spectroscopy.
Physical Review Letters **86**, 2154–2157, (2001).

[33] M. T. Zanni, N.-H. Ge, Y. S. Kim, and R. M. Hochstrasser.
Two-dimensional IR spectroscopy can be designed to eliminate the diagonal peaks and expose only the crosspeaks needed for structure determination.
Proceedings of the National Academy of Sciences **98**, 11265–11270, (2001).

[34] C. Cohen-Tannoudji, J. Dupont-Roc, and G. Grynberg.
Atom - Photon Interactions: Basic Process and Appilcations.
Wiley-VCH Verlag GmbH & Co. KGaA, Weinheim, (2004).

[35] T. K. Yee and T. K. Gustafson.
Diagrammatic analysis of the density operator for nonlinear optical calculations: Pulsed and cw responses.
Physical Review A **18**, 1597–1617, (1978).

[36] S. A. J. Druet and J.-P. E. Taran.
Cars spectroscopy.
Progress in Quantum Electronics **7**, 1–72, (1981).

[37] H.-S. Tan.
Theory and phase-cycling scheme selection principles of collinear phase coherent multi-dimensional optical spectroscopy.
The Journal of Chemical Physics **129**, 124501, (2008).

[38] O. Schmidt, M. Bauer, C. Wiemann, R. Porath, M. Scharte, O. Andreyev, G. Schönhense, and M. Aeschlimann.
Time-resolved two photon photoemission electron microscopy.
Applied Physics B: Lasers and Optics **74**, 223–227, (2002).

[39] D. Keusters, H.-S. Tan, and W. S. Warren.
Role of pulse phase and direction in two-dimensional optical spectroscopy.
The Journal of Physical Chemistry A **103**, 10369–10380, (1999).

[40] P. Tian, D. Keusters, Y. Suzaki, and W. S. Warren.
Femtosecond phase-coherent two-dimensional spectroscopy.
Science **300**, 1553–1555, (2003).

[41] A. M. Weiner, J. P. Heritage, and E. M. Kirschner.
High-resolution femtosecond pulse shaping.
Journal of the Optical Society of America B **5**, 1563–1572, (1988).

[42] M. M. Wefers and K. A. Nelson.
Generation of high-fidelity programmable ultrafast optical waveforms.
Optics Letters **20**, 1047–1049, (1995).

[43] A. M. Weiner.
Femtosecond Pulse Shaping Using Spatial Light Modulators.
Review of Scientific Instruments **71**, 1929–1960, (2000).

[44] C. Strüber.
Ultrafast coherent control and multidimensional spectroscopy on the nanoscale.
Dissertation, Universität Bielefeld, (2014).

[45] A. Galler and T. Feurer.
Pulse shaper assisted short laser pulse characterization.
Applied Physics B: Lasers and Optics **90**, 427–430, (2008).

[46] C. E. Shannon.
Communication in the presence of noise.
Proceedings of the IRE **37**, 10–21, (1949).

[47] H. Nyquist.
Certain Topics in Telegraph Transmission Theory.
Proceedings of the IEEE **90**, 280 – 305, (2002).

[48] S. Fechner.
Quantenkontrolle im Zeit-Frequenz-Phasenraum.
Dissertation, Universität Würzburg, (2008).

[49] R. Trebino.
Frequency-resolved optical gating: the measurement of ultrashort laser pulses.
Springer, New York, (2002).

[50] C. Iaconis and I. Walmsley.
Spectral phase interferometry for direct electric-field reconstruction of ultrashort optical pulses.
Optics Letters **23**, 792–794, (1998).

[51] D. N. Fittinghoff, J. L. Bowie, J. N. Sweetser, R. T. Jennings, M. A. Krumbügel, K. W. DeLong, R. Trebino, and I. A. Walmsley.
Measurement of the intensity and phase of ultraweak, ultrashort laser pulses.
Optics Letters **21**, 884–886, (1996).

[52] C. Schneider.
Mapping of surface plasmon polariton fields by time-resolved photoemission electron microscopy: experiments, simulations, and applications.
Dissertation, Technische Universität Kaiserslautern, (2013).

[53] P. Melchior.
Plasmonic Near-Field and Magnetic Domain Imaging by Laser-based Photoemission Electron Microscopy.
Dissertation, Technische Universität Kaiserslautern, (2014).

[54] M. A. Green.
Thin-film solar cells: review of materials, technologies and commercial status.
Journal of Materials Science: Materials in Electronics **18**, 15–19, (2007).

[55] G. Beaucarne.
Silicon Thin-Film Solar Cells.
Advances in OptoElectronics **2007**, 36970, (2007).

[56] A. V. Shah, H. Schade, M. Vanecek, J. Meier, E. Vallat-Sauvain, N. Wyrsch, U. Kroll, C. Droz, and J. Bailat.
Thin-film silicon solar cell technology.
Progress in Photovoltaics: Research and Applications **12**, 113–142, (2004).

[57] A. Shah, P. Torres, R. Tscharner, N. Wyrsch, and H. Keppner.
Photovoltaic Technology: The Case for Thin-Film Solar Cells.
Science **285**, 692–698, (1999).

[58] J. Zhao and M. Green.
Optimized antireflection coatings for high-efficiency silicon solar cells.
IEEE Transactions on Electron Devices **38**, 1925–1934, (1991).

[59] V. E. Ferry, M. A. Verschuuren, H. B. T. Li, E. Verhagen, R. J. Walters, R. E. I. Schropp, H. A. Atwater, and A. Polman.
Light trapping in ultrathin plasmonic solar cells.
Optics Express **18**, A237–A245, (2010).

[60] F. Lükermann, U. Heinzmann, and H. Stiebig.
Plasmon enhanced resonant defect absorption in thin a-Si:H n-i-p devices.
Applied Physics Letters **100**, 253907, (2012).

[61] H. A. Atwater and A. Polman.
Plasmonics for improved photovoltaic devices.
Nature Materials **9**, 205–213, (2010).

[62] I. Tobías, A. Luque, and A. Martí.
Light intensity enhancement by diffracting structures in solar cells.
Journal of Applied Physics **104**, 034502, (2008).

[63] P. Bermel, C. Luo, L. Zeng, L. C. Kimerling, and J. D. Joannopoulos.
Improving thin-film crystalline silicon solar cell efficiencies with photonic crystals.
Optics Express **15**, 16986–17000, (2007).

[64] J. Müller, B. Rech, J. Springer, and M. Vanecek.
TCO and light trapping in silicon thin film solar cells.
Solar Energy **77**, 917–930, (2004).

[65] K. Vynck, M. Burresi, F. Riboli, and D. S. Wiersma.
Photon management in two-dimensional disordered media.
Nature Materials **11**, 1017–1022, (2012).

[66] E. Yablonovitch and G. Cody.
Intensity enhancement in textured optical sheets for solar cells.
IEEE Transactions on Electron Devices **29**, 300–305, (1982).

[67] Z. Yu, A. Raman, and S. Fan.
Fundamental limit of nanophotonic light trapping in solar cells.
Proceedings of the National Academy of Sciences **107**, 17491–17496, (2010).

[68] S. Basu Mallick, N. P. Sergeant, M. Agrawal, J.-Y. Lee, and P. Peumans.
Coherent light trapping in thin-film photovoltaics.
MRS Bulletin **36**, 453–460, (2011).

[69] P. W. Anderson.
Absence of Diffusion in Certain Random Lattices.
Physical Review **109**, 1492–1505, (1958).

[70] A. Lagendijk, B. v. Tiggelen, and D. S. Wiersma.
Fifty years of Anderson localization.
Physics Today **62**, 24–29, (2009).

[71] D. Differt.
Lokalisation ultrakurzer Laserpulse in randomisierten Nanostrukturen.
Dissertation, Universität Bielefeld, (2016).

[72] M. Merschdorf, W. Pfeiffer, A. Thon, S. Voll, and G. Gerber.
Photoemission from multiply excited surface plasmons in Ag nanoparticles.
Applied Physics A **71**, 547–552, (2000).

[73] G. Farkas, C. Toth, and A. Kohazi-Kis.
Above-threshold multiphoton photoelectric effect of a gold surface.
Optical Engineering **32**, 2476–2480, (1993).

[74] F. Guthrie.
On a New Relation between Heat and Electricity.
Proceedings of the Royal Society of London **21**, 168–169, (1872).

[75] O. W. Richardson.
The emission of electricity from hot bodies.
Longmans, Green & Co., London, (1921).

[76] D. Meschede.
Gerthsen Physik.
Springer, Berlin Heidelberg, (2006).

[77] P. Biswas, R. Atta-Fynn, and D. A. Drabold.
Experimentally constrained molecular relaxation: The case of hydrogenated amorphous silicon.
Physical Review B **76**, 125210, (2007).

[78] J. Dong and D. A. Drabold.
Atomistic Structure of Band-Tail States in Amorphous Silicon.
Physical Review Letters **80**, 1928–1931, (1998).

[79] I. N. Bronstein, K. A. Semendyayev, G. Musiol, and H. Muehlig.
Handbook of Mathematics.
Fourth edition. Springer, Berlin Heidelberg, (2004).

[80] M. P. V. Albada and A. Lagendijk.
Observation of Weak Localization of Light in a Random Medium.
Physical Review Letters **55**, 2692–2695, (1985).

[81] D. E. Khmel'nitskii.
Localization and coherent scattering of electrons.
Physica B+C **126**, 235–241, (1984).

[82] D. S. Wiersma, P. Bartolini, A. Lagendijk, and R. Righini.
Localization of light in a disordered medium.
Nature **390**, 671–673, (1997).

[83] P. A. Lee and T. V. Ramakrishnan.
Disordered electronic systems.
Reviews of Modern Physics **57**, 287–337, (1985).

[84] E. Abrahams, P. W. Anderson, D. C. Licciardello, and T. V. Ramakrishnan.
Scaling Theory of Localization: Absence of Quantum Diffusion in Two Dimensions.
Physical Review Letters **42**, 673–676, (1979).

[85] S. I. Bozhevolnyi, V. S. Volkov, E. Devaux, J.-Y. Laluet, and T. W. Ebbesen.
Channel plasmon subwavelength waveguide components including interferometers and ring resonators.
Nature **440**, 508–511, (2006).

[86] M. L. Brongersma and V. M. Shalaev.
The Case for Plasmonics.
Science **328**, 440 –441, (2010).

[87] D. K. Gramotnev and S. I. Bozhevolnyi.
Plasmonics beyond the diffraction limit.
Nature Photonics **4**, 83–91, (2010).

[88] A. J. Haes and R. P. V. Duyne.
A unified view of propagating and localized surface plasmon resonance biosensors.
Analytical and Bioanalytical Chemistry **379**, 920–930, (2004).

[89] M. Rycenga, C. M. Cobley, J. Zeng, W. Li, C. H. Moran, Q. Zhang, D. Qin, and Y. Xia.
Controlling the Synthesis and Assembly of Silver Nanostructures for Plasmonic Applications.
Chemical Reviews **111**, 3669–3712, (2011).

[90] J. Takahara, S. Yamagishi, H. Taki, A. Morimoto, and T. Kobayashi.
Guiding of a one-dimensional optical beam with nanometer diameter.
Optics Letters **22**, 475–477, (1997).

[91] E. Moreno, F. J. Garcia-Vidal, S. G. Rodrigo, L. Martin-Moreno, and S. I. Bozhevolnyi.
Channel plasmon-polaritons: modal shape, dispersion, and losses.
Optics Letters **31**, 3447–3449, (2006).

[92] C. Lemke, T. Leißner, S. Jauernik, A. Klick, J. Fiutowski, J. Kjelstrup-Hansen, H.-G. Rubahn, and M. Bauer.
Mapping surface plasmon polariton propagation via counter-propagating light pulses.
Optics Express **20**, 12877–12884, (2012).

[93] C. Rewitz, T. Keitzl, P. Tuchscherer, J.-S. Huang, P. Geisler, G. Razinskas, B. Hecht, and T. Brixner.
Ultrafast Plasmon Propagation in Nanowires Characterized by Far-Field Spectral Interferometry.
Nano Letters **12**, 45–49, (2012).

[94] R. Zia, J. A. Schuller, A. Chandran, and M. L. Brongersma.
Plasmonics: the next chip-scale technology.
Materials Today **9**, 20–27, (2006).

[95] C. Rewitz, G. Razinskas, P. Geisler, E. Krauss, S. Goetz, M. Pawłowska, B. Hecht, and T. Brixner.
Coherent Control of Plasmon Propagation in a Nanocircuit.
Physical Review Applied **1**, 014007, (2014).

[96] S. Kumar, N. I. Kristiansen, A. Huck, and U. L. Andersen.
Generation and Controlled Routing of Single Plasmons on a Chip.
Nano Letters **14**, 663–669, (2014).

[97] M. Hensen.
Concentrating Light: Nano-devices for spectroscopy, ultra-fast current injection and energy transport.
Dissertation, Universität Bielefeld, (2016).

[98] P. B. Johnson and R. W. Christy.
Optical Constants of the Noble Metals.
Physical Review B **6**, 4370–4379, (1972).

[99] W. L. Barnes.
Surface plasmon–polariton length scales: a route to sub-wavelength optics.
Journal of Optics A: Pure and Applied Optics **8**, S87, (2006).

[100] E. J. R. Vesseur, F. J. García de Abajo, and A. Polman.
Modal Decomposition of Surface-Plasmon Whispering Gallery Resonators.
Nano Letters **9**, 3147–3150, (2009).

[101] E. J. R. Vesseur and A. Polman.
Plasmonic Whispering Gallery Cavities As Optical Nanoantennas.
Nano Letters **11**, 5524–5530, (2011).

[102] Y. S. Joe, A. M. Satanin, and C. S. Kim.
Classical analogy of Fano resonances.
Physica Scripta **74**, 259, (2006).

[103] Z. Guo, Y. Zhang, Y. DuanMu, L. Xu, S. Xie, and N. Gu.
Facile synthesis of micrometer-sized gold nanoplates through an aniline-assisted route in ethylene glycol solution.
Colloids and Surfaces A: Physicochemical and Engineering Aspects **278**, 33–38, (2006).

[104] X. Wu, R. Kullock, E. Krauss, and B. Hecht.
Single-crystalline gold microplates grown on substrates by solution-phase synthesis.
Crystal Research and Technology **50**, 595–602, (2015).

[105] J.-S. Huang, V. Callegari, P. Geisler, C. Brüning, J. Kern, J. C. Prangsma, X. Wu, T. Feichtner, J. Ziegler, P. Weinmann, M. Kamp, A. Forchel, P. Biagioni, U. Sennhauser, and B. Hecht.
Atomically flat single-crystalline gold nanostructures for plasmonic nanocircuitry.
Nature Communications **1**, 150, (2010).

[106] K.-P. Chen, V. P. Drachev, J. D. Borneman, A. V. Kildishev, and V. M. Shalaev.
Drude Relaxation Rate in Grained Gold Nanoantennas.
Nano Letters **10**, 916–922, (2010).

[107] X. Wu, P. Geisler, E. Krauss, R. Kullock, and B. Hecht.
Silica–gold bilayer-based transfer of focused ion beam-fabricated nanostructures.
Nanoscale **7**, 16427–16433, (2015).

[108] D. T. Schoen, T. Coenen, F. J. García de Abajo, M. L. Brongersma, and A. Polman.
The Planar Parabolic Optical Antenna.
Nano Letters **13**, 188–193, (2013).

[109] M. Merschdorf, C. Kennerknecht, and W. Pfeiffer.
Collective and single-particle dynamics in time-resolved two-photon photoemission.
Physical Review B **70**, 193401, (2004).

[110] A. Kiejna and K. F. Wojciechowski.
Metal Surface Electron Physics.
First edition. Pergamon, Oxford, (1996).

[111] C. A. Marocico and J. Knoester.
Intermolecular resonance energy transfer in the presence of a dielectric cylinder.
Physical Review A **79**, 053816, (2009).

[112] D. Martín-Cano, L. Martín-Moreno, F. J. García-Vidal, and E. Moreno.
Resonance Energy Transfer and Superradiance Mediated by Plasmonic Nanowaveguides.
Nano Letters **10**, 3129–3134, (2010).

[113] P. Törmä and W. L. Barnes.
Strong coupling between surface plasmon polaritons and emitters: a review.
Reports on Progress in Physics **78**, 013901, (2015).

[114] R. Chikkaraddy, B. de Nijs, F. Benz, S. J. Barrow, O. A. Scherman, E. Rosta, A. Demetriadou, P. Fox, O. Hess, and J. J. Baumberg.
Single-molecule strong coupling at room temperature in plasmonic nanocavities.
Nature **535**, 127–130, (2016).

[115] L. D. Barron.
Molecular light scattering and optical activity.
Cambridge University Press, Cambridge, (2004).

[116] P. Fischer and F. Hache.
Nonlinear optical spectroscopy of chiral molecules.
Chirality **17**, 421–437, (2005).

[117] M. Bonmarin and J. Helbing.
Polarization control of ultrashort mid-IR laser pulses for transient vibrational circular dichroism measurements.
Chirality **21**, E298–E306, (2009).

[118] A. Trivonov, I. Buchvarov, A. Lohr, F. Würthner, and T. Fiebig.
Broadband femtosecond circular dichroism spectrometer with white-light polarization control.
Review of Scientific Instruments **81**, 1–6, (2010).

[119] H. Rhee, I. Eom, S.-H. Ahn, and M. Cho.
Coherent electric field characterization of molecular chirality in the time domain.
Chemical Society Reviews **41**, 4457–4466, (2012).

[120] A. Steinbacher, J. Buback, P. Nuernberger, and T. Brixner.
Precise and Rapid Detection of Optical Activity for Accumulative Femtosecond Spectroscopy.
Optics Express **20**, 11838–11854, (2012).

[121] J. Meyer-Ilse, D. Akimov, and B. Dietzek.
Recent advances in ultrafast time-resolved chirality measurements: perspective and outlook.
Laser & Photonics Reviews **7**, 495–505, (2013).

[122] K. Hiramatsu and T. Nagata.
Communication: Broadband and ultrasensitive femtosecond time-resolved circular dichroism spectroscopy.
The Journal of Chemical Physics **143**, 121102, (2015).

[123] D. M. Lipkin.
Existence of a New Conservation Law in Electromagnetic Theory.
Journal of Mathematical Physics **5**, 696–700, (1964).

[124] Y. Tang and A. E. Cohen.
Optical Chirality and Its Interaction with Matter.
Physical Review Letters **104**, 163901, (2010).

[125] J. S. Choi and M. Cho.
Limitations of a superchiral field.
Physical Review A **86**, 063834, (2012).

[126] D. P. Craig and T. Thirunamachandran.
New approaches to chiral discrimination in coupling between molecules.
Theoretical Chemistry Accounts **102**, 112–120, (1999).

[127] Y. Tang and A. E. Cohen.
Enhanced Enantioselectivity in Excitation of Chiral Molecules by Superchiral Light.
Science **332**, 333–336, (2011).

[128] B. K. Canfield, S. Kujala, K. Laiho, K. Jefimovs, J. Turunen, and M. Kauranen.
Chirality arising from small defects in gold nanoparticle arrays.
Optics Express **14**, 950–955, (2006).

[129] S. Zhang, H. Wei, K. Bao, U. Håkanson, N. J. Halas, P. Nordlander, and H. Xu.
Chiral Surface Plasmon Polaritons on Metallic Nanowires.
Physical Review Letters **107**, 096801, (2011).

[130] A. Guerrero-Martínez, J. L. Alonso-Gómez, B. Auguié, M. M. Cid, and L. M. Liz-Marzán.
From individual to collective chirality in metal nanoparticles.
Nano Today **6**, 381–400, (2011).

[131] Z. Fan and A. O. Govorov.
Chiral Nanocrystals: Plasmonic Spectra and Circular Dichroism.
Nano Letters **12**, 3283–3289, (2012).

[132] F. Eftekhari and T. J. Davis.
Strong chiral optical response from planar arrays of subwavelength metallic structures supporting surface plasmon resonances.
Physical Review B **86**, 075428, (2012).

[133] A. Christofi, N. Stefanou, G. Gantzounis, and N. Papanikolaou.
Giant Optical Activity of Helical Architectures of Plasmonic Nanorods.
The Journal of Physical Chemistry C **116**, 16674–16679, (2012).

[134] I. Fernandez-Corbaton, M. Fruhnert, and C. Rockstuhl.
Dual and Chiral Objects for Optical Activity in General Scattering Directions.
ACS Photonics **2**, 376–384, (2015).

[135] I. Fernandez-Corbaton, M. Fruhnert, and C. Rockstuhl.
Objects of Maximum Electromagnetic Chirality.
Physical Review X **6**, 031013, (2016).

[136] B. Hopkins, A. N. Poddubny, A. E. Miroshnichenko, and Y. S. Kivshar.
Circular dichroism induced by Fano resonances in planar chiral oligomers.
Laser & Photonics Reviews **10**, 137–146, (2016).

[137] A. Papakostas, A. Potts, D. M. Bagnall, S. L. Prosvirnin, H. J. Coles, and N. I. Zheludev.
Optical Manifestations of Planar Chirality.
Physical Review Letters **90**, 107404, (2003).

[138] A. V. Rogacheva, V. A. Fedotov, A. S. Schwanecke, and N. I. Zheludev.
Giant Gyrotropy due to Electromagnetic-Field Coupling in a Bilayered Chiral Structure.
Physical Review Letters **97**, 177401, (2006).

[139] V. K. Valev, N. Smisdom, A. V. Silhanek, B. De Clercq, W. Gillijns, M. Ameloot, V. V. Moshchalkov, and T. Verbiest.
Plasmonic Ratchet Wheels: Switching Circular Dichroism by Arranging Chiral Nanostructures.
Nano Letters **9**, 3945–3948, (2009).

[140] J. K. Gansel, M. Thiel, M. S. Rill, M. Decker, K. Bade, V. Saile, G. v. Freymann, S. Linden, and M. Wegener.
Gold Helix Photonic Metamaterial as Broadband Circular Polarizer.
Science **325**, 1513–1515, (2009).

[141] B. Auguié, J. L. Alonso-Gómez, A. Guerrero-Martínez, and L. M. Liz-Marzán.
Fingers Crossed: Optical Activity of a Chiral Dimer of Plasmonic Nanorods.
The Journal of Physical Chemistry Letters **2**, 846–851, (2011).

[142] C. Helgert, E. Pshenay-Severin, M. Falkner, C. Menzel, C. Rockstuhl, E.-B. Kley, A. Tünnermann, F. Lederer, and T. Pertsch.
Chiral Metamaterial Composed of Three-Dimensional Plasmonic Nanostructures.
Nano Letters **11**, 4400–4404, (2011).

[143] M. Hentschel, M. Schäferling, T. Weiss, N. Liu, and H. Giessen.
Three-Dimensional Chiral Plasmonic Oligomers.
Nano Letters **12**, 2542–2547, (2012).

[144] X. Shen, C. Song, J. Wang, D. Shi, Z. Wang, N. Liu, and B. Ding.
Rolling Up Gold Nanoparticle-Dressed DNA Origami into Three-Dimensional Plasmonic Chiral Nanostructures.
Journal of the American Chemical Society **134**, 146–149, (2012).

[145] Y. Zhao, M. A. Belkin, and A. Alù.
Twisted optical metamaterials for planarized ultrathin broadband circular polarizers.
Nature Communications **3**, 870, (2012).

[146] X. Yin, M. Schäferling, B. Metzger, and H. Giessen.
Interpreting Chiral Nanophotonic Spectra: The Plasmonic Born–Kuhn Model.
Nano Letters **13**, 6238–6243, (2013).

[147] V. K. Valev, J. J. Baumberg, C. Sibilia, and T. Verbiest.
Chirality and Chiroptical Effects in Plasmonic Nanostructures: Fundamentals, Recent Progress, and Outlook.
Advanced Materials **25**, 2517–2534, (2013).

[148] A. O. Govorov.
Plasmon-Induced Circular Dichroism of a Chiral Molecule in the Vicinity of Metal Nanocrystals. Application to Various Geometries.
The Journal of Physical Chemistry C **115**, 7914–7923, (2011).

[149] A. O. Govorov and Z. Fan.
Theory of Chiral Plasmonic Nanostructures Comprising Metal Nanocrystals and Chiral Molecular Media.
ChemPhysChem **13**, 2551–2560, (2012).

[150] A. García-Etxarri and J. A. Dionne.
Surface-enhanced circular dichroism spectroscopy mediated by nonchiral nanoantennas.
Physical Review B **87**, 235409, (2013).

[151] H. Zhang and A. O. Govorov.
Giant circular dichroism of a molecule in a region of strong plasmon resonances between two neighboring gold nanocrystals.
Physical Review B **87**, 075410, (2013).

[152] T. J. Davis and D. E. Gómez.
Interaction of localized surface plasmons with chiral molecules.
Physical Review B **90**, 235424, (2014).

[153] M. L. Nesterov, X. Yin, M. Schäferling, H. Giessen, and T. Weiss.
The Role of Plasmon-Generated Near Fields for Enhanced Circular Dichroism Spectroscopy.
ACS Photonics **3**, 578–583, (2016).

[154] E. Hendry, T. Carpy, J. Johnston, M. Popland, R. V. Mikhaylovskiy, A. J. Lapthorn, S. M. Kelly, L. D. Barron, N. Gadegaard, and M. Kadodwala.
Ultrasensitive detection and characterization of biomolecules using superchiral fields.
Nature Nanotechnology **5**, 783–787, (2010).

[155] N. A. Abdulrahman, Z. Fan, T. Tonooka, S. M. Kelly, N. Gadegaard, E. Hendry, A. O. Govorov, and M. Kadodwala.
Induced Chirality through Electromagnetic Coupling between Chiral Molecular Layers and Plasmonic Nanostructures.
Nano Letters **12**, 977–983, (2012).

[156] B. M. Maoz, Y. Chaikin, A. B. Tesler, O. Bar Elli, Z. Fan, A. O. Govorov, and G. Markovich.
Amplification of Chiroptical Activity of Chiral Biomolecules by Surface Plasmons.
Nano Letters **13**, 1203–1209, (2013).

[157] W. Ma, H. Kuang, L. Xu, L. Ding, C. Xu, L. Wang, and N. A. Kotov.
Attomolar DNA detection with chiral nanorod assemblies.
Nature Communications **4**, 2689, (2013).

[158] Y. Zhao, L. Xu, W. Ma, L. Wang, H. Kuang, C. Xu, and N. A. Kotov.
Shell-Engineered Chiroplasmonic Assemblies of Nanoparticles for Zeptomolar DNA Detection.
Nano Letters **14**, 3908–3913, (2014).

[159] R. Tullius, A. S. Karimullah, M. Rodier, B. Fitzpatrick, N. Gadegaard, L. D. Barron, V. M. Rotello, G. Cooke, A. Lapthorn, and M. Kadodwala.
"Superchiral" Spectroscopy: Detection of Protein Higher Order Hierarchical Structure with Chiral Plasmonic Nanostructures.
Journal of the American Chemical Society **137**, 8380–8383, (2015).

[160] J. Yan, S. Hou, Y. Ji, and X. Wu.
Heat-enhanced symmetry breaking in dynamic gold nanorod oligomers: the importance of interface control.
Nanoscale **8**, 10030–10034, (2016).

[161] M. Schäferling, X. Yin, and H. Giessen.
Formation of chiral fields in a symmetric environment.
Optics Express **20**, 26326–26336, (2012).

[162] T. J. Davis and E. Hendry.
Superchiral electromagnetic fields created by surface plasmons in nonchiral metallic nanostructures.
Physical Review B **87**, 085405, (2013).

[163] D. Lin and J.-S. Huang.
Slant-gap plasmonic nanoantennas for optical chirality engineering and circular dichroism enhancement.
Optics Express **22**, 7434–7445, (2014).

[164] S. Yoo, M. Cho, and Q.-H. Park.
Globally enhanced chiral field generation by negative-index metamaterials.
Physical Review B **89**, 161405, (2014).

[165] M. I. Stockman, S. V. Faleev, and D. J. Bergman.
Coherent control of femtosecond energy localization in nanosystems.
Physical Review Letters **88**, 067402, (2002).

[166] M. I. Stockman and P. Hewageegana.
Nanolocalized Nonlinear Electron Photoemission under Coherent Control.
Nano Letters **5**, 2325–2329, (2005).

[167] M. I. Stockman.
Nanoplasmonics: past, present, and glimpse into future.
Optics Express **19**, 22029–22106, (2011).

[168] M. Aeschlimann, M. Bauer, D. Bayer, T. Brixner, F. J. García de Abajo, W. Pfeiffer, M. Rohmer, C. Spindler, and F. Steeb.
Adaptive subwavelength control of nano-optical fields.
Nature **446**, 301–304, (2007).

[169] P. Tuchscherer, C. Rewitz, D. V. Voronine, F. J. García de Abajo, W. Pfeiffer, and T. Brixner.
Analytic coherent control of plasmon propagation in nanostructures.
Optics Express **17**, 14235–14259, (2009).

[170] M. Aeschlimann, M. Bauer, D. Bayer, T. Brixner, S. Cunovic, A. Fischer, P. Melchior, W. Pfeiffer, M. Rohmer, C. Schneider, C. Strüber, P. Tuchscherer, and D. V. Voronine.
Optimal open-loop near-field control of plasmonic nanostructures.
New Journal of Physics **14**, 033030, (2012).

[171] W. Pfeiffer, M. Aeschlimann, and T. Brixner.
Coherent control of nano-optical excitations.
In M. Agio and A. Alù (Eds.), *Optical Antennas*, pp. 135–156. Cambridge University Press, Cambridge, (2013).

[172] F. J. García de Abajo.
Interaction of Radiation and Fast Electrons with Clusters of Dielectrics: A Multiple Scattering Approach.
Physical Review Letters **82**, 2776, (1999).

[173] T. Brixner.
Adaptive Femtosecond Quantum Control.
Dissertation, Universität Würzburg, (2001).

[174] T. Brixner.
Poincaré representation of polarization-shaped femtosecond laser pulses.
Applied Physics B: Lasers and Optics **76**, 531–540, (2003).

[175] H. Poincaré.
Théorie mathématique de la lumière II. Nouvelles études sur la diffraction.–Théorie de la dispersion de Helmholtz.
Georges Carré, Paris, (1892).

[176] T. Brixner and G. Gerber.
Femtosecond polarization pulse shaping.
Optics Letters **26**, 557–559, (2001).

[177] T. Brixner, G. Krampert, P. Niklaus, and G. Gerber.
Generation and characterization of polarization-shaped femtosecond laser pulses.
Applied Physics B: Lasers and Optics **74**, 133–144, (2002).

[178] R. Selle, P. Nuernberger, F. Langhojer, F. Dimler, S. Fechner, G. Gerber, and T. Brixner.
Generation of polarization-shaped ultraviolet femtosecond pulses.
Optics Letters **33**, 803–805, (2008).

[179] P. Nuernberger, R. Selle, F. Langhojer, F. Dimler, S. Fechner, G. Gerber, and T. Brixner.
Polarization-shaped femtosecond laser pulses in the ultraviolet.
Journal of Optics A: Pure and Applied Optics **11**, 085202, (2009).

[180] M. Plewicki, S. Weber, F. Weise, and A. Lindinger.
Independent control over the amplitude, phase, and polarization of femtosecond pulses.
Applied Physics B **86**, 259–263, (2006).

[181] L. Polachek, D. Oron, and Y. Silberberg.
Full control of the spectral polarization of ultrashort pulses.
Optics Letters **31**, 631–633, (2006).

[182] M. Ninck, A. Galler, T. Feurer, and T. Brixner.
Programmable common-path vector field synthesizer for femtosecond pulses.
Optics Letters **32**, 3379–3381, (2007).

[183] O. Masihzadeh, P. Schlup, and R. A. Bartels.
Complete polarization state control of ultrafast laser pulses with a single linear spatial light modulator.
Optics Express **15**, 18025–18032, (2007).

[184] F. Weise and A. Lindinger.
Full control over the electric field using four liquid crystal arrays.
Optics Letters **34**, 1258–1260, (2009).

[185] C. Schwarz, O. Hüter, and T. Brixner.
Full vector-field control of ultrashort laser pulses utilizing a single dual-layer spatial light modulator in a common-path setup.
Journal of the Optical Society of America B: Optical Physics **32**, 933–945, (2015).

[186] J. Petersen, J. Volz, and A. Rauschenbeutel.
Chiral nanophotonic waveguide interface based on spin-orbit interaction of light.
Science **346**, 67–71, (2014).

[187] J. R. Rouxel, V. Y. Chernyak, and S. Mukamel.
Non-local real-space analysis of chiral optical signals.
Chemical Science **7**, 6824–6831, (2016).

[188] F. Träger.
Springer handbook of lasers and optics.
Second edition. Springer, Berlin, (2012).

Danksagung (Acknowledgements)

Zum Abschluss will ich die Gelegenheit nutzen, mich bei all denjenigen zu bedanken, die mich während meiner Zeit als Doktorand unterstützt und entweder direkt oder indirekt zu den Ergebnissen dieser Dissertation beigetragen haben. Ohne diese Personen wäre meine Doktorarbeit in dieser Form nicht möglich gewesen. Mein besonderer Dank gilt

- meinem Doktorvater **Prof. Dr. Tobias Brixner**, der mir die Möglichkeit gegeben hat, in seiner Arbeitsgruppe an einem spannenden Forschungsgebiet zu arbeiten. Insbesondere möchte ich mich bei ihm für die Sicherstellung der Finanzierung meiner Doktorandenstelle bedanken sowie für das Vertrauen, das er mir entgegengebracht hat. Er hat mir den Freiraum gelassen, meine eigenen Ideen zu entwickeln und umzusetzen, war dabei aber auch immer darauf bedacht, die einzelnen Projekte in die richtigen Bahnen zu lenken.

- **Prof. Dr. Walter Pfeiffer**, der innerhalb des „near-field control“ (NFC) Projektes ein wichtiger Diskussionspartner war und das Projekt mit seiner Erfahrung, seinem Wissen und seinen Ideen stets vorangetrieben hat.

- **Prof. Dr. Martin Aeschlimann**, der für das NFC Projekt sein Labor zur Verfügung gestellt hat und während der Messzeiten in Kaiserslautern immer ein offenes Ohr für das NFC Team hatte.

- **allen ehemaligen und aktuellen Mitgliedern des NFC Teams** für das exzellente Teamwork und jedem einzelnen für seinen Beitrag zu den erreichten Forschungsergebnissen. Gerade während der Messzeiten war es wichtig, immer an einem Strang zu ziehen und sich bei Rückschlägen nicht unterkriegen zu lassen. Es hat jedesmal Spaß gemacht, nach Kaiserslautern zu fahren und in dieser angenehmen Atmosphäre zu arbeiten. Namentlich seien hier erwähnt:
  Dr. Alexander Fischer, **Benjamin Frisch**, **Dr. Matthias Hensen**, **Bernhard Huber**, **Dr. Pascal Melchior**, **Dr. Martin Piecuch**, **Dr. Christian Schneider**, **Dr. Christian Strüber**, **Dr. Philip Thielen**, **Dr. Philip Tuchscherer**, **Dr. Dmitri V. Voronine**.

- **Prof. Dr. Harald Giessen**, **Jun.-Prof. Dr. Thomas Weiss** und **Dr. Martin Schäferling** für die sehr gute und unkomplizierte Zusammenarbeit sowie für den zielgerichteten Meinungsaustauch. Im Speziellen möchte ich Martin für die MESME Simulationen danken und dafür, dass er jederzeit auf meine Fragen eingegangen ist und mir mit seiner Erfahrung sowie seinem Fachwissen enorm weitergeholfen hat.

- **Enno Krauss** für die Probenherstellung der elliptischen Goldkavitäten. An dieser Stelle auch vielen Dank an **Prof. Dr. Bert Hecht**, der diese Kooperation bereitwillig genehmigt und aktiv mitunterstützt hat.

- den Festangestellten unseres Lehrstuhls **Sabine Fuchs**, **Belinda Böhm**, **Andrea Gehring**, **Anna Rosenfeldt** und **Sandra Stoudek**, die durch ihre Tätigkeiten für einen reibungslosen organisatorischen Ablauf innerhalb der Arbeitsgruppe sorgen. Insbesondere möchte ich mich bei Andrea und Anna dafür bedanken, dass sie mir stets eine große Hilfe waren, wenn Probleme mit Anträgen und Formularen aufgetreten sind.

- **allen Angestellten der Elektronik- und Feinmechanik-Werkstatt** für die Bereitschaft, die Wünsche und Ideen der Gruppenmitglieder sachgemäß und zeitnah umzusetzen.

- **Dr. Roland Colditz** für die unkomplizierte Handhabung und Organisation des PC Praktikums.

- **Sabine Stahl** für ihre uneingeschränkte Hilfsbereitschaft und ihr stets zuvorkommendes Verhalten.

- **Prof. Dr. Patrick Nürnberger**, der sich nie für eine Diskussion zu schade war und einem mit seinem immensen Fachwissen stets weiterhelfen konnte.

- **all meinen (ehemaligen) Zimmerkollegen** für eine überaus angenehme Büroatmosphäre und den respektvollen Umgang miteinander. Im Speziellen möchte ich mich bei **Dr. Christoph Schwarz**, **Dr. Stefan Rützel**, **Dr. Andreas Steinbacher** und **Sebastian Röding** dafür bedanken, dass sie immer dazu bereit waren, mir bei Fragen und Problemen mit Rat und Tat zur Seite zu stehen.

- **Dr. Stefan Rützel**, **Dr. Andreas Steinbacher** und **Dr. Matthias Hensen** für das Korrekturlesen von Teilen dieser Arbeit.

- **allen ehemaligen und aktuellen Gruppenmitgliedern der PC1** für das tolle Arbeitsklima und die interessanten Diskussionen miteinander, die vor allem während der Mittags- und der später eingeführten Bananenpause entstanden sind. Es hat unheimlich viel Spaß gemacht, in dieser Gruppe zu arbeiten, vor allem aufgrund der großen Hilfsbereitschaft untereinander.
  An dieser Stelle möchte ich mich ganz besonders bei den Mitgliedern bedanken, mit denen ich meine Vorliebe für das Ansehen bzw. Besuchen von Sportereignissen teilen durfte: **Sebastian Götz**, **Dr. Matthias Hensen**, **Bernhard Huber**, **Dr. Federico Koch**, **Sebastian Röding**, **Dr. Stefan Rützel**, **Dr. Christoph Schwarz** und **Dr. Andreas Steinbacher**.

- meinen ehemaligen Kommilitonen und Freunden **Dr. Thomas Keitzl**, **Peter Kiefel**, **Dr. Christoph Klöffel**, **Dr. Andreas Kuhlmann**, **Dr. Jonathan Prechtel** und **Jan Salomon**, mit denen ich eine wunderschöne Studienzeit verbringen durfte und deren akademische bzw. berufliche Laufbahnen eine zusätzliche Motivation geliefert haben, die Doktorarbeit erfolgreich abzuschließen.

- all meinen Freunden aus vergangengen Schultagen, mit denen ich trotz teilweise großer räumlicher Distanzen immer noch regelmäßig Kontakt pflege: **Steffen Gebert**, **Dr. Friedrich Geiger**, **Eiko Gramlich**, **Sven Hausknecht**, **Tobias Hofmann**, **Sebastian Königer**, **Bastian Mattlener**, **Sebastian Ott**, **Stefan Philipp**, **Markus Scheller**, **Dr. Stefan Schuhladen** und **Johannes Uhde**. Die schönen gemeinsamen Erlebnisse in den letzten Jahren haben mir geholfen, den Kopf frei zu kriegen und anstehende Aufgaben mit neuem Elan anzugehen.

- meinen Schwiegereltern **Renate** und **Josef Schröder** sowie meiner Schwägerin **Nadine Schröder**. Sie haben mir stets gut zugesprochen und immer motivierend auf mich eingewirkt.

- meiner Schwester **Dr. Daniela Kramer** sowie meinem Bruder **Thomas Kramer** und dessen Familie (**Andrea**, **Greta** und **Frieda**). Sie waren mir immer eine große Stütze und haben mich oftmals an die wirklich wichtigen Dinge im Leben erinnert.

- meiner Großtante **Margarete Wolf** für ihre finanzielle und moralische Unterstützung während meiner akadamischen Ausbildung. Durch ihren Glauben an mich und meine Fähigkeiten hat sie mir auch in schwierigen Zeiten das Gefühl gegeben, meine Ziele erreichen zu können.

- meinen Eltern **Hildegard** und **Rudolf Kramer**, die mich auf meinem bisherigen Lebensweg immer tatkräftig unterstützt haben und auch heute noch jedesmal für mich da sind, wenn ich ihre Hilfe bzw. ihren Rat brauche.

- meiner Frau **Vanessa**, die mich mit ihrer positiven und optimistischen Denkweise vor allem immer dann aufgebaut hat, wenn es einmal nicht so gut lief. Ich möchte mich bei ihr auch für das Verständnis bedanken, das sie aufgebracht hat, wenn ich aufgrund von Messzeiten oder Schreibphasen nicht soviel Zeit für sie hatte. Vielen Dank Vanessa für deine bedingungslose Unterstützung, deine immense Geduld mit mir und für die Liebe, die du mir entgegenbringst.